



GRAZ UNIVERSITY OF TECHNOLOGY
INSTITUTE FOR
THERMAL TURBOMACHINERY AND MACHINE DYNAMICS



Innovative Numerical Calculation of Transitional Flow with Turbomachinery Application

Dipl.-Ing. (FH) Maria Elisabeth Collins

Doctoral Dissertation

submitted to the
Faculty of Mechanical Engineering and Economic Sciences
of Graz University of Technology
for the degree of a doctor of engineering sciences (Dr. techn.)

First Expert: Ao.Univ.-Prof. Dipl.-Ing. Dr.techn. Wolfgang SANZ

Second Expert: Ao.Univ.-Prof. Dipl.-Ing. Dr.techn. Reinhard WILLINGER

Graz, June 2012

Funded by the Austrian Aviation Programme TAKE OFF of the Austrian Research
Promotion Agency (FFG) / Federal Ministry for Transport, Innovation and
Technology within the Project CFD-TRANS

EIDESSTATTLICHE ERKLÄRUNG

Ich erkläre an Eides statt, dass ich die vorliegende Arbeit selbstständig verfasst, andere als die angegebenen Quellen/Hilfsmittel nicht benutzt und die den benutzten Quellen wörtlich und inhaltlich entnommenen Stellen als solche kenntlich gemacht habe.

Maria Elisabeth Collins

Graz, Juni 2012

STATUTORY DECLARATION

I declare that I have authored this thesis independently, that I have not used other than the declared sources / resources and that I have explicitly marked all material which has been quoted either literally or by content from the used sources.

Maria Elisabeth Collins

Graz, June 2012

“Anyone who has never made a mistake has never tried anything new.”

– Albert Einstein.

Acknowledgements

This work was done during my employment as a research assistant at the Institute for Thermal Turbomachinery and Machine Dynamics at the Graz University of Technology. At this point I want to thank all people, without whose support this work would not have been possible. Special thanks go to Univ.-Prof. Dr.-Ing. Franz Heitmeir who inspired me already during my studies at the FH Joanneum.

I would especially like to thank my doctoral thesis supervisor Ao.Univ.-Prof. Dr.techn. Wolfgang Sanz for giving me the chance to do this work and for supporting me throughout the whole project. He was at all times available for discussions.

I also want to acknowledge Ao.Univ.-Prof. Dipl.-Ing. Dr.techn. Reinhard Willinger for the review of my thesis.

Special thanks go to Dr. René Pecnik and to Dr. Paul Pieringer for being always accessible for my questions according the in-house flow solver LINARS, which was developed by them.

And not to be forgotten, I would like to thank my former diploma students Dipl.-Ing. Roland Burgstaller for supporting me during the validation of the different correlations for the transition model and Dipl.-Ing. Simon Dorfer for supporting me during the test rig construction as well as the measurement campaigns for the relaminarisation test case and Dipl.-Ing. Bünyamin Yagdi for supporting me with the new mesh generator and with the validation of different test cases.

Thanks go to my colleagues at the Institute for tolerating me as a CFD-guy and for having many amusing tee-, oh sorry, coffee-breaks and to Ao.Univ.-Prof. Dipl.-Ing. Dr.techn. Jakob Woisetschläger for the interesting discussions about everything under the sun.

I would like to thank my parents to support me during my studies, my friends Johanna and Manuela for tolerating me after work while talking about my activities and problems.

And last but not least I would like to thank my husband Herbert for helping me in every possible way and to be so appreciative and patient with me.

Financial support for this work was provided by the Austrian Aviation Programme TAKE OFF of the Austrian Research Promotion Agency (FFG) within the Project CFD-TRANS.

Maria Elisabeth Collins
Graz, June 2012

For my husband Herbert.

Kurzfassung

Die vorliegende Arbeit beschäftigt sich mit der korrekten Modellierung des Strömungsphänomens Transition in thermischen Turbomaschinen. Transition beschreibt den Übergang zwischen laminarer und turbulenter Strömung. Im Detail werden drei Transitionsmoden genauer betrachtet, die Bypass Transition, die ablöseinduzierte Transition und die Relaminarisierung.

Es werden zwei Modelle vorgestellt, die auf der Lösung der zeitlich gemittelte Navier-Stokes (RANS) Gleichungen basieren und in den institutseigenen Strömungslöser eingebaut sind. Das ζ - f Modell basiert auf der Idee des Reynolds Stress Transport Modells (RSTM), welches die Anisotropie der Transition modelliert. Das zweite vorgestellte Modell ist das $\gamma - Re_\theta$ Transitionsmodell, dessen Formulierung ohne lokale Grenzschichtparameter auskommt. Dieses Modell wird mit Hilfe dreier Korrelationen geschlossen, wobei nur eine davon in der originalen Modellbeschreibung enthalten ist. Für die restlichen zwei Korrelationen wurden Vorschläge von anderen Forschungsgruppen herangezogen, sowie eine eigene Korrelation entwickelt.

Die Validierung der beiden vorgestellten Modelle zeigt, dass beide Modelle gute Ergebnisse sowohl für die Bypass Transition als auch für die ablöseinduzierte Transition liefern können. Zusätzlich wurde das zweite Transitionsmodell mit der eigenen Korrelation auf den Transitionsmodus Relaminarisierung angewendet, und zeigt für 2D Testfälle eine sehr gute Übereinstimmung mit Messdaten.

Abstract

The correct modeling of the flow phenomenon transition in turbomachinery is the main goal of this work. This phenomenon describes the transition between laminar and turbulent flow in the boundary layer. Three different modes of transition are described in detail, by-pass transition, separation-induced transition as well as reverse transition, also called relaminarisation.

Two different models were presented, based on solving the Reynolds-averaged Navier-Stokes(RANS) equations, and implemented in the in-house flow solver. The ζ - f model is based on the idea of the Reynolds Stress Transport Model (RSTM), which also models the turbulent anisotropy. The second presented model is the $\gamma - Re_\theta$ transition model, which can be formulated without using any local boundary layer parameters. This model is closed with three empirical correlations, only one of them is given in the original work. Other research groups found solutions for the two missing correlations, and also an own in-house correlation was developed.

The validation of both presented models show for bypass transition as well as for separation-induced transition satisfying results. Additionally a validation of the second model with the in-house correlations for the transition mode relaminarisation shows a very good agreement to the experimental data.

Contents

1. Introduction	1
2. Basic Principles of Flow Modeling	4
2.1. Equations of Fluid Motion	4
2.2. Fluid Properties	5
2.3. RANS – Reynolds-Averaged Navier-Stokes	6
2.4. Turbulence Modeling in Turbomachinery Flows	9
2.4.1. Reynolds Stress Transport Model	11
2.4.2. Boussinesq-assumption for the $\overline{\rho u_i'' u_j''}$ -Tensor	13
2.5. Turbulence Models based on the Boussinesq approach	13
2.5.1. Spalart Allmaras Turbulence Model	13
2.5.2. Standard $k - \varepsilon$ Model	15
2.5.3. Wilcox $k - \omega$ Model	16
2.5.4. Menter $k - \omega$ shear-stress-transport (SST) Modell	16
3. Transition Modeling in Turbomachinery	18
3.1. Transition Modes	18
3.2. Transition Influencing Parameters	20
3.3. Modelling Approaches - State of the Art	21
3.3.1. Empirical Transition Models (intermittency concept)	22
3.3.2. Turbulence models with an extension for transition modeling derived from RSTM	26
4. Hanjalic $k - \varepsilon - \zeta - f$ Transition Model	27
4.1. Durbin's $v^2 f$ Model	27
4.2. Model Equations for ζ and f	29
4.3. Validation	30
4.3.1. Notes on Paper 1	31
4.3.2. Notes on Paper 2	32
Paper 1: Application of the zeta-f-turbulence model to steady transitional flow.	33
Paper 2: Application of the zeta-f-turbulence model to steady transitional flow.	46
5. $\gamma - Re_\theta$ Transition Model	53
5.1. Main Model Equations	53

5.2.	Coupling with the Turbulence Model	56
5.3.	Correlations for Re_{θ_c} , F_{length} and Re_{θ_t}	57
5.3.1.	Correlations for Re_{θ_t}	57
5.3.2.	Correlation by Elsner et al. (2008)	59
5.3.3.	Correlation by Sorensen (2009)	60
5.3.4.	Correlation by Malan et al. (2009)	61
5.3.5.	Correlation by Langtry and Menter (2009)	61
5.3.6.	Correlation by Kelterer	62
5.4.	Validation Part 1	63
5.4.1.	Notes on Paper 3	64
5.4.2.	Notes on Paper 4	65
	Paper 3: Computation of Laminar-Turbulent Transition in Turbomachinery Using The Correlation Based $\gamma - Re_{\theta}$ Transition Model.	67
	Paper 4: Application of the gamma-Retheta transition model to transitional flow.	78
6.	Relaminarisation	89
6.1.	Modes of Relaminarisation	89
6.2.	Valuation Methods for Relaminarisation	92
6.3.	Why is relaminarisation of interest?	94
6.4.	Notes on Paper 5	96
	Paper 5: Numerical Investigation of the Effect of Tip Leakage Flow on an Aggressive S-Shaped Intermediate Turbine Duct.	97
6.5.	Validation of the Relaminarisation Test Case TTMRelam	109
6.5.1.	Testcase Description: TTMRelam	109
6.5.2.	Experimental Results: TTMRelam	112
6.5.3.	Calculation Results: TTMRelam	113
6.6.	Validation of the Relaminarisation Test Case T100	115
6.6.1.	Testcase Description: T100	115
6.6.2.	Experimental Results: T100	117
6.6.3.	Calculation Results: T100	118
6.7.	Investigation of AIDA HP Stator	120
6.7.1.	Testcase Description: AIDA HP Stator	120
6.7.2.	Calculation Results: AIDA HP Stator	120
7.	Conclusion and Recommendations	123
A.	Appendix	125
	Bibliography	134
	Curriculum Vitae	135

List of Figures

2.1.	Classification of turbulence models according to their complexity	9
2.2.	Classification of turbulence models, from Lücke (1997)	10
3.1.	Natural Transition, from White (1974)	18
3.2.	Separation bubble, from Mayle (1991)	19
3.3.	Typical hot-wire measurement of velocity with the corresponding inter- mittency function, from Steelant and Dick (1996)	22
6.1.	Velocity and skin friction distribution in the case of relaminarisation in a diffusor caused by dissipation, from Narasimha and Sreenivasan (1979) . .	90
6.2.	Schematic diagram of relaminarisation in highly accelerated flows, from Sreenivasan (1982)	91
6.3.	Broad classification of the flow field into various regions, from Sreenivasan (1982)	92
6.4.	Relaminarisation in an accelerated boundary layer just before and after acceleration, from Narasimha and Sreenivasan (1979)	93
6.5.	AIDA: total pressure in plane C, comparison of CFD with experiments . .	95
6.6.	AIDA test turbine with HP turbine stage	109
6.7.	TTMRelam measurement section in the transonic wind tunnel, from Dor- fer (2011)	110
6.8.	TTMRelam measurement setup, from Dorfer (2011)	110
6.9.	Laser vibrometer design, from Köberl (2011)	111
6.10.	TTMRelam: LV measurement positions, from Dorfer (2011)	112
6.11.	TTMRelam power spectrum of scanning LV, from Dorfer (2011)	112
6.12.	TTMRelam: calculation grid	113
6.13.	TTMRelam: BL thickness and geometry of the counter contour	114
6.14.	TTMRelam: skin friction coefficient c_f and shape factor H_{12}	114
6.15.	Geometry of the T100 blade and positions of the hot film measurements, from Nichtawitz (2009)	115
6.16.	Schematical description of the hotfilm measurement method, from Nitsche and Brunn (2005)	116
6.17.	Typical time signals of laminar, transitional and turbulent flow measured with hot film probes, from Nichtawitz (2009)	116
6.18.	T100 data from the hot film measurements, from Nichtawitz (2009)	117
6.19.	T100 blade with pressure coefficient and hot film measurement positions .	118
6.20.	T100 acceleration parameter K and shape factor H_{12}	119

6.21. AIDA HP stator: multiblock mesh	121
6.22. AIDA HP stator: blade geometry at mid section and boundary layer thickness on the pressure side	121
6.23. AIDA HP stator: acceleration parameter K and shape factor H_{12} on the pressure side at mid section	122
A.1. Boundary layer thickness calculation, from Pecnik (2001)	126
A.2. Boundary layer edge velocity on pressure and suction side, from Schobeiri and Ozturk (2009)	127

List of Tables

2.1. RSTM unknowns	12
2.2. Outline of several RANS turbulence models	13
4.1. Constants for the $k - \varepsilon - \zeta - f$ model	30
6.1. TTMRelam: Boundary conditions for the calculation	113
6.2. Geometry data of the T100 cascade	115
6.3. T100: Boundary conditions for the calculation	116
6.4. AIDA HP stator: Boundary conditions for the calculation	120

Nomenclature

Latin Symbols

$a_1 = \sqrt{C_\mu}$	Bradshaw constant
c_f	skin friction coefficient
c_i	empirical constant
c_p	specific thermal energy with constant pressure
c_p	pressure coefficient
c_v	specific thermal energy with constant volume
e	total energy
E_i	destruction/relaminarisation term for different CFD models
f_i	vector of external mass forces
f	elliptic relaxation
F_i	blending function for different CFD models
g	gravity
h	heat transfer
H_{12}	shape factor
I_t	intermittency function
$k = \frac{1}{2}\overline{u_i''u_i''}$	turbulent kinetic energy
$K = \nu/U_\infty^2 dU/dx$	acceleration parameter
L	length scale
\mathcal{M}_{ij}	pressure acceleration term
$Ma = \sqrt{\kappa RT}$	konvective Mach-number
\mathcal{N}_{u_i}	Navier-Stokes operator
n_e	number of samples
n	dimensionful spot production parameter
\hat{n}	dimensionless spot production parameter

\mathcal{P}_{ij}	production of the Reynolds stresses
p	pressure
Pr	Prandtl number
P_i	production term for different CFD models
Q	generic source term
q_i	heat flow rate vector
R	gas constant
R_T	viscosity ratio
Re_θ	momentum-thickness Reynolds number
$Re_{\theta t}$	transition onset momentum-thickness Reynolds number (based on freestream conditions)
$\tilde{R}e_{\theta t}$	transition onset momentum-thickness Reynolds number (obtained from a transport equation)
$Re_x = \rho LU \mu$	Reynolds number
R_ν	vorticity Reynolds number
R_y	wall-distance based turbulent Reynolds number
R_i	Richardson number
s_i	constants
S_{ij}	strain rate tensor
s	space
\mathcal{T}_{ij}	turbulent transport term
t	time
T	temperature
T	turbulent time scale
$Tu = 100\sqrt{2k/3U_\infty^2}$	turbulent intensity
U	velocity
$u_i, (u, v, w)$	velocity vector
\mathcal{V}_{ij}	viscous acceleration term
$\overline{v'^2}$	turbulent normal strain component
$x_i, (x, y, z)$	Cartesian space vector
X_{sst}	cross diffusion term SST model
X_ω	cross diffusion term $k - \omega$ model

y^+ dimensionless wall distance

Greek Symbols

δ boundary layer thickness
 δ_{ij} Kronecker-delta
 Δ Laplace operator
 ε_{ij} dissipation of the Reynolds stresses
 ε isotropic turbulent dissipation
 γ intermittency
 κ Karman constant in the SA turbulence model
 κ isentropic exponent
 λ thermal conductivity
 λ_θ pressure gradient parameter
 μ dynamic viscosity
 μ_v volume viscosity
 ∇ Nabla operator, vector differential operator
 ω specific turbulence dissipation rate
 $\Omega_{ij} = 0.5 (\partial u_i / \partial x_j - \partial u_j / \partial x_i)$ vorticity tensor
 σ turbulent Prantl number in the SA turbulence model
 Φ generic variable
 Π_{ij} pressure strain covariance
 ρ fluid density
 σ_{ij} stress tensor
 σ Emmon's dimensionless spot propagation parameter
 $\sigma_\zeta, \sigma_f, \sigma_k, \sigma_\varepsilon, \sigma_\omega$ constants for different turbulence or transition models
 τ_{ij} deviatoric stress tensor
 θ momentum thickness

Subscripts

$(\cdot)_{lam}$ laminar

$(\cdot)_{le}$	leading edge
$(\cdot)_0$	referenz
$(\cdot)_t$	turbulent
$(\cdot)_{tr}$	transition onset
$(\cdot)_{turb}$	turbulent
$(\cdot)_\infty$	free stream
$(\cdot)_w$	wall

Superscripts

$(\cdot)^C$	compressible
$(\cdot)^I$	incompressible
$(\cdot)^{lam}$	laminar
$(\cdot)^{turb}$	turbulent

Other Symbols

$\widehat{(\cdot)}$	Fourier transformation
$\overline{(\cdot)}$	mean value
$\overline{\overline{(\cdot)}}$	Reynolds decomposition
$\widetilde{(\cdot)}$	density weighted Favre decomposition
$\langle \cdot \rangle$	scalar product
$(\cdot)'$	fluctuation part
$(\cdot)''$	Favre-fluctuation part

Abbreviations

AIDA	Aggressive Intermediate Duct Aerodynamics
CFD	Computational Fluid Dynamics
DNS	Direct Numerical Simulation
FSTI	free stream turbulent intensity

IP	linear isotropization of turbulence production
LES	Large Eddy Simulation
PRC	pressure recovery coefficient
RANS	Reynolds-averaged Navier-Stokes
RSTM	Reynolds-stress transport model
SA	Spalart and Allmaras
SGS	subgrid-scale
SSG	Speziale, Sakar, Gatski
SST	shear stress transport
ZPG	zero pressure gradient

1. Introduction

Engine manufacturers have to design more and more efficient aircraft engines because of the rising air traffic and the involved environmental pollution. The constructions must be light and compact. To improve the efficiency of a turbine the best way is to improve the flow path. Getting a light design means to reduce the number of stages and blades per stage.

One possibility for a redesign is to shorten the length of the intermediate turbine duct between the high-pressure turbine and the low-pressure turbine through innovative flow guidance. So-called S-shaped ducts, which are shorter and lighter than common ducts can be used. This leads to a reduction in fuel consumption, which again leads to a lower environmental pollution. Research for such an enhancement was supported by the European Commission and performed within the project AIDA (Aggressive Intermediate Duct Aerodynamics).

Beneath experimental investigations on different duct geometries within the AIDA project also computational fluid dynamics (CFD) must be performed to simulate the complex flows and predict their effects for a cheaper redesign. CFD is a very useful tool for optimizing turbine blades as well as for designing duct contours. Today's mathematical and numerical models should be able to adequately simulate flows with separation, transition or relaminarisation in a correct way. But industrial CFD-packages often do not show satisfying results for aggressively designed intermediate turbine ducts because they usually do not consider the proper physical description of such phenomena like transition and relaminarisation.

Due to the fact that experiments cannot find all phenomena within such an intermediate turbine duct clearly, only a CFD calculation can throw light on complex flow phenomena like separation, transition of the boundary layer as well as relaminarisation. CFD codes must be able to calculate such phenomena. Therefore the project CFD-TRANS was conducted. Main goal of this project was to provide a reliable modeling of complex transitional turbine flows with the focus on intermediate turbine ducts between the high-pressure and the low-pressure turbine. Basis for the research in this thesis is the experimental work done at the Institute for Thermal Turbomachinery and Machine Dynamics within the project AIDA (Göttlich et al. (2005), Göttlich et al. (2007), Marn et al. (2007), Marn (2008)).

The three-dimensional transient turbulent flow within aircraft engines is often effected by secondary flows, and thus counts to the most difficult applications for CFD codes. Within the last years the capacity of computers rose enormously which allows to use CFD

within the design process of jet engines. One topic where further investigations have to be done is turbulence and the linked process of transition from laminar to turbulent, which is a phenomenon that is very difficult to capture. Transition is a process that is often intermittent in jet engines, that means that the flow is temporarily laminar or turbulent. These complex processes are hard to predict, but such predictions are of great interest for engineering applications.

Transition in turbomachinery as described by Mayle (1991) is divided into the following modes:

- Natural Transition (occurs when the free-stream turbulence intensity is very low)
- Bypass Transition (most common mode in turbomachinery, occurs at a higher free-stream turbulence intensity)
- Separated-Flow Transition within a separated shear layer
- Periodic-Unsteady Transition (occurring when wakes from the upstream turbine blade impinge on the following blade)
- Reverse Transition as a reversion of the laminar-to-turbulent transition (occurs within strongly accelerating flows like in high-pressure turbines)

The most common form of transition occurring in aircraft engines is the so-called bypass transition. Therefore many models for its description are in use, most of them are empirical models. The first algebraic models are based on the idea of Abu-Ghannam and Shaw (1980) to set correlations for the transition onset and the transition length. The modified version by Drela (1995) is widely used nowadays. The implementation of algebraic models for three-dimensional flows is a complicated task and therefore higher transition models use transport-equation approaches, e.g. by Lodefier and Dick (2005b) and by Pecnik et al. (2003). These models usually show reasonable results for bypass transition, but the prediction of separation-induced transition and of relaminarisation often lacks. Although the phenomenon of relaminarisation within strongly accelerating flows was experimentally investigated very early (Narashima and Screenivasan (1973); Rhee and Cho (2005)), no satisfying model for relaminarisation has been yet published. In most nowadays used programs for designing turbines the used time-averaged Navier-Stokes description does not allow the calculation of relaminarisation due to the lack of suitable models, and therefore a significant amount of research has still to be carried out to find an adequate form of transition modelling, which can also be used for the design process.

So the main goal of this work is to get an improved reliable CFD code with proper advanced transition models which are able to predict transitional flows with separation and relaminarisation.

Chapter 2 describes the basic principles as well as the numerical methods for transition modeling in turbomachinery. In Chapter 3 the state of the art of transition modeling is described in detail. Chapter 4 presents the $\zeta - f$ model as an advanced turbulence model

allowing transition prediction as well as its validation. Chapter 5 describes an advanced transition model, the correlation based $\gamma - Re_\theta$ transition model in detail, as well as its validation. In Chapter 6 a closer look to the last transition mode, the relaminarisation, is taken, describing a test case measured at our Institute for Thermal Turbomachinery and Machine Dynamics at Graz University of Technology. Two additional 2D testcases where relaminarisation is observed in the measurements and one 3D test case are validated. Chapter 7 contains the conclusion and some recommendations for the future.

Five authored or co-authored papers are presented within this thesis to show the own contributions. In Chapter 4 Paper 1 and Paper 2 describe the validation of the $k-\varepsilon-\zeta-f$ turbulence model by Hanjalić et al. (2004). In Chapter 5 Paper 3 and Paper 4 explain the in-house correlation for the correlation based $\gamma - Re_\theta$ transition model by Menter et al. (2006). Finally in Chapter 6 Paper 5 demonstrates the application of the Spalart Allmaras turbulence model to the AIDA duct, which shows, that for an understanding of the flow behaviour also simple models can be helpful.

2. Basic Principles of Flow Modeling

In this chapter the basic principles of fluid flow modeling are presented. The important turbulence models which are coupled with the transition models in Chapter 4 and Chapter 5 will be summarized briefly.

2.1. Equations of Fluid Motion

The equations of fluid flow have been known for more than 100 years and are the three laws of conservation for physical systems:

Conservation of Mass

The time conservation of the mass in terms of the density ρ in solenoidal flow results in:

$$\frac{\partial \rho}{\partial t} + \frac{\partial \rho u_i}{\partial x_i} = 0. \quad (2.1)$$

Conservation of Momentum

The conservation of momentum equation is

$$\frac{\partial \rho u_i}{\partial t} + \frac{\partial \rho u_i u_j}{\partial x_j} = \frac{\partial \sigma_{ij}}{\partial x_j} + \rho f_i. \quad (2.2)$$

Using the assumption of a Newton fluid the internal stresses can be separated in the shear stress and the conventional pressure:

$$\sigma_{ij} = \tau_{ij} - p \delta_{ij} \quad (2.3)$$

The external mass forces f_i (gravity) can be neglected, because they are small for the gaseous fluids in thermal turbomachinery.

Conservation of Energy

The conservation of energy is derived from the first law of thermodynamics. The time rate of change of the internal total energy per volume units e should be in balance with the work done by the system and the heat transfer. This leads to the following equation, where τ_{ij} is the viscous stress tensor and q_j is the heat flow.

$$\frac{\partial \rho e}{\partial t} + \frac{\partial \rho u_j e}{\partial x_j} = -\frac{\partial u_j p}{\partial x_j} + \frac{\partial u_i \tau_{ij}}{\partial x_j} - \frac{\partial q_j}{\partial x_j}. \quad (2.4)$$

2.2. Fluid Properties

The set of conservation equations are valid for all fluids and for all flow conditions. To close this set of equations some assumptions have to be done. The fluid behaves as a Newtonian fluid in which the viscous stresses can be related to the fluid motion by a constitutive relation of the following form.

$$\tau_{ij} = 2\mu S_{ij}^C + \mu_v \frac{\partial u_k}{\partial x_k} \delta_{ij}, \quad (2.5)$$

with μ_v as the volume viscosity or second viscosity (see Wilcox (2002)) and with S_{ij}^C as the strain rate tensor for compressible fluids

$$S_{ij}^C = \frac{1}{2} \underbrace{\left(\frac{\partial u_i}{\partial x_j} + \frac{\partial u_j}{\partial x_i} \right)}_{S_{ij}^I} - \frac{1}{3} \frac{\partial u_k}{\partial x_k} \delta_{ij}, \quad (2.6)$$

With the Sutherland law the dynamic viscosity μ for gases can be calculated as follows:

$$\frac{\mu(T)}{\mu_0(T_0)} = \left(\frac{T}{T_0} \right)^{\frac{3}{2}} \frac{T_0 + C}{T + C} \quad (2.7)$$

with the following Sutherland-constants for air:

$$\mu_0 = 1.876 \cdot 10^{-5} \text{ kg/(ms)}, \quad T_0 = 303.15 \text{ K}, \quad C = 110.4 \text{ K}.$$

The law of heat conduction, also known as Fourier's law, allows to calculate the heat flow over a surface as following:

$$q_j = -\lambda \frac{\partial T}{\partial x_j} \quad (2.8)$$

The coefficient of thermal conductivity λ has a similar behaviour in gases as the dynamic viscosity μ expressed by the Prandtl-number Pr :

$$\lambda = \frac{\mu c_p}{Pr}, \quad \text{with : } Pr = 0.7, c_p = \text{constant (for air)}. \quad (2.9)$$

The relation between density ρ , pressure p , inner energy e^i and temperature T is taken for ideal gas with the following equations of state:

$$\begin{aligned} \frac{p}{\rho} &= RT, \quad \kappa = \frac{c_p}{c_v}, \\ e^i &= \frac{e}{\rho} = c_v T = \frac{1}{\kappa - 1} \frac{p}{\rho}, \\ e &= \frac{1}{\kappa - 1} p + \rho \frac{u_k u_k}{2}. \end{aligned}$$

2.3. RANS – Reynolds-Averaged Navier-Stokes

The above set of equations is named Navier-Stokes equations in CFD. A complete solution of these equations without any further simplification is done by Direct Numerical Simulation (DNS). But DNS is inapplicable for complex engineering tasks because of the high computational power demand due to the high calculation grid resolution and hence small time scales.

A simplification has to be performed. One method for simplifying/modeling these equations is to average them with the so-called Reynolds decomposition. In the literature many explanations of the Reynolds decomposition can be found for example Rotta (1972), Wilcox (2002) or Pope (2000) just to mention a few. In this work the explanation by Hanjalić (2005) is taken.

Reynolds decomposition

Osborne Reynolds (1895) proposed to decompose the instantaneous property $\widehat{\Phi}$ (velocity, pressure, density, temperature,...) into a mean $\overline{\Phi}$ and fluctuations around the mean Φ' to simplify the description of turbulence:

$$\widehat{\Phi} = \overline{\Phi} + \Phi' \quad (2.10)$$

For stationary flow the 'time mean' can be used:

$$\overline{\widehat{\Phi}} = \overline{\Phi}(x_i) = \lim_{\tau \rightarrow \infty} \frac{1}{\tau} \int_0^\tau \widehat{\Phi}(x_i, t) dt \quad (2.11)$$

so that

$$\overline{\Phi'} = \lim_{\tau \rightarrow \infty} \frac{1}{\tau} \int_0^\tau \Phi'(x_i, t) dt = 0 \quad (2.12)$$

This approach can also be used for unsteady flow, when the flow varies significantly with time by using the 'ensemble mean'-averaging over n_e samples:

$$\overline{\Phi}(x_i, t) = \lim_{n_e \rightarrow \infty} \frac{1}{n_e} \sum_{i=1}^{n_e} \widehat{\Phi}(x_i, t). \quad (2.13)$$

Some mathematical rules have to be valid when applying the Reynolds decomposition (see Hanjalić (2005)) for two instantaneous variables in a turbulent fluid flow: $\widehat{\Phi}_1 = \overline{\Phi}_1 + \Phi'_1$ and $\widehat{\Phi}_2 = \overline{\Phi}_2 + \Phi'_2$

- multiplication with a constant C:

$$\overline{C \widehat{\Phi}} = C \overline{\widehat{\Phi}} = C \overline{\Phi}$$

- addition and subtraction:

$$\overline{\widehat{\Phi}_1 \pm \widehat{\Phi}_2} = \overline{\widehat{\Phi}_1} \pm \overline{\widehat{\Phi}_2} = \overline{\Phi}_1 \pm \overline{\Phi}_2$$

- differentiation and integration (with s as the time or space coordinate):

$$\overline{\frac{\partial \widehat{\Phi}}{\partial s}} = \frac{\partial \overline{\widehat{\Phi}}}{\partial s} = \frac{\partial \overline{\Phi}}{\partial s} \quad \overline{\int \widehat{\Phi} ds} = \int \overline{\widehat{\Phi}} ds = \int \overline{\Phi} ds$$

- multiplication:

$$\begin{aligned} \overline{\Phi'_1 \Phi'_2} &\neq \overline{\Phi'_1} \overline{\Phi'_2} \\ \overline{\Phi'_1 \Phi'_2} &\neq 0 \quad \text{Note: } \overline{\Phi'_1} = 0 ; \overline{\Phi'_2} = 0 \\ \overline{\widehat{\Phi}_1 \widehat{\Phi}_2} &= \overline{(\overline{\Phi}_1 + \Phi'_1)(\overline{\Phi}_2 + \Phi'_2)} = \overline{\Phi}_1 \overline{\Phi}_2 + \underbrace{\overline{\Phi_1 \Phi'_2}}_{=0} + \underbrace{\overline{\Phi'_1 \Phi_2}}_{=0} + \overline{\Phi'_1 \Phi'_2} = \overline{\Phi}_1 \overline{\Phi}_2 + \overline{\Phi'_1 \Phi'_2} \end{aligned}$$

similar for a triple product (see Wilcox (2002)):

$$\overline{\widehat{\Phi}_1 \widehat{\Phi}_2 \widehat{\Phi}_3} = \overline{\Phi}_1 \overline{\Phi}_2 \overline{\Phi}_3 + \overline{\Phi'_2 \Phi'_3} \overline{\Phi}_1 + \overline{\Phi'_1 \Phi'_3} \overline{\Phi}_2 + \overline{\Phi'_1 \Phi'_2} \overline{\Phi}_3 + \overline{\Phi'_1 \Phi'_2 \Phi'_3}$$

- averaging the fluctuation:

$$\overline{\Phi'} = 0$$

Applying this averaging to the conservation of mass equation (eq. 2.1) the Reynolds-averaged compressible conservation of mass equation results:

$$\frac{\partial \bar{\rho}}{\partial t} + \frac{\partial \bar{\rho} u_i}{\partial x_i} + \frac{\partial \overline{\rho' u_i'}}{\partial x_i} = 0. \quad (2.14)$$

Comparing this equation with the non Reynolds-averaged mass conservation equation an additional term appears:

$$\frac{\partial \overline{\rho' u_i'}}{\partial x_i} \quad (2.15)$$

For incompressible flows this term is zero, but for compressible flows the density fluctuation and the velocity fluctuation are correlated and therefore it is not equal to zero. By averaging many more additional terms arise in the other two conservation equations (eqs. 2.2-2.4).

Favré averaging

Favré (1965) proposed to divide the flow quantity into the Favré average (marked with \sim) and the fluctuation part (marked with $''$) similar to equation (2.10):

$$\hat{\Phi} = \tilde{\Phi} + \Phi''. \quad (2.16)$$

The Favré average is obtained by a density-based averaging of the flow quantities and is proposed for the compressible Navier-Stokes equations:

$$\tilde{\Phi} = \frac{1}{\bar{\rho}} \lim_{T \rightarrow \infty} \frac{1}{T} \int_t^{t+T} \rho_{(t)} \Phi_{(t)} dt = \frac{\overline{\rho \Phi}}{\bar{\rho}}. \quad (2.17)$$

Unlike to the Reynolds decomposition the mean of the fluctuation is not equal to zero.

$$\overline{\Phi''} = -\overline{\rho' \Phi'} / \bar{\rho} \neq 0 \quad (2.18)$$

but the density-average of the fluctuation. This can be shown by constituting equation (2.16) into equation (2.17):

$$\begin{aligned} \bar{\rho} \tilde{\Phi} &= \overline{\rho \Phi} \\ &= \overline{(\bar{\rho} + \rho')(\tilde{\Phi} + \Phi'')} = \bar{\rho} \tilde{\Phi} + \underbrace{\overline{\rho' \tilde{\Phi}}}_{=0} + \overline{\rho \Phi''} \\ &\rightarrow \overline{\rho \Phi''} = 0. \end{aligned}$$

Reynolds/Favré-averaged conservation equations

Below the Reynolds/Favré-averaged compressible Navier-Stokes equations are presented, using the Reynolds decomposition for the density ρ and the pressure p , and the Favré-averaging for the velocity \tilde{u} and the temperature T . The details of the averaging can be found in Pecnik (2007).

Conservation of Mass

$$\frac{\partial \bar{\rho}}{\partial t} + \frac{\partial \bar{\rho} \tilde{u}_i}{\partial x_i} = 0 \quad (2.19)$$

Conservation of Momentum

$$\frac{\partial \bar{\rho} \tilde{u}_i}{\partial t} + \frac{\partial \bar{\rho} \tilde{u}_i \tilde{u}_j}{\partial x_j} = -\frac{\partial \bar{p}}{\partial x_i} + \frac{\partial \bar{\tau}_{ij}}{\partial x_j} - \frac{\partial \overline{\rho u_i'' u_j''}}{\partial x_j} \quad (2.20)$$

Conservation of Energy

$$\frac{\partial \bar{\rho} \tilde{e}}{\partial t} + \frac{\partial \bar{\rho} \tilde{u}_j \tilde{e}}{\partial x_j} = -\frac{\partial \tilde{u}_j \bar{p}}{\partial x_j} + \frac{\partial \tilde{u}_i \bar{\tau}_{ij}}{\partial x_j} - \frac{\partial \tilde{u}_i \overline{\rho u_i'' u_j''}}{\partial x_j} - \frac{\partial (q_j^{lam} + q_j^{turb} + T_j)}{\partial x_j}. \quad (2.21)$$

The term $\overline{\rho u_i'' u_j''}$ are the so-called Reynolds stresses. In order to close these equations, there are two approaches, which are described in the following section.

2.4. Turbulence Modeling in Turbomachinery Flows

In this chapter a short overview of turbulence modeling in turbomachinery is given and the main equations of the turbulence models used for the transition models in Chapter 4 and Chapter 5 are described.

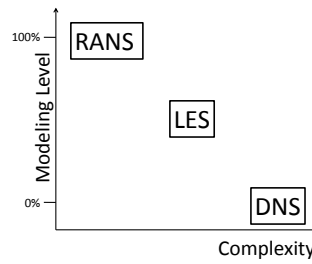


Figure 2.1.: Classification of turbulence models according to their complexity

In Fig. 2.1 the complexity of turbulence models is compared to their modeling level and in Fig. 2.2 the classification of turbulence models is shown. As already mentioned the Direct Numerical Simulation (DNS) is applicable only for simple flow problems and it is used to study flow phenomena like transition in detail. DNS is also used for the development of turbulence models, because the simulation gives a deeper insight than experiments. Large eddy simulation (LES) resolves large flow structures; small structures, which are not captured by the grid have to be modeled with so-called subgrid-scale (SGS) models. The computational effort is also very high, so that in most engineering applications statistic models based on RANS are applied, either first-order closures using the Boussinesq assumption or second-order closures as the Reynolds Stress Transport Model (RSTM). Both closure types model the Reynolds stresses $\overline{\rho u_i'' u_j''}$, which are derived from the averaging process, in order to close the system of equations (2.20, 2.21).

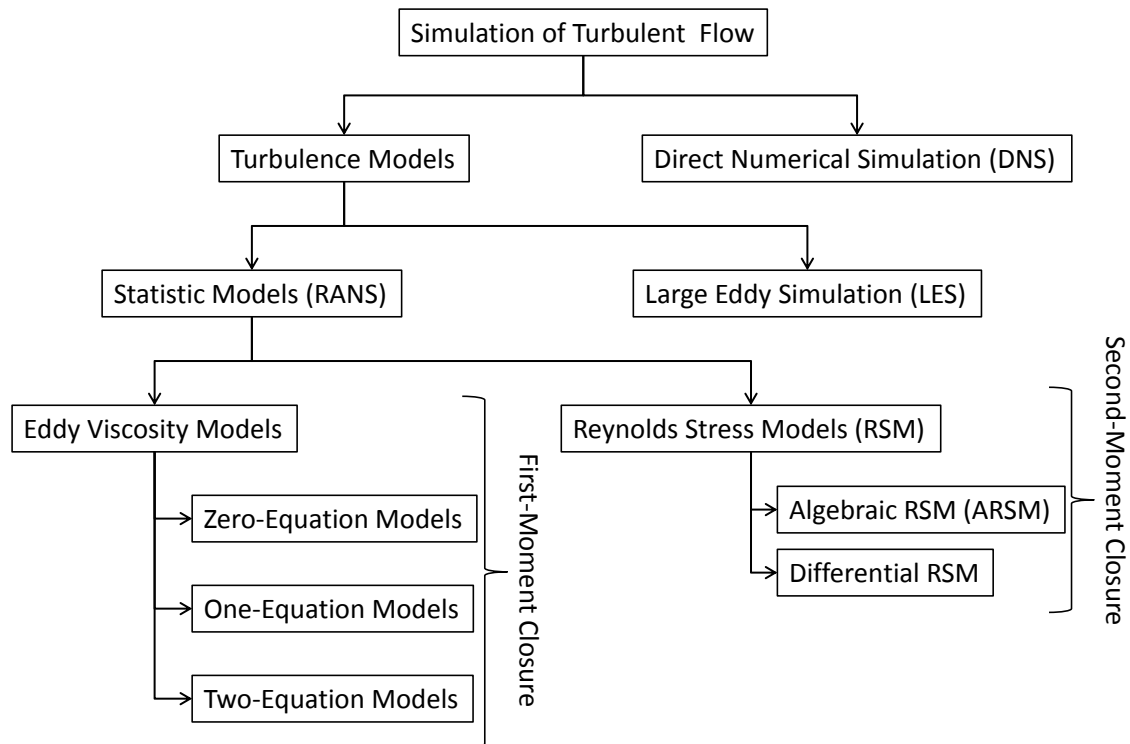


Figure 2.2.: Classification of turbulence models, from Lücke (1997)

2.4.1. Reynolds Stress Transport Model

One method for prescribing the Reynolds stresses is to use transport equations for the Reynolds stresses (Reynolds Stress Transport Model - RSTM). The reason for not widely using this method is the large computational effort, because seven additional equations have to be solved beneath the RANS equations. Chou (1945) and Rotta (1951) were the first who suggested the turbulence closure using the RSTM, but they did not carry out any numerical computations (Wilcox (2002)). Pecnik (2007) showed in his PhD work, that turbulence models derived from RSTM like the Turbulent Potential Model by Wang and Perot (2002) and the $v^2 - f$ model by Durbin (1993) have a great potential predicting bypass transition.

The derivation of the compressible RSTM is taken from Wilcox (2002) and Adumitroaie et al. (1998):

$$\overline{u_i'' \mathcal{N}(u_j) + u_j'' \mathcal{N}(u_i)} = 0 \quad (2.22)$$

with the 'Navier-Stokes operator' $\mathcal{N}(u_i)$

$$\mathcal{N}(u_i) : \frac{\partial \rho u_i}{\partial t} + \frac{\partial \rho u_i u_j}{\partial x_j} + \frac{\partial p}{\partial x_i} - \frac{\partial \tau_{ij}}{\partial x_j} = 0. \quad (2.23)$$

The resulting transport equations can be written as:

$$\frac{\partial \overline{\rho u_i'' u_j''}}{\partial t} + \frac{\partial \overline{\rho u_i'' u_j'' \tilde{u}_k}}{\partial x_k} = \mathcal{P}_{ij} + \Pi_{ij} - \bar{\rho} \varepsilon_{ij} + \frac{\partial \mathcal{J}_{ijk}}{\partial x_k} - \mathcal{M}_{ij} + \mathcal{V}_{ij}. \quad (2.24)$$

In equation 2.24 \mathcal{P}_{ij} is the production of the Reynolds stresses

$$\mathcal{P}_{ij} = -\overline{\rho u_i'' u_k''} \frac{\partial \tilde{u}_j}{\partial x_k} - \overline{\rho u_k'' u_j''} \frac{\partial \tilde{u}_i}{\partial x_k}. \quad (2.25)$$

Π_{ij} is the pressure strain covariance, describing the interaction of the velocity and the pressure fluctuations:

$$\Pi_{ij} = \overline{p' \left(\frac{\partial u_i''}{\partial x_j} + \frac{\partial u_j''}{\partial x_i} \right)}. \quad (2.26)$$

The dissipation term $\bar{\rho} \varepsilon_{ij}$ in equation (2.24) is:

$$\bar{\rho} \varepsilon_{ij} = \overline{\tau_{jk}'' \frac{\partial u_i''}{\partial x_k}} + \overline{\tau_{ki}'' \frac{\partial u_j''}{\partial x_k}}. \quad (2.27)$$

When applying the approach of equation (2.22), the turbulent dissipation for incompressible fluids results to:

$$\bar{\rho} \varepsilon_{ij} = 2\mu \overline{\frac{\partial u_i'}{\partial x_k} \frac{\partial u_j'}{\partial x_k}} \quad (2.28)$$

Local isotropy can be expected, when using the Kolmogorov hypothesis, which says that the dissipation effects the smallest turbulent scales. This results in:

$$\bar{\rho}\varepsilon_{ij} = \frac{2}{3}\bar{\rho}\varepsilon\delta_{ij}. \quad (2.29)$$

For near-wall applications this assumption is not valid any more and therefore a transport/model equation for the dissipation has to be provided.

The turbulent transport terms for compressible flows are:

$$\mathcal{T}_{ijk} = \overline{\rho u_i'' u_j'' u_k''} + \overline{p' u_j''} \delta_{ik} + \overline{p' u_i''} \delta_{jk} - \overline{u_i'' \tau_{kj}''} - \overline{u_j'' \tau_{ki}''} \quad (2.30)$$

and for incompressible flows:

$$\mathcal{T}_{ijk} = \overline{\rho u_i' u_j' u_k'} + \overline{p' u_j'} \delta_{ik} + \overline{p' u_i'} \delta_{jk} - \nu \frac{\partial \overline{u_i' u_j'}}{\partial x_k}. \quad (2.31)$$

The pressure acceleration term \mathcal{M}_{ij} is defined as follows:

$$\mathcal{M}_{ij} = \overline{u_i''} \frac{\partial \bar{p}}{\partial x_j} - \overline{u_j''} \frac{\partial \bar{p}}{\partial x_i} \quad (2.32)$$

The viscous acceleration term \mathcal{V}_{ij} in equation 2.24 is defined as follows:

$$\mathcal{V}_{ij} = \overline{u_j''} \frac{\partial \overline{\tau_{ki}}}{\partial x_k} + \overline{u_i''} \frac{\partial \overline{\tau_{jk}}}{\partial x_k} \quad (2.33)$$

This set of equations leads to additional 22 new unknowns. The unknowns are presented in Table 2.1, with accounting for all symmetries.

Table 2.1.: RSTM unknowns

Unknowns:	number of unknowns:	from:
$\overline{u_i'' u_j'' u_k''}$	10	turbulent transport term
$\overline{\tau_{jk}''} \frac{\partial u_i''}{\partial x_k} + \overline{\tau_{ki}''} \frac{\partial u_j''}{\partial x_k}$	6	dissipation term
$\overline{p' \left(\frac{\partial u_i''}{\partial x_j} + \frac{\partial u_j''}{\partial x_i} \right)}$	6	pressure strain covariance

Closing this set of equations is usually done by modeling the pressure strain covariance Π_{ij} , the dissipation ε_{ij} and the turbulent transport term \mathcal{T}_{ijk} (see Chapter 4).

2.4.2. Boussinesq-assumption for the $\overline{\rho u_i'' u_j''}$ -Tensor

The Boussinesq (1877) assumption for closing the Reynolds-Averaged Navier Stokes (RANS) equations by introducing the concept of an eddy viscosity is one of the easiest and most common methods.

It states that the Reynolds stress tensor is proportional to the shear rate tensor and can be written as following:

$$-\overline{\rho u_i'' u_j''} = 2\mu_t \bar{S}_{ij}^C - \frac{2}{3} \bar{\rho} k \delta_{ij}, \quad (2.34)$$

with \bar{S}_{ij}^C as the mean strain rate tensor (see eq. 2.6) and the turbulent kinetic energy k defined as follows:

$$k = \frac{\overline{\rho u_i'' u_j''}}{2\bar{\rho}} \quad (2.35)$$

2.5. Turbulence Models based on the Boussinesq approach

The turbulence models based on the Boussinesq assumption can be classified by the number of additional transport equations, that must be solved along with the RANS equations. Table 2.2 lists several turbulence models.

Table 2.2.: Outline of several RANS turbulence models

number of additional equations:	transport variables	model name
Zero		mixing length model
One	$\tilde{\nu}_t$... modified/High Reynolds eddy viscosity	Spalart Allmaras model
Two	k ... kinetic energy ε ... dissipation	$k - \varepsilon$ model
	k ... kinetic energy ω ... turbulent frequency specific dissipation	$k - \omega$ model

2.5.1. Spalart Allmaras Turbulence Model

The turbulence model by Spalart and Allmaras (1994) is one of the most used turbulence models and counts to the one-equation models. It comes originally from the aerodynam-

ics and is limited to flows with a low level of freestream turbulence intensity. It is used in this work without any modifications, but is presented here for the sake of completeness. A very good summary of this model can also be found in Menter (1996).

One additional transport equation for the high Reynolds eddy viscosity $\tilde{\nu}_t$ has to be solved, which is coupled with the eddy viscosity in the following way:

$$\nu_t = \tilde{\nu}_t f_{v1}; \quad f_{v1} = \frac{\chi^3}{\chi^3 + c_{v1}^3}; \quad \chi = \frac{\tilde{\nu}_t}{\nu} \quad (2.36)$$

The transport equation for the high Reynolds eddy viscosity $\tilde{\nu}_t$ is given as follows:

$$\frac{D\tilde{\nu}_t}{Dt} = \underbrace{c_{b1}\tilde{\nu}_t\tilde{S}}_{\text{production term}} - \underbrace{c_{w1}f_w\left(\frac{\tilde{\nu}_t}{y}\right)^2}_{\text{destruction term}} + \underbrace{\frac{c_{b2}}{\sigma}\frac{\partial\tilde{\nu}_t}{\partial x_i}\frac{\partial\tilde{\nu}_t}{\partial x_i} + \frac{1}{\sigma}\frac{\partial}{\partial x_i}\left[(\nu + \tilde{\nu}_t)\frac{\partial\tilde{\nu}_t}{\partial x_i}\right]}_{\text{viscous diffusion term}} \quad (2.37)$$

The first term on the right hand side of eq. (2.37) is the production term, the second term is the destruction term and the last two terms are the viscous diffusion terms. y is the distance to the nearest wall and \tilde{S} is the absolute value of the vorticity. The model functions are defined as followed:

$$\tilde{S} = S + \frac{\tilde{\nu}_t}{\kappa^2 y^2} f_{v2}; \quad f_{v2} = 1 - \frac{\chi}{1 + \chi f_{v1}} \quad (2.38)$$

with S as the strain rate.

The blending function f_w in the destruction term is defined as:

$$f_w = g \left[\frac{1 + c_{w3}^6}{g^6 + c_{w3}^6} \right]^{1/6}; \quad g = r + c_{w2}(r^6 - r); \quad r = \frac{\tilde{\nu}_t}{\tilde{S}\kappa^2 y^2} \quad (2.39)$$

The constants are:

$$\begin{aligned} c_{b1} &= 0.1355; & c_{b2} &= 0.622; & c_{v1} &= 7.1; \\ c_{w1} &= \frac{c_{b1}}{\kappa^2} + \frac{1 + c_{b2}}{\sigma}; & c_{w2} &= 0.3; & c_{w3} &= 2; \\ \kappa &= 0.41; & \sigma &= \frac{2}{3}; \end{aligned} \quad (2.40)$$

The boundary condition for $\tilde{\nu}_t$ at the wall is zero, and in the free-stream (inflow) the values are small ($\tilde{\nu}_t/\nu \sim 10$).

The Spalart and Allmaras (1994) model is used in this work to get a fast converged solution of the turbulent flow. The different transition models are started from this

solution. Our application of this model can be seen in Paper 5 (see section 6.4), dealing with the AIDA test case, where the influence of the tip gap of the high pressure rotor is investigated.

2.5.2. Standard $k - \varepsilon$ Model

The standard $k - \varepsilon$ model uses two additional transport equations, one for the turbulent kinetic energy k and one for the dissipation ε . Launder and Sharma (1974) present the standard $k - \varepsilon$ model as follows:

$$\frac{\partial \rho k}{\partial t} + \frac{\partial \rho u_j k}{\partial x_j} - \frac{\partial}{\partial x_j} \left[\left(\mu + \frac{\mu_t}{\sigma_k} \right) \frac{\partial k}{\partial x_j} \right] = \rho P_k - \rho \varepsilon \quad (2.41)$$

$$\frac{\partial \rho \varepsilon}{\partial t} + \frac{\partial \rho u_j \varepsilon}{\partial x_j} - \frac{\partial}{\partial x_j} \left[\left(\mu + \frac{\mu_t}{\sigma_\varepsilon} \right) \frac{\partial \varepsilon}{\partial x_j} \right] = \frac{\varepsilon}{k} (C_{\varepsilon 1} \rho P_k - C_{\varepsilon 2} \rho \varepsilon). \quad (2.42)$$

The production of the turbulent kinetic energy is found using the Boussinesq approximation:

$$P_k = -\overline{\rho u'_i u'_j} \frac{\partial u_j}{\partial x_i} = \mu_t S^2 \quad (2.43)$$

Due to the fact that many $k - \varepsilon$ models suffer from too much turbulent kinetic energy in the area of the stagnation point, which gets transported further downstream and distort the rest of the solution, the common approach of Kato and Launder (1993) is used. This approach suggest to multiply with the local vorticity. To keep the dimension of the production term, the strain rate tensor is used.

$$P_k = \mu_t S^2 \quad (2.44)$$

The eddy viscosity $\nu_t = \mu_t / \rho$ in (eq. 2.34) is proportional to a turbulent velocity U_t and in a turbulent length scale L_t due to dimensional reasons as suggested by Prandtl (1925) within his mixing length model. For the $k - \varepsilon$ model the turbulent kinetic energy and the turbulent dissipation are used for the velocity scale $U_t = \sqrt{k}$ and the length scale $L_t = k^{3/2} / \varepsilon$, which leads to:

$$\mu_t = C_\mu \rho \frac{k^2}{\varepsilon} \quad (2.45)$$

with C_μ as the anisotropy parameter.

The constants of this model are:

$$C_{\varepsilon 1} = 1.45; \quad C_{\varepsilon 2} = 1.92; \quad C_\mu = 0.09;$$

$$\sigma_k = 1; \quad \sigma_\varepsilon = 1.3;$$

The main disadvantage of the $k - \epsilon$ model is its failing in calculating semi-viscous ($y^+ < 30$) boundary layer areas.

2.5.3. Wilcox $k - \omega$ Model

The Wilcox $k - \omega$ model (Wilcox (1988)) uses two additional transport equations, one for the turbulent kinetic energy k and one for the specific dissipation $\omega = \epsilon/k$. The ω transport equation is derived by substituting ϵ by ωk in the ϵ equation (2.42). The resulting transport equations are as follows:

$$\frac{\partial \rho k}{\partial t} + \frac{\partial \rho u_j k}{\partial x_j} - \frac{\partial}{\partial x_j} \left[\left(\mu + \frac{\mu_t}{\sigma_k} \right) \frac{\partial k}{\partial x_j} \right] = \rho P_k - \rho C_\mu k \omega \quad (2.46)$$

$$\frac{\partial \rho \omega}{\partial t} + \frac{\partial \rho u_j \omega}{\partial x_j} - \frac{\partial}{\partial x_j} \left[\left(\mu + \frac{\mu_t}{\sigma_\omega} \right) \frac{\partial \omega}{\partial x_j} \right] = \rho \frac{\omega}{k} C_{\omega 1} P_k - \rho C_{\omega 2} \omega^2 + X_\omega \quad (2.47)$$

with the cross-diffusion term X_ω which results from the transformation.

$$X_\omega = \frac{2}{k} \left(\mu + \frac{\mu_t}{\sigma_\omega} \right) \frac{\partial k}{\partial x_j} \frac{\partial \omega}{\partial x_j}. \quad (2.48)$$

Wilcox (1988) suggested to neglect this term for simplicity.

The constants for this model are:

$$C_{\omega 1} = 13/25; \quad C_{\omega 2} = 9/125; \quad C_\mu = 0.09;$$

$$\sigma_k = \sigma_\omega = 2; \quad C_\mu = 0.09;$$

The $k - \omega$ model is very sensitive to the influence of the far field and the boundary conditions.

2.5.4. Menter $k - \omega$ shear-stress-transport (SST) Modell

Menter (1994) suggested to combine both models to use their positive characteristics and to avoid their above mentioned disadvantages. This can be reached by introducing a blending function, which sets the cross diffusion term X_ω in the wall region equal to zero and enables it from the mid of the boundary layer. Substituting $\mu_t = \rho k / \omega$ in the cross diffusion term X_ω leads to the SST cross diffusion term X_{SST} :

$$X_{SST} = \frac{2\rho}{\sigma_\omega \omega} \frac{\partial k}{\partial x_j} \frac{\partial \omega}{\partial x_j}. \quad (2.49)$$

The blending function F_1 is:

$$\begin{aligned} F_1 &= \tanh(\Gamma_1^4) \\ \Gamma_1 &= \min \left[\max \left(\frac{500\nu}{y^2\omega}, \frac{\sqrt{k}}{C_\mu\omega y} \right), \frac{4\rho\sigma_2 k}{y^2 X_{SST}} \right] \end{aligned} \quad (2.50)$$

The model equations of the *shear-stress-transport* (SST) $k - \omega$ turbulence model are as follows:

$$\frac{\partial \rho k}{\partial t} + \frac{\partial \rho u_j k}{\partial x_j} - \frac{\partial}{\partial x_j} \left[\left(\mu + \frac{\mu_t}{\sigma_k} \right) \frac{\partial k}{\partial x_j} \right] = \rho P_k - \rho C_\mu \omega k \quad (2.51)$$

$$\begin{aligned} \frac{\partial \rho \omega}{\partial t} + \frac{\partial \rho u_j \omega}{\partial x_j} - \frac{\partial}{\partial x_j} \left[\left(\mu + \frac{\mu_T}{\sigma_\omega} \right) \frac{\partial \omega}{\partial x_j} \right] &= C_{\omega 1} \frac{\rho}{\mu_T} P_k - C_{\omega 2} \rho \omega^2 \\ &+ (1 - F_1) X_{SST}. \end{aligned} \quad (2.52)$$

The model constants are redefined with the blending function F_1 (Menter (1994)):

$$\phi = F_1 \phi_1 + (1 - F_1) \phi_2 \begin{cases} \sigma_{k,1} = 1.18, & \sigma_{\omega,1} = 2.0, & C_{\omega 1,1} = 0.075, & C_{\omega 2,1} = 0.553 \\ \sigma_{k,2} = 1.0, & \sigma_{\omega,2} = 1.167, & C_{\omega 1,2} = 0.0828, & C_{\omega 2,2} = 0.44. \end{cases} \quad (2.53)$$

Menter (1994) suggested to redefine the eddy viscosity definition as follows:

$$\mu_t = \min \left[\rho \frac{k}{\omega}, \rho \frac{a_1 k}{|\Omega| F_2} \right], \quad (2.54)$$

to calculate the turbulent shear stresses in the boundary layer with positive pressure gradient without any connection to the dissipation. Ω is the vorticity and the constant $a_1 = \sqrt{C_\mu} = 0.3$ as the so-called Bradshaw-constant.

The blending function F_2 in equation (2.54) assures that the limitation of the eddy viscosity is not used in free shear layer.

$$\begin{aligned} F_2 &= \tanh(\Gamma_2^2) \\ \Gamma_2 &= \max \left(\frac{2\sqrt{k}}{C_\mu \omega y}, \frac{500\nu}{y^2\omega} \right) \end{aligned} \quad (2.55)$$

3. Transition Modeling in Turbomachinery

In this chapter an introduction to transition modeling in turbomachinery is given. At first the different transition modes suggested by Mayle (1991) are described in detail, followed by the description of different influencing parameters. At the end of the chapter the most common modeling approaches are adduced.

3.1. Transition Modes

Natural Transition

Natural Transition occurs usually at low freestream turbulence intensities $Tu_\infty < 0.5\%$. White (1974) described the process that takes place when the boundary layer gets turbulent naturally (see Fig. 3.1). Fanned through very small disturbances the laminar boundary layer builds unstable 2D Tollmien-Schlichting waves, which change into spanwise vorticity waves also called λ -structures followed by a 3D vortex breakdown. Turbulent spots are built before the flow changes into a fully turbulent flow.

For turbomachinery this mode of transition is not that important than the both following modes.

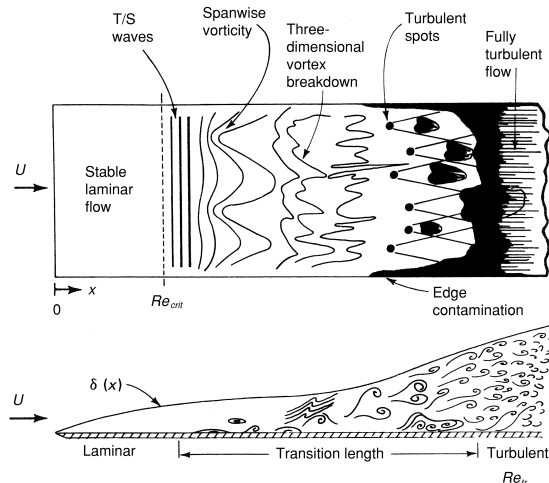


Figure 3.1.: Natural Transition, from White (1974)

Bypass Transition

Bypass transition occurs usually at higher freestream turbulence intensities $Tu_\infty > 0.5\%$, where the first two stages of the natural transition are skipped, and the building of turbulent spots happens faster. There is no strict division between natural transition and bypass transition. Bypass transition is the most common transitional mode in turbomachinery.

Separated-Flow Transition

When a laminar boundary-layer separates, transition may occur in the free-shear-layer-like flow near the bubble surface, especially in the presence of an adverse pressure gradient. The flow then reattaches as turbulent boundary layer. An indication of a separation bubble is the constant velocity or pressure plateau (see Fig. 3.2). The reattached boundary layer has a lower velocity in the near wall region and a larger boundary layer thickness. Short separation bubbles can be used to force a turbulent boundary layer.

Separated flow transition can occur behind boundary layer trip wires and when an adverse pressure gradient is present. Especially for low pressure turbines with a relatively low Re number, it appears near the point of minimum pressure on the suction side or near the leading edge on the pressure side. It is after the bypass transition the most common mode in gas turbines.

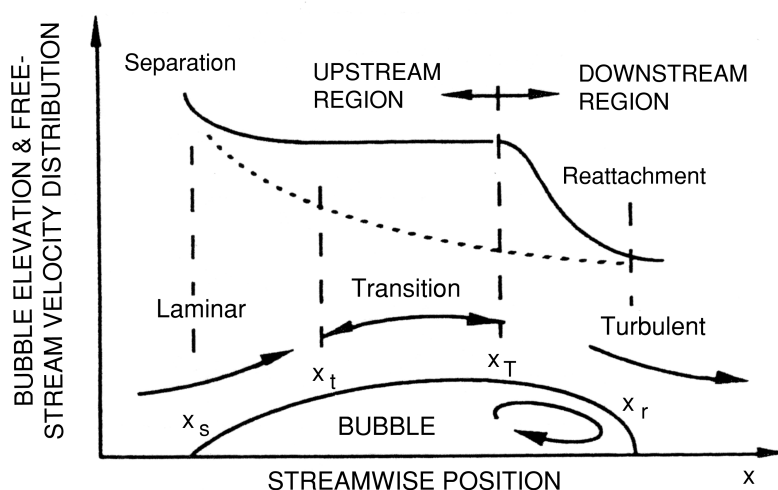


Figure 3.2.: Separation bubble, from Mayle (1991)

Wake Induced Transition

This mode of transition can occur in multi-stage configurations. Periodic passing wakes from upstream airfoils affect an intermittent earlier transition on the following blade. In transonic cascades the periodic passing of trailing edge shock waves from an upstream cascade also affects transition. Transition induced by wakes and shocks bypass the natural transition process due to their high level of disturbance. Between the passage of one wake/shock and the next one, transition may occur by other modes.

Reverse Transition

Reverse Transition is - as the name implies - the revision of the transition process, so the transition from turbulent to laminar flow. It is also often called relaminarisation. A closer look at this mode of transition can be found in Chapter 6.

3.2. Transition Influencing Parameters

The different transition modes can be influenced by several parameters. Some of these parameters are described in the following.

Reynolds Number

The boundary layer behaviour is influenced by the Reynolds number. High Reynolds numbers increase the heat transfer and a turbulent boundary layer is formed earlier. Low Reynolds number flows are dominated by viscous forces and not by inertial forces, so that disturbances are damped and the boundary layer remains laminar.

Turbulence Intensity

Similar to the influence of the Reynolds number also the turbulence intensity level influences the production of disturbances. Flow in turbomachinery have usually a higher turbulence intensity ($Tu > 1\%$) so that the turbulent disturbances rise, which leads to a thicker boundary layer, and thus results in a faster transition from laminar to turbulent. If the turbulent length scale has the same dimension as the boundary layer thickness the effect of turbulent intensity gets even more important. In cases of a thin boundary layer the influence gets smaller.

Pressure Gradient

The decreasing pressure in an accelerated flow has a stabilising effect on the disturbances and, if strong enough, may even cause relaminarisation as shown by Mayle (1991). An adverse pressure gradient promotes transition by decelerating the flow. Therefore it is very important to understand the influence of adverse pressure gradient on transition.

Surface Roughness

Disturbances in laminar boundary layers get amplified by the surface roughness and they promote the transition to turbulent. The roughness elements must have a critical height to influence the transition behaviour. Special roughness element geometries can damp the disturbances and delay the transition onset, eg. shark skin surface (e.g. Kikuchi et al. (2004)).

Compressibility

Only at high Mach numbers ($Ma > 2$) compressibility has an effect on transition. In turbomachinery with $Ma \leq 1.5$ the influence of compressibility on transition can be neglected (see Boyle and Simon (1998)).

Additional influence parameters with minor relevance can be heat transfer, acoustic fluctuations, etc.

3.3. Modelling Approaches - State of the Art

Although several successes were achieved with some turbulence models, no turbulence model not even the RSTM, is able to predict transitional boundary layer without any additional modeling. But for the design of airfoils, to get an optimum efficiency, a good knowledge of the flow behaviour around this airfoil, especially the location of transition is required. As already mentioned in Section 2.4 DNS will not be discussed within this work, because of its enormous calculation power needed for engineering applications. In the following some RANS approaches are described to model transition.

3.3.1. Empirical Transition Models (intermittency concept)

The most common transition mode in turbomachinery is the bypass transition. Flow in the transitional zone is partly turbulent and partly laminar, because of the building of turbulent spots (see description in Section 3.1). This behaviour can be derived from measurements (see Fig. 3.3). Describing the transition with an intermittency factor γ , which gives the fraction of time when the flow is turbulent, seems useful (Emmons (1951)). The intermittency factor γ is derived from the time mean of the intermittency function I_t .

$$\gamma = \lim_{T \rightarrow \infty} \frac{1}{T} \int_t^{t+T} I_t dt \quad (3.1)$$

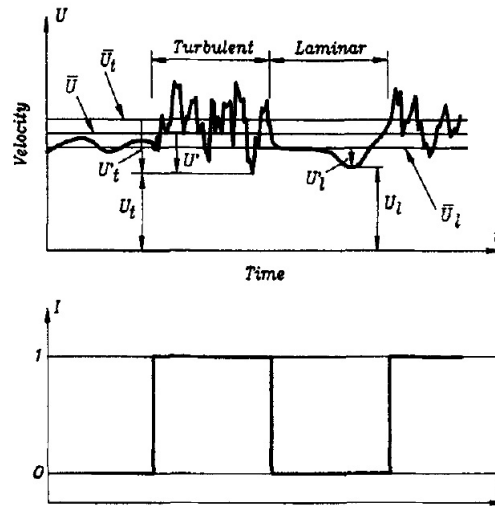


Figure 3.3.: Typical hot-wire measurement of velocity with the corresponding intermittency function, from Steelant and Dick (1996)

If the flow is laminar the intermittency function is equal to zero, and if the flow is turbulent the intermittency function is equal to one.

$$\gamma = \begin{cases} 0 & \text{laminar} \\ 0 < \gamma < 1 & \text{intermitting transitional flow} \\ 1 & \text{turbulent} \end{cases} \quad (3.2)$$

The intermittency factor can be used to trigger turbulence in the RANS equations. There are two concepts. The first one is to multiply the turbulent viscosity with the intermittency to obtain the effective viscosity. The second concept is to trigger the

turbulent production term in the k-equation by multiplying the production term with the intermittency γ .

$$\mu_{eff} = \mu_{lam} + \gamma \cdot \mu_{turb} \quad (3.3)$$

$$P_{k,eff} = \gamma \cdot P_k \quad (3.4)$$

There are many concepts for describing the intermittency factor based on measurement data. One of the first was the model of Dhawan and Narasimha (1958). The most common models are the model of Abu-Ghannam and Shaw (1980) and that of Mayle (1991).

Algebraic Transition Models

Dhawan and Narasimha (1958) presented a model for the intermittency factor distribution along solid walls:

$$\gamma = \begin{cases} 1 - \exp\left[-\frac{n\sigma}{U_\infty}(x - x_{tr})^2\right] & (x \geq x_{tr}) \\ 0 & (x < x_{tr}) \end{cases} \quad (3.5)$$

where U_∞ is the freestream velocity, x_{tr} is the transition onset location, n is the turbulent spot production rate per unit distance in the spanwise direction and σ is Emmons' dimensionless spot propagation parameter, which has the value of about 0.27 (suggested by Schubauer and Klebanoff (1955), see Mayle (1991)). In this model the transition onset x_{tr} has to be set.

Abu-Ghannam and Shaw (1980) related the start of transition in terms of Re_{θ_t} to the turbulence intensity Tu and the pressure gradient parameter λ_θ . They found the following correlation for the start of transition:

$$Re_{\theta_t} = 163 + \exp\left[F(\lambda_\theta)\left(1 - \frac{Tu_{le}}{6.91}\right)\right] \quad (3.6)$$

with

$$F(\lambda_\theta) = \begin{cases} \lambda_\theta \leq 0 : & 6.91 + 12.75\lambda_\theta + 63.64\lambda_\theta^2 \\ \lambda_\theta > 0 : & 6.91 + 2.48\lambda_\theta - 12.27\lambda_\theta^2 \end{cases} \quad (3.7)$$

and with

$$\lambda_\theta = \frac{\rho\theta^2}{\mu} \frac{dU}{ds} \quad (3.8)$$

They also found a relation between the start of transition and the length of transition:

$$Re_{L\gamma} = 5 \cdot Re_{\theta_t}^{0.8} \quad (3.9)$$

The end of transition location is a function of the transition onset location and the length of transition:

$$Re_E = Re_{\theta_t} + 3.36 \cdot Re_{L\gamma} = 16.8 \cdot Re_{\theta_t}^{0.8} \quad (3.10)$$

Mayle (1991) introduced the local Reynolds number $Re_x = Ux/\nu$ into the expression of *Dhawan and Narasimha (1958)*:

$$\gamma = 1 - \exp \left[-\hat{n}\sigma (Re_x - Re_{xt})^2 \right] \quad (3.11)$$

where \hat{n} is the dimensionless spot production parameter:

$$\hat{n} = \frac{n\nu^2}{U^3} \quad (3.12)$$

Mayle compared many different correlations (among them also that one of *Abu-Ghannam and Shaw (1980)*) and then suggested following relations for the dimensionless spot production parameter:

$$\hat{n} = \left(1.5 \cdot 10^{-11} Tu_\infty^{7/4} \right) \quad (3.13)$$

and for the momentum thickness Reynolds number at transition onset:

$$Re_{\theta_t} = 400 \cdot Tu^{-5/8} \quad (3.14)$$

This formulation bears to the problem, that the parameters boundary layer thickness and the momentum thickness Reynolds number are non-local, which complicates CFD application. An additional problem is that all these formulations are one-dimensional which leads to some unsolved questions when implementing into a three-dimensional flow solver. Therefore *Steelant and Dick (1996)* suggested to handle the intermittency with a transport equation.

Transition Modeling using an Intermittency Transport Equation

Some of the issues that arise when discussing algebraic transition models can be addressed when using an intermittency transport equation to model transitional flow. A transport equation allows the determination of the transport variables in the whole flow field and thus to implement it more easily in a three-dimensional environment.

Steelant and Dick (1996) defined their intermittency transport equation by differentiating the algebraic intermittency equation 3.11 with respect to x .

$$\frac{d\gamma}{dx} = 2(1 - \gamma)\hat{n}\sigma_{ZPG} \cdot \frac{U_\infty^2}{\nu^2} \cdot (x - x_{tr}) \quad (3.15)$$

Now the equation has to be multiplied with ρu_s to get a one-dimensional transport equation,

$$\rho u_s \frac{d\gamma}{dx} = 2(1 - \gamma)\beta_\gamma \rho u_s \quad (3.16)$$

where u_s is the velocity along a streamline and

$$\beta_\gamma = \hat{n}\sigma_{ZPG} \cdot \frac{U_\infty^2}{\nu^2} \cdot (x - x_{tr}) \quad (3.17)$$

A two-dimensional unsteady transport equation can be obtained, which is the basis for further developments.

$$\frac{\partial \rho \gamma}{\partial t} + \frac{\partial \rho u_i \gamma}{\partial x_i} = (1 - \gamma) \beta_\gamma \rho \sqrt{u^2 + v^2} \quad (3.18)$$

For non-zero pressure gradient flows the acceleration parameter K is taken to get the acceleration effects into the equations.

$$\hat{n}\sigma = (\hat{n}\sigma)_{ZPG} \cdot \text{PRC} \quad (3.19)$$

where the pressure recovery coefficient PRC is evaluated with the Steelant and Dick (1996) correlation described as

$$\text{PRC} = \begin{cases} (474 \cdot Tu_{le}^{-2.9})^{1 - \exp(2 \cdot 10^6 K_\infty)} & K_\infty < 0 \\ 10^{-3227 \cdot K_\infty^{0.5985}} & K_\infty \geq 0 \end{cases} \quad (3.20)$$

The acceleration parameter K is defined as:

$$K = \frac{\nu}{U^2} \frac{dU}{ds} \quad (3.21)$$

This model is also the basis of the enhanced transition model by Steelant and Dick (2001) as well as of the transition model of Huang and Suzen (2000), which was validated with our in-house flow solver LINARS by Pecnik (2007).

$\zeta - \gamma$ by Lodefier and Dick (2005a)

This model is an additional enhancement of the Steelant and Dick (2001) transition model already mentioned above. The authors of this contribution split the intermittency into two contributions, the near-wall intermittency γ and the free-stream factor ζ . This model shows very accurate results, when applying to turbomachinery flow (see Kubacki et al. (2009)- application to wake-induced transition).

$\gamma - Re_\theta$ model by Menter et al. (2006)

The detailed description of the $\gamma - Re_\theta$ model by Menter et al. (2006) and the corresponding validation can be found in Chapter 5.

3.3.2. Turbulence models with an extension for transition modeling derived from RSTM

The following models are derived from the Reynolds Stress Transport Model (RSTM, see Section 2.4.1), although the RSTM itself can not predict transition in its usual form. The main idea of models derived from the RSTM is to get information about the turbulent anisotropy without solving all transport equations of the original RSTM.

 $v^2 f$ model by Durbin (1991)

A detailed description of the $v^2 f$ model by Durbin (1991) as well as the corresponding validation can be found in Pecnik (2007). For the sake of completeness and to understand the application of the derived $\zeta - f$ model by Hanjalić et al. (2004) the main model equations can be found in Section 4.1.

 $\zeta - f$ model by Hanjalić et al. (2004)

The detailed description of the $\zeta - f$ model by Hanjalić et al. (2004) and the corresponding validation can be found in Chapter 4.

4. Hanjalic $k - \varepsilon - \zeta - f$ Transition Model

The $k - \varepsilon - \zeta - f$ model by Hanjalić et al. (2004) is an enhancement of the $k - \varepsilon - v^2 - f$ model by Durbin (1991). Both models are derived from the idea of closing the RANS equations with a RSTM (described in Chapter 2.4.1). To avoid the stability difficulties of the $k - \varepsilon - v^2 f$ model, Hanjalić et al. (2004) proposed an eddy viscosity model based on Durbin's elliptic relaxation concept, where the $\overline{v'^2}$ transport equation is replaced by the one of ζ , the velocity scale ratio $\zeta = \overline{v'^2}/k$. The transport equation for ζ can be directly obtained from the $\overline{v'^2}$ and the k equation of the original model by Durbin.

4.1. Durbins $v^2 f$ Model

The $v^2 f$ model has already been validated at our institute by Pecnik (2007) and is mentioned here just for the sake of completeness. Additionally to the $k - \varepsilon$ model two more equations are taken into account. The first equation is a transport equation for the turbulent normal strain component normal to wall v'^2 , which controls production of $\overline{u'v'}$, and the second equation is an elliptic relaxation equation, which accounts for non-local pressure effects and models the turbulence redistribution to $\overline{v'^2}$.

The definition of the eddy viscosity is:

$$\mu_t = C_\mu^v \rho v^2 T \quad (4.1)$$

The model equations for the $v^2 f$ model are as follows:

$$\frac{\partial \rho k}{\partial t} + \frac{\partial \rho u_i k}{\partial x_i} - \frac{\partial}{\partial x_i} \left[\left(\mu + \frac{\mu_t}{\sigma_k} \right) \frac{\partial k}{\partial x_i} \right] = \rho (P_k - \varepsilon) \quad (4.2)$$

$$\frac{\partial \rho \varepsilon}{\partial t} + \frac{\partial \rho u_i \varepsilon}{\partial x_i} - \frac{\partial}{\partial x_i} \left[\left(\mu + \frac{\mu_t}{\sigma_\varepsilon} \right) \frac{\partial \varepsilon}{\partial x_i} \right] = \frac{\rho}{T} (C_{\varepsilon 1} P_k - C_{\varepsilon 2} \varepsilon) \quad (4.3)$$

$$\frac{\partial \rho v^2}{\partial t} + \frac{\partial \rho u_i v^2}{\partial x_i} - \frac{\partial}{\partial x_i} \left[\left(\mu + \frac{\mu_t}{\sigma_{v^2}} \right) \frac{\partial v^2}{\partial x_i} \right] = \rho \left(f - N \frac{v^2}{k} \varepsilon \right) \quad (4.4)$$

$$L^2 \nabla^2 f - f = \frac{C_1 - 1}{T} \left(\frac{v^2}{k} - \frac{2}{3} \right) - C_2 \frac{2 P_k}{3 k} + (N - 1) \frac{1}{T} \frac{v^2}{k}. \quad (4.5)$$

The turbulent time scale T and length scale L are defined as follows with some limiters to avoid singularities and to be suitable for regions with high shear rates and low vorticity

(e.g. stagnation point flows):

$$T = \max \left[\min \left(\frac{k}{\varepsilon}, \frac{ak}{\sqrt{6} C_\mu^v |S^C| v^2} \right), C_\tau \left(\frac{\nu^3}{\varepsilon} \right)^{1/2} \right], \quad (4.6)$$

$$L = C_L \max \left[\min \left(\frac{k^{3/2}}{\varepsilon}, \frac{k^{3/2}}{\sqrt{6} C_\mu^v |S^C| v^2} \right), C_\eta \left(\frac{\nu^3}{\varepsilon} \right)^{1/4} \right]. \quad (4.7)$$

The model constants for the $k - \varepsilon$ model are the standard values, except for $\sigma_\varepsilon = 1.0$ and $C_{\varepsilon 1}$, which is given with the following correlation:

$$C_{\varepsilon 1} = 1.4(1 + 0.045\sqrt{v^2/k}); \quad (4.8)$$

Concluding the model constants are as follows:

$$\begin{aligned} C_\mu^v = 0.22; \quad \sigma_k = 1.0; \quad C_{\varepsilon 2} = 1.92; \quad \sigma_{v^2} = 1.0; \\ C_1 = 1.4; \quad C_2 = 0.45; \quad a = 0.6; \quad C_\tau = 6.0. \end{aligned}$$

Depending on the taken value of N , introduced by Lien and Durbin (1996), the remaining parameters are as follows:

$$\begin{aligned} N = 1 : \quad \sigma_\varepsilon = 1.3; \quad C_\eta = 85.0; \quad C_L = 0.25 \\ N = 6 : \quad \sigma_\varepsilon = 1.0; \quad C_\eta = 70.0; \quad C_L = 0.23 \end{aligned}$$

The boundary conditions at the wall are:

$$k_W = 0; \quad \varepsilon_W = 2\nu_1 k_1 / y_1^2; \quad v_W^2 = 0; \quad f_W = -(24 - 4N) \nu_1^2 v_1^2 / \varepsilon_1 y_1^4 \quad (4.9)$$

and at the inlet of the flow field:

$$k_i = 3/2 T u_i^2 U_i^2; \quad \varepsilon_i = C_\mu^{3/4} k_i^{3/2} / l_{m,i}; \quad v_i^2 = 2/3 k_i; \quad df/dn_i = 0, \quad (4.10)$$

where the index '1' corresponds to the value in the cell center of the wall cell.

In the $k - \varepsilon - v^2 - f$ model a better capturing of the stress anisotropy in the wall boundary layer is reached by replacing the conventional simple linear isotropization of turbulence production (IP) by the SSG model of Speziale et al. (1991) for modeling the rapid part of the pressure-strain term.

The model description of the $v^2 - f$ model can be found in the original paper by Durbin (1991) as well as in Pecnik (2007) with some in-house-code specific changes.

Modification of Lien et al. (1998)

The above mentioned model is said to predict transitional boundary layers without any coupling with an intermittency function, but has the lack of a too early transition to turbulence, which can be delayed by the ad-hoc modification suggested by Lien et al. (1998). This modification is described in more detail in Pecnik (2007).

$$C_{\varepsilon 1}^* = C_{\varepsilon 1} + f_T, \quad \text{mit: } f_T = 0.4 e^{-0.1 Re_T}. \quad (4.11)$$

The main disadvantage of this model is, that it suffers from stability problems due to the wall boundary condition of f_W and the therein occurring y^4 ($N = 6$) and a low convergence rate.

4.2. Model Equations for ζ and f

To avoid the above mentioned difficulties of the $v^2 f$ model, Hanjalić et al. (2004) suggested to introduce a dimensionless velocity scale ratio $\zeta = \overline{v'^2}/k$ instead of v'^2 . The transport equation can be derived directly from the $\overline{v'^2}$ and the k equation of the $v^2 f$ model. The above described transformation yields the following equation for ζ :

$$\frac{\partial \rho \zeta}{\partial t} + \frac{\partial \rho u_i \zeta}{\partial x_i} - \frac{\partial}{\partial x_i} \left[\left(\mu + \frac{\mu_t}{\sigma_\zeta} \right) \frac{\partial \zeta}{\partial x_i} \right] = \rho f - \rho \frac{\zeta}{k} P_k + \frac{2}{k} \left(\mu + \frac{\mu_t}{\sigma_\zeta} \right) \frac{\partial \zeta}{\partial x_i} \frac{\partial k}{\partial x_i} \quad (4.12)$$

The last term of equation (4.12) is the so-called "cross diffusion" term, which is a consequence of the transformation. In order to reduce the ζ equation to a source-sink-diffusion form this term is omitted.

$$\frac{\partial \rho \zeta}{\partial t} + \frac{\partial \rho u_i \zeta}{\partial x_i} - \frac{\partial}{\partial x_i} \left[\left(\mu + \frac{\mu_t}{\sigma_\zeta} \right) \frac{\partial \zeta}{\partial x_i} \right] = \rho f - \rho \frac{\zeta}{k} P_k \quad (4.13)$$

The $\zeta - f$ equations are coupled with the $k - \varepsilon$ model in the same way as in the $k - \varepsilon - v^2 - f$ model (see eqs. 4.2 and 4.3).

Both models, the $k - \varepsilon - v^2 - f$ model and the $k - \varepsilon - \zeta - f$ model, should give the same results, but there are two computational advantages of the $k - \varepsilon - \zeta - f$ model: The new model equation for ζ contains the turbulent kinetic energy production P_k , which can be easier reproduced than ε (see eq. 2.42 in Chapter 2). The second advantage can be found in the wall boundary condition for the relaxation variable f_w , where the denominator is y^2 instead of y^4 in the $k - \varepsilon - v^2 - f$ model, which gives a better numerical stability when coming closer to the wall.

$$f_w = \lim_{y \rightarrow 0} \frac{-2\nu\zeta}{y^2} \quad (4.14)$$

Due to replacing the conventional simple linear isotropization of turbulence production (IP) by the SSG model of Speziale et al. (1991) for modeling the rapid part of the pressure-strain term, the following f equation can be derived for the ζ - f - model:

$$L^2 \nabla^2 f - f = \frac{1}{\tau} \left(c_1 + C_2' \frac{P_k}{\varepsilon} \right) \left(\zeta - \frac{2}{3} \right) - \left(\frac{C_4}{3} - C_5 \right) \frac{P}{k} \quad (4.15)$$

After adopting the coefficients of the SSG pressure strain model and neglecting the last term of the above equation because of dimensionality reasons:

$$L^2 \nabla^2 f - f = \frac{1}{\tau} \left(c_1 + C_2' \frac{P_k}{\varepsilon} \right) \left(\zeta - \frac{2}{3} \right) \quad (4.16)$$

As suggested by Hanjalić et al. (2004) the model is completed by imposing the Kolmogorov time τ and length scale L combined with the realization constraints suggested by ?, who introduced the 'min' bound of the turbulence length scale to suppress the overprediction of the eddy viscosity in stagnation point regions with high normal stress rates:

$$\tau = \max \left[\min \left(\frac{k}{\varepsilon}, \frac{0.6}{\sqrt{6} C_\mu |S| \zeta} \right), C_\tau \left(\frac{\nu}{\varepsilon} \right)^{1/2} \right] \quad (4.17)$$

$$L = C_L \max \left[\min \left(\frac{k^{3/2}}{\varepsilon}, \frac{k^{1/2}}{\sqrt{6} C_\mu |S| \zeta} \right), C_\eta \left(\frac{\nu^3}{\varepsilon} \right)^{1/4} \right] \quad (4.18)$$

The eddy viscosity μ_t is defined in analogy to the definition in Durbin's $k - \varepsilon - v^2 - f$ model:

$$\mu_t = C_\mu \zeta \rho k \tau \quad (4.19)$$

The model constants for the $k - \varepsilon - \zeta - f$ model are given in Table 4.1.

Table 4.1.: Constants for the $k - \varepsilon - \zeta - f$ model

C_μ	$C_{\varepsilon 1}$	$C_{\varepsilon 2}$	c_1	C_2'	C_L	C_T	C_ν	σ_k	σ_ε	σ_ζ
0.22	$1.4(1 + 0.012/\zeta)$ $+0.4 \exp(-0.1 Re_T)$	1.9	0.4	0.65	0.36	6	85	1	1.3	1.2

4.3. Validation

The validation of the $k - \varepsilon - \zeta - f$ model was done with the well known ERCOFTAC flat plate test cases and with the low-pressure cascade test case T106A. This validation was done within Paper 1 and Paper 2.

4.3.1. Notes on Paper 1

Titel:	Application of the zeta-f-turbulence model to steady transitional flow.
Authors:	K. RAMADANI, M.E. KELTERER, R. PECNIK, W. SANZ
Published:	ETC paper 093, Conference proceedings of the 8 th European Turbomachinery Conference, Graz, Austria, 2009

Abstract

In Paper 1 the $k - \varepsilon - v^2 - f$ model and the $k - \varepsilon - \zeta - f$ model, both derived from Reynolds stress turbulence model as simplified second moment closures, were implemented into the in-house 3D RANS flow solver LINARS. Both models are based on the $k - \varepsilon$ turbulence model and simulate the turbulence redistribution close to the wall which plays an important role within the transition process. The second model is an enhancement from the first one for stability reasons and has already been applied successfully in a commercial code for automotive flows. Both models are applied to turbomachinery flows in this paper. But first they are validated on the ERCOFTAC test cases T3A and T3C2. Then they are applied to the steady flow in a T106A turbine cascade using a compressible as well as an incompressible flow solver based on the artificial compressibility concept. Especially the $k - \varepsilon - \zeta - f$ model shows very promising results. This validation is described in Paper 1.

Results

The main work of the author within Paper 1 was the validation of the $k - \varepsilon - \zeta - f$ model to turbomachinery flow compared to the $k - \varepsilon - v^2 - f$ model, by applying the model to the incompressible steady flow in the T106A turbine cascade. The implementation work was done by Pecnik (2007) within his PhD thesis and the validation with the ERCOFTAC test cases was done by Ramadani (2007) within his master thesis.

Both models show good results for the flat plate test case without pressure gradient (T3A) (see *Figs. 1* and *2*). For the non-zero pressure gradient flow (T3C2) both models show a too early transition onset and a too rapid transition compared with the experiments (see *Fig. 3*). When applying both models to the cascade test case T106A two different calculations were done, one using the time-marching code without any preconditioning and thus the outlet Mach number is set to 0.4 for convergence reasons, although the flow is incompressible. This is an approach which is also applied by other research groups using time-marching solver, because the influence of the compressibility can be considered as very small at this low Mach numbers. The second solver uses artificial compressibility as suggested by Shin (2001) for incompressible flows.

In the compressible calculation, the $k - \varepsilon - v^2 - f$ model shows a minimum in the skin friction coefficient, but does not predict any separation whereas the $k - \varepsilon - \zeta - f$ predicts separation, but the transition onset is too late for both free stream turbulence intensity levels (see *Figs. 5* and *6*). In the incompressible calculation the results for the $k - \varepsilon - v^2 - f$ model are similar to the compressible calculation. The $k - \varepsilon - \zeta - f$ model predicts the separation zone quite well for the lower free stream turbulence intensity of 0.5% and shows a minimum in the skin friction coefficient for the higher free stream turbulence intensity of 4.0% (see *Figs. 7* and *8*). Further validations on the $k - \varepsilon - \zeta - f$ are performed for Paper 2.

4.3.2. Notes on Paper 2

Titel:	Application of the zeta-f-turbulence model to steady transitional flow.
Authors:	M.E. KELTERER, K. RAMADANI, R. PECNIK, W. SANZ
Published:	ERCFTAC Bulletin 80, pp. 35-40, 2009

Abstract

In Paper 2 the validation of the $k - \varepsilon - \zeta - f$ model with the T106 cascade test case was performed in more detail compared to Paper 1. Additionally a boundary layer analysis is done.

Results

The validation of the $k - \varepsilon - \zeta - f$ model applied to the T106A cascade test case in terms of pressure coefficient c_p and skin friction coefficient c_f are presented in Paper 2 (*Figs. 2-9*). The analysis of the boundary layer flow in terms of the shape factor H_{12} is presented (see *Figs. 10* and *11*) using two different calculation methods for the boundary layer thickness. The method of Schobeiri and Ozturk (2009) and a second method based on the assumption of a constant pressure in the boundary layer are used. Both methods show the same tendency but with different absolute values. The simulation results show that the shape factor starts to decrease, when the skin friction coefficient starts to increase indicating a transition from laminar to turbulent flow. This work also shows the great potential of the $k - \varepsilon - \zeta - f$ model to predict transitional flows in turbomachinery applications.

Paper 1

K. Ramadani, M.E. Kelterer, R. Pecnik, W. Sanz

Application of the zeta- f -turbulence model to steady
transitional flow.

ETC paper 093
presented at the European Turbomachinery Conference
Graz, Austria, 2009

APPLICATION OF THE ZETA-F-TURBULENCE MODEL TO STEADY TRANSITIONAL FLOW

K. Ramadani – M.E. Kelterer – R. Pecnik – W. Sanz

Institute for Thermal Turbomachinery and Machine Dynamics
Graz University of Technology
Graz, Austria
wolfgang.sanz@tugraz.at

ABSTRACT

The accurate numerical simulation of the flow through turbomachinery depends on the correct prediction of boundary-layer transition phenomena. Reynolds stress turbulence models consider more flow physics and model the turbulence redistribution close to the wall which plays an important role within the transition process. Therefore in this work two turbulence models, namely the $k-\varepsilon-v^2-f$ and the $k-\varepsilon-\zeta-f$ model, are applied to turbomachinery flows. The second model is advanced from the first one for stability reasons and is already applied successfully in a commercial code for automotive flows.

Both models are validated on the ERCOFTAC test cases T3A and T3C2. Furthermore, they are also applied to the steady flow in a T106A turbine cascade with a compressible code as well as with an incompressible code based on the artificial compressibility concept. Especially the $k-\varepsilon-\zeta-f$ model shows very promising results.

NOMENCLATURE

Latin Letters

c	chord length
c_f	skin friction coefficient $c_f = \tau_w / (\rho U^2 / 2)$
c_p	pressure coefficient $c_p = (p_{t,in} - p_w) / (p_{t,in} - p_{out})$
C	model parameter
H_{12}	shape Factor
k	turbulent kinetic energy
L	flat plate length or length scale
l_m	turbulent mixing length
Ma	Mach number
p	pressure
P_k	turbulence production term
Re	Reynolds number
Re_T	turbulence Reynolds number $Re_T = k^2 / (\varepsilon \nu)$
S	magnitude of strain rate
u, v, U	velocity
y	wall distance

Greek Letters

ε	turbulence dissipation rate
ζ	velocity scale ratio
ν	kinematic viscosity
ρ	density
τ_w	wall shear stress

Subscripts/Superscripts

ax	axial
in	inlet
is	isentropic
out	outlet
t	total
T	turbulent
w	wall
+	dimensionless

Abbreviations

FSTI	free stream turbulence intensity
RANS	Reynolds averaged Navier-Stokes
RSS	Reynolds shear stress

INTRODUCTION

In turbomachines and especially in aircraft engines the Reynolds numbers that determine the evolution of the boundary layers can be relatively low. So a large part of the flow along the blade surfaces is often laminar or transitional. The boundary layer development, losses, efficiency and

heat transfer are greatly affected by the laminar-to-turbulent transition. Due to the high turbulence levels by-pass transition is the dominant form of transition in turbomachinery.

The ability to accurately predict the transition process is crucial for the design of efficient and reliable machines. Considerable effort has been spent on adapting standard two-equation turbulence models to predict transition for various kinds of flows. So Schmidt and Patankar (1991) and Savill (1993) showed the ability of two-equation low-Reynolds turbulence models to predict transition in boundary layer flows. But they also found that no model performed satisfactorily over a wide range of flow cases and conditions.

Besides these "pure" turbulence models, an increasing number of transition models are being developed from empirical correlations. Mostly they are based on an intermittency γ which gives the fraction of time when the flow is turbulent and which is used to modify the turbulent viscosity in the main equations. The different approaches can be divided into simpler algebraic models (e.g. Solomon et al., 1996) and more complex transport models (Steelant and Dick, 2001; Pecnik et al., 2003; Menter et al., 2004). Reasonable results can be achieved with these models but their high empiricism demands a continuous tuning of the model parameters in order to get accurate results for different flow situations. Additionally, most of these transition models need the evaluation of integral boundary layer parameters which make their implementation in general three-dimensional flow solvers difficult. A positive example for a transition model not using integral boundary layer parameters is the intermittency transport model of Savill, Launder and Younis (Savill 1996, Savill 2002a, Savill 2002b). They used it together with a low-Re Reynolds Stress Transport model and reported promising results.

Numerical investigations of transitional flows showed that Reynolds stress models with low-Reynolds-number modifications seem to perform better than two-equation turbulence models (Hanjalic and Hadzic, 1996). Reasons may be that they account for anisotropy of the free-stream and near-wall stress field, and particularly their ability to reproduce the normal-to-the-wall velocity fluctuations. Another merit is the exact treatment of the turbulence production and of effects of streamline curvature (Hadzic and Hanjalic, 1999). Therefore there is hope that also related Reynolds stress transport models with considerably less computational efforts are also able to predict laminar-to-turbulent transition in satisfying accuracy.

Among these models the $k-\varepsilon-v^2-f$ (V2F) turbulence model of Durbin (1995) is very promising and was investigated for turbomachinery applications by Sanz et al. in 2007. It showed good results for steady flows, but proved to be numerically unstable. Therefore in 2004 Hanjalic et al. suggested modifications to the V2F model in order to improve its numerical stability. Their $k-\varepsilon-\zeta-f$ (ZETA-F) model has already been incorporated in a commercial CFD code for automotive flows (Basara, 2005) and showed very promising results. In order to support the search for more general transition modelling, in this work the ZETA-F model is applied to transitional turbomachinery flows and compared with measurements and V2F calculations. Furthermore this work explores the difference in the solution of the flow around a turbine blade in case an incompressible or a compressible solver is used for low Mach number computations.

NUMERICAL METHOD

The computations were performed using the in-house Navier-Stokes code LINARS, developed at Graz University of Technology (Pecnik et al., 2005). The compressible Reynolds/Favre-averaged Navier-Stokes (RANS) equations are solved in conservative form by means of a fully-implicit time-marching finite-volume method on structured curvilinear grids in multiblock alignment. The inviscid (Euler) fluxes are discretized with the upwind flux-difference splitting method of Roe (1981). In order to achieve a high order of spatial accuracy a total variation diminishing (TVD) scheme with third-order interpolation was applied to get the state vector at each cell interface. The viscous flux vector at the cell interfaces is constructed with a second-order accurate central-differencing scheme using Green's theorem. To obtain a linear set of the governing equations the Newton-Raphson procedure is applied for the discretization in time. This method allows accurate

unsteady calculations as well as improves convergence for steady calculations. The main flow equations and the turbulence equations are solved sequentially.

Time-marching algorithms show bad convergence behaviour for flows of low Mach number due to their incompressible character. Therefore, even for incompressible test cases the computations are performed assuming increased velocities. In order to avoid this problem, LINARS can also be run with an artificial compressibility method (Shin, 2001) for incompressible flows. In this work compressible and incompressible solutions are presented for the incompressible test cases in order to show the influence of compressibility.

TURBULENCE MODELS

In this work the two following turbulence models are implemented into the LINARS code and applied to steady transitional flow: the $k-\varepsilon-v^2-f$ model (V2F) of Durbin (1995) and the $k-\varepsilon-\zeta-f$ model (ZETA-F) of Hanjalic et al. (2004). Both models have been derived from Reynolds stress transport models and they can be seen as simplified second moment closures. The wall damping effect is incorporated by modelling an auxiliary equation as a measure for the normal to the wall fluctuations. The main difference of these two models is that the V2F models solves for v'^2 (in case of y aligned with the wall normal v'^2 corresponds to the Reynolds stress component R22) whereas the ZETA-F model solves for the ratio v'^2/k as the anisotropy measure of near wall turbulence. The anisotropy of these models, as well as LES studies by Yang et al. (1994) which showed that the turbulence fluctuation in the wall-normal direction v' plays an important role within the transition process, motivate to apply the V2F model to transitional flows without any additional intermittency function (see also Lien et al., 1998).

The turbulent scales k and ε are provided by the standard $k-\varepsilon$ model for the V2F as well as for the ZETA-F model.

$$\frac{\partial k}{\partial t} + \bar{u}_j \frac{\partial k}{\partial x_j} = \frac{\partial}{\partial x_j} \left[\left(\nu + \frac{\nu_T}{\sigma_k} \right) \frac{\partial k}{\partial x_j} \right] + P_k - \varepsilon \quad (1)$$

$$\frac{\partial \varepsilon}{\partial t} + \bar{u}_j \frac{\partial \varepsilon}{\partial x_j} = \frac{\partial}{\partial x_j} \left[\left(\nu + \frac{\nu_T}{\sigma_\varepsilon} \right) \frac{\partial \varepsilon}{\partial x_j} \right] + \frac{C_{\varepsilon 1} P_k - C_{\varepsilon 2} \varepsilon}{T} \quad (2)$$

A detailed summary of the models is given below.

$k-\varepsilon-v^2-f$ (V2F) Model

The eddy viscosity and the auxillary equations of the V2F turbulence model are defined by the following relations:

$$\mu_T = C_\mu \rho \bar{v}^2 T \quad (3)$$

$$\frac{\partial \bar{v}^2}{\partial t} + \bar{u}_j \frac{\partial \bar{v}^2}{\partial x_j} = \frac{\partial}{\partial x_j} \left[\left(\nu + \frac{\nu_T}{\sigma_k} \right) \frac{\partial \bar{v}^2}{\partial x_j} \right] + N k f - \frac{\bar{v}^2}{k} \varepsilon \quad (4)$$

$$L^2 \frac{\partial^2 f}{\partial x_j^2} - f = \frac{C_1}{T} \left(\frac{\bar{v}^2}{k} - \frac{2}{3} \right) - C_2 \frac{P_k}{k} - \frac{1}{T} \left(\frac{\bar{v}^2}{k} - \frac{2}{3} \right) + (N-1) \frac{\bar{v}^2}{k T} \quad (5)$$

where the turbulence time scale T and the length scale L are given with:

$$T = \min \left[\max \left[\frac{k}{\varepsilon}, 6 \sqrt{\frac{\mu}{\rho \varepsilon}} \right], \frac{0.6k}{\sqrt{3} C_\mu |S| \bar{v}^2} \right] \quad (6)$$

$$L = C_L \max \left[\min \left[\frac{k^{2/3}}{\varepsilon}, \frac{k^{2/3}}{\sqrt{6} C_\mu |S| \bar{v}^2} \right], C_\mu \frac{(\mu/\rho)^{2/3}}{\varepsilon^{1/4}} \right] \quad (7)$$

The ‘‘min’’ bound of the turbulence scales corresponds to the realizability constraint of Durbin (Medic and Durbin, 2002), which suppresses the overprediction of the eddy viscosity in stagnation point regions with high rates of normal strain. The ‘‘max’’ bound considers that the turbulence scales cannot be less than the corresponding Kolmogorov scales

The elliptical relaxation equation (5) for the turbulence redistribution factor f accounts for non-local pressure effects associated with velocity pressure gradient correlations. It is used to model the mechanism of the redistribution of turbulent kinetic energy in the v'^2 -equation and its behaviour in the near-wall region.

This model has been used successfully by the authors to simulate transitional boundary layers on flat plate test cases and to predict the secondary flow field through a transonic turbine guide vane (Pecnik et al., 2005; Sanz et al., 2007).

The model equations and the appendant constants are given in Table 1. In Eqs. (4) and (5) $N = 6$ according to Lien and Durbin (1996) which allows a Dirichlet wall boundary condition $f=0$ instead of $f_w \sim 1/y^4$ in order to avoid numerical difficulties.

In the f equation the realizability constraints in the definitions of T and L (min functions) are omitted for stability (see Sanz et al., 2007). The $C_{\varepsilon l}$ function of the production term of the ε -equation $C_{\varepsilon l} P_k/T$ is adapted as suggested by Lien et al. (1998) (second term of $C_{\varepsilon l}$ definition in Table 1).

The inlet boundary conditions for k and ε are set in order to reproduce the desired free-stream turbulence intensity along the plate. v'^2 is set to $2/3k$ in the free-stream and at the inlet a von Neumann condition is set for f . At solid walls, k and v'^2 are zero as well as f due to the modification of Lien and Durbin (1996). The boundary condition for ε , $\varepsilon_w = 2vk/y^2$ can cause instabilities and thus limits the size of the time step.

k- ε - ζ -f (ZETA-F) Model

The V2F suffers from stability problems and often needs many iterations for convergence. To avoid these difficulties, Hanjalic et al (2004) proposed a modified V2F model by introducing a dimensionless velocity scale ratio $\zeta = v'^2/k$ instead of v'^2 . The transport equation for ζ can be directly obtained from the v'^2 - and k -equations of the V2F model. The transformation yields to:

$$\frac{\partial \zeta}{\partial t} + u_j \frac{\partial \zeta}{\partial x_j} = \frac{\partial}{\partial x_j} \left(\left(v + \frac{v_T}{\sigma_\zeta} \right) \frac{\partial \zeta}{\partial x_j} \right) + f - \frac{\zeta}{k} P_k + \frac{2}{k} \left(v + \frac{v_T}{\sigma_\zeta} \right) \frac{\partial \zeta}{\partial x_j} \frac{\partial k}{\partial x_j} \quad (8)$$

The last term on the right-hand-side, the ‘‘cross diffusion’’, is significant only in the near-wall region. However, in order to simplify the equation into a source-sink diffusion form it is neglected and the constants are retuned for compensation.

The new ζ equation contains the turbulence kinetic energy production P_k instead of the dissipation ε which can be easier reproduced correctly. As a second advantage the boundary condition for the relaxation variable f is $f_w = -(2v\zeta)/y^2$, compared to $f_w \sim 1/y^4$ as in the original V2F model. f_w has the same form as ε_w and can be treated together in the numerical procedure. These modifications enhance the stability in the computational procedure.

In the ZETA-F model the rapid component of the pressure-strain term is modelled with the more advanced quasi linear SSG model of Speziale et al. (1991) instead of the simpler assumption of isotropisation of production in the V2F model.

Rearranging the f equation and neglecting some small terms the final form can be written as:

$$L^2 \frac{\partial^2 f}{\partial x_j^2} - f = \frac{1}{T} \left(c_1 + C_2 \frac{P_k}{\varepsilon} \right) \left(\zeta - \frac{2}{3} \right) \quad (9)$$

The eddy viscosity is defined in analogy to the definition in Durbin’s V2F model. The ZETA-F model is completed by imposing the Kolmogorov time and length scale as shown below. Table 1 lists all coefficients of the V2F and ZETA-F model.

$$v_T = C_\mu \zeta k T \quad (10)$$

$$T = \max \left[\min \left[\frac{k}{\varepsilon}, \frac{a}{\sqrt{6} C_\mu |S| \zeta} \right], C_T \sqrt{\frac{v}{\varepsilon}} \right] \quad (11)$$

$$L = C_L \max \left[\min \left[\frac{k^{3/2}}{\varepsilon}, \frac{k^{1/2}}{\sqrt{6}C_\mu |S| \zeta} \right], C_\eta \left(\frac{v^3}{\varepsilon} \right)^{1/4} \right] \quad (12)$$

Table 1: Coefficients of V2F and ZETA-F model

$v^2 - f$:	C_μ	$C_{\varepsilon 1}$	$C_{\varepsilon 2}$	C_1	C_2	C_L	C_T	C_η	σ_k	σ_ε	
	0.22	$1.4 \left(1 + 0.045 \sqrt{k/v'^2} \right) + 0.4 \exp(-0.1 \text{Re}_T)$	1.9	1.4	0.3	0.23	6	70	0.5	1.3	
$\zeta - f$:	C_μ	$C_{\varepsilon 1}$	$C_{\varepsilon 2}$	c_1	C'_2	C_L	C_T	C_η	σ_k	σ_ε	σ_ζ
	0.22	$1.4 \left(1 + 0.012 / \zeta \right) + 0.4 \exp(-0.1 \text{Re}_T)$	1.9	0.4	0.65	0.36	6	85	1	1.3	1.2

The in-house code LINARS solves the k , ε and v^2/ζ equations implicit in a coupled manner, whereas the elliptic equation for f is solved separately for each time iteration.

RESULTS AND DISCUSSION

Flat Plate Test Cases

As a first assessment numerical results are compared with the well-documented ERCOFTAC experimental data obtained from transitional flows over adiabatic flat plates with sharp leading edges (Savill, 1992). These experiments were chosen to test the ability of the models to predict bypass transition under the effects of free-stream turbulence with zero and varying pressure gradient conditions. In this work the test cases T3A with zero pressure gradient and T3C2 with non-uniform pressure gradient along the plate are presented. The main experimental data Reynolds number and free-stream turbulence intensity (FSTI) as well as the turbulence boundary conditions imposed at the grid inlet ($x/L = -0.1$ for T3A and $x/L = -0.13$ for T3C2) are summarized in Table 2.

FSTI and turbulent mixing length at the inlet were chosen that way that the measured FSTI along the plate is matched. For the calculation of the inlet turbulent dissipation from turbulent kinetic energy and turbulent mixing length $C_\mu=0.09$ is used.

Table 2 : Boundary conditions for the flat plate test cases

test case	Re_L	FSTI _{in} [%]	$l_{m,in}$ [mm]	L [mm]
T3A	527881	5.6 (3.3)	0.205	300
T3C2	656000	3.6 (2.7)	1	1500

For the T3A test case an H grid with 80 grid points in stream wise and 64 grid points in normal-to-wall direction is used (y^+ -value < 0.5 , stretching factor of 1.16, ~ 40 cells inside the boundary layer).

In Fig. 1 the skin friction coefficient and the shape factor, values which characterize the transition process, are shown. Both models show good agreement with the measurements and capture the transition location well. In the fully turbulent region, the ZETA-F is closer to the measurements of skin friction and shape factor, but both models have in common that they underpredict the skin friction value in the turbulent boundary layer.

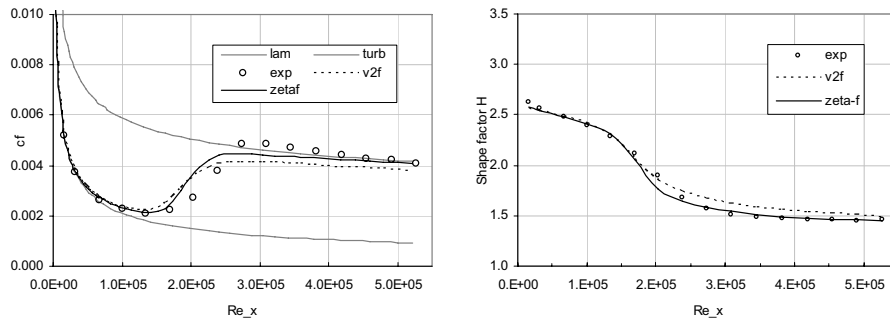


Fig. 1: Skin friction and shape factor over plate Reynolds number for the test case T3A

In Fig. 2 the dimensionless turbulence quantities shear stress $\overline{u'v'^+}$ and normal-to-wall stress $\overline{v'^2}$ over the dimensionless wall distance y^+ are presented giving better insight into the boundary layer behaviour. The normal Reynolds stress $\overline{v'^2}$ is solved directly with a transport equation. The turbulent shear stress $\overline{u'v'^+}$ is calculated using following assumptions: $u'v' = -C_\mu v^2 T (du/dy)$.

The first two diagrams of Fig. 2 show the turbulence quantities within the transitional zone whereas the third diagram shows the fully developed turbulent flow region. The profiles in the transitional zone are in very good agreement with the experimental data, especially in the early transitional zone. At $Re_x = 238400$ the V2F better predicts the normal stress, whereas the shear stress is overpredicted by both models considerably. In the fully turbulent region both models overpredict shear and normal stresses. In the outer region of the boundary layer the magnitude of the turbulent stresses of the V2F model decrease earlier indicating a smaller boundary layer thickness.

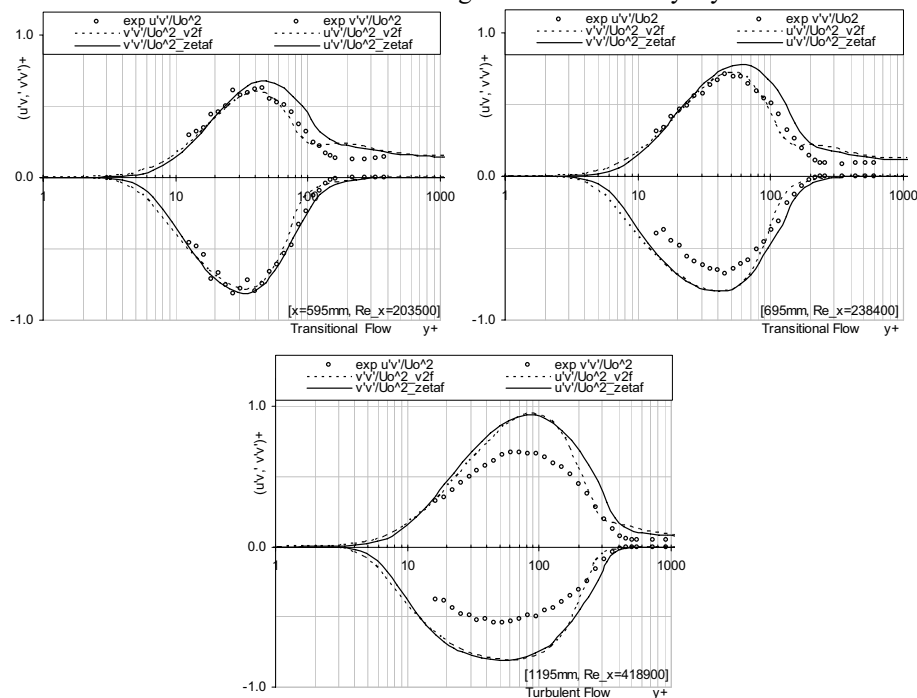


Fig. 2: Boundary layer turbulence profiles at three different streamwise positions for the T3A test case

The results for the non-uniform pressure gradient test case T3C2 are given in Fig. 3. This case is characterized by a combined favourable and adverse pressure gradient over the plate typical for an aft loaded turbine blade. In order to obtain the prescribed pressure distribution a contoured opposite wall was designed. The grid has 290 grid points in streamwise and 80 grid points in normal-to-wall direction (grid stretching factor of 1.13, $y^+ < 0.5$). Again the turbulent boundary conditions were estimated to match the measured FSTI distribution along the plate and are given in Table 2. Here, both models predict a slightly too early transition onset and a too rapid transition compared with the experimental data. The V2F model is closer to the experimental data. Both models predict the decline in skin friction after transition. In general the simulation can be characterized as very satisfactory.

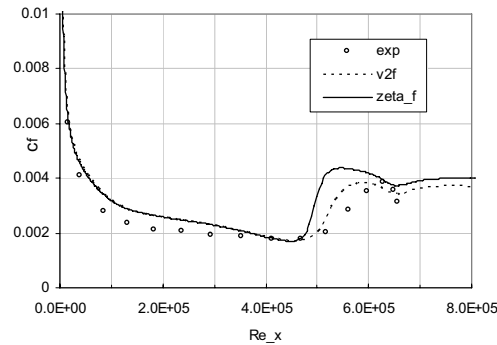


Fig. 3: Skin fraction over Re_x for the T3C2 test case

Low Pressure Turbine Cascade T106A

Because the calculations of the flat plate test cases showed satisfactory results for both models, as a next validation step the calculation of the steady transitional flow through the low pressure turbine cascade T106A is performed. This flow was experimentally investigated at the Whittle Laboratory from Stieger (2001) for a low FSTI and Opoka and Hodson (2005) for a higher FSTI. This flow is very challenging, because by-pass transition as well as separated-flow transition can occur on the suction side depending on the inlet FSTI. Fig. 4 shows the blade geometry and the used computational grid consisting of 5 blocks with an O-block wrapping around the blade. The O-block contains 320×88 grid cells with a maximum y^+_{\max} value below 1 along most of the blade surface.

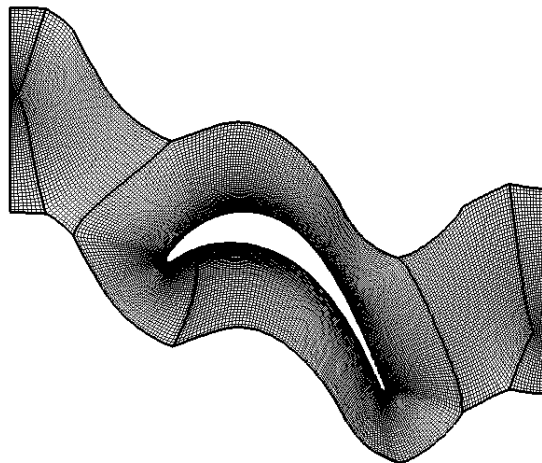


Fig. 4: Computational grid for T106A cascade flow (O-block with 320 x 88 cells)

The main goal of the experiments was to study the influence of unsteady inflow conditions on the transitional blade flow. The unsteady inflow is provided by moving bars, located 70 mm upstream of the cascade inlet. In this work only the steady flow without bars is investigated, but further unsteady simulations are envisaged. Table 3 gives the main operating conditions from the experiments used for the numerical investigations. The inlet Mach number is very low, so that the flow can be considered as fully incompressible.

Table 3: Main operating conditions of the T106A cascade

$Re_{out,c}$	M_{in}	FSTI [%]	c [mm]	l_{ax} [mm]	Pitch [mm]
160000	~ 0.02	0.5 and 4.0	198	85.97	158.2

Fig. 5 and Fig. 6 show the measured pressure distribution on blade suction and pressure side for both inlet FSTI. At a surface position of $s/s_{max}=0.44$ the peak suction position occurs. From this point the boundary layer decelerates under the influence of an adverse pressure gradient. In the case of the lower freestream turbulence, the suction surface boundary layer separates at a surface position of $s/s_{max}=0.63$ indicated by the start of a pressure ‘‘plateau’’. It extends up to a $s/s_{max}=0.83$, where the transition process starts which leads to a recovery of the surface pressure. At a surface distance of $s/s_{max}=0.9$, the boundary layer is attached again. In the case of the higher freestream turbulence, the pressure distribution on the suction side lacks the pressure plateau between $s/s_{max}=0.6$ and $s/s_{max}=0.8$. This suggests that by-pass transition prevents the formation of a separation bubble.

Compressible Results

Although the flow is incompressible, the first calculations are done with our time-marching code without any preconditioning and thus the outlet Mach number is set to 0.4 for convergence reasons. This approach is also applied by other groups who use time-marching codes, since the influence of compressibility is considered as small at this low Mach number. The measurement data do not include the turbulent mixing length or turbulent dissipation at the inflow, so that these values are varied at the inlet. This is done by imposing different turbulence Reynolds numbers, which is considered as a dimensionless measure of turbulence (according to Pope, 2000), ranging from $Re_{\tau}=50$ to 500. The turbulence Reynolds number allows to calculate the turbulence mixing length using the turbulence kinetic energy.

Fig. 5 shows the measured and computed pressure distribution for an inlet FSTI of 0.5 % as well as the resulting skin friction distribution along the blade suction side. The values on the pressure side are in very good agreement with the experimental data, whereas a remarkable deviation can be observed along the whole suction side. The pressure distribution of the V2F model does not indicate any separation for all inlet Re_{τ} numbers, which is confirmed by the skin friction distribution. On the other hand, the ZETA-F model is able to predict the laminar separation bubble on the suction side. For $Re_{\tau}=50$ the separation onset is predicted at $s/s_{max}=0.75$ compared to the measured value of 0.63, but the length of the separation zone is very similar (see skin friction distribution). The results for an inlet Re_{τ} of 200 and 500 are also given in Fig. 5 for the ZETA-F model, but they predict a slightly further downstream separation onset and a shorter bubble. So for the further presentations, mainly results for $Re_{\tau} = 50$ are depicted. This value corresponds to a mixing length of 1.5% chord length for 0.5% inlet FSTI and of 0.2% chord length for the higher inlet FSTI of 4.0%. For the 4% case a $Re_{\tau}=500$ results in the same mixing length of 1.5% chord length as for the 0.5% case at $Re_{\tau}=50$.

The situation is similar for the case with an inlet FSTI=4% (see Fig.6). Both models give similar results for the pressure distribution besides the small bulge at about $s/s_{max} = 0.8$. This bulge is also predicted by the ZETA-F model, but again too far downstream. The measurements indicate that the boundary layer is close to separation, whereas the skin friction for ZETA-F shows a small

separation bubble. This bubble is only predicted by $Re_T=50$, but not for higher Re_T values at the inlet. The skin friction distribution shows local minima at about $s/s_{max}=0.7$. Only the ZETA-F model shows a small separation zone for $Re_T=50$. The sharp increase at $s/s_{max} > 0.8$ indicates beginning transitional flow. For $Re_T=500$, no separation is predicted. It is interesting that the ZETA-F model is more sensible to variations of Re_T than the V2F model.

The better results of the ZETA-F model could be caused by the improved modelling of the shear stress and production of turbulent kinetic energy (see model description above).

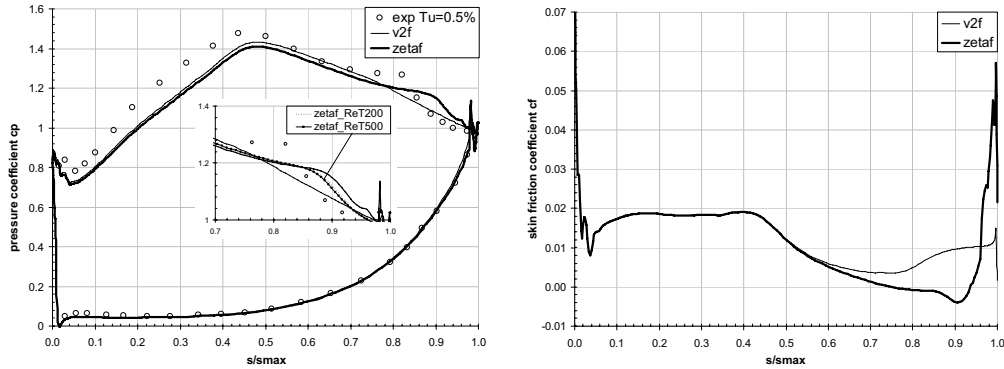


Fig. 5: Calculated and measured pressure coefficient along the T106A cascade with 0.5% FSTI

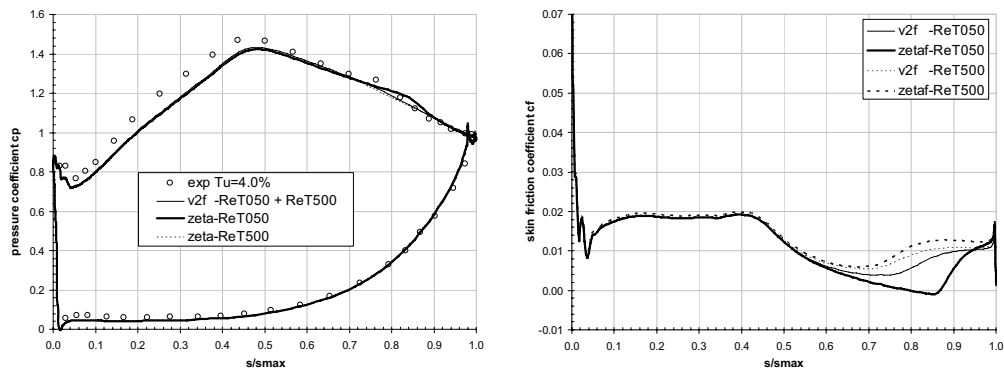


Fig. 6: Calculated and measured pressure coefficient along the T106A cascade with 4% FSTI

Incompressible Results

Finally the T106A turbine cascade is calculated with the incompressible code version of LINARS using artificial compressibility (Shin, 2001). For comparing the incompressible calculation with the compressible one ($Re_T=50$), the mixing length is set equal in both calculations, which corresponds to $Re_T=100$ in the incompressible case.

For both inlet FSTI the agreement with the measured pressure distribution is much better, especially for 4% inlet FSTI (see Fig. 7 and Fig. 8). The main reason for this disagreement of the compressible calculation is the too high Mach number of 0.4 used for the compressible calculation and the thus resulting compressibility effects.

The V2F model is again not able to predict any separation. For the 0.5 % FSTI case the ZETA-F model predicts the separation onset closer to the measured location, the length of the separation zone is slightly too small. The skin friction distribution is similar to the compressible calculations, whereas the V2F model seems to predict a rapid transition to turbulence closely after the peak pressure location.

For the inlet 4 % FSTI case the incompressible calculation does not predict any separation, although the ZETA-F prediction has a minimum at $s/s_{\max}=0.6$. The V2F model predicts transition even more upstream due to the higher free-stream turbulence.

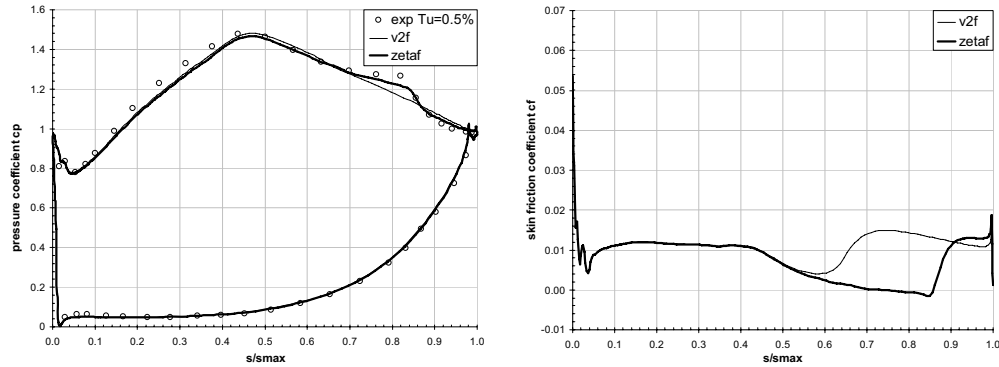


Fig. 7: Calculated and measured pressure coefficient along the T106A cascade with 0.5% FST

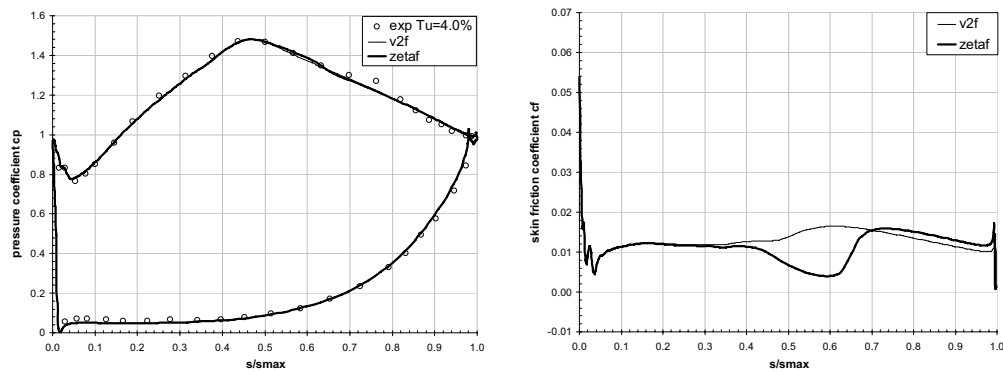


Fig. 8: Calculated and measured pressure coefficient along the T106A cascade with 4% FST

CONCLUSIONS

In order to improve the reliability of numerical transition prediction, two modern turbulence models, the V2F model of Durbin (1995) and the ZETA-F model of Hanjalic et al. (2004) are investigated for turbomachinery flows. Both models are derived from the Reynolds stress model and thus have good chances to satisfactorily predict laminar-to-turbulent transition. The second model is an advancement of the first one with a better numerical stability. Both models do not need an intermittency function.

As first test cases the transitional boundary layer is calculated for two flat-plate flows with zero and varying pressure gradient. The V2F model performs very well with the modification for transition prediction suggested by Lien et al. (1998), and also the ZETA-F model shows good results with the same modification.

Finally, the predictions of the steady transitional flow around the T106A low pressure turbine cascade are compared with the measurements. The V2F is not able to predict the observed suction side separation zone in all calculations, transition to turbulence occurs more upstream. The ZETA-F model is able to predict the separation bubble on the suction side for 0.5 % inlet FSTI, although a little bit too far downstream. For the 4 % inlet FSTI the agreement with the measurements is excellent, especially for the incompressible calculation. In general, the incompressible calculations give better results than the compressible code. In our calculations the ZETA-F model shows a great potential to predict transitional flows in turbomachinery applications. It will be applied to the

unsteady T106A cascade with wake-induced transition in the near future.

ACKNOWLEDGEMENTS

The support by the Austrian Federal Ministry of Transport, Innovation and Technology (BMVIT) within the Austrian Aviation Program “TAKE OFF” for the project “CFD-Trans” as well as by the Austrian Science Foundation (FWF) for the grant P16761 “Steady and Unsteady Transition Modeling” is gratefully acknowledged.

REFERENCES

- Basara B. (2005): *Calculation of vortex shedding from a circular cylinder in uniform and shear flows*. Proceedings of 2005 ASME Fluids Engineering Division Summer Meeting, FEDSM2005, pp. 2295-2300.
- Durbin P.A. (1995): *Separated Flow Computations with the $k-\varepsilon-v^2$ model*; In AIAA J., Vol 33, pp.659-664.
- Hadzic I. and Hanjalic K. (1999): *Separation-Induced Transition to Turbulence: Second-Moment Closure Modelling*, Flow Turbulence and Combustion, 1999, Vol. 63, pp. 153-173
- Hanjalić K., Popovac M. and Hadžiabdić M (2004): *A robust near-wall elliptic-relaxation eddy-viscosity turbulence model for CFD*, In International Journal of Heat and Fluid Flows, Vol. 25, pp. 1047-1051.
- Hanjalic K. and Hadzic I. (1996): *Modelling the Transition Phenomena With Statistical Turbulence Closure Models*, In: Henkes, R.A.W.M. and van Ingen, J.L. (eds.) “Transitional Boundary Layers in Aeronautics”. North- Holland, Amsterdam.
- Lien F.S., Durbin P.A. (1996): *Non-Linear $k-\varepsilon-v^2$ -Modeling with Application to High-Lift*, Summer Program Proceedings, Center for Turbulence Research, NASA/Stanford University, pp. 5-22.
- Lien F.S., Kalitzin G. and Durbin P.A. (1998): *RANS Modelling for Compressible and Transitional Flows*, CTR Proceedings of the Summer Program 1998.
- Medic G. and Durbin P.A. (2002): *Toward Improved Pre-diction of Heat Transfer on Turbine Blades*, Journal of Turbomachinery, Vol. 124, pp. 187-192
- Menter F.R., Langtry R.B., Likki S.R., Suzen Y.B. and Huang P.G. (2004): *A Correlation-Based Transition model Using Local Variables, Part 1-Model Formulation*, GT2004-53452, ASME Turbo Expo 2004, Vienna, Austria
- Opoka M. M. and Hodson H. H.(2005): *An Experimental Investigation of the Unsteady Transition Process on the High Lift T106A Turbine Blade*, In the Proceedings of ISABE-2005-1277, Munich, Germany, 4th-9th September 2005.
- Pecnik R., Sanz W., Gehrler A. and Woisetschlaeger J. (2003): *Modeling of Laminar-Turbulent Transition Using Two Different Intermittency Transport Equations*, Flow, Turbulence and Combustion, 2003, Vol. 70, pp. 299-323
- Pecnik R., Pieringer P. and Sanz W. (2005): *Numerical Investigation of the Secondary Flow of a Transonic Turbine Stage Using Various Turbulence Closures*, ASME paper GT2005-68754, ASME Turbo Expo 2005, Reno-Tahoe, Nevada, USA.
- Pope S.B. (2000): *Turbulent Flows*, Cambridge University Press.
- Roe P.L. (1981): *Approximate Riemann Solver, Parameter Vectors and Differencing Scheme*, Journal of Computational Physics Vol 43, pp. 357-372.
- Sanz W., Pecnik R., Tratnig A. and Heitmeir F. (2007): *Application of modern turbulence models to steady transitional flow*, ETC 2007, Athena, Greece.
- Savill A M. (1992): *A synthesis of T3 Test Case Predictions, Numerical Simulation of Unsteady Flows and Transition to Turbulence*, O. P. et al., ed., Cambridge University Press, pp. 404-442.
- Savill A.M. (1993): *Some Recent Progress in the Turbulence Modelling of By-Pass Transition* in “Near Wall Turbulent Flow” by So, Speziale and Lauenders (eds.), Elsevier Science (New York).
- Savill A.M. (1996): *One-point closures applied to transition* in “Turbulence and Transition Modelling - Lecture Notes from the ERCOFTAC/IUTAM Summerschool Held in Stockholm,

- 12-20 June, 1995” by D.S. Henningson et al.(eds.), Kluwer Academic Pub. Group, Chap. 6., p 233-268.
- Savill A.M. (2002a): *By-Pass Transition using Conventional Closures* in “Closure Strategies for Turbulent and Transitional Flows” by Launder B.E. and Sandham N.D. (eds.), Cambridge University Press, Chapter 17, pp 464-492.
- Savill A.M. (2002b): *New Strategies in Modelling By-Pass Transition* in “Closure Strategies for Turbulent and Transitional Flows” by Launder B.E. and Sandham N.D. (eds.), Cambridge University Press, Chapter 18, pp 493-521.
- Schmidt R.C. and Patankar S.V. (1991): *Simulating Boundary Layer Transition with Low-Reynolds $k-\varepsilon$ Turbulence Models: Part 1 – An Evaluation of Prediction Characteristics*, ASME Journal of Turbomachinery, Vol. 113, pp. 10-17
- Shin S. (2001): *Reynolds-Averaged Navier-Stokes Computation of Tip Clearance Flow in a Compressor Cascade Using an Unstructured Grid*, PhD thesis, Virginia Polytechnic Institute and State University, Blacksburg, Virginia, USA.
- Solomon W.J., Walker G.J. and Gostelow J.P. (1996): *Transition Length Prediction for Flows With Rapidly Changing Pressure Gradients*, ASME J.of Turbomachinery, Vol. 113, pp. 744-751
- Speziale C.G., Sarkar S. and Gatski T.B. (1991): *Modelling the pressure-strain correlation of turbulence: an invariant dynamical systems approach*, J. Fluid Mech., Vol 227, pp. 245-272.
- Steelant J. and Dick E. (2001): *Modeling of Laminar-Turbulent Transition for High Freestream Turbulence*, Journal of Fluids Engineering, Vol. 123, pp. 22-30
- Stieger R. D. (2002): *The Effects of Wakes on Separating Boundary Layers in Low Pressure Turbines*, PhD thesis, Cambridge University Engineering Department, February 2002.
- Yang Z., Voke P.R. and Savill A.M. (1994): *Mechanism and Models of Boundary Layer Receptivity deduced from Large-Eddy Simulation of Bypass Transition, Direction and Large-Eddy Simulation Vol 1*, P. R. Voke, L. Kleiser & J. Chollet (eds.) 225-236, Kluwer Academic Publishers.

Paper 2

M.E. Kelterer, K. Ramadani, R. Pecnik, W. Sanz

Application of the zeta- f -turbulence model to steady transitional flow.

APPLICATION OF THE ZETA-F TURBULENCE MODEL TO STEADY TRANSITIONAL FLOW

M.E. Kelterer, K. Ramadani, R. Pecnik, W. Sanz

Institute for Thermal Turbomachinery and Machine Dynamics, Graz University of Technology, Austria.

Abstract

The accurate numerical simulation of the flow through turbomachinery depends on the correct prediction of boundary-layer transition phenomena. Reynolds stress turbulence models consider more flow physics and model the turbulence redistribution close to the wall which plays an important role within the transition process. Therefore in this paper the $k-\varepsilon-\zeta-f$ turbulence model is applied to turbomachinery flows. The $k-\varepsilon-\zeta-f$ turbulence model is for stability reasons advanced from the $k-\varepsilon-v^2-f$ turbulence model which has already been applied successfully in a commercial code for automotive flows.

The $k-\varepsilon-\zeta-f$ model is validated on the ERCOFTAC test cases T3A and T3C2. Furthermore, it is also applied to the steady flow in a T106A turbine cascade with a compressible code as well as with an incompressible code based on the artificial compressibility concept. It shows very promising results.

1 Introduction

In turbomachines and especially in aircraft engines the Reynolds numbers that determine the evolution of the boundary layers can be relatively low. So a large part of the flow along the blade surfaces is often laminar or transitional. The boundary layer development, losses, efficiency and heat transfer are greatly affected by the laminar-to-turbulent transition. Due to the high turbulence levels by-pass transition is the dominant form of transition in turbomachinery.

The ability to accurately predict the transition process is crucial for the design of efficient and reliable machines. Numerical investigations of transitional flows showed that Reynolds stress models with low-Reynolds-number modifications seem to perform better than two-equation turbulence models (see [1]). Reasons may be that they account for the near wall anisotropy and particularly their ability to reproduce the normal-to-the-wall velocity fluctuations. Another merit is the exact treatment of the turbulence production and of effects of streamline curvature (see [2]). Therefore there is hope that also related Reynolds stress transport models with considerably less computational efforts are also able to predict laminar-to-turbulent transition in satisfying accuracy.

Among these models the $k-\varepsilon-v^2-f$ (V2F) turbulence model of Durbin [3] is very promising and was investigated for turbomachinery applications by Sanz et al. in 2007 [4]. It showed good results for steady flows, but proved to be numerically unstable. Therefore in 2004 Hanjalic et al. [5] suggested modifications to the V2F model in order to improve its numerical stability. Their $k-\varepsilon-\zeta-f$ (ZETA-F) model has already been incorporated in a commercial CFD code for automotive flows (see [6])

and showed very promising results. In order to support the search for more general transition modelling, in this work the ZETA-F model is applied to transitional turbomachinery flows and compared with measurements and V2F calculations. Furthermore this work explores the difference in the solution of the flow around a turbine blade in case an incompressible or a compressible solver is used for low Mach number computations.

2 Numerical Method

The computations were performed using the in-house Navier-Stokes code LINARS, developed at Graz University of Technology (Pecnik et al., 2005 [7]). The compressible Reynolds/Favre-averaged Navier-Stokes (RANS) equations are solved in conservative form by means of a fully-implicit time-marching finite-volume method on structured curvilinear grids in multiblock alignment. The inviscid (Euler) fluxes are discretized with the upwind flux-difference splitting method of Roe (1981) [8]. In order to achieve a high order of spatial accuracy a total variation diminishing (TVD) was used. The viscous flux vector at the cell interfaces is constructed with a second-order accurate central-differencing scheme using Green's theorem. The steady state solution is obtained by iteratively solving (Newton-Raphson procedure) the linearized Navier-Stokes equations using a Line Gauss-Seidel solver. The main flow equations and the turbulence equations are solved sequentially.

Time-marching algorithms show bad convergence for flows at low Mach numbers due to the ill-conditioned set of equations (stiff equation system) (see [9]). To overcome this problem the Mach number has been increased by retaining the Reynolds number for the herein presented test cases. A second approach to overcome the ill-conditioned equation system is by artificially changing the speed of sound by using the artificial compressibility method (Shin, 2001 [10]). The results obtained for the turbine blade are shown for both solution approaches to point out the differences.

3 Turbulence Model

In this work the $k-\varepsilon-\zeta-f$ turbulence model (ZETA-F) of Hanjalic et al. (2004) [5] is implemented into the LINARS code and applied to steady transitional flows. This model is an advancement of Durbin's $k-\varepsilon-v^2-f$ model (1995) [3]. Both models have been derived from Reynolds stress transport models and can be seen as simplified second moment closures. The near-wall turbulence damping is modeled with an elliptic auxiliary equation. The main difference of these two models is that the V2F model solves the dimensional value of the normal-to-wall Reynolds stress component whereas the ZETA-F model solves a non-dimensional value $-v'^2/k$ (interpretable as

the turbulence anisotropy). LES studies by Yang et al. (1994) [11] showed that the turbulence fluctuation in the wall-normal direction v' plays an important role within the transition process. This motivates to use the aforementioned models to use them to simulate transitional flows without using intermittency functions as they carry some information about the near wall turbulence anisotropy (see also Lien et al., 1998 [12]).

$k-\varepsilon-\zeta-f$ (ZETA-F) Model

The turbulent scales k and ε are provided by the standard $k-\varepsilon$ model for the ZETA-F model.

The V2F suffers from stability problems and often needs many iterations for convergence. To avoid these difficulties, Hanjalic et al [5] proposed a modified V2F model by introducing a dimensionless turbulent velocity scale ratio $\zeta = v'^2/k$ instead of v'^2 . The transport equation for ζ can be directly obtained from the v'^2 - and k -equations of the V2F model. The transformation yields to:

$$\frac{\partial \zeta}{\partial t} + \overline{u_j} \frac{\partial \zeta}{\partial x_j} = \frac{\partial}{\partial x_j} \left(\left(\nu + \frac{\nu_T}{\sigma_\zeta} \right) \frac{\partial \zeta}{\partial x_j} \right) + f - \frac{\zeta}{k} P_k + \frac{2}{k} \left(\nu + \frac{\nu_T}{\sigma_\zeta} \right) \frac{\partial \zeta}{\partial x_j} \frac{\partial k}{\partial x_j} \quad (1)$$

The last term on the right-hand-side, the "cross diffusion", is significant only in the near-wall region. However, in order to simplify the equation into a source-sink diffusion form it is neglected and the constants are returned for compensation.

The new ζ equation contains the turbulence kinetic energy production P_k instead of the dissipation ε which can be easier reproduced correctly. As a second advantage the boundary condition for the relaxation variable f is $f_w = -(2\nu\zeta)/y^2$, compared to $f_w \sim 1/y^4$ as in the original V2F model. f_w has the same form as ε_w and can be treated together in the numerical procedure. These modifications enhance the stability in the computational procedure.

In the ZETA-F model the rapid component of the pressure-strain term is modelled with the more advanced quasi linear SSG model of Speziale et al. (1991) [13] instead of the simpler assumption of isotropisation of production in the V2F model.

Rearranging the f equation and neglecting some small terms the final form can be written as:

$$L^2 \frac{\partial^2 f}{\partial x_j^2} - f = \frac{1}{T} \left(c_1 + C'_2 \frac{P_k}{\varepsilon} \right) \left(\zeta - \frac{2}{3} \right) \quad (2)$$

The eddy viscosity is defined in analogy to the definition in Durbin's V2F model. The ZETA-F model is completed by imposing the Kolmogorov time and length scale as shown below. The following coefficients are used for the ZETA-F model: $C_\mu = 0.22$, $C_{\varepsilon 1} = 1.4(1 + 0.012/\zeta) + 0.4 \exp(-0.1 Re_T)$, $C_{\varepsilon 2} = 1.9$, $c_1 = 0.4$, $C'_2 = 0.65$, $C_L = 0.36$, $C_T = 6$, $C_\eta = 85$, $\sigma_k = 1$, $\sigma_\varepsilon = 1.3$, $\sigma_\zeta = 1.2$.

$$\nu_T = C_\mu \zeta k T \quad (3)$$

$$T = \max \left[\min \left[\frac{k}{\varepsilon}, \frac{a}{\sqrt{6} C_\mu |S| \zeta} \right], C_T \sqrt{\frac{\nu}{\varepsilon}} \right] \quad (4)$$

$$L = C_L \max \left[\min \left[\frac{k^{3/2}}{\varepsilon}, \frac{k^{1/2}}{\sqrt{6} C_\mu |S| \zeta} \right], C_\eta \left(\frac{\nu^3}{\varepsilon} \right)^{1/4} \right] \quad (5)$$

The in-house code LINARS solves the k , ε and v'^2/ζ equations implicit in a coupled manner, whereas the elliptic equation for f is solved separately for each time iteration.

4 Results and Discussion

As a first assessment numerical results were compared with the well-documented ERCOFTAC experimental data obtained from transitional flows over adiabatic flat plates with sharp leading edges [14]. These experiments were chosen to test the ability of the models to predict by-pass transition under the effects of free-stream turbulence with zero and varying pressure gradient conditions. The results of this evaluation can be found in Ramadani et al. [15].

Because the calculations of the flat plate test cases showed satisfactory results for both models, as a next validation step the calculation of the steady transitional flow through the low pressure turbine cascade T106A is performed. This flow was experimentally investigated at the Whittle Laboratory from Stieger (2001) [16] for a low free stream turbulent intensity (FSTI) and Opoka and Hodson (2008) [17] for a higher FSTI. This flow is very challenging, because by-pass transition as well as separated-flow transition can occur on the suction side depending on the inlet FSTI. Figure 1 shows the blade geometry and the used computational grid consisting of 5 blocks with an O-block wrapping around the blade. The O-block contains 320×88 grid cells with a maximum y_{max}^+ value below 1 along most of the blade surface.

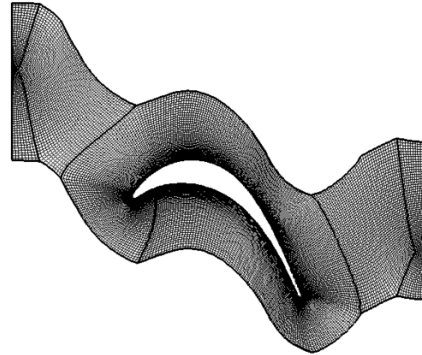


Figure 1: Computational grid for T106A cascade flow (O-block with 320×88 cells).

The main goal of the experiments was to study the influence of unsteady inflow conditions on the transitional blade flow. The unsteady inflow is provided by moving bars, located 70 mm upstream of the cascade inlet. In this work only the steady flow without bars is investigated, but further unsteady simulations are envisaged. Table 1 gives the main operating conditions from the experiments used for the numerical investigations. The inlet Mach number is very low, so that the flow can be considered as fully incompressible. Figure 2 and Figure 3 show the measured pressure distribution on blade suction and pressure side for both inlet FSTI. At a surface position of $s/s_{max} = 0.44$ the peak suction occurs. From this point the boundary layer decelerates under the influence of an adverse pressure gradient. In

$Re_{out,c}$	Inlet Mach number	FSTI [%]	Chord length [mm]	l_{ax} [mm]	Pitch [mm]
--------------	-------------------	----------	-------------------	---------------	------------

160000 ~ 0.02 0.5 & 4.0 198 85.97 158.2

Table 1: Main operating conditions of the T106A cascade.

the case of the lower free-stream turbulence, the suction surface boundary layer separates at a surface position of $s/s_{max} = 0.63$ indicated by the start of a pressure "plateau". It extends up to a $s/s_{max} = 0.83$, where the transition process starts which leads to a recovery of the surface pressure. At a surface distance of $s/s_{max} = 0.9$, the boundary layer is attached again. In the case of the higher free-stream turbulence, the pressure distribution on the suction side lacks the pressure plateau between $s/s_{max} = 0.6$ and $s/s_{max} = 0.8$. This suggests that bypass transition prevents the formation of a separation bubble.

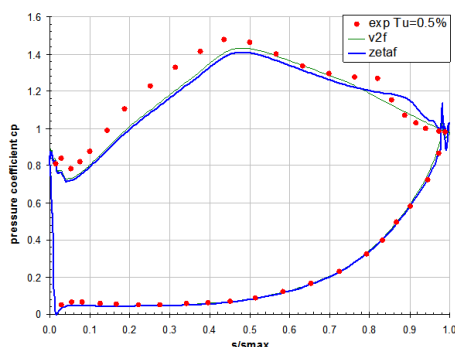


Figure 2: Pressure coefficient along the T106A cascade with 0.5% FSTI.

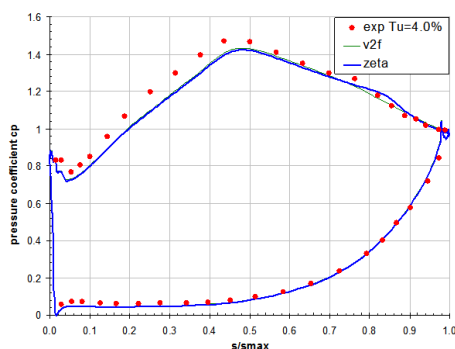


Figure 3: Pressure coefficient along the T106A cascade with 4% FSTI.

4.1 Compressible Results

Although the flow is incompressible, the first calculations were done with the time-marching code without

any preconditioning and thus the outlet Mach number is set to 0.4, whereas the Reynolds number matches the experiment. The measurement data does not include the turbulent mixing length or turbulent dissipation at the inflow, so that these values are varied at the inlet. This is done by imposing different turbulence mixing lengths. For an inlet FSTI a relative turbulence mixing length (l_{mix}/l) of 0.015 is used, and for the higher FSTI a relative turbulence mixing length of 0.002 is used.

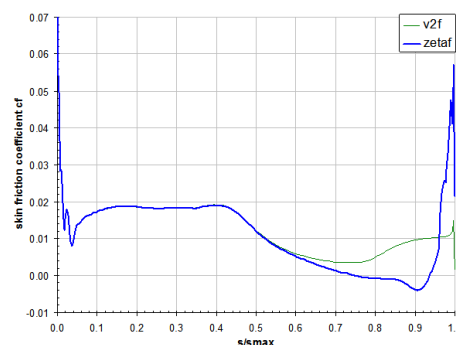


Figure 4: Skin Friction Coefficient along suction side of the T106A cascade with 0.5% FSTI.

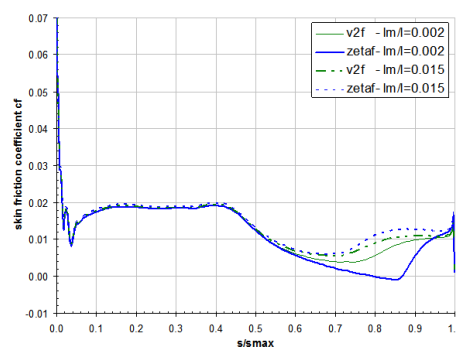


Figure 5: Skin Friction Coefficient along suction side of the T106A cascade with 4% FSTI.

Figure 2 shows the measured and computed pressure distribution for an inlet FSTI of 0.5% and Figure 4 shows the resulting skin friction distribution along the blade suction side. The values on the pressure side are in very good agreement with the experimental data, whereas a remarkable deviation can be observed along the whole suction side. The pressure distribution of the V2F model does not indicate any separation for all different turbulence mixing lengths, which is confirmed by the skin friction distribution. On the other hand, the ZETA-F model is able to predict the laminar separation bubble on the suction side. For $l_{mix}/l = 0.015$ the separation onset is predicted at $s/s_{max} = 0.75$ compared to the measured value of 0.63, but the length of the separation zone is very similar (see skin friction distribution). The results for higher l_{mix}/l were also calculated, but they predict a slightly further downstream separation onset and a shorter bubble. Best agreement was found for

$l_{mix}/l = 0.015$ and $l_{mix}/l = 0.002$ for the lower FSTI respectively for the higher FSTI).

The situation is similar for the case with an inlet FSTI=4% (see Figure 3 and Figure 5). Both models give similar results for the pressure distribution besides the small bulge at about $s/s_{max} = 0.8$. This bulge is also predicted by the ZETA-F model, but again too far downstream. The measurements indicate that the boundary layer is close to separation, whereas the skin friction for ZETA-F shows a small separation bubble. This bubble is only predicted by $l_{mix}/l = 0.002$, but not for higher l_{mix}/l values at the inlet. The skin friction distribution shows local minima at about $s/s_{max} = 0.7$. Only the ZETA-F model shows a small separation zone for $l_{mix}/l = 0.002$. The sharp increase at $s/s_{max} > 0.8$ indicates beginning transitional flow. For the same mixing length as used in the lower inlet FSTI case ($l_{mix}/l = 0.015$), no separation is predicted. It is interesting that the ZETA-F model is more sensible to variations of the turbulence mixing length than the V2F model.

The better results of the ZETA-F model could be caused by the improved modelling of the shear stress and of the production of turbulent kinetic energy (see model description above).

4.2 Incompressible Results

Finally the T106A turbine cascade is calculated with the incompressible code version of LINARS using artificial compressibility (Shin, 2001 [10]). For comparing the incompressible calculation with the compressible one, the mixing length is set equal in both calculations.

For both inlet FSTI the agreement with the measured pressure distribution is much better, especially for 4% inlet FSTI (see Figure 6 and Figure 7). The main reason for this disagreement of the compressible calculation is the too high Mach number of 0.4 used for the compressible calculation and the thus resulting compressibility effects.

The V2F model is again not able to predict any separation. For the 0.5% FSTI case the ZETA-F model predicts the separation onset closer to the measured location, the length of the separation zone is slightly too small. The skin friction distribution (see Figure 8 and Figure 9) is similar to the compressible calculations, whereas the V2F model seems to predict a rapid transition to turbulence closely after the peak pressure location.

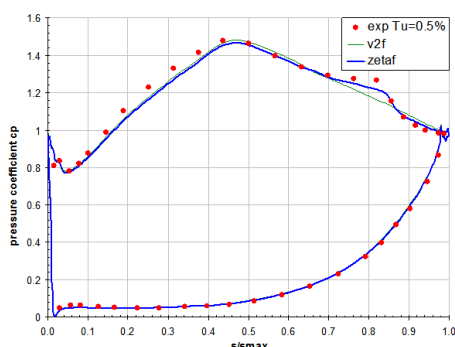


Figure 6: Pressure coefficient along the T106A cascade with 0.5% FSTI.

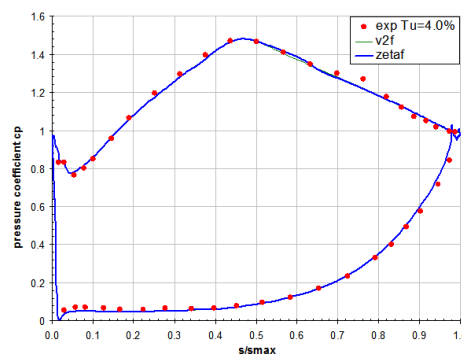


Figure 7: Pressure coefficient along the T106A cascade with 4% FSTI.

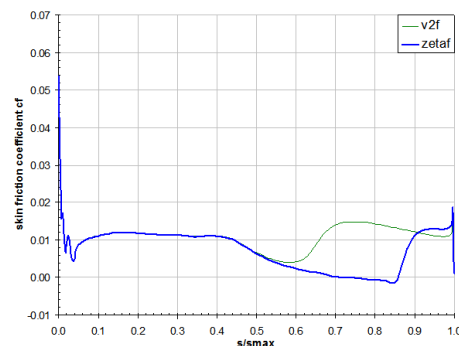


Figure 8: Skin Friction Coefficient along suction side of the T106A cascade with 0.5% FSTI.

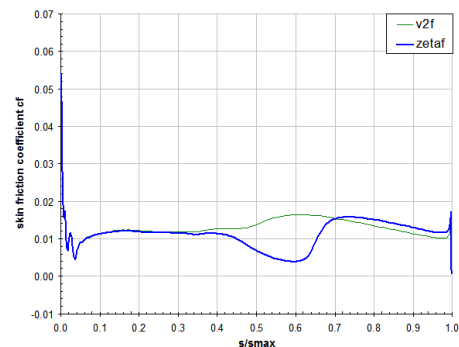


Figure 9: Skin Friction Coefficient along suction side of the T106A cascade with 4% FSTI.

For the 4% inlet FSTI case the incompressible calculation does not predict any separation, although the ZETA-F prediction has a minimum at $s/s_{max} = 0.6$. The V2F model predicts transition even more upstream due to the higher free-stream turbulence.

The comparison of the measured and the computed shape factor along the blade suction side for an inlet

FSTI of 0.5% and 4.0% is shown in Figures 10 and 11. Because of the difficulties in determining the boundary layer thickness, two methods calculating the boundary layer thickness are used, the method of Schobeiri et al. (2009) [18] and a method based on the assumption of a constant pressure in the boundary layer. Both methods lead to similar distributions with a peak at the same location but to different absolute values. According to Schlichting [19] the peak in the shape factor indicates the location of the transition onset. So in Figures 10 and 11 the shape factor starts to decrease when the skin friction increases, indicating laminar-to-turbulent transition. The computed peak in the shape factor is slightly more upstream than in the measurements, although the separation occurs a little bit earlier in the measurements. This leads to the conclusion that in the measurements the separation zone remains longer laminar before the transition occurs than in the calculation, where the separated flow triggers transition much earlier.

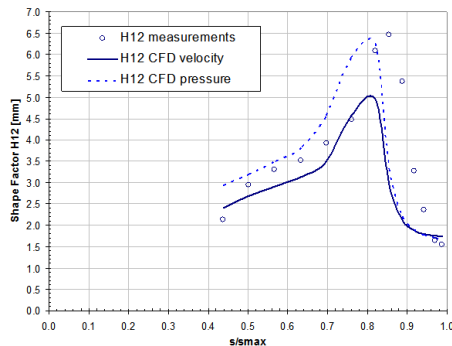


Figure 10: Shape factor along the T106A cascade with 0.5% FSTI.

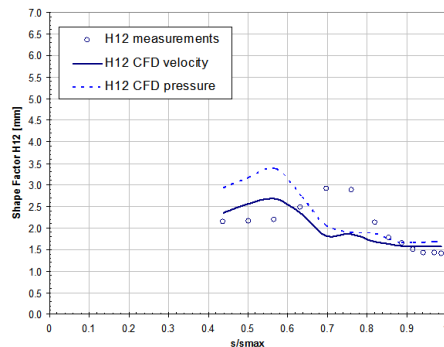


Figure 11: Shape factor along the T106A cascade with 4% FSTI.

5 Conclusion

In order to improve the reliability of numerical transition prediction, the ZETA-F model of Hanjalic et al. (2004) is investigated for turbomachinery flows and compared to the V2F model of Durbin (1995). Both models are derived from the Reynolds stress model and thus

have good chances to satisfactorily predict laminar-to-turbulent transition. The ZETA-F model is an advancement of the V2F model with a better numerical stability. Both models do not need an intermittency function.

The predictions of the steady transitional flow around the T106A low pressure turbine cascade are compared with the measurements and the V2F model. The ZETA-F model is able to predict the separation bubble on the suction side for 0.5% inlet FSTI, although a little bit too far downstream. For the 4% inlet FSTI the agreement with the measurements is excellent, especially for the incompressible calculation. The shape factor shows that the transition takes place much earlier in the separation zone than in the measurements. In general, the incompressible calculations give better results than the compressible code. In our calculations the ZETA-F model shows a great potential to predict transitional flows in turbomachinery applications.

Nomenclature

c_f	skin friction coefficient
$c_f = \tau_w / (\rho U^2 / 2)$	
c_p	pressure coefficient
$c_p = (p_{t,in} - p_w) / (p_{t,in} - p_{out})$	
C	model parameter
H_{12}	shape factor
k	turbulent kinetic energy
L	flat plate length or length scale
p	pressure
P_k	turbulence production term
Re	Reynolds number
S	magnitude of strain rate
u, v, U	velocity
y	wall distance
ε	turbulence dissipation rate
ζ	velocity scale ratio
ν	kinematic viscosity
ρ	density

Sub/Superscripts

ax	axial
in	inlet
out	outlet
w	wall
$+$	dimensionless

Acknowledgements

The work was supported by the Austrian Federal Ministry of Transport, Innovation and Technology (BMVIT) within the Austrian Aviation Program "TAKE OFF" (project "CFD-TRANS") as well as by the Austrian Science Foundation (FWF) (project P16761 "Steady and Unsteady Transition Modeling").

References

- [1] Hanjalic K. and Hadzic I. (1996): Modelling the Transition Phenomena With Statistical Turbulence Closure Models, In: Henkes, R.A.W.M. and van Ingen, J.L. (eds.) "Transitional Boundary Layers in Aeronautics". North-Holland, Amsterdam.
- [2] Hadzic I. and Hanjalic K. (1999): Separation-Induced Transition to Turbulence: Second-Moment Closure Modelling, Flow Turbulence and Combustion, 1999, Vol. 63, pp. 153-173.
- [3] Durbin P.A. (1995): Separated Flow Computations with the $k - \nu^2$ model; In AIAA J., Vol 33, pp.659-664.
- [4] Sanz W., Pecnik R., Tratnig A. and Heitmeir F. (2007): Application of modern turbulence models to steady transitional flow,

ETC 2007, Athena, Greece.

[5] Hanjali? K., Popovac M. and Haddiabdi? M (2004): A robust near-wall elliptic-relaxation eddy-viscosity turbulence model for CFD, In International Journal of Heat and Fluid Flows, Vol. 25, pp. 1047-1051.

[6] Basara B. (2005): Calculation of vortex shedding from a circular cylinder in uniform and shear flows. Proceedings of 2005 ASME Fluids Engineering Division Summer Meeting, FEDSM2005, pp. 2295-2300.

[7] Pecnik R., Pieringer P. and Sanz W. (2005): Numerical Investigation of the Secondary Flow of a Transonic Turbine Stage Using Various Turbulence Closures. ASME paper GT2005-68754, ASME Turbo Expo 2005, Reno-Tahoe, Nevada, USA.

[8] Roe P.L. (1981): Approximate Riemann Solver, Parameter Vectors and Differencing Scheme, Journal of Computational Physics Vol 43, pp. 357-372.

[9] Reed C.L., Anderson D.A.(1997): Application of low speed preconditioning to the compressible Navier-Stokes equations. AIAA Paper 97-0873.

[10] Shin S. (2001): Reynolds-Averaged Navier-Stokes Computation of Tip Clearance Flow in a Compressor Cascade Using an Unstructured Grid. PhD thesis, Virginia Polytechnic Institute and State University, Blacksburg, Virginia, USA.

[11] Yang Z., Voke P.R. and Savill A.M. (1994): Mechanism and Models of Boundary Layer Receptivity deduced from Large-Eddy Simulation of Bypass Transition. Direct and Large-Eddy Simulation Vol 1, P. R. Voke, L. Kleiser & J. Chollet (eds.) 225-236, Kluwer Academic Publishers.

[12] Lien F.S., Kalitzin G. and Durbin P.A. (1998): RANS Modelling for Compressible and Transitional Flows, CTR Proceedings of the Summer Program 1998.

[13] Speziale C.G., Sarkar S. and Gatski T.B. (1991): Modelling the pressure-strain correlation of turbulence: an invariant dynamical systems approach. J. Fluid Mech., Vol 227, pp. 245-272.

[14] Savill A M. (1992): A synthesis of T3 Test Case Predictions. Numerical Simulation of Unsteady Flows and Transition to Turbulence, O. P. et al., ed., Cambridge University Press, pp. 404-442.

[15] Ramdani K., Kelterer M.E., Pecnik R., Sanz W. (2009): Application of the ZETA Application of the ZETA-F-Turbulence Model to Steady Transitional Flow. In the Proceedings of the 8th European Conference on Turbomachinery, Fluid Dynamics and Thermodynamics, 23-27 March 2009, Graz, Austria, pp. 119-130.

[16] Stieger R. D. (2002): The Effects of Wakes on Separating Boundary Layers in Low Pressure Turbines, PhD thesis, Cambridge University Engineering Department, February 2002.

[17] Opoka M. M. and Hodson H. H.(2008): An Experimental Investigation of the Unsteady Transition Process on the High Lift T106A Turbine Blade, Journal of Propulsion and Power 24 (3), p. 424-432.

[18] Schobeiri M.T., and B. Ozturk (2009): Experimental Study of the Effects of Periodic Unsteady Wakes on Flow Separation in Low Pressure Turbines. NASA/CR-2009-214831.

[19] Schlichting H. and Gerster K. (2005): Grenzschicht-Theorie. Springer, Berlin Heidelberg.

5. $\gamma - Re_\theta$ Transition Model

The correlation based transition model by Menter et al. (2006) and by Langtry et al. (2006) consists of two additional transport equations added to the SST turbulence model. There is no need of any free-stream flow information, so no non-local parameters have to be calculated, which makes the model very attractive for 3D simulations.

5.1. Main Model Equations

The main idea of this model is to describe the momentum-thickness Reynolds number Re_θ with the vorticity Reynolds number Re_v , whose definition is given as follows:

$$Re_v = \frac{\rho y^2}{\mu} \left| \frac{\partial u}{\partial y} \right| = \frac{\rho y^2}{\mu} S \quad (5.1)$$

The vorticity Reynolds number of the Blasius boundary layer is scaled to have the maximum of one inside the boundary layer. The maximum of the profile is proportional to the momentum-thickness Reynolds number and can therefore be related to the transition correlations of Menter et al. (2002):

$$Re_\theta = \frac{\max(Re_v)}{2.193} \quad (5.2)$$

The transport equation for the intermittency γ is defined as follows:

$$\frac{\partial \rho \gamma}{\partial t} + \frac{\partial \rho u_i \gamma}{\partial x_i} = P_\gamma - E_\gamma + \frac{\partial}{\partial x_i} \left[\left(\mu + \frac{\mu_t}{\sigma_f} \right) \frac{\partial \gamma}{\partial x_i} \right] \quad (5.3)$$

The source term P_γ and the destruction/relaminarisation term E_γ are defined as follows:

$$P_\gamma = F_{length} c_{a1} \rho S [\gamma F_{onset}]^{0.5} (1 - c_{e1} \gamma) \quad (5.4)$$

$$E_\gamma = c_{a2} \rho \Omega \gamma F_{turb} (c_{e2} \gamma - 1) \quad (5.5)$$

In P_γ (eq. 5.4) F_{length} is an empirical correlation for the length of the transition process. F_{onset} is a function of the vorticity Reynolds number Re_v , the transition Reynolds

number $Re_{\theta C}$ and the viscosity ratio R_T . It controls the location of the transition onset by triggering the intermittency production and depends on the following relations:

$$F_{onset} = \max(F_{onset2} - F_{onset3}, 0.0) \quad (5.6)$$

$$F_{onset2} = \min(\max(F_{onset1}, F_{onset1}^4), 2.0) \quad (5.7)$$

$$F_{onset3} = \max\left(1 - \left(\frac{R_T}{2.5}\right)^3, 0.0\right) \quad (5.8)$$

$$R_T = \frac{\rho k}{\mu \omega} \quad (5.9)$$

$$F_{onset1} = \frac{Re_v}{2.193 \cdot Re_{\theta c}} \quad (5.10)$$

$$Re_v = \frac{\rho y^2}{\mu} S \quad (5.11)$$

In E_γ (eq. 5.5) F_{turb} disables the destruction/relaminarisation source term E_γ outside the laminar boundary layer:

$$F_{turb} = e^{-(R_T/4)^4} \quad (5.12)$$

The constants for the intermittency transport equation published by Menter et al. (2006) are:

$$\begin{aligned} c_{e1} &= 1.0; & c_{a1} &= 1.0; \\ c_{e2} &= 50; & c_{a2} &= 0.03; \\ \sigma_f &= 1.0 \end{aligned} \quad (5.13)$$

They are later modified by Langtry (2006) and Langtry and Menter (2009) to:

$$\begin{aligned} c_{e1} &= 1.0; & c_{a1} &= 2.0; \\ c_{e2} &= 50; & c_{a2} &= 0.06; \\ \sigma_f &= 1.0 \end{aligned} \quad (5.14)$$

The transition onset is triggered if the vorticity Reynolds number becomes larger than the critical Reynolds number (see eq. 5.10). So γ is controlled by the critical Reynolds number. The critical Reynolds number as well as the parameter F_{length} are related to a second transport variable $\tilde{Re}_{\theta t}$ by empirical correlations.

The transport equation for the momentum thickness Reynolds number $\tilde{Re}_{\theta t}$ is defined as follows:

$$\frac{\partial \rho \tilde{Re}_{\theta t}}{\partial t} + \frac{\partial \rho u_i \tilde{Re}_{\theta t}}{\partial x_i} = P_{\theta t} + \frac{\partial}{\partial x_i} \left[\sigma_{\theta t} (\mu + \mu_t) \frac{\partial \tilde{Re}_{\theta t}}{\partial x_i} \right] \quad (5.15)$$

with the following source term, which is designed to force the transport scalar $\tilde{Re}_{\theta t}$ to be equal to the local value of a turbulent momentum thickness Reynolds number $Re_{\theta t}$. The empirical correlations for $Re_{\theta t}$ are described in Chapter 5.3:

$$P_{\theta t} = c_{\theta t} \frac{\rho}{t} \left(Re_{\theta t} - \tilde{Re}_{\theta t} \right) (1.0 - F_{\theta t}) \quad (5.16)$$

with t as the time scale:

$$t = \frac{500\mu}{\rho U^2} \quad (5.17)$$

The blending function $F_{\theta t}$ controls the production term and allows the transport scalar $\tilde{Re}_{\theta t}$ to diffuse in the boundary layer from the freestream. In the freestream the blending function is equal to zero and in the boundary layer it is equal to one. The blending function is defined as follows:

$$F_{\theta t} = \min \left(\max \left(F_{\text{wake}} \cdot e^{-\left(\frac{y}{\delta}\right)^4}, 1.0 - \left(\frac{\gamma - 1/c_{e2}}{1.0 - 1/c_{e2}} \right)^2 \right), 1.0 \right) \quad (5.18)$$

$$F_{\text{wake}} = e^{\left(\frac{Re_\omega}{1e+5}\right)^2} \quad Re_\omega = \frac{\rho \omega y^2}{\mu}; \quad (5.19)$$

$$\delta = \frac{50\Omega y}{U} \cdot \delta_{\text{BL}}; \quad \delta_{\text{BL}} = \frac{15}{2} \theta_{\text{BL}}; \quad \theta_{\text{BL}} = \frac{\tilde{Re}_{\theta t} \mu}{\rho U} \quad (5.20)$$

F_{wake} ensures that the blending function $F_{\theta t}$ is not active downstream an airfoil/blade in the wake region. The constants for the momentum thickness Reynolds number equation (by Menter et al. (2006)) are as follows:

$$c_{\theta t} = 0.03; \quad \sigma_{\theta t} = 10.0 \quad (5.21)$$

and later changed by Langtry (2006) to

$$c_{\theta t} = 0.03; \quad \sigma_{\theta t} = 2.0 \quad (5.22)$$

The boundary condition for the intermittency γ is zero normal flux at the wall and equal to 1 at an inlet. The boundary condition for the momentum thickness Reynolds

number $\tilde{Re}_{\theta t}$ is zero flux at the wall. At the inlet it should be calculated from empirical correlations described in Chapter 5.3 using the freestream turbulence intensity.

There is a modification suggested by Menter et al. (2006) to use an effective intermittency to consider also separation-induced transition:

$$\gamma_{\text{eff}} = \max(\gamma, \gamma_{\text{sep}}) \quad (5.23)$$

$$\gamma_{\text{sep}} = \min \left\{ s_1 \cdot \max \left[\left(\frac{Re_v}{s_0 Re_{\theta t}} \right) - 1.0, 0.0 \right] F_{\text{reattach}}, s_2 \right\} F_{\theta t} \quad (5.24)$$

$$F_{\text{reattach}} = e^{-(Re_T/s_f)^4} \quad (5.25)$$

with the following constants published by Menter et al. (2006):

$$\begin{aligned} s_1 &= 8.0; s_2 = 5.0 \\ s_0 &= 2.193; s_f = 15 \end{aligned} \quad (5.26)$$

Later modified constants were published by Langtry (2006) and Langtry and Menter (2009):

$$\begin{aligned} s_1 &= 2.0; s_2 = 2.0 \\ s_0 &= 3.235; s_f = 20 \end{aligned} \quad (5.27)$$

For closing the model, empirical correlations are required for the three parameters $Re_{\theta c}$, F_{length} and $Re_{\theta t}$:

$$Re_{\theta c} = f(\tilde{Re}_{\theta t}) \quad (5.28)$$

$$F_{\text{length}} = f(\tilde{Re}_{\theta t}) \quad (5.29)$$

$$Re_{\theta t} = f(Tu, \dots)_{\text{freestream}} \quad (5.30)$$

Correlations suggested by different research groups are presented in Chapter 5.3.

5.2. Coupling with the Turbulence Model

The transition model is coupled with the SST turbulence model (Menter (1994)) as follows:

$$\frac{\partial \rho k}{\partial t} + \frac{\partial \rho u_i k}{\partial x_i} = \tilde{P}_k - \tilde{D}_k + \frac{\partial}{\partial x_i} \left[(\mu + \mu_t \sigma_k) \frac{\partial k}{\partial x_i} \right] \quad (5.31)$$

$$\frac{\partial \rho \omega}{\partial t} + \frac{\partial \rho u_i \omega}{\partial x_i} = \alpha \frac{P_k}{\nu_t} - D_\omega + CD_\omega + \frac{\partial}{\partial x_i} \left[(\mu + \mu_T \sigma_\omega) \frac{\partial \omega}{\partial x_i} \right] \quad (5.32)$$

$$\tilde{P}_k = \gamma_{\text{eff}} P_k \quad (5.33)$$

$$\tilde{D}_k = \min [\max (\gamma_{\text{eff}}, 0.1), 1.0] D_k \quad (5.34)$$

where P_k and D_k are the original production and destruction terms of the SST model. There is also a change in the blending function F_1 needed, introducing a max limiter:

$$F_1 = \max (F_{1\text{orig}}, F_3) \quad (5.35)$$

where $F_{1\text{orig}}$ is the original SST blending function.

$$F_3 = e^{-\left(\frac{R_\gamma}{120}\right)^8} \quad (5.36)$$

$$R_\gamma = \frac{\rho y \sqrt{k}}{\mu} \quad (5.37)$$

Note that the production term is just modified for the k -equation and not for the ω equation (see Menter et al. (2006)).

5.3. Correlations for $Re_{\theta c}$, F_{length} and $Re_{\theta t}$

In this chapter all correlations tested by the author are described in detail. This correlations are needed to close the transition model. Four different correlations by other research groups (Elsner et al. (2008), Sorensen (2009), Malan et al. (2009) and Langtry and Menter (2009)) and an own in-house correlation are shown

5.3.1. Correlations for $Re_{\theta t}$

The correlation for the transition momentum thickness Reynolds number was first given by Menter et al. (2006) and was changed by Langtry (2006). The last version is also used by Langtry and Menter (2009) when publishing their complete set of correlations.

The correlation is based on the following parameters:

$$\lambda_\theta = \frac{\rho\theta^2}{\mu} \frac{dU}{ds} \quad (5.38)$$

$$Tu = 100 \frac{\sqrt{2k/3}}{U} \quad (5.39)$$

where dU/ds is the acceleration in streamwise direction and can be computed with the derivatives of the velocity U in all three directions:

$$U = (u^2 + v^2 + w^2)^{\frac{1}{2}} \quad (5.40)$$

$$\frac{dU}{dx} = \frac{1}{2} (u^2 + v^2 + w^2)^{-\frac{1}{2}} \cdot \left[2u \frac{du}{dx} + 2v \frac{dv}{dx} + 2w \frac{dw}{dx} \right] \quad (5.41)$$

$$\frac{dU}{dy} = \frac{1}{2} (u^2 + v^2 + w^2)^{-\frac{1}{2}} \cdot \left[2u \frac{du}{dy} + 2v \frac{dv}{dy} + 2w \frac{dw}{dy} \right] \quad (5.42)$$

$$\frac{dU}{dz} = \frac{1}{2} (u^2 + v^2 + w^2)^{-\frac{1}{2}} \cdot \left[2u \frac{du}{dz} + 2v \frac{dv}{dz} + 2w \frac{dw}{dz} \right] \quad (5.43)$$

$$\frac{dU}{ds} = \left[(u/U) \frac{dU}{dx} + (v/U) \frac{dU}{dy} + (w/U) \frac{dU}{dz} \right] \quad (5.44)$$

Using the streamline direction is not Galilean invariant, but this deficiency is present within many correlation-based models.

Version by Menter et al. (2006)

The correlation for $Re_{\theta t}$ is defined as follows:

$$Re_{\theta t} = 803.73 [Tu + 0.6067]^{-1.027} F(\lambda_\theta, K) \quad (5.45)$$

$$F(\lambda_\theta, K) = \begin{cases} \lambda_\theta \leq 0 : & 1 - [-10.32\lambda_\theta - 89.47\lambda_\theta^2 - 265.51\lambda_\theta^3] e^{[-Tu/3.0]} \\ \lambda_\theta > 0 : & 1 + [0.0962 [K10^6] + 0.148 [K10^6]^2 \\ & + 0.0141 [K10^6]^3] \times (1 - e^{[-Tu/1.5]}) \\ & + 0.556 [1 - e^{[-23.9\lambda_\theta]}] e^{[-Tu/1.5]} \end{cases} \quad (5.46)$$

$$-0.1 \leq \lambda_\theta \leq 0.1; \quad -3 \times 10^{-6} \leq K \leq 3 \times 10^{-6}; \quad Re_{\theta t} \geq 20 \quad (5.47)$$

Version by Langtry (2006) and Langtry and Menter (2009)

The correlation for $Re_{\theta t}$ is defined as follows:

$$Re_{\theta t} = \begin{cases} Tu \leq 1.3 : & [1173.51 - 589.428Tu + \frac{0.2196}{Tu^2}] F(\lambda_\theta) \\ Tu > 1.3 : & 331.50 [Tu - 0.5658]^{-0.671} F(\lambda_\theta) \end{cases} \quad (5.48)$$

$$F(\lambda_\theta) = \begin{cases} \lambda_\theta \leq 0 : & 1 - [-12.986\lambda_\theta - 123.66\lambda_\theta^2 - 405.689\lambda_\theta^3] e^{[-Tu/1.5]^{1.5}} \\ \lambda_\theta > 0 : & 1 + 0.275 [1 - e^{[-35.0\lambda_\theta]}] e^{[-Tu/0.5]} \end{cases} \quad (5.49)$$

$$-0.1 \leq \lambda_\theta \leq 0.1; \quad Tu \geq 0.027; \quad Re_{\theta t} \geq 20 \quad (5.50)$$

This empirical correlation effects the source term of the transport equation [see eq. (5.16)] for the transition onset momentum thickness Reynolds number $\tilde{Re}_{\theta t}$. The above mentioned equations (eqs. 5.38 - 5.49) have to be solved iteratively. At first an initial guess is necessary for the local value of the momentum thickness θ_t , based on the zero-pressure gradient solution of equation (5.45) or (5.48) and the local values of the velocity U , the density ρ and the viscosity μ . With this guess the equations (5.45)-(5.46) or (5.48)-(5.49) are solved by iterating the value of θ_t .

5.3.2. Correlation by Elsner et al. (2008)

The set of correlations for $Re_{\theta c}$ and F_{length} by Elsner et al. (2008) is presented in this chapter. Elsner et al. (2008) also calibrated their correlation with flat-plate test cases of zero and non-zero pressure gradient. They used the constants for the γ transport equation given in eq. (5.15) by Langtry (2006), the constants for the $\tilde{Re}_{\theta t}$ transport equation given in eq. (5.22) by Langtry (2006) and the constants for the separation-induced modification given in eq. (5.26) by Menter et al. (2006). They implemented their correlation into the commercial flow solver FLUENT and showed promising results for steady and unsteady transitional flows. The difference to the suggestion of Menter et al. (2006) designing the correlation as a function of the local $\tilde{Re}_{\theta t}$ value is that Elsner et al. (2008) used the maximum value of $\tilde{Re}_{\theta t}$ from near the wall, $\tilde{Re}_{\theta t, max}$. Later the

authors suggested to use the mean value of $\tilde{Re}_{\theta t}$ at the wall $\langle \tilde{Re}_{\theta t} \rangle_{\text{wall}}$, which again contradicts the original idea of the model of using only local information.

The following relation was used to reduce the dependency between $Re_{\theta c}$ and $\tilde{Re}_{\theta t}$ to only one value:

$$Re_{\theta c} = F_P \cdot \tilde{Re}_{\theta t} \quad (5.51)$$

The correlations are calculated as a function of $\tilde{Re}_{\theta t}$:

$$F_{length} = \begin{cases} \tilde{Re}_{\theta t, max} < 250 : & 0.5 \\ \tilde{Re}_{\theta t, max} \geq 250 : & 0.274 + 0.0039 \cdot \tilde{Re}_{\theta t} - 2.13 \cdot 10^{-5} \cdot \tilde{Re}_{\theta t}^2 \\ & + 3.65 \cdot 10^{-8} \cdot \tilde{Re}_{\theta t}^3 \end{cases} \quad (5.52)$$

$$F_P = \begin{cases} \tilde{Re}_{\theta t, max} \leq 525 : & 4.15 \cdot 10^{-9} \cdot \tilde{Re}_{\theta t}^3 - 4.85 \cdot 10^{-6} \cdot \tilde{Re}_{\theta t}^2 \\ & + 7.493 \cdot 10^{-4} \cdot \tilde{Re}_{\theta t} + 0.773 \\ \tilde{Re}_{\theta t, max} > 525 : & 4.15 \cdot 10^{-9} \cdot \tilde{Re}_{\theta t}^3 - 4.85 \cdot 10^{-6} \cdot \tilde{Re}_{\theta t}^2 \\ & + 7.493 \cdot 10^{-4} \cdot \tilde{Re}_{\theta t} + 0.773 \end{cases} \quad (5.53)$$

5.3.3. Correlation by Sorensen (2009)

Sorensen (2009) implemented his correlation to his in-house code designed for wind energy application and showed promising results for steady transitional flows. He used the constants for the γ transport equation given in eq. (5.14) by Menter et al. (2006), the constants for the $\tilde{Re}_{\theta t}$ transport equation given in eq. (5.22) by Langtry (2006) and the constants for the separation-induced modification given in eq. (5.27) by Langtry (2006). He used the correlation by Menter et al. (2006) for $Re_{\theta t}$ (see Eqs. (5.45) -(5.47)).

$$Re_{\theta c} = \beta \left(\frac{\tilde{Re}_{\theta t} + 12000}{25} \right) + (1 - \beta) \left(\frac{7 \cdot \tilde{Re}_{\theta t} + 10}{10} \right) \quad (5.54)$$

$$\beta = \tanh \left[\left(\frac{\tilde{Re}_{\theta t} - 100}{400} \right)^4 \right] \quad (5.55)$$

$$F_{length} = \min \left[150 \cdot \exp \left[- \left(\frac{\tilde{Re}_{\theta t}}{120} \right)^{1.2} \right] + 0.1, 30 \right] \quad (5.56)$$

Sorensen (2009) took the constants $c_{a1}, c_{a2}, c_{e1}, c_{e2}$ as published in Menter et al. (2006) for the intermittency equation. This can be seen as dividing the production and the destruction term by a factor of 2 and leads to different correlations compared to other research groups. Sorensen (2009) used four zero-pressure gradient flat test cases to find his correlation.

5.3.4. Correlation by Malan et al. (2009)

Malan et al. (2009) implemented their correlation in the commercial CFD code Star-CCM+. They used the constants for the γ transport equation given in eq. (5.15) by Langtry (2006), the constants for the $\tilde{Re}_{\theta t}$ transport equation given in eq. (5.22) by Langtry (2006) and the constants for the separation-induced modification given in eq. (5.27) by Langtry (2006). They also used the correlation by Langtry (2006) and Langtry and Menter (2009) for $Re_{\theta t}$ (see eqs. (5.48) -(5.50)).

$$Re_{\theta c} = \min \left(0.615 \tilde{Re}_{\theta t} + 61.5, \tilde{Re}_{\theta t} \right) \quad (5.57)$$

$$F_{length} = \min \left(\exp \left(7.168 - 0.01173 \tilde{Re}_{\theta t} \right) + 0.5, 300 \right) \quad (5.58)$$

5.3.5. Correlation by Langtry and Menter (2009)

Although the correlations for $Re_{\theta c}$ and for F_{length} were not published in the original model presentation (Menter et al. (2006)) due to confidentiality, Langtry and Menter finally decided to publish their correlation in 2009.

$$Re_{\theta c} = \begin{cases} \tilde{Re}_{\theta t} \leq 1870 : & \left[\tilde{Re}_{\theta t} - \left(396.035 \cdot 10^{-2} + (-120.656 \cdot 10^{-4}) \tilde{Re}_{\theta t} \right. \right. \\ & \left. \left. + (-868.230 \cdot 10^{-6}) \tilde{Re}_{\theta t}^2 + (-696.506 \cdot 10^{-9}) \tilde{Re}_{\theta t}^3 \right. \right. \\ & \left. \left. + (174.105 \cdot 10^{-12}) \tilde{Re}_{\theta t}^4 \right] \right. \\ \tilde{Re}_{\theta t} > 1870 : & \left[\tilde{Re}_{\theta t} - \left(593.11 + (\tilde{Re}_{\theta t} - 1870.0) \cdot 0.482 \right) \right] \end{cases} \quad (5.59)$$

$$F_{length} = \begin{cases} \tilde{Re}_{\theta t} < 400 : & \left[398.189 \cdot 10^{-1} + (119.270 \cdot 10^{-4}) \tilde{Re}_{\theta t} \right. \\ & \left. + (-132.567 \cdot 10^{-6}) \tilde{Re}_{\theta t}^2 \right] \\ 400 \leq \tilde{Re}_{\theta t} < 596 : & \left[263.404 + (-123.939 \cdot 10^{-2}) \tilde{Re}_{\theta t} \right. \\ & \left. + (194.548 \cdot 10^{-5}) \tilde{Re}_{\theta t}^2 \right. \\ & \left. + (-101.695 \cdot 10^{-8}) \tilde{Re}_{\theta t}^3 \right] \\ 596 \leq \tilde{Re}_{\theta t} < 1200 : & \left[0.5 - (\tilde{Re}_{\theta t} - 596.0) \cdot 3.0 \cdot 10^{-4} \right] \\ 1200 \leq \tilde{Re}_{\theta t} : & [0.3188] \end{cases} \quad (5.60)$$

5.3.6. Correlation by Kelterer

The author used the constants for the γ transport equation (eq. 5.15) by Langtry (2006), the constants for the $\tilde{Re}_{\theta t}$ transport equation (eq. 5.22) by Langtry (2006) and the constants for the separation-induced modification (eq. 5.27) by Langtry (2006). The $Re_{\theta t}$ -correlation was used as suggested by Menter et al. (2006) (see eqs. (5.45) - (5.47)).

For calibrating the in-house correlation the well known ERCOFTAC flat plate test cases described by Savill (1992) were applied and for an enhancement of the correlation the T106 test case by Hoheisel (1982) and Hoheisel (1990) were used.

The procedure for finding the fitting correlation for the in-house code is very similar to that reported by Sorensen (2009), Elsner et al. (2008) and Malan et al. (2009). The correlations are calculated as a function of the local $\tilde{Re}_{\theta t}$ value. The following relation was used to reduce the dependency between $Re_{\theta c}$ and $\tilde{Re}_{\theta t}$ to only one value:

$$Re_{\theta c} = F_P \cdot \tilde{Re}_{\theta t} \quad (5.61)$$

Parametric runs were performed, with a fixed value F_P and varying F_{length} . It shows that the production term depends linearly on the value F_{length} as given in eq. (5.4). In order to increase the production term the value F_{length} has to be risen. An increase in the production term leads to a faster building of intermittency, which results in a shorter transition zone and a slightly faster transition onset.

The next step is to fix the value F_{length} and to vary F_P in order to find an optimum pair of values for these two parameters. A high F_P value results in a high value of $Re_{\theta c}$ and this results in a delayed transition onset whereas a small value results in a more upstream transition onset.

Finally, additional parametric runs were necessary to find an optimum fitting value of Re_{θ_c} for the best value of F_{length} , so that an optimum parameter triple (Re_{θ_c} , F_{length} and \tilde{Re}_{θ_t}) for the test case is determined. This was done for each of the five calibration test cases and with the optimum values of each test case the following correlations could be derived:

$$Re_{\theta_c} = \begin{cases} \tilde{Re}_{\theta_t} \leq 215 & \left[1.02 \cdot \tilde{Re}_{\theta_t} - 35 + \tanh \left(- \left(\frac{\tilde{Re}_{\theta_t} - 138}{54} \right) \right) \cdot 36 \right] \\ \tilde{Re}_{\theta_t} > 215 & \left[\tanh \left(- \left(\frac{\tilde{Re}_{\theta_t} - 215}{15} \right) \right) \cdot 45 + 155 \right] \end{cases} \quad (5.62)$$

$$F_{length} = \min \left[250 \cdot \exp \left[- \left(\frac{\tilde{Re}_{\theta_t}}{130} \right)^{1.7} \right] + 10, 40 \right] \quad (5.63)$$

This correlation showed very good results for flat plate test cases (T3A, T3B, T3C1, T3C2 and T3C4), as discussed in the following section *Notes on Paper 3*. But when applying this correlation to cascade test cases, there is a lack in predicting separation-induced transition.

Therefore the T106 test case for three different Reynolds numbers (Hoheisel (1990)) was additionally taken into account for the in-house correlation which leads to the improved correlation as shown below and further discussed in *Notes on Paper 4*.

$$Re_{\theta_c} = \begin{cases} \tilde{Re}_{\theta_t} \leq 215 : & \left[1.02 \cdot \tilde{Re}_{\theta_t} - 35 + \tanh \left(- \left(\frac{\tilde{Re}_{\theta_t} - 138}{54} \right) \right) \cdot 36 \right] \\ 215 < \tilde{Re}_{\theta_t} \leq 270 : & \left[\tanh \left(- \left(\frac{\tilde{Re}_{\theta_t} - 215}{16} \right) \right) \cdot 45 + 155 \right] \\ \tilde{Re}_{\theta_t} > 270 : & \left[\tanh \left(- \left(\frac{\tilde{Re}_{\theta_t} - 575}{16} \right) \right) \cdot 252 + 450 \right] \end{cases} \quad (5.64)$$

$$F_{length} = \min \left[215 \cdot \exp \left[- \left(\frac{\tilde{Re}_{\theta_t}}{120} \right)^{1.08} \right] + 1.5, 40 \right] \quad (5.65)$$

5.4. Validation Part 1

Historically the author of this work tested three different correlations published by other authors, which all did not show acceptable agreement of the simulation results with the experimental data of the flat plate test cases. As a consequence the author had

to design an own correlation, called in-house correlation or Kelterer correlation in the course of this work. When applying this in-house correlation to cascade test cases the author realized that the in-house correlation did not give correct results for the cascade test cases although having shown good results for the flat plate test cases. Therefore the in-house correlation was redesigned, which made it better fitting for the validated cascade test cases. Concluding the correlation study all correlations are compared to the recently published correlations (Langtry and Menter (2009)) by the authors of the original basic model (Menter et al. (2006)).

5.4.1. Notes on Paper 3

Titel:	Computation of Laminar-Turbulent Transition in Turbomachinery Using The Correlation Based $\gamma - Re_\theta$ Transition Model.
Authors:	M.E. KELTERER, R. PECNIK, W. SANZ
Published:	ASME paper GT2010-22207, Conference proceedings of the ASME Turbo Expo, Glasgow, Scotland, 2010

Abstract

In Paper 3 the correlation based transition model by Menter et al. (2006) was implemented in the in-house 3D RANS flow solver LINARS. The model is based on the $k - \omega$ SST turbulence model. Correlation closures by different research groups like Elsner et al. (2008), Sorensen (2009) and Malan et al. (2009) were used in the in-house code by the author of this thesis. These different correlation closures were tested on their ability to predict bypass transition and separation-induced transition by applying the transition model to the ERCOFTAC flat plate test cases (Savill (1992)).

Paper 3 describes the different closure techniques and their assets and drawbacks. The procedure of how the correlation was developed is also explained in detail.

Results

The missing correlations of the original $\gamma - Re_\theta$ model by Menter et al. (2006) as found by three different research groups (Elsner et al. (2008), Sorensen (2009) and Malan et al. (2009)) are presented (see *Fig 1-3*). These correlations show good results within their codes, but when implementing these correlations into the in-house code, the results are not satisfactory (see *Fig 4*). Therefore the author of this work decided to design an own correlation, fitting to the in-house code. The correlation (see *eq. (30)*) is based on the calibration (see *Table 2*) with five flat plate test cases (T3A, T3B, T3C1, T3C2 and T3C4) from the well known ERCOFTAC data base. The new correlation shows very

good results for the flat plate test cases (see *Fig 8-12*). When firstly using the new correlation for turbomachinery application (Low Pressure Turbine Cascade T106A measured by Stieger (2002) and Opoka and Hodson (2005); Low Pressure Turbine Cascade T106 measured by Hoheisel (1990)), the in-house correlation was able to show a minimum of the skin friction coefficient in front of the transition zone, but did not confirm the separation bubble (see *Fig 14-17*). The results are auspicious but it was realized that more work on getting a reliable prediction has to be done.

The main statement of this work is that the $\gamma - Re_\theta$ transition model and its correlations seem to depend strongly on the code where they are implemented which was also confirmed by Malan (2010). To get a deeper insight into these code dependencies more numerical investigations have to be done and they are presented in Paper 4.

5.4.2. Notes on Paper 4

Titel:	Application of the gamma–Retheta transition model to transitional flow.
Authors:	M.E. KELTERER, R. BURGSTALLER, W.SANZ
Published:	ISAIF paper ISAIF10-091, Conference proceedings of the 10th International Symposium on Experimental and Computational Aerothermodynamics of Internal Flows, Brussels, Belgium, 2011

Abstract

In Paper 4 the correlation based transition model by Menter et al. (2006) was validated against the LP turbine cascade T106 measured by Hoheisel (1990) in more detail. Correlations for Re_{θ_c} , F_{length} and Re_{θ_t} by Malan et al. (2009), Langtry and Menter (2009) and by Kelterer et al. (2010)(in-house correlation; first validation calculations were shown in Paper 3) are validated. To improve the accuracy of the results, the in-house correlation was calibrated by additional test cases.

Results

Applying the first correlation by Kelterer et al. (2010) (see *eqs. (24 + 25)*) to the T106 test case (see *Fig 1*), the results show a strong deviation from the measurements regarding transition (see *Fig 4* and *Fig 5*). To get a more general correlation to better predict separation-induced transition occurring on e.g. LP turbine blades, the T106 test case was taken into account additionally to the flat plate test cases from the ERCOFTAC data base for calibrating the in-house correlation. The correlation is extended and is again formulated in terms of \tilde{Re}_{θ_t} (see *Table 2* and *eqs. (27 + 28)*). After calibrating the in-house correlation it is applied to the T106 turbine flow, showing an improvement in the flow prediction (see *Fig 8-19*). The assumption that the correlations strongly depend

on the code and the way of implementation as it was concluded by the authors for the flat plate test cases could not be affirmed for the cascade test cases. There is just a light dependency between the correlations and the code, which can be seen by comparing the new in-house correlation (NIC) with the correlation by Malan et al. (2009) (MA) (see *Fig. 8-19*).

Paper 3

M.E. Kelterer, R. Pecnik, W. Sanz

Computation of Laminar-Turbulent Transition in
Turbomachinery Using The Correlation Based $\gamma - Re_\theta$
Transition Model.

ASME paper GT2010-22207
presented at the ASME Turbo Expo
Glasgow, Scotland, 2010

GT2010-22207

COMPUTATION OF LAMINAR-TURBULENT TRANSITION IN TURBOMACHINERY
 USING THE CORRELATION BASED $\gamma-RE_\theta$ TRANSITION MODEL

M.E. Kelterer, R. Pecnik¹, W. Sanz

Institute for Thermal Turbomachinery and Machine Dynamics
 Graz University of Technology, Graz, Austria
 wolfgang.sanz@tugraz.at

ABSTRACT

The accurate numerical simulation of the flow through turbomachinery depends on the correct prediction of boundary-layer transition phenomena. Especially heat transfer and skin friction investigations demand a reliable simulation of the transition process. Many models have been developed to simulate the transition process, ranging from simple algebraic models to very sophisticated transport models. But nearly all models suffer from the need to determine boundary layer parameters and from their difficult application in three-dimensional flows.

Therefore, in this work the correlation based $\gamma-Re_\theta$ transition model developed by Menter and Langtry is implemented into the in-house Reynolds-averaged Navier-Stokes solver. This model avoids the calculation of non-local parameters and is thus very suitable for three-dimensional general flow situations. Two additional transport equations, one for the intermittency and one for the momentum thickness Reynolds number, which is a criterion for the transition onset, are added to the well known SST turbulence model by Menter. Instead of the proprietary model correlations by Menter et al. the authors used correlations by other research groups within the in-house code and tested these correlations for simple flat-plate test cases. The non-satisfying results indicate a strong code dependency of the model. Therefore also in-house correlations are presented and validated.

A comprehensive study of the model performance on the well known ERCOFTAC flat plate test cases is performed. After this validation the model is applied to the steady flow in a T106A and a T106 turbine cascade.

INTRODUCTION

In turbomachines and especially in aircraft engines the Reynolds numbers that determine the evolution of the boundary layers can be relatively low. So a large part of the flow along the blade surfaces is often laminar or transitional. The boundary layer development, losses, efficiency and heat transfer are greatly affected by the laminar-to-turbulent transition. Due to the relatively high turbulence levels by-pass transition is the dominant form of transition in turbomachinery.

The ability to accurately predict the transition process is crucial for the design of efficient and reliable machines. Considerable effort has been spent on adapting standard two-equation turbulence models to predict transition for various kinds of flows. So Schmidt and Patankar [1] and Savill [2] showed the ability of two-equation low-Reynolds turbulence models to predict transition in boundary layer flows. But they also found that no model performed satisfactorily over a wide range of flow cases and conditions.

Besides these "pure" turbulence models, an increasing number of transition models are being developed from empirical correlations. Mostly they are based on an intermittency γ which gives the fraction of time when the flow is turbulent and which is used to modify the turbulent viscosity in the main equations. The different approaches can be divided into simpler algebraic models (e.g. Solomon et al. [3]) and more complex transport models (Steelant and Dick [4]; Pecnik et al. [5]; Menter et al. [6]) as well as transition models not using integral boundary layer parameters like the intermittency transport model of Savill, Launder and Younis [7-9]. They used it together with a low-Re Reynolds Stress Transport model and reported promising results.

Among these models the $\gamma-Re_\theta$ model by Menter et al. ([6], [10-14]) is very promising, because only local information is

¹ Current address: Center of Turbulence Research, Stanford University, Stanford, CA, USA.

used to activate the production term in the intermittency equation. To implement the model in the in-house code, there is the need of correlations for two parameters: $Re_{\theta C}$, which is the critical Reynolds number where the intermittency starts to increase in the boundary layer, and F_{length} , which is an indicator for the transition length. These two parameters are not given in the original work due to proprietary reasons.

In order to use this transition model for the in-house Reynolds averaged Navier-Stokes solver already published correlation by other authors (Malan et al [15], Sorensen [16] and Elsner et al.[17]) as well as an own correlation are implemented and tested.

NUMERICAL METHOD

The computations were performed using the in-house Navier-Stokes code LINARS, developed at Graz University of Technology (Pecnik et al. [18]). The compressible Reynolds/Favre-averaged Navier-Stokes (RANS) equations are solved in conservative form by means of a fully-implicit time-marching finite-volume method on structured curvilinear grids in multiblock alignment. The inviscid (Euler) fluxes are discretized with the upwind flux-difference splitting method of Roe [19]. In order to achieve a high order of spatial accuracy a total variation diminishing (TVD) scheme with third-order interpolation was applied to get the state vector at each cell interface. The viscous flux vector at the cell interfaces is constructed with a second-order accurate central-differencing scheme using Green's theorem. To obtain a linear set of the governing equations the Newton-Raphson procedure is applied for the discretization in time. This method allows accurate unsteady calculations as well as improves convergence for steady calculations. The main flow equations and the turbulence equations are solved sequentially. .

MODEL DESCRIPTION

The $\gamma - Re_\theta$ correlation based transition model of Menter et al. [6;10-14] is based on two transport equations: the intermittency equation, which is used to trigger the transition process and the transport equation of the momentum thickness Reynolds number $Re_{\theta_{tld}}$.

The model is based on the idea that the momentum thickness Reynolds number which describes the transition process can be related to the vorticity Reynolds number:

$$Re_v = \frac{\rho y^2}{\mu} \frac{\partial u}{\partial y} = \frac{\rho y^2}{\mu} S \quad (1)$$

$$Re_\theta = \frac{Re_{v,max}}{2.193} \quad (2)$$

The transport equation for the intermittency is formulated as:

$$\frac{\partial(\rho\gamma)}{\partial t} + \frac{\partial(\rho U_j \gamma)}{\partial x_j} = P_\gamma - E_\gamma + \frac{\partial}{\partial x_j} \left[\left(\mu + \frac{\mu_t}{\sigma_f} \right) \frac{\partial \gamma}{\partial x_j} \right] \quad (3)$$

where the production of the intermittency is defined as:

$$P_\gamma = F_{length} c_{a1} \rho S [\gamma F_{onset}]^{1.5} (1 - \gamma) \quad (4)$$

and the destruction/relaminarization term is:

$$E_\gamma = c_{a2} \rho \Omega \gamma F_{urb} (c_{e2} \gamma - 1) \quad (5)$$

In Eq. (4), F_{length} controls the length of the transition zone. S is the strain rate. F_{onset} triggers the intermittency production and thus the transition onset. F_{onset} is a function of the vorticity Reynolds number Re_v , the transition Reynolds number $Re_{\theta C}$ and the viscosity ratio R_T as described below:

$$Re_v = \frac{\rho y^2 S}{\mu} \quad (6)$$

$$F_{onset1} = \frac{Re_v}{2.193 Re_{\theta C}} \quad (7)$$

$$F_{onset2} = \min[\max(F_{onset1}, F_{onset1}^4), 2.0] \quad (8)$$

$$R_T = \frac{\rho k}{\mu \omega} \quad (9)$$

$$F_{onset3} = \max\left[1 - \left(\frac{R_T}{2.5}\right)^3, 0.0\right] \quad (10)$$

$$F_{onset} = \max(F_{onset2} - F_{onset3}, 0.0) \quad (11)$$

$$F_{urb} = e^{-(R_T/14)^4} \quad (12)$$

$$c_{e1} = 1.0; c_{a1} = 2.0; c_{e2} = 50; c_{a2} = 0.06; \sigma_f = 1.0$$

If the vorticity Reynolds number becomes remarkably larger than the critical Reynolds number, the transition onset is triggered. The critical Reynolds number gives the location where the intermittency first starts to increase in the boundary layer. It is related to $Re_{\theta_{tld}}$ by an empirical correlation as well as F_{length} in the production term.

The boundary condition for γ at a wall is zero normal flux and at an inlet equal to 1.

The transport equation for the transition momentum thickness Reynolds number is formulated as:

$$\frac{\partial(\rho \tilde{Re}_\theta)}{\partial t} + \frac{\partial(\rho U_j \tilde{Re}_\theta)}{\partial x_j} = P_\theta + \frac{\partial}{\partial x_j} \left[\sigma_\theta (\mu + \mu_t) \frac{\partial \tilde{Re}_\theta}{\partial x_j} \right] \quad (13)$$

where the source term is:

$$P_\theta = c_\theta \frac{\rho}{t} (Re_\theta - \tilde{Re}_\theta) (1.0 - F_\theta) \quad (14)$$

It is defined to force the transported scalar $Re_{\theta_{tld}}$ to match the local value of the transition momentum thickness Reynolds number calculated from an empirical correlation outside the boundary layer and obtained from measurements of transitional flows. Menter et al.[6] suggest a correlation based on Mayle, Abu-Ghannam and Shaw and Drela. This correlation was slightly changed by Langtry [13]. All further model equations and parameters are taken as published by Menter et al. [6].

The momentum thickness has only a physical meaning within 1D, but Menter used it for the boundary layer transition in the whole area of the boundary layer using an additional equation. With the source term he tried to introduce the transition criterion and with the transport equation he added the transition criterion with upstream flow information. The transition momentum thickness Reynolds number is not

physical term, it is only a good idea to have a transition criterion in the whole boundary layer.

The boundary condition for $Re_{\theta_{tld}}$ at a wall is zero flux. At an inlet the boundary condition for $Re_{\theta_{tld}}$ should be calculated based on the inlet turbulence intensity with the Re_{θ} correlation from Menter et al. [6].

This transition model is coupled with the SST turbulence model as proposed by Menter et al. [6] by multiplying the production term and the destruction term in the k-equation of the SST model with the intermittency.

For separation-induced transition there is a need of using an effective intermittency in the k transport equation which combines the influences of bypass and separated-flow transition:

$$\gamma_{sep} = \min \left\{ s_1 \cdot \max \left[\left(\frac{Re_v}{3.235 Re_\theta} \right) - 1.0, 0.0 \right] F_{reattach}, s_2 \right\} F_\theta$$

$$s_1 = 2.0, \quad s_2 = 2.0 \quad (15)$$

$$F_{reattach} = e^{-(Re_\tau/20)^4} \quad (16)$$

$$\gamma_{eff} = \max(\gamma, \gamma_{sep}) \quad (17)$$

To close the model, three empirical correlations are required for $Re_{\theta C}$ and F_{length} , Re_{θ} .

$$Re_{\theta C} = f(\tilde{Re}_\theta) \quad (18)$$

$$F_{length} = f(\tilde{Re}_\theta) \quad (19)$$

$$Re_\theta = f(Tu, \dots)_{freestream} \quad (20)$$

Whereas the correlation for the transition momentum thickness Reynolds number is given by Menter et al. [6] and slightly different by Langtry [13], the correlations for $Re_{\theta C}$ and F_{length} as functions of $Re_{\theta_{tld}}$ are not published due to proprietary reasons. Since Re_{θ} is used to specify $Re_{\theta_{tld}}$ (see Eq.(14)), $Re_{\theta C}$ and F_{length} must also be strong functions of $Re_{\theta_{tld}}$. Thus it is clear, that the empirical correlations of Eqs. (18, 19) are valid only when used with the appropriate Re_{θ} correlation (Eq. (20)).

In order to close this transition model, other research groups proposed correlations for these two parameters which were implemented in our in-house code and evaluated.

CORRELATIONS BY OTHER AUTHORS

In order to close the transition model by Menter et al. [6], two empirical correlations are needed which control the transition onset and the transition length. Three research groups proposed correlations which were tested with our in-house code and are discussed here:

Malan et al. [15]:

The correlations for the critical Reynolds number and the F_{length} parameter of the production term (Eq. (4)) are:

$$Re_{\theta C, Malan} = \min(0.615 \tilde{Re}_\theta + 61.5; \tilde{Re}_\theta) \quad (21)$$

$$F_{length, Malan} = \min(\exp(7.168 - 0.01173 \tilde{Re}_\theta) + 0.5; 300) \quad (22)$$

Both parameters are a function of $Re_{\theta_{tld}}$ as proposed by Menter et al. [6]. Malan et al. implemented the transition model into the commercial CFD code StarCCM+ and derived the correlations for the Langtry model [13] for Re_{θ} using four flat-plate test cases where they achieve good agreement with experimental data. They also applied their correlations to several flow cases including interior and exterior flows. They concluded that further refinement of their correlations in order to extend their range of applicability would be necessary.

Sorensen [16]:

Sorensen found more complex correlation functions also based on $Re_{\theta_{tld}}$. He used the correlation of Menter et al. [6] for the transition momentum thickness Reynolds number. His numerical experiments were done with an in-house code.

$$Re_{\theta C, Sorensen} = \beta \left(\frac{\tilde{Re}_\theta + 12000}{25} \right) + (1 - \beta) \left(\frac{7 \cdot \tilde{Re}_\theta + 100}{10} \right) \quad (23)$$

$$\beta = \tanh \left[\left(\frac{\tilde{Re}_\theta - 100}{400} \right)^4 \right] \quad (24)$$

$$F_{length, Sorensen} = \min \left[150 \cdot \exp \left[- \left(\frac{\tilde{Re}_\theta}{120} \right)^{1.2} \right] + 0.1; \quad 30 \right] \quad (25)$$

Sorensen sets the constant $c_{a1}=1.0$ instead of $c_{a1}=2.0$ as in Menter et al (2006) [6], which can be seen as multiplying the value F_{length} with 0.5 and the constant $c_{a2}=0.03$ instead of $c_{a2}=0.06$, which is equal to multiplying the destruction term (Eq. (5)) with 0.5.

Sorensen tuned his correlations with four zero-pressure-gradient flat-plate test cases, where he also achieved good agreement. He then applied his correlations to 3D exterior flows showing improvements compared to fully-turbulent flow simulations.

Elsner et al. [17]:

Another set of correlations were presented by Elsner et al. [17]. They also calibrated their model with flat-plate test cases of zero and non-zero pressure gradient. He also used the correlation of Menter et al. [11] for Re_{θ} . Implementing their correlations into the commercial flow solver FLUENT they could show promising results for steady and unsteady transitional flows.

Their correlations are not functions of the local value of $Re_{\theta_{tld}}$, but of the maximum value of $Re_{\theta_{tld, max}}$ determined in the wall vicinity. Later on [20] suggested to use the mean value of $Re_{\theta_{tld, average}}$ at the wall.

$$Re_{\theta C} = F_p \tilde{Re}_\theta \quad (26)$$

$$\tilde{Re}_{\theta, max} < 250 : \quad F_{length} = 0.5$$

$$\tilde{Re}_{\theta, max} \geq 250 : \quad F_{length} = 0.274 + 0.0039 \tilde{Re}_{\theta, max} - 2.13 \cdot 10^{-5} \tilde{Re}_{\theta, max}^2 + 3.65 \cdot 10^{-8} \tilde{Re}_{\theta, max}^3 \quad (27)$$

$$\begin{aligned} \tilde{Re}_{\theta \max} &\leq 525: \\ F_p &= 4.15 \cdot 10^{-9} \tilde{Re}_{\theta \max}^3 - 4.85 \cdot 10^{-6} \tilde{Re}_{\theta \max}^2 \\ &\quad + 7.493 \cdot 10^{-4} \tilde{Re}_{\theta \max} + 0.773; \end{aligned} \quad (28)$$

$$\begin{aligned} \tilde{Re}_{\theta \max} &> 525: \\ F_p &= -6.09 \cdot 10^{-10} \tilde{Re}_{\theta \max}^3 + 2.05 \cdot 10^{-6} \tilde{Re}_{\theta \max}^2 \\ &\quad - 0.0023 \tilde{Re}_{\theta \max} + 1.165; \end{aligned}$$

Elsner et al also used the constant $S_1=8$ and $S_2=5$ in the correlation for separated-flow transition as originally suggested by Menter et al. [6].

In Figs. 1 and 2 the correlations of Malan et al and of Sorensen are shown. The F_{length} correlation of Sorensen is corrected by the factor 0.5 because of the different parameter c_{a1} used in the production term. The correlations show very big differences eg. the F_{length} value of Malan is approximately 10 times the value of Sorensen. On the other hand, the $Re_{\theta C}$ value is larger in the correlation of Sorensen for $Re_{\theta \text{tld}} < 700$.

The two parameters, F_{length} and $Re_{\theta C}$, affect the transition in a different way. A higher F_{length} value leads to a higher production term, and this results in a faster transition process. If $Re_{\theta C}$ is high, the F_{onset} value is small and this reduces the production term. So a high $Re_{\theta C}$ value can be compensated by a high F_{length} value. Also the higher F_{length} is, the shorter is the transition zone. This consideration indicates that several optimum combinations of F_{length} and $Re_{\theta C}$ exist, also assumed by Suluksna et al. [21].

Also a different $Re_{\theta t}$ correlation will lead to different correlations for $Re_{\theta C}$ and F_{length} as explained above. This may also be a reason for the difference of the two correlations by Malan et al and Sorensen. But it is astonishing how different the correlations of these working groups are.

Due to the different independent variable used by Elsner ($Re_{\theta \text{tld_max}}$ instead of the local $Re_{\theta \text{tld}}$), their correlation cannot be directly compared (see Fig 3). But it is interesting that F_{length} shows the opposite trend compared to the other two correlations. $Re_{\theta C}$ achieves much lower values than in the other two correlations.

All three correlations with the respective correlation for $Re_{\theta t}$ are implemented in the in-house code and applied to the zero-pressure gradient flat-plate flow T3A of the ERCOFTAC test series, where all authors reported very good agreement with the experimental data. Fig 4 shows the measured and calculated skin friction coefficient for this flow. The results show very large differences and all three correlations implemented differ remarkably from the experiments and the result presented by Menter et al [6] for his model. The Sorensen result shows a too early transition onset, but with a good agreement in the transition length. The result with the correlation by Malan et al shows a too late transition onset, and also the transition length is predicted too long. The Elsner result shows a too early transition onset and a much too long transition zone.

These discrepancies with the measurement data is disappointing and indicates that the way of implementation and the flow solver itself heavily influence the result of the

transition model (Two researchers used a commercial code and one an in-house code.).

Therefore in this work an own correlation is developed for the in-house Navier-Stokes solver and also calibrated with flat-plate test cases.

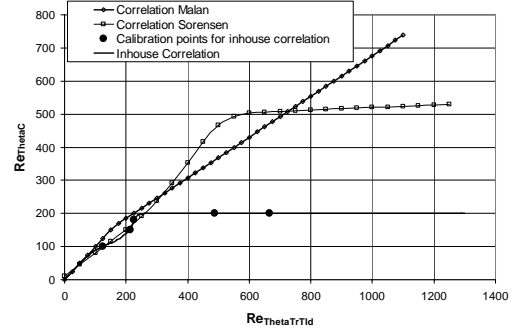


Fig 1: Correlation $Re_{\theta C}$ by Malan et al [15] and Sorensen [16]

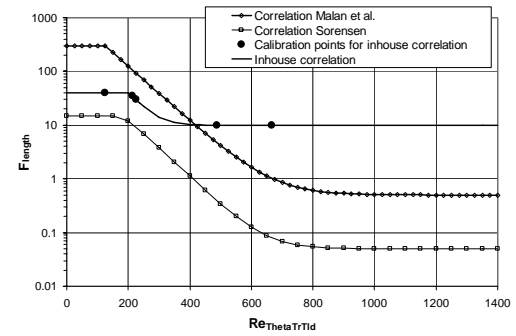


Fig 2: Correlation F_{length} by Malan et al [15] and Sorensen [16]

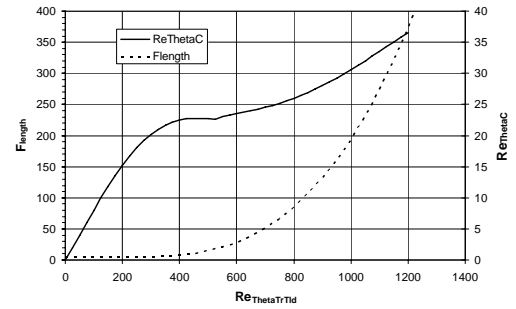


Fig 3: Correlation F_{length} and $Re_{\theta C}$ by Elsner et al [17]

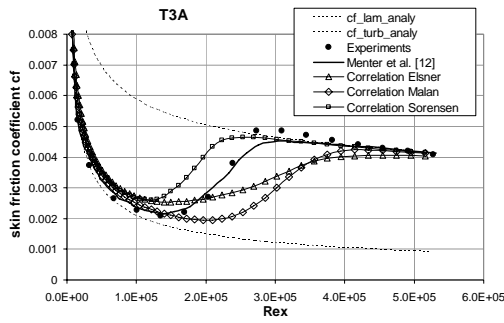


Fig 4: T3A test case with different correlations

MODEL CALIBRATION

For calibrating the correlations the well known ERCOFTAC flat plate test cases [22] were used. The numerical results are compared with experimental data obtained for transitional flows over adiabatic flat plates with sharp leading edges. These experiments were designed to test the ability of turbulence models to predict transitional flow under the effects of free-stream turbulence at zero and varying pressure gradient conditions. The tuning was done for two zero pressure gradient test cases (T3A and T3B) as well as for three non-zero pressure gradient test cases (T3C1, T3C2 and T3C4).

Table 1: Inlet conditions for calibration test cases

Case	U_{inlet} ($m\ s^{-1}$)	Tu (%)	μ/μ	ρ ($kg\ m^{-3}$)	μ ($kg\ m\ s$)
T3A	5.4	3.0	13.3	1.2	1.8e-5
T3B	9.4	6.14	100.0	1.2	1.8e-5
T3C1	6.3	8.0	40	1.2	1.8e-5
T3C2	5.3	3.0	11	1.2	1.8e-5
T3C4	1.37	3.0	8	1.2	1.8e-5

The procedure for finding the correlations is mainly the same as reported by all three researchers.

The authors decided to calculate the correlations as a function of the local $Re_{\theta_{tld}}$ as proposed by Sorensen [16] and Malan et al. [15]. For developing the correlation the following relation between $Re_{\theta C}$ and $Re_{\theta_{tld}}$ was used which allows reducing the dependency between $Re_{\theta C}$ and $Re_{\theta_{tld}}$ to one value:

$$Re_{\theta C} = F_p \cdot \tilde{Re}_a \tag{29}$$

First parametric runs were performed, where F_p was set constant and F_{length} was varied. In Fig 5 the F_{length} variation is shown for the T3A test case for $F_p=0.8$ (F_p variation ranges from $F_p=0.1 - 1.0$). The production term depends linearly on the F_{length} value, so that a rise of F_{length} directly increases the production term. A higher production term leads to a faster building of intermittency, which results in slightly faster transition onset and a shorter transition zone.

Then calculations the other way round were performed varying F_p for a fixed value of F_{length} in order to find an optimum pair of values for these two parameters. Fig 6 shows this procedure again for the T3A test case for $F_{length}=15$ (F_{length} variation ranges from $F_p=0.5 - 50$). A small value of F_p is connected to a small value of $Re_{\theta C}$ and this results in an earlier transition onset whereas a larger value results in a delayed onset.

Finally, a further series of parametric runs was performed to find values for $Re_{\theta C}$ instead for F_p for a fixed value of F_{length} shown in Fig. 7 for $F_{length}=40$. The $Re_{\theta C}$ -variation ranges from $Re_{\theta C}=100 \dots 400$.

This procedure was done for a large variety of input values, which allows to find an optimum for the parameters F_{length} , $Re_{\theta C}$ and F_p for each of the five calibration test cases. With the relation given in Eq (29) the corresponding $Re_{\theta_{tld}}$ could be found. The optimum parameters for all 5 calibration test cases are given in Table 2.

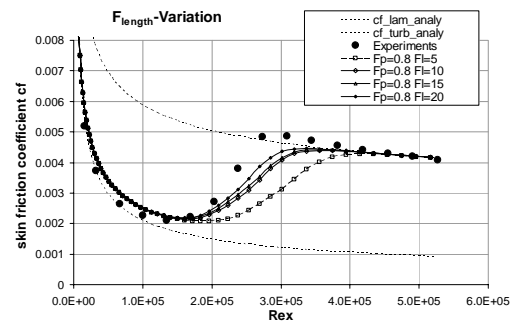


Fig 5: F_{length} -Variation

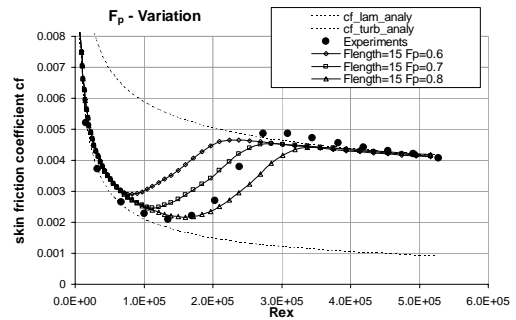


Fig 6: F_p -variation

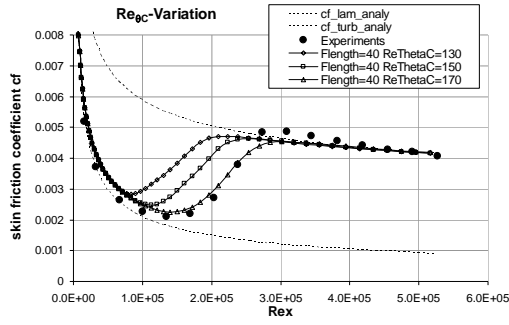


Fig 7: Re_{0C} -variation

Table 2: Calibration result

Case	local Re_{0_old}	Re_{0C}	F_{length}	F_P
T3A	225	180	30	0.8
T3B	125	100	40	0.8
T3C1	214	150	35	0.7
T3C2	488	200	10	0.41
T3C4	667	200	10	0.3

With the values of these five test cases the following correlations for Re_{0C} and F_{length} are extracted in similarity to the correlations by Sorensen. Figs. 1 and 2 show the correlations as function of Re_{0_old} . The F_{length} value is in-between the other two correlations of [15] and [16], whereas the Re_{0C} correlation gives much smaller values than compared to the other ones.

$$\tilde{Re}_a < 215 :$$

$$Re_{\tilde{a}} = 1.02 \cdot \tilde{Re}_a - 35 + \tanh\left(-\left(\frac{\tilde{Re}_a - 138}{54}\right)\right) \cdot 36$$

$$\tilde{Re}_a > 215 :$$

$$Re_{\tilde{a}} = \tanh\left(\frac{\tilde{Re}_a - 215}{15}\right) \cdot 45 + 155$$

$$F_{length} = \min\left[250 \cdot \exp\left[-\left(\frac{\tilde{Re}_a}{130}\right)^{1.7}\right] + 10; 40\right]$$

RESULTS AND DISCUSSION

For testing the steady flow behaviour of the model, several test cases with various inlet boundary conditions were taken into account. Besides the flat-plate test cases on which the in-house correlation is based on, the correlation is also validated with the low pressure turbine cascade T106A measured by the Whittle lab as well as with the turbine cascade T106 measured by Hoheisel [23].

Flat Plate Test Cases T3A, T3B, T3C1, T3C2, T3C4

The calculation results of the flat-plate test cases are shown in the following Figs 8-12 with the skin friction coefficient. For

the T3A test case (Fig. 8) the in-house correlation results in a slightly too early transition onset, but in good agreement in the transition length. Fig. 8 also shows the result published by Menter et al. [12].

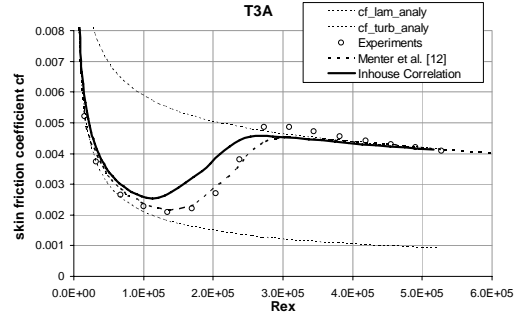


Fig 8: Skin friction coefficient for T3A

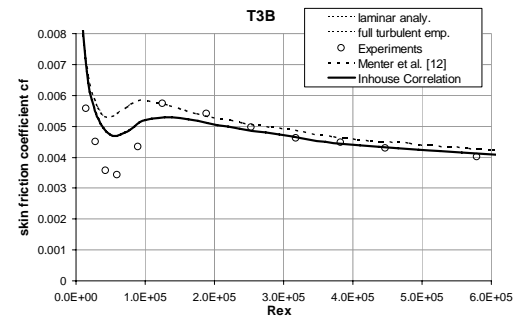


Fig 9: Skin friction coefficient for T3B

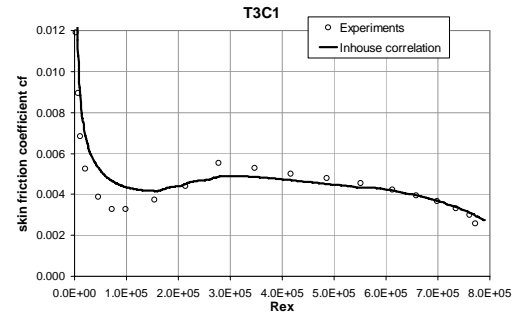


Fig 10: Skin friction coefficient for T3C1

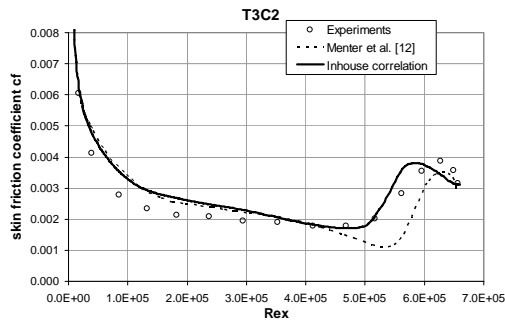


Fig 11: Skin friction coefficient for T3C2

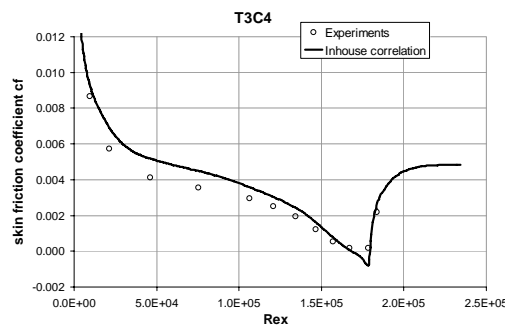


Fig 12: Skin friction coefficient for T3C4

The transition onset for the T3B test case (Fig. 9) is compared with the measurements- a little bit too early, but the end of transition is predicted very well. The result is even closer to the measurements than the one by Menter et al. [12]. The result for the T3C1 test case (Fig. 10) is similar to the case before (T3B) with a slightly too early transition onset. But the general agreement with the experimental data is good. The T3C2 test case (Fig. 11) shows a very late transition onset, which is also captured well compared to Menter et al. [12]. The last flat-plate flow (T3C4) used for the calibration of the own correlations shows a small separation zone (Fig. 12). It is captured very well as well as the general trend of the skin friction indicating the model can also be applied to separation induced transition.

Summing up it can be said that the correlation developed in this work predicts the measured flow-behaviour of the flat-plate test cases very well. But as these flows were used for calibration, it is a mandatory result.

Low Pressure Turbine Cascade T106A

As a first real validation step the steady transitional flow through the low pressure turbine cascade T106A is calculated.

This flow was experimentally investigated at the Whittle Laboratory by Stieger for a low FSTI [24] and Opoka and Hodson for a higher FSTI [25]. This flow is very challenging, because by-pass transition as well as separated-flow transition can occur on the suction side depending on the inlet FSTI. Fig 13 shows the blade geometry and the used computational grid consisting of 5 blocks with an O-block wrapping around the blade. The O-block contains 320×88 grid cells with a maximum y^+_{max} value below 1 along most of the blade surface.

The main goal of the experiments was to study the influence of unsteady inflow conditions on the transitional blade flow. The unsteady inflow is provided by moving bars, located 70 mm upstream of the cascade inlet. In this work only the steady flow without bars is investigated, but further unsteady simulations are envisaged. Table 3 gives the main operating conditions from the experiments used for the numerical investigations. The inlet Mach number is very low, so that the flow can be considered as fully incompressible.

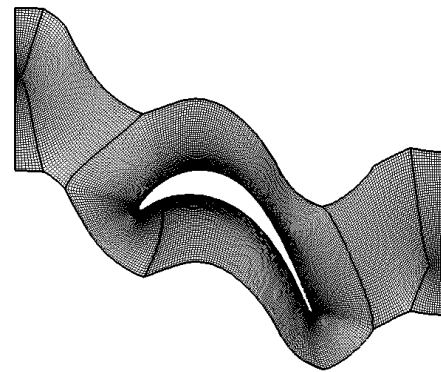
Fig 13: Computational grid for T106A cascade flow (O-block with 320×88 cells)

Table 3: Main operating conditions of the T106A cascade

$Re_{out,c}$	M_{in}	FSTI [%]	c [mm]	l_{ax} [mm]	Pitch [mm]
160000	~ 0.02	0.5, 4.0	198	170.22	158.2

Fig 14 shows the measured pressure distribution on blade suction and pressure side for an inlet FSTI=4%. At a surface position of $s/s_{max}=0.44$ the peak suction position occurs. From this point the boundary layer decelerates under the influence of an adverse pressure gradient. The pressure distribution on the suction side slightly indicates a deviation of the continuous deceleration, but lacks the pressure plateau between $s/s_{max}=0.6$ and $s/s_{max}=0.8$ as measured for lower FSTI. This suggests that by-pass transition prevents the formation of a separation bubble in this flow.

To show the difference between the calculation without and with transition model, the T106A test case with the higher

FSTI (4%) is calculated with the pure SST model (KO-SST) as well as with the transition model with the in-house correlations.

The pressure coefficient distribution in Fig 14 shows a difference between the calculation without and with transition model especially in the second half of the suction side. The result with the transition model shows the tendency of a flow close to separation beginning at $s/s_{max}=0.7$ as indicated by the measurements. On the other hand the results for the pure turbulence model show a continuous pressure decrease in this region.

The skin friction coefficient distribution of Fig. 15 shows large differences. The result using the transition model gives lower skin friction values than the fully turbulent solution and it has a clear minimum in the zone on the suction side as discussed above.

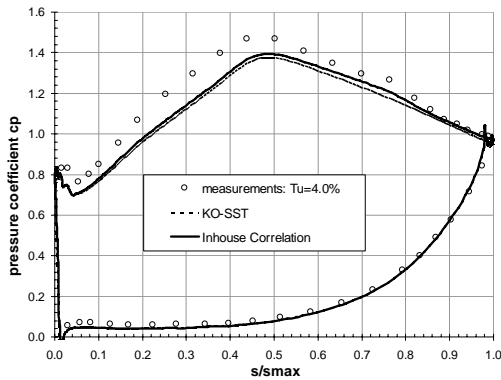


Fig 14: pressure distribution for T106A

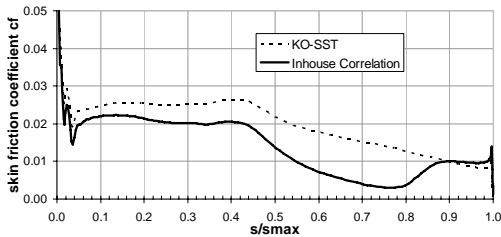


Fig 15: skin friction coefficient for T106A

Turbine Cascade T106

The second validation test case with turbomachinery content is the T106 test case. The flow was experimentally investigated by Hoheisel [23]. Separated-flow transition can occur on the suction side depending on the inlet FSTI. The used computational grid consisting of 5 blocks with an H-block structure around the blade, with 588 grid cells around the blade with a maximum y^+_{max} value below 1 along the blade surface.

In this work the steady flow was investigated for the lowest FSTI of 0.8%. Table 4 gives the main operating conditions from the experiments used for the numerical investigations. The inlet Mach number is comparable to the dimensions of a real engine.

Table 4: Main operating conditions of the T106 cascade

$Re_{out,c}$	M_{out}	FSTI [%]	c [mm]	l_{ax} [mm]	Pitch [mm]
500000	0.59	0.8	100	85.97	79.9

Again the T106 test case is calculated with the turbulence model (KO-SST) as well as with the transition model to see the difference between the calculation without and with transition model.

The pressure coefficient distribution in Fig 16 shows a difference between the calculation without and with transition model especially on the suction side.

The skin friction coefficient distribution of Fig. 17 shows large differences. The result using the transition model gives lower skin friction values than the fully turbulent solution and it has a minimum at $x/l=0.7$, where the measurements show a separation.

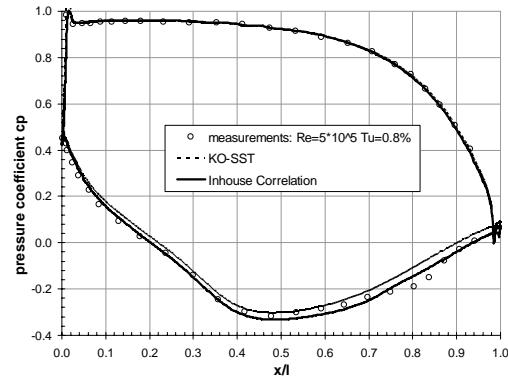


Fig 16: pressure distribution T106

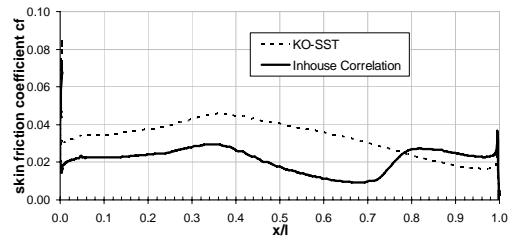


Fig 17: skin friction coefficient for T106

These first applications of the in-house correlation to turbomachinery flow are promising, but much further validation cases and calibration work needs to be done to obtain a trustworthy correlation.

NOMENCLATURE

c_f	skin friction coefficient
c_p	pressure coefficient;
	$c_p = (p_01 - p) / (p_01 - p_2)$
	$c_{p(T106)} = (p - p_2) / (p_01 - p_2)$
k	turbulent kinetic energy
p	local static pressure
p_{01}	inlet total pressure
p_2	static outlet pressure
Re_θ	momentum thickness Reynolds number, $\rho\theta U_o/\mu$
$Re_{\theta c}$	critical Reynolds number
$Re_{\theta a}$	transition onset momentum thickness Reynolds number
\tilde{Re}_a	Local transition onset momentum thickness Reynolds number, obtained from transport equations
R_T	Viscosity ratio $\rho k / (\mu \omega)$
Re_v	Vorticity (strain rate) Reynolds number $\rho \gamma^2 S / \mu$
S	absolute value of strain rate, $(2 S_{ij} S_{ij})^{1/2}$
S_{ij}	Strain rate tensor, $1/2(\delta u_i/\delta y_j + \delta u_j/\delta x_i)$
t	time
Tu	free-stream turbulence intensity (FSTI)
U	velocity
y	distance to nearest wall

Greek symbols:

γ	near wall intermittency factor
μ_t	turbulent viscosity
μ	molecular viscosity
ρ	density
ω	specific turbulence dissipation rate
Ω	absolute value of vorticity, $(2 \Omega_{ij} \Omega_{ij})^{1/2}$
Ω_{ij}	Strain rate tensor, $1/2(\delta u_i/\delta y_j + \delta u_j/\delta x_i)$

Abbreviations:

FSTI	free-stream turbulence intensity
------	----------------------------------

CONCLUSIONS

The paper deals with the missing correlations of the $\gamma - Re_\theta$ transition model by Menter et al.[6]. Correlations for onset location and transition length from other authors (Malan et al. [15], Sorensen [16], Elsner et al. [17]) were implemented in the in house code. Applying these correlations to the calculation of the zero-pressure-gradient T3A flow shows strong deviations from the measurements, indicating that the correlations strongly depend on the code and the way of implementation. Therefore in this work own correlations were developed with the risk that they are also only valid for the own in-house CFD code. Flat plate test cases from the ERCOFTAC data base are taken for calibrating the in-house correlation. The correlation was formulated in terms of $Re_{\theta_{tld}}$ as also proposed by Malan et al. [15]

and Sorensen [16]. After calibrating the in-house correlation they are applied to turbomachinery flow, the T106A cascade test case and the T106 cascade test case, showing an improvement of the flow prediction.

The main statement of this work is that the $\gamma - Re_\theta$ transition model and its correlations seem to depend strongly on the code where they are implemented. The new correlation presented in this work works well with the in-house code, but also the other authors showed good results with their own correlations. Therefore more numerical investigations have to be done to get more insight into these code dependencies.

For the own correlation, getting a better fitting correlation more test cases must be used for calibration in order to obtain a trustworthy correlation.

ACKNOWLEDGMENTS

The support by the Austrian Federal Ministry of Transport, Innovation and Technology (BMVIT) within the Austrian Aviation Program "TAKE OFF" for the project "CFD-TRANS" is gratefully acknowledged.

REFERENCES

- [1] Schmidt R.C. and Patankar S.V. (1991): *Simulating Boundary Layer Transition with Low-Reynolds $k-\epsilon$ Turbulence Models: Part 1 – An Evaluation of Prediction Characteristics*, ASME Journal of Turbomachinery, Vol. 113, pp. 10-17.
- [2] Savill A.M. (1993): *Some Recent Progress in the Turbulence Modelling of By-Pass Transition* in "Near Wall Turbulent Flow" by So, Speziale and Lauenders (eds.), Elsevier Science (New York).
- [3] Solomon W.J., Walker G.J. and Gostelow J.P. (1996): *Transition Length Prediction for Flows With Rapidly Changing Pressure Gradients*, ASME J.of Turbomachinery, Vol. 113, pp. 744-751.
- [4] Steelant J. and Dick E. (2001): *Modeling of Laminar-Turbulent Transition for High Freestream Turbulence*, Journal of Fluids Engineering, Vol. 123, pp. 22-30.
- [5] Pecnik R., Sanz W., Gehr A. and Woisetschlaeger J. (2003): *Modeling of Laminar-Turbulent Transition Using Two Different Intermittency Transport Equations*, Flow, Turbulence and Combustion, 2003, Vol. 70, pp. 299-323.
- [6] Menter F.R., Langtry R.B., Likki S.R., Suzen Y.B. and Huang P.G. (2004): *A Correlation-Based Transition model Using Local Variables, Part 1-Model Formulation*, GT2004-53452, ASME Turbo Expo 2004, Vienna, Austria.
- [7] Savill A.M. (1996): *One-point closures applied to transition* in "Turbulence and Transition Modelling - Lecture Notes from the ERCOFTAC/IUTAM Summerschool Held in Stockholm, 12-20 June, 1995" by D.S. Henningson et al.(eds.), Kluwer Academic Pub. Group, Chap. 6., p 233-268.
- [8] Savill A.M. (2002a): *By-Pass Transition using Conventional Closures* in "Closure Strategies for Turbulent and Transitional Flows" by Launder B.E. and Sandham

- N.D. (eds.), Cambridge University Press, Chapter 17, pp 464-492.
- [9] Savill A.M. (2002b): *New Strategies in Modelling By-Pass Transition* in "Closure Strategies for Turbulent and Transitional Flows" by Launder B.E. and Sandham N.D. (eds.), Cambridge University Press, Chapter 18, pp 493-521.
- [10] R.B. Langtry, F.R. Menter, S.R. Likki, Y.B. Suzen, P.G. Huang, S. Völker. *A Correlation-Based Transition Model Using Local Variables – Part II: Test Cases and Industrial Applications*. Journal of Turbomachinery, 128: 423-434, 2006.
- [11] R.B. Langtry and F.R. Menter. *Transition Modeling for General CFD Applications in Aeronautics*. AIAA Paper 2005-522, 43rd AIAA Aerospace Sciences Meeting and Exhibit, Reno, NV, January 10-13, 2005.
- [12] Menter F.R., R. Langtry and S. Völker (2006): *Transition Modelling for General Purpose CFD Codes*. Flow Turbulence Combust 77:277-303.
- [13] R.B. Langtry. *A Correlation-Based Transition Model using Local Variables for Unstructured Parallelized CFD codes*. PhD thesis, Institut für Thermische Strömungsmaschinen und Maschinenlaboratorium, Universität Stuttgart, 2006.
- [14] Langtry R.B., Gola J. and Menter F.R. (2006): *Predicting 2D Airfoil and 3D Wind Turbine Rotor Performance using a Transition Model for General CFD Codes*. AIAA 2006-395.
- [15] Malan P., Suluksna K. and Juntasaro E. (2009): *Calibrating the gamma-ReTheta Transition Model for Commercial CFD*. AIAA 2009-1142.
- [16] Sorensen N.N. (2009): *CFD Modelling of Laminar-turbulent Transition for Airfoils and Rotors Using the gamma-Re_theta Model*. Wind Energy (2009).
- [17] Elsner W., Piotrowski W. and Drobniak S. (2008): *Transition Prediction On Turbine Blade Profile With Intermittency Transport Equation*. GT 2008-50796, ASME Turbo Expo 2008, Berlin, Germany.
- [18] Pecnik R., Pieringer P. and Sanz W. (2005): *Numerical Investigation of the Secondary Flow of a Transonic Turbine Stage Using Various Turbulence Closures*, ASME paper GT2005-68754, ASME Turbo Expo 2005, Reno-Tahoe, Nevada, USA.
- [19] Roe P.L. (1981): *Approximate Riemann Solver, Parameter Vectors and Differencing Scheme*, Journal of Computational Physics Vol 43, pp. 357-372.
- [20] Elsner W., Piotrowski W. and Warzecha P. (2009): *Transition Modelling With Intermittency Transport Equations*. Ercoftac Bulletin 80.
- [21] Suluksna K., Dechaumphai P. and Juntasaro E. (2009): *Correlations for modelling transition boundary layer under influences of freestream turbulence and pressure gradient*. International Journal of Heat and Fluid Flow 30 (2009): 66-75.
- [22] Savill A. M. (1992): *A synthesis of T3 Test Case Predictions, Numerical Simulation of Unsteady Flows and Transition to Turbulence*, O. P. et al., ed., Cambridge University Press, pp. 404-442.
- [23] Hoheisel H. (1990): *Test Case E/CA-6 Subsonic Turbine Cascade T106*. in Test Cases for Computation of Internal Flows in Aero Engine Components, AGARD-AR-275, July.
- [24] Stieger R. D. (2002): *The Effects of Wakes on Separating Boundary Layers in Low Pressure Turbines*, PhD thesis, Cambridge University Engineering Department, February 2002.
- [25] Opoka M. M. and Hodson H. H. (2005): *An Experimental Investigation of the Unsteady Transition Process on the High Lift T106A Turbine Blade*, In the Proceedings of ISABE-2005-1277, Munich, Germany, 4th-9th September 2005.

Paper 4

M.E. Kelterer, R. Burgstaller, W.Sanz

Application of the gamma–Retheta transition model
to transitional flow.

ISAIF paper ISAIF10-091
presented at the 10th International Symposium on Experimental
and Computational Aerothermodynamics of Internal Flows
Brussels, Belgium, 2011

Proceedings of the 10th International Symposium on Experimental and Computational Aerothermodynamics of Internal Flows
4-7 July 2011, Brussels, Belgium

ISAI10-091

Application of the gamma- Re_{θ} transition model to transitional flow

M. E. Kelterer, R. Burgstaller, and W. Sanz

Institute for Thermal Turbomachinery and Machine Dynamics, Graz University of Technology
Inffeldgasse 25A, 8020 Graz/Austria, wolfgang.sanz@tugraz.at

Abstract

The accurate numerical simulation of the flow through turbomachinery depends on the correct prediction of boundary-layer transition phenomena. Especially heat transfer and skin friction investigations demand a reliable simulation of the transition process. Many models have been developed to simulate the transition process, ranging from simple algebraic models to very sophisticated transport models. But nearly all models suffer from the need to determine boundary layer parameters and from their difficult application in three-dimensional flows.

Therefore, the correlation based gamma- Re_{θ} transition model developed by Menter and Langtry is applied to turbomachinery flow. This model avoids the calculation of non-local parameters and is thus very suitable for three-dimensional general flow situations. Two additional transport equations, one for the intermittency and one for the momentum thickness Reynolds number, which is a criterion for the transition onset, are added to the well-known SST turbulence model by Menter. The model which is implemented into the in-house Reynolds-averaged Navier-Stokes solver combined with in-house correlations has already showed good results in a comprehensive calibration study on the well-known ERCOFTAC flat plate test cases.

In order to test the model for turbomachinery applications, it is applied to the flow in a T106 turbine cascade measured by Hoheisel. To improve the accuracy of the results, the in-house correlation has been calibrated by additional test cases.

Keywords: RANS equations; transitional flow, turbomachinery application, correlation based transition model.

Introduction

In turbomachines and especially in aircraft engines the Reynolds numbers that determine the evolution of the boundary layers can be relatively low. So a large part of the flow along the blade surfaces is often laminar or transitional. The boundary layer development, losses, efficiency and heat transfer are greatly affected by the laminar-to-turbulent transition. Due to the relatively high turbulence levels by-pass transition is the dominant form of transition in turbomachinery.

There are several methods used for simulating transitional flow, simpler algebraic models (e.g. Solomon et al. [1]) and more complex transport models (Steelant and Dick [2]; Pecnik et al. [3]; Menter et al. [4]). Among these models the $\gamma-Re_{\theta}$ model by Menter and Langtry ([4-10]) is very promising, because it is one of few models using only local information to simulate transition. To implement the model in the in-house code, there is the need of correlations for two parameters: $Re_{\theta c}$, which is the critical Reynolds number where the intermittency starts to increase in the boundary layer, and F_{length} , which is an indicator for the transition length. These two parameters are not given in the original work due to proprietary reasons.

In order to use this transition model for the in-house Reynolds averaged Navier-Stokes solver, an inhouse correlation was developed [11] based on and validated with flat plate test cases [12]. In this work this correlation is applied to a low-pressure turbine profile with suction side separation in order to recalibrate it and does extend its applicability to separation induced transition. It is also compared to already published correlations by other authors (Malan et al [13], Langtry and Menter [10]).

Calibration Test Case T106

In this work an additional test case was added to calibrate the inhouse correlation for test cases with turbomachinery content, the T106 test case. The flow was experimentally investigated by Hoheisel [16]. The main geometry settings of the T106 cascade are a chord length of 100mm, an axial blade length of 85.97mm and a pitch of 79.9mm. Separated-flow transition can occur on the suction side close to the trailing edge depending on the inlet FSTI. The used computational grid consists of 5 blocks with an O-block structure around the blade, with a maximum y^+_{max} value below 1 along the blade surface (see Fig. 3). For all calculations the same mesh was used.

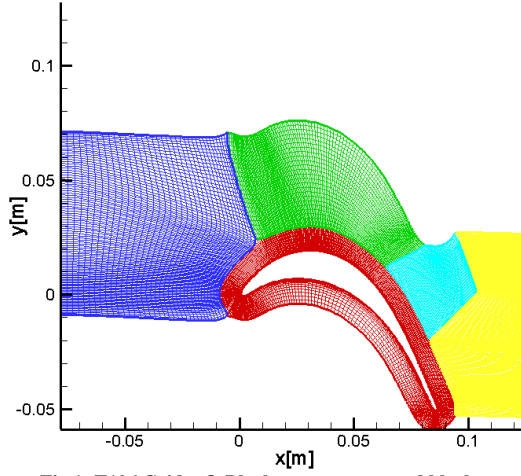


Fig 1: T106 Grid – O-Block structure around block

Table 1: Main operating conditions of the T106 cascade

$Re_{out,c}$	M_{out}	FSTI [%]
150000	0.59	0.5
		4.0
300000	0.59	0.5
		4.0
500000	0.59	0.5
		4.0

In this work the steady flow was investigated for a lower and a higher FSTI. Table 1 gives the main operating conditions from the experiments used for the numerical investigations. The inlet Mach number is comparable with a real engine. The experiments show, that for smaller Reynolds numbers the separation zone on the suction side is much larger than for higher Reynolds numbers.

Numerical method

The computations were performed using the in-house Navier-Stokes code LINARS, developed at Graz University of Technology (Pecnik et al. [14]). The compressible Reynolds/Favre-averaged Navier-Stokes (RANS) equations are solved in conservative form by means of a fully-implicit time-marching finite-volume method on structured curvilinear grids in multiblock alignment. The inviscid (Euler) fluxes are discretized with the upwind flux-difference splitting method of Roe [15]. In order to achieve a high order of spatial accuracy a total variation diminishing (TVD) scheme with third-order interpolation was applied to get the state vector at each cell interface. The viscous flux vector at the cell interfaces is constructed with a second-order accurate central-differencing scheme using Green's theorem. To obtain a linear set of the governing equations the Newton-Raphson procedure is applied for the

discretization in time. This method allows accurate unsteady calculations as well as improves convergence for steady calculations. The main flow equations and the turbulence equations are solved sequentially.

Transition Model

The $\gamma-Re_\theta$ correlation based transition model of Menter and Langtry [4-10] is based on two transport equations: the intermittency equation, which is used to trigger the transition process and the transport equation of the momentum thickness Reynolds number $Re_{\theta,tld}$.

The model is based on the idea that the momentum thickness Reynolds number which describes the transition process can be related to the vorticity Reynolds number Re_v :

$$Re_v = \frac{\rho y^2}{\mu} \frac{\partial u}{\partial y} = \frac{\rho y^2}{\mu} S \quad (1)$$

$$Re_\theta = \frac{Re_{v,max}}{2.193} \quad (2)$$

The transport equation for the intermittency is formulated as:

$$\frac{\partial(\rho\gamma)}{\partial t} + \frac{\partial(\rho U_j \gamma)}{\partial x_j} = P_\gamma - E_\gamma + \frac{\partial}{\partial x_j} \left[\left(\mu + \frac{\mu_t}{\sigma_f} \right) \frac{\partial \gamma}{\partial x_j} \right] \quad (3)$$

where the production of the intermittency is defined as:

$$P_\gamma = F_{length} c_{a1} \rho S [y F_{onset}]^{0.5} (1 - \gamma) \quad (4)$$

and the destruction/relaminarization term is:

$$E_\gamma = c_{a2} \rho \Omega \gamma F_{turb} (c_{e2} \gamma - 1) \quad (5)$$

In Eq. (4), F_{length} controls the length of the transition zone. S is the strain rate. F_{onset} triggers the intermittency production and thus the transition onset. F_{onset} is a function of the vorticity Reynolds number Re_v , the transition Reynolds number $Re_{\theta c}$ and the viscosity ratio R_T as described below:

$$F_{onset1} = \frac{Re_v}{2.193 Re_{\theta c}} \quad (6)$$

$$F_{onset2} = \min[\max(F_{onset1}, F_{onset1}^4), 2.0] \quad (7)$$

$$R_T = \frac{\rho k}{\mu \omega} \quad (8)$$

$$F_{onset3} = \max\left[1 - \left(\frac{R_T}{2.5}\right)^3, 0.0\right] \quad (9)$$

$$F_{onset} = \max(F_{onset2} - F_{onset3}, 0.0) \quad (10)$$

$$F_{turb} = e^{-(R_T/4)^4} \quad (11)$$

$$c_{e1} = 1.0; c_{a1} = 2.0; c_{e2} = 50; c_{a2} = 0.06; \sigma_f = 1.0$$

If the vorticity Reynolds number becomes remarkably larger than the critical Reynolds number, the transition onset is triggered. So the critical Reynolds number determines the location where the intermittency first starts to increase in the boundary layer. It is related to $Re_{\theta,tld}$ by an empirical correlation, F_{length} in the

production term is also related to $Re_{\theta_{tld}}$. The boundary condition for γ at a wall is zero normal flux and at the inlet equal to 1.

The transport equation for the transition momentum thickness Reynolds number is formulated as:

$$\frac{\partial(\rho \tilde{Re}_\alpha)}{\partial t} + \frac{\partial(\rho U_j \tilde{Re}_\alpha)}{\partial x_j} = P_\alpha + \frac{\partial}{\partial x_j} \left[\sigma_\alpha (\mu + \mu_t) \frac{\partial \tilde{Re}_\alpha}{\partial x_j} \right] \quad (12)$$

where the source term is:

$$P_\alpha = c_\alpha \frac{\rho}{t} (Re_\alpha - \tilde{Re}_\alpha) (1.0 - F_\alpha) \quad (13)$$

It is defined in such a way to force the transported scalar $Re_{\theta_{tld}}$ to match the local value of the transition momentum thickness Reynolds number calculated from an empirical correlation obtained from measurements of transitional flows. Menter et al.[4] suggest a correlation based on Abu-Ghannam and Shaw [17]; Mayle [18] and Drela [19]. This correlation was slightly changed by Langtry [8]. All further model equations and parameters are taken and used in this investigation as published by Menter et al. [4].

The momentum thickness has only a physical meaning within 1D, for 3D it is no physical term, but Menter used it for having a transition criterion in the whole boundary layer. The source term is used to introduce the transition criterion and the transport equation allows to add upstream flow information.

The boundary condition for $Re_{\theta_{tld}}$ at a wall is zero flux. At an inlet the boundary condition for $Re_{\theta_{tld}}$ is calculated based on the inlet turbulence intensity with the Re_{θ_t} correlation from Menter et al. [4].

This transition model is coupled with the SST turbulence model as proposed by Menter et al. [4] by multiplying the production term and the destruction term in the k-equation of the SST model with the intermittency.

For separation-induced transition there is a need of using an effective intermittency in the k transport equation which combines the influences of bypass and separated-flow transition:

$$\gamma_{sep} = \min \left\{ s_1 \cdot \max \left[\left(\frac{Re_v}{3.235 Re_\alpha} \right) - 1.0, 0.0 \right] F_{reattach}, s_2 \right\} F_\alpha$$

$$s_1 = 2.0, \quad s_2 = 2.0 \quad (14)$$

$$F_{reattach} = e^{-(Re_v/20)^2} \quad (15)$$

$$\gamma_{eff} = \max(\gamma, \gamma_{sep}) \quad (16)$$

To close the model, three empirical correlations are required for Re_{θ_C} , F_{length} and Re_{θ_t} .

$$Re_{\theta_C} = f(\tilde{Re}_\alpha) \quad (17)$$

$$F_{length} = f(\tilde{Re}_\alpha) \quad (18)$$

$$Re_{\theta_t} = f(Tu, \dots)_{freestream} \quad (19)$$

Since Re_{θ_t} is used to specify $Re_{\theta_{tld}}$ (see Eq.(13)), Re_{θ_C} and F_{length} must also be strong functions of $Re_{\theta_{tld}}$.

Thus it is clear, that the empirical correlations of Eqs. (17, 18) are valid only when used with the appropriate Re_{θ_t} correlation (Eq. (19)).

Whereas the correlation for the transition momentum thickness Reynolds number is given by Menter et al. [4] and in a slightly different version by Langtry [8], the correlations for Re_{θ_C} and F_{length} as functions of $Re_{\theta_{tld}}$ were not published in the original model presentation [4] due to proprietary reasons.

In order to close this transition model, other research groups as well as the authors proposed correlations for these two parameters which were implemented in the in-house code and evaluated [11].

In 2009 Langtry and Menter [10] finally published their missing correlations, which were also implemented into our code to compare it with the in-house correlation.

Investigated Correlations

In order to close the transition model by Menter et al. [4], two empirical correlations are needed which control the transition onset and the transition length. In the following three different closure correlations which were tested with our in-house code, are discussed:

Correlation by Langtry and Menter [10] – LM:

The correlation of LM is implemented in the commercial CFD software programme CFX from version 11 on. The correlations for the critical Reynolds number and the F_{length} parameter of the production term (Eq. (4)) are:

$$Re_{\theta_{t_Menter}} = \begin{cases} \tilde{Re}_\alpha \leq 1870: \\ \left[\tilde{Re}_\alpha - (396.035 \cdot 10^{-2} + (-120.656 \cdot 10^{-4}) \tilde{Re}_\alpha \right. \\ \left. + (868.230 \cdot 10^{-6}) \tilde{Re}_\alpha^2 + (-696.506 \cdot 10^{-9}) \tilde{Re}_\alpha^3 \right. \\ \left. + (174.105 \cdot 10^{-12}) \tilde{Re}_\alpha^4 \right] \\ \tilde{Re}_\alpha > 1870: \\ \left[\tilde{Re}_\alpha - (593.11 + (\tilde{Re}_\alpha - 1870.0) \cdot 0.482) \right] \end{cases} \quad (20)$$

$$F_{length_Menter} = \begin{cases} \tilde{Re}_\alpha < 400: \\ \left[398.189 \cdot 10^{-1} + (119.270 \cdot 10^{-4}) \tilde{Re}_\alpha \right. \\ \left. + (-132.567 \cdot 10^{-6}) \tilde{Re}_\alpha^2 \right] \\ 400 \leq \tilde{Re}_\alpha < 596: \\ \left[263.404 + (-123.939 \cdot 10^{-2}) \tilde{Re}_\alpha \right. \\ \left. + (194.548 \cdot 10^{-5}) \tilde{Re}_\alpha^2 + (-101.695 \cdot 10^{-8}) \tilde{Re}_\alpha^3 \right] \\ 596 \leq \tilde{Re}_\alpha < 1200: \\ \left[0.5 - (\tilde{Re}_\alpha - 596.0) \cdot 3.0 \cdot 10^{-4} \right] \\ 1200 \leq \tilde{Re}_\alpha \\ [0.3188] \end{cases} \quad (21)$$

Correlation by Malan et al. [13] – MA:

The corresponding correlations for the two parameters of the production term (Eq. (4)) are:

$$Re_{\theta_c_Malan} = \min(0.615 \tilde{Re}_\theta + 61.5; \tilde{Re}_\theta) \quad (22)$$

$$F_{length_Malan} = \min(\exp(7.168 - 0.01173 \tilde{Re}_\theta) + 0.5; 300) \quad (23)$$

Both parameters are a function of Re_{θ_tld} as proposed by Menter et al. [4]. Malan et al. implemented the transition model into the commercial CFD code StarCCM+ and derived the correlations for the Langtry model [8] for Re_{θ_c} using four flat-plate test cases where they achieve good agreement with the experimental data. They also applied their correlations to several flow cases including interior and exterior flows. They concluded that further refinement of their correlations in order to extend their range of applicability would be necessary.

Correlation by Kelterer et al. [11] – KE:

Before the LM correlation was published several research groups tried to find good fitting correlations for the transition model. At first the authors implemented several correlations by some of these research groups, but the results for some flat plate test cases did not agree with their published results. So it was concluded that an own correlation is needed which fits to the inhouse flow solver [11]

The correlations for the critical Reynolds number and the F_{length} parameter of the production term (Eq. (4)) are:

$$\tilde{Re}_\theta \leq 215 : \\ Re_{\theta_c} = 1.02 \cdot \tilde{Re}_\theta - 35 + \tanh\left(-\left(\frac{\tilde{Re}_\theta - 138}{54}\right)\right) \cdot 36 \quad (24)$$

$$\tilde{Re}_\theta > 215 : \\ Re_{\theta_c} = \tanh\left(\frac{\tilde{Re}_\theta - 215}{15}\right) \cdot 45 + 155$$

$$F_{length} = \min\left[250 \cdot \exp\left[-\left(\frac{\tilde{Re}_\theta}{130}\right)^{1.7}\right] + 10; 40\right] \quad (25)$$

In Figs. 1 and 2 the three different correlations are compared (LM – red line, MA – green line and KE – blue line). The correlations show very big differences e.g. the F_{length} value of MA is at lower values of Re_{θ_tld} (0...200) approximately 10 times the value of KE as well as of LM and for higher Re_{θ_tld} values (800 and higher) the KE correlation is approximately 10 times the value of MA as well as of LM. On the other hand, the Re_{θ_c} value is much higher for the ME as well as for the LM correlation for $Re_{\theta_tld} > 400$, where the KM is limited to a Re_{θ_c} value equal 200.

The two parameters, F_{length} and Re_{θ_c} , affect the transition in a different way. A larger F_{length} value leads to a larger production term, and this results in a faster transition process. If Re_{θ_c} is high, the F_{onset} value is small and this reduces the production term. So a high Re_{θ_c} value can be compensated by a high F_{length} value.

Also the higher F_{length} is, the shorter is the transition zone. This consideration indicates that several optimum combinations of F_{length} and Re_{θ_c} exist, as also assumed by Suluksna et al. [20].

Also a different Re_{θ_c} correlation will lead to different correlations for Re_{θ_c} and F_{length} as explained above. This may also be a reason for the differences in the three correlations.

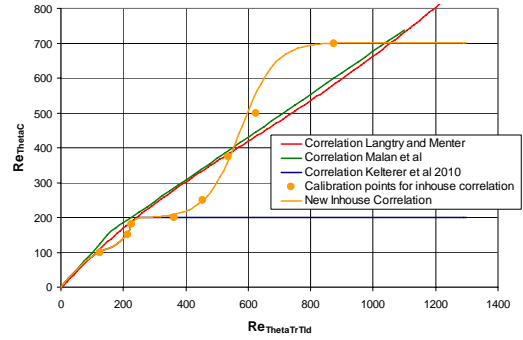


Fig 2: Correlation Re_{θ_c} by Malan et al [13], Langtry and Menter [10] and Kelterer et al [11]

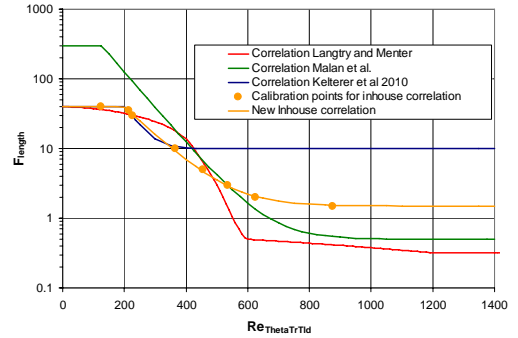


Fig 3: Correlation F_{length} by Malan et al [13], Langtry and Menter [10] and Kelterer et al [11]

Model Validation

All three correlations with the corresponding correlation for Re_{θ_c} were implemented into the in-house code and applied to flat plate test cases. The results showed very large differences and the inhouse correlation showed the best agreement with the experiments ([11]).

In this study all these before mentioned correlations were applied to the T106 turbine cascade test case. The two following figures (Fig. 4 and Fig. 5) show the calculated pressure coefficient as well as the corresponding skin friction coefficient for all three before mentioned correlations compared with the experimental results for a Reynolds number of 300000 at a FSTI of 0.5%. The experiments show a small

separation zone with transition to turbulent as indicated by the flat region in the pressure distribution. Looking at the pressure coefficient in Fig. 4 and at the skin friction coefficient in Fig. 5 the LM correlation (red line) as well as the MA correlation (green line) show the behaviour seen in the experiments and also predict the start of the separation zone as well as the length of the separation zone reasonably. At the end the correct prediction of transition to turbulence can be seen in Fig. 4 by the agreement of the pressure distribution at the flat region. The KE correlation (blue line) shows a too early transition to turbulent flow and so predicts a much too small separation zone.

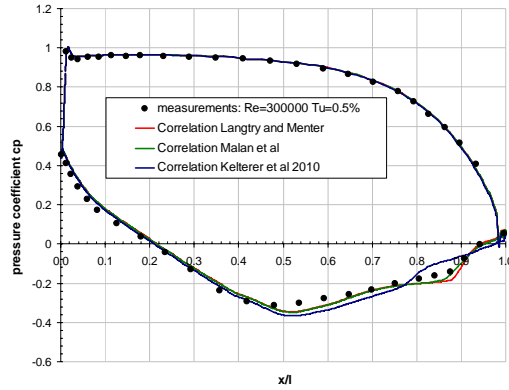


Fig 4: T106: pressure coefficient at $Re=300000$ for FSTI of 0.5% with different correlations

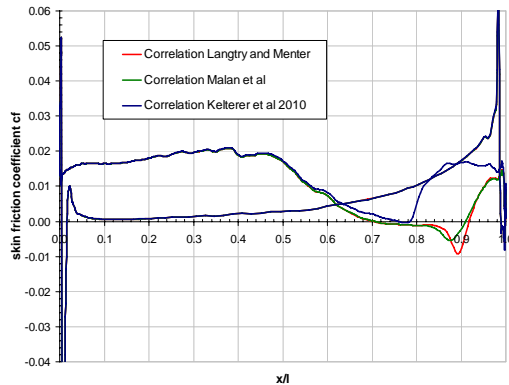


Fig 5: T106: skin friction coefficient at $Re=300000$ for FSTI of 0.5% with different correlations

This bad prediction of the measurement data was also observed for all Re numbers. Therefore it was decided to enhance the own correlation by considering the T106 data.

Model Calibration

For enhancing the own correlation, the T106 test case [16] described before was used as an additional calibration case. The parameter tuning was done for three different Reynolds numbers with a FSTI of 0.5%. The reason for taking just the FSTI=0.5% into account is because with the lower FSTI separation induced transition occurs over a range of Re numbers. The procedure for finding the correlations is mainly the same as reported by other authors (e. g. [11], [13], [21]).

The authors decided to calculate the correlations as a function of the local $Re_{\theta,ld}$ as proposed by Sorensen [21] and Malan et al. [13]. For developing the correlations the following relation between $Re_{\theta C}$ and $Re_{\theta,ld}$ was used which allows reducing the dependency between $Re_{\theta C}$ and $Re_{\theta,ld}$ to one value:

$$Re_{\theta C} = F_p \cdot \tilde{Re}_\theta \quad (26)$$

The authors try to find an optimum triple of F_p , F_{length} and $Re_{\theta C}$ which matches the experimental data best. For a detailed description the authors refer to their previous paper dealing with the derivation of the correlations for their transition model [11].

The optimum parameters for the T106 calibration test cases are given in Table 2. There are also the new parameters for two ERCOFTAC flat plate test cases, which had to be adjusted to get a smoother calibration curve.

Table 2: Calibration result

Case	U_{inlet} ($m s^{-1}$)	Tu (%)	local $Re_{\theta,ld}$	$Re_{\theta C}$	F_{length}	F_p
T3C2	5.3	3.0	454	250	5	0.55
T3C4	1.37	3.0	364	200	10	0.55
Case	Re	Tu (%)	local $Re_{\theta,ld}$	$Re_{\theta C}$	F_{length}	F_p
T106	150000	0.5	535	375	3	0.7
	300000	0.5	625	500	2	0.8
	500000	0.5	875	700	1.5	0.8

With the values of these calibration test cases the following correlations for F_{length} (Eq. (27)) and $Re_{\theta C}$ (Eq. (28)) and are extracted to a correlation.

$$F_{length} = \min \left[215 \cdot \exp \left[- \left(\frac{\tilde{Re}_\theta}{120} \right)^{1.08} \right] + 1.5; 40 \right] \quad (27)$$

$$\tilde{Re}_\theta \leq 215 :$$

$$Re_{\theta C} = 1.02 \cdot \tilde{Re}_\theta - 35 + \tanh \left(- \left(\frac{\tilde{Re}_\theta - 138}{54} \right) \right) \cdot 36 \quad (28 a)$$

$$\begin{aligned}
 & 215 < \tilde{Re}_{\theta} \leq 270 : \\
 & Re_{\theta} = \tanh\left(\frac{\tilde{Re}_{\theta} - 215}{16}\right) \cdot 45 + 155 \\
 & \tilde{Re}_{\theta} > 270 : \\
 & Re_{\theta} = \tanh\left(\frac{\tilde{Re}_{\theta} - 575}{16}\right) \cdot 252 + 450
 \end{aligned}
 \tag{28 b}$$

Figs. 2 and 3 show the correlations for F_{length} and for $Re_{\theta C}$ as function of $Re_{\theta_{tld}}$ for the new inhouse correlation – NIC (orange line). The $Re_{\theta C}$ value does not change in the range $Re_{\theta_{tld}} \leq 270$, but from there on it raises over the MA and LM correlations, but again ends with a constant $Re_{\theta C}$ value of 700 from $Re_{\theta_{tld}} \geq 875$ on.

The F_{length} correlation stays the same to $Re_{\theta_{tld}} < 180$ and decreases to a value of $F_{length}=1.5$ reached at $Re_{\theta_{tld}}=1150$. The NIC correlation for F_{length} is now approximately 10 times lower than the KE, and at a similar level as the MA and LM correlations.

Results and discussion

For verifying the behaviour of the code the new correlation is validated with the calibration test cases T3C2 and the T3C4 test cases as well as the turbine cascade T106. It sounds a little bit confusing that the authors validate a correlation taking the calibration test cases into account.

The reason is that the calibration is done with constant values of F_{length} , F_p and $Re_{\theta C}$ in the whole flow field, whereas the use of the correlation itself allows locally varying values. This verification can be considered a final control of the enhanced correlation.

Flat Plate Test Cases T3C2, T3C4

Due to the recalibration of the inhouse correlation in a value range where the flat plate test cases T3C2 and T3C4 are located these two test cases are shown here. In the following two figures, the skin friction coefficient for these two test cases is shown comparing the new inhouse correlation with the other before discussed correlations.

For the T3C2 test case the NIC correlation and gives similar results as the MA and the LM correlation. It shows a slightly too late and too short transition zone.

For the T3C4 test case, the NIC correlation is a little bit better in predicting the separation zone, than the LM and the MA correlation.

The new inhouse correlation (NIC) for these two flat plate test cases shows a worse agreement with the experiments but still reasonable fitting with the first correlation. This adaption was necessary to improve the prediction of turbine cascades with separation induced transition.

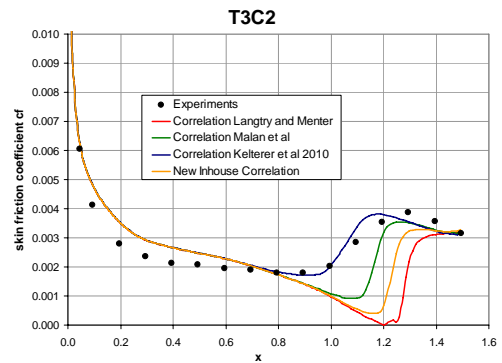


Fig 6: Skin friction coefficient for T3C2

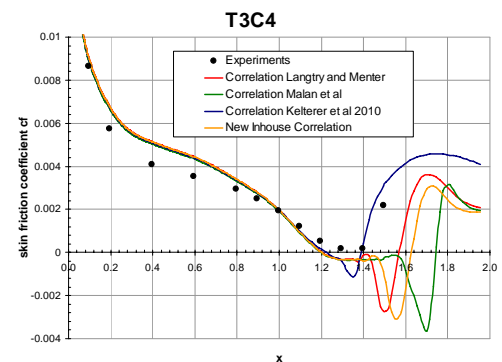


Fig 7: Skin friction coefficient for T3C4

Turbine Cascade T106

The new inhouse correlation was also applied to the calibration test case T106. In the following figures (Figs. 9-19) the comparison between the LM, the MA and the new inhouse correlation (NIC) is shown for three different Reynolds numbers for the two FSTIs.

FSTI=0.5%

For the lowest Re number of 150000 and the lower FSTI of 0.5% the experiments show a very large laminar separation zone (from $x/l=0.85$ [16]) which lasts to the trailing edge, no transition to turbulence can be seen. Looking at the pressure coefficient in Fig. 8 and at the skin friction coefficient in Fig. 11 all three correlations show the behaviour seen in the experiments. The LM correlation (red line) shows a too early separation onset, the MA correlation (green line) and the NIC correlation (blue line) show a nearly congruent result, both predict the start of the separation zone slightly too early, but the laminar separation zone is predicted well.

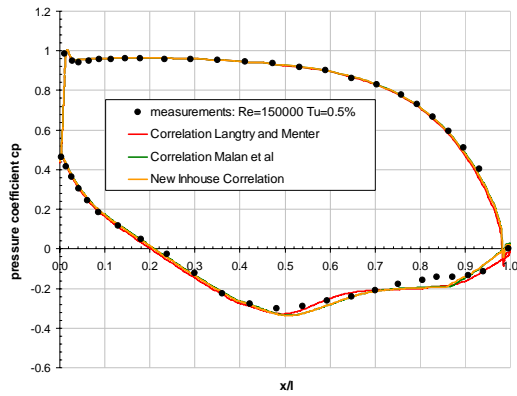


Fig 8: T106 pressure coefficient at Re=150000 for FSTI of 0.5%

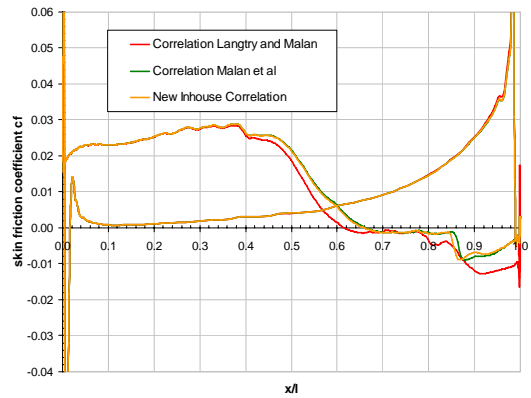


Fig 11: T106 skin friction coefficient at Re=150000 for FSTI of 0.5%

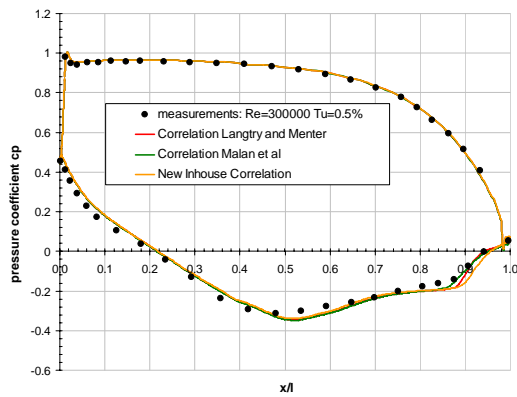


Fig 9: T106 pressure coefficient at Re=300000 for FSTI of 0.5%

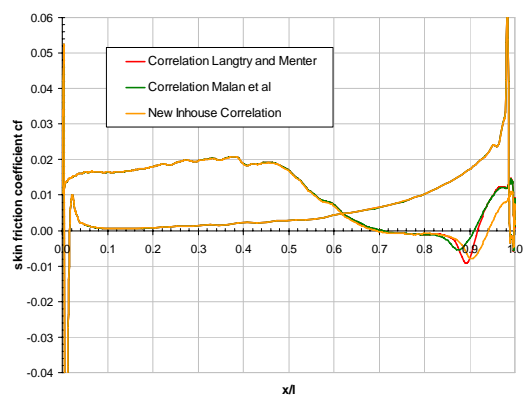


Fig 12: T106 skin friction coefficient at Re=300000 for FSTI of 0.5%

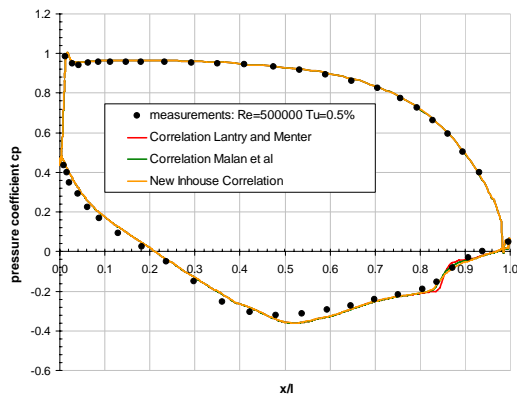


Fig 10: T106 pressure coefficient at Re=500000 for FSTI of 0.5%

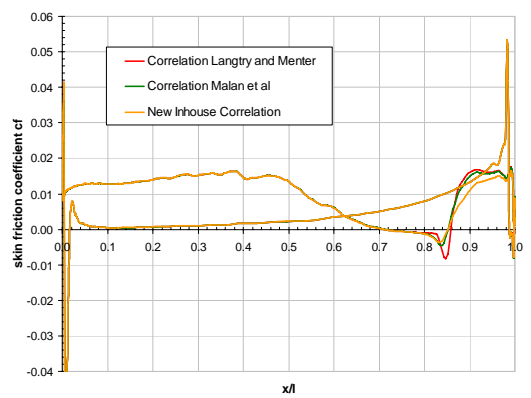


Fig 13: T106 skin friction coefficient at Re=500000 for FSTI of 0.5%

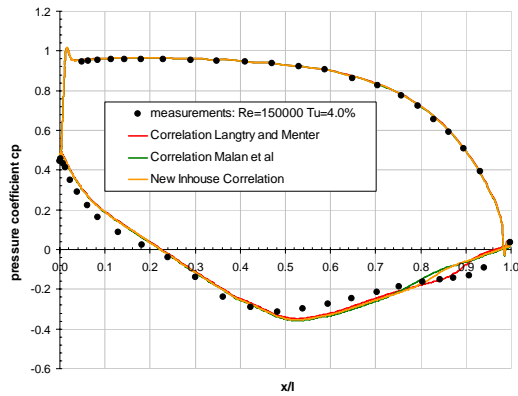


Fig 14: T106 pressure coefficient at Re=150000 for FSTI of 4.0%

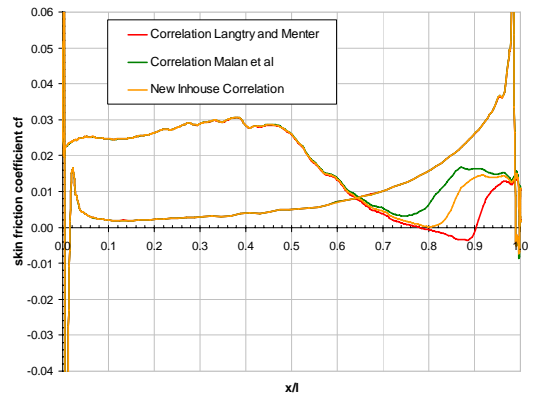


Fig 17: T106 skin friction coefficient at Re=150000 for FSTI of 4.0%

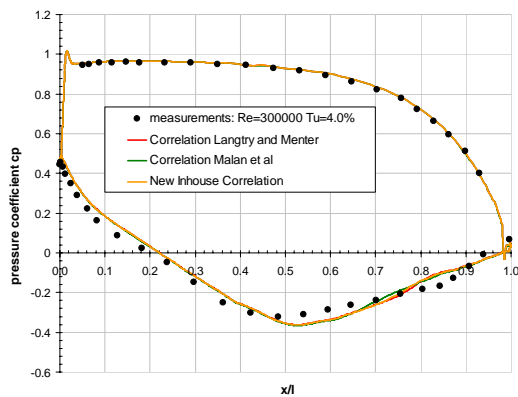


Fig 15: T106 pressure coefficient at Re=300000 for FSTI of 4.0%

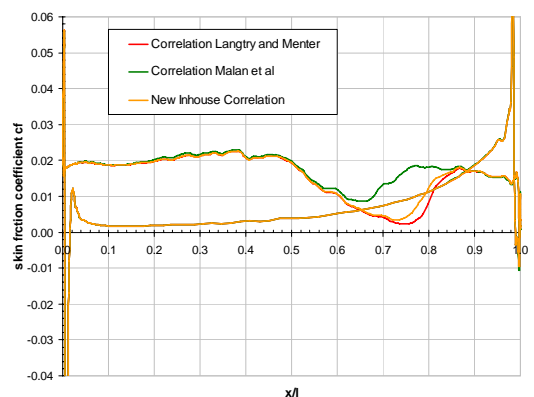


Fig 18: T106 skin friction coefficient at Re=300000 for FSTI of 4.0%

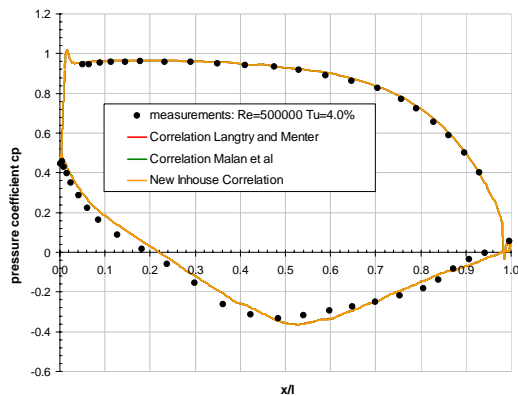


Fig 16: T106 pressure coefficient at Re=500000 for FSTI of 4.0%

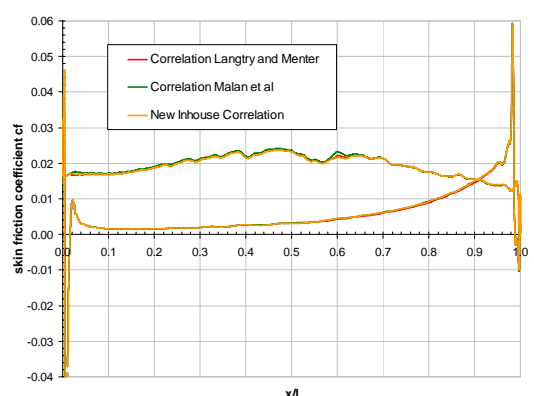


Fig 19: T106 skin friction coefficient at Re=500000 for FSTI of 4.0%

For a Re number of 300000 and the lower FSTI of 0.5% the experiments show a smaller separation zone with transition to turbulent. Looking at the pressure coefficient in Fig. 5 and at the skin friction coefficient in Fig. 8 all three correlations show the correct start of the separation zone and just differ in the length of the separation zone. MA predicts the shortest separation zone, followed by the LM correlation; the NIC correlation shows the largest separation zone. Also the transition to turbulent flow is predicted correctly which can be seen in Fig. 9 looking at slope of the pressure coefficient on the suction side in the area of $x/l=0.88\dots0.92$; these slope is correctly predicted.

For the highest Re number of 500000 and the lower FSTI of 0.5% the experiments show a separation zone which lasts from $x/l=0.7$ to $x/l=0.9$. Looking at the pressure coefficient in Fig. 6 and at the skin friction coefficient in Fig. 9 the LM correlation as well as the MA correlation again show the behaviour seen in the experiments. The start of the separation zone is predicted correctly, but there is a small deficiency in predicting the correct length of the separation zone. The LM correlation shows a slightly larger separation zone than MA and NIC.

FSTI=4.0%

For the lowest Re number of 150000 and the higher FSTI of 4.0% the experiments indicate that there is again a laminar separation zone that extends to the trailing edge of the blade. Looking at the pressure coefficient in Fig. 14 and at the skin friction coefficient in Fig. 17 all three correlations show a transition to turbulence in contrast to the experiments. The LM correlation shows a small separation zone, followed by a transition to turbulent flow. An early transition without any separation can be seen in the predictions using MA as well as NIC.

For a Re number of 300000 and the highest Re number of 500000 Hoheisel suspects that in the experiments both laminar and turbulent boundary layer conditions can occur. Looking at the pressure coefficient in Fig. 11 and at the skin friction coefficient in Fig. 14 for the $Re=300000$, the LM correlation results are very similar to that one of NIC, and again the MA correlation tends to predict a too early transition to turbulent flow. For the $Re=500000$ all three correlations show the same results of a fully turbulent BL.

Concluding the results for all three correlations, for the lower FSTI the calculations show that the correlations tend to predict a slightly earlier separation onset than shown in the experiments. Also the transition to turbulent flow is predicted a little bit too early for the lower FSTI, but for the higher FSTI this behaviour of the correlations can be seen more explicitly, which was also reported by Lutum and Cottier [22]. The LM correlation tends to predict a too large separation zone, what can be seen in the skin friction coefficient distribution. The MA correlation is very sensible to a

FSTI variation, what can be seen in the strong variation of the skin friction coefficient between the 0.5% and the 4.0% FSTI compared to the variation predicted by the other correlations. The NIC correlation tends to predict a slightly too large separation zone for the lower FSTI of 0.5% but can be compared with the results of MA and for the higher FSTI of 4.0% the NIC correlation shows a too early transition onset. The similar behaviour of the MA and the NIC correlation can be explained by the form of the correlation itself (see Fig. 2 and Fig. 3), because for these cases where the two correlations nearly fit to each other the calibration points from the NIC are similar to the correlation by Malan. All three correlations show rather good results for the cascade test cases, only the MA correlation lacks slightly in predicting the flow for higher FSTIs. This tendency was not valid when testing the flat plate test cases with the different correlations.

Conclusions

The paper deals with the before missing correlations of the $\gamma-Re_{\theta}$ transition model by Menter et al.[3]. Correlations from other authors (Malan et al. [13], Langtry and Menter [10]) were implemented in the in house code and compared with the inhouse correlation [11]. Applying these correlations to the cascade test case T106, the calculations with the correlation by Kelterer et al for different Reynolds numbers shows strong deviations from the measurements. To get a more general correlation to better predict separation induced transition as it occurs on e.g. LP turbine blades, the T106 test case was taken into account additionally to the flat plate test cases from the ERCOFTAC data base for calibrating the in-house correlation. The correlation was formulated in terms of $Re_{\theta,uid}$ as originally proposed by Malan et al. [13] and Sorensen [21]. After calibrating the in-house correlation it is applied to T106 turbomachinery flow, showing an improvement of the flow prediction.

The assumption that the correlations strongly depend on the code and the way of implementation as it was concluded by the authors for the flat plate test cases could not be affirmed for the cascade test cases. There is just a light dependency of the correlations on the code, what can be seen comparing the new inhouse correlation (NIC) with the Malan et al correlation (MA).

Acknowledgements

The support by the Austrian Federal Ministry of Transport, Innovation and Technology (BMVIT) within the Austrian Aviation Program "TAKE OFF" for the project "CFD-TRANS" is gratefully acknowledged.

The authors also want to thank Paul Malan for the inspiring discussions according correlation design.

Nomenclature

c_f	skin friction coefficient
c_p	pressure coefficient; $c_p = (p - p_2)/(p_{01} - p_2)$
k	turbulent kinetic energy
p	local static pressure
p_{01}	inlet total pressure
p_2	static outlet pressure
Re_θ	momentum thickness Reynolds number, $\rho\theta U_o/\mu$
$Re_{\theta C}$	critical Reynolds number
Re_θ	transition onset momentum thickness Reynolds number
\tilde{Re}_θ	Local transition onset momentum thickness Reynolds number, obtained from transport equations
$Re_{\theta_{std}}$	
R_T	Viscosity ratio $\rho k/(\mu\omega)$
Re_V	Vorticity (strain rate) Reynolds number $\rho y^2 S/\mu$
S	absolute value of strain rate, $(2 S_{ij} S_{ij})^{1/2}$
S_{ij}	Strain rate tensor, $1/2(\delta u_i/\delta y_j + \delta u_j/\delta x_i)$
t	time
Tu	free-stream turbulence intensity (FSTI)
U	velocity
y	distance to nearest wall

Greek symbols:

γ	near wall intermittency factor
μ_t	turbulent viscosity
μ	molecular viscosity
ρ	density
ω	specific turbulence dissipation rate
Ω	absolute value of vorticity, $(2 \Omega_{ij} \Omega_{ij})^{1/2}$
Ω_{ij}	Strain rate tensor, $1/2(\delta u_i/\delta y_j + \delta u_j/\delta x_i)$

Abbreviations:

FSTI	free-stream turbulence intensity
------	----------------------------------

References

- [1] Solomon W.J., Walker G.J., Gostelow J.P. (1996), Transition Length Prediction for Flows With Rapidly Changing Pressure Gradients, ASME J. of Turbomachinery, Vol. 113, pp. 744-751
- [2] Steelant J., Dick E. (2001), Modeling of Laminar-Turbulent Transition for High Freestream Turbulence, Journal of Fluids Engineering, Vol. 123, pp. 22-30
- [3] Pecnik R., Sanz W., Gehrler A., Woisetschlaeger J. (2003), Modeling of Laminar-Turbulent Transition Using Two Different Intermittency Transport Equations, Flow, Turbulence and Combustion, 2003, Vol. 70, pp. 299-323
- [4] Menter F.R., Langtry R.B., Likki S.R., Suzen Y.B., Huang P.G. (2004), A Correlation-Based Transition model Using Local Variables, Part 1-Model Formulation, GT2004-53452, ASME Turbo Expo 2004, Vienna, Austria
- [5] R.B. Langtry, F.R. Menter, S.R. Likki, Y.B. Suzen, P.G. Huang, S. Völker (2006), A Correlation-Based Transition Model Using Local Variables – Part II: Test Cases and Industrial Applications. Journal of Turbomachinery, Vol. 128, pp.423-434
- [6] R.B. Langtry, F.R. Menter (2005), Transition Modeling for General CFD Applications in Aeronautics. AIAA Paper 2005-522, 43rd AIAA Aerospace Sciences Meeting and Exhibit, Reno, NV, January 10-13
- [7] Menter F.R., R.Langtry, S.Völker (2006), Transition Modelling for General Purpose CFD Codes. Flow Turbulence Combust 77:277-303
- [8] R.B. Langtry (2006), A Correlation-Based Transition Model using Local Variables for Unstructured Parallelized CFD codes. PhD thesis, Institut für Thermische Strömungsmaschinen und Maschinenlaboratorium, Universität Stuttgart
- [9] Langtry R.B., Gola J., Menter F.R. (2006), Predicting 2D Airfoil and 3D Wind Turbine Rotor Performance using a Transition Model for General CFD Codes. AIAA 2006-395
- [10] Langtry R.B., Menter F.R. (2009), Correlation-Based Transition Modeling for Unstructured Parallelized Computational Fluid Dynamics Codes, In AIAA Journal Vol. 47, No. 12, December 2009
- [11] Kelterer M., Pecnik R., Sanz W. (2010), Computation of Laminar-Turbulent Transition in Turbomachinery Using The Correlation Based gamma-Re_Theta Transition Model. GT2010-22207, ASME Turbo Expo 2010, Glasgow, Scotland
- [12] Savill A M. (1992), A synthesis of T3 Test Case Predictions, Numerical Simulation of Unsteady Flows and Transition to Turbulence, O. P. et al., ed., Cambridge University Press, pp. 404-442
- [13] Malan P., Suluksna K., Juntasaro E. (2009), Calibrating the gamma-ReTheta Transition Model for Commercial CFD. AIAA 2009-1142
- [14] Pecnik R., Pieringer P., Sanz W. (2005), Numerical Investigation of the Secondary Flow of a Transonic Turbine Stage Using Various Turbulence Closures, ASME paper GT2005-68754, ASME Turbo Expo 2005, Reno-Tahoe, Nevada, USA
- [15] Roe P.L. (1981), Approximate Riemann Solver, Parameter Vectors and Differencing Scheme, Journal of Computational Physics Vol 43, pp. 357-372
- [16] Hoheisel H. (1990), Test Case E/CA-6 Subsonic Turbine Cascade T106. in Test Cases for Computation of Internal Flows in Aero Engine Components, AGARD-AR-275, July
- [17] Abu-Ghannam, B.J. and Shaw, R. (1980), Natural Transition of Boundary Layers – The Effects of Turbulence, Pressure Gradient, and Flow History. J. Mech. Eng. Sci., Vol. 22, No. 5, pp. 213-228
- [18] Mayle, R.E., (1991), The Role of Laminar-Turbulent Transition in Gas Turbine Engines. ASME Journal of Turbomachinery, Vol. 113, pp. 509-537.
- [19] Drela, M., (1995), MISES Implementation of Modified Abu-Ghannam and Shaw Transition Criteria. MIT Aero-Astro.
- [20] Suluksna K., Dechaumphai P., Juntasaro E. (2009), Correlations for modelling transition boundary layer under influences of freestream turbulence and pressure gradient. International Journal of Heat and Fluid Flow 30 (2009): 66-75
- [21] Sorensen N.N. (2009), CFD Modelling of Laminar-turbulent Transition for Airfoils and Rotors Using the gamma-Re_theta Model. Wind Energy
- [22] Lutum E. and Cottier F. (2011), Aerothermal predictions on a highly loaded turbine blade including effects of flow separation. In Conference Proceedings of 9th European Conference on Turbomachinery, Fluid Dynamics and Thermodynamics, held in Istanbul/Turkey 21-25 March 2011: pp. 1581-1591

6. Relaminarisation

In this chapter the stepmotherly treated transition mode *Reverse Transition* is described in detail. After the explanation of the different relaminarisation modes, the main intention of the author for this chapter will be described in Chapter 6.3, followed by three calculation test cases, to show the ability of the $\gamma - Re_\theta$ transition model to predict relaminarisation.

The mode *Reverse Transition* is a very important mode of transition for thermal turbomachinery, which can occur among others on the pressure side of high pressure turbine blades. It has already been mentioned by Mayle (1991) in his famous review on transitional flow as relaminarisation. Relaminarisation is the transition from turbulent back to laminar flow.

Relaminarisation gets more and more important for turbine designers when influencing the boundary layer to change to turbulent, which is stated by Gad-el Hak (2000), who described control systems to reduce skin friction in turbulent wall-bounded flows.

Narasimha and Sreenivasan (1979) described relaminarisation in more detail, and divided it into different modes.

6.1. Modes of Relaminarisation

The modes of relaminarisation can be divided into three main modes, the *Reversion by Dissipation*, the *Reversion in Stable Stratified Flows* and the *Reversion in Highly Accelerated Flows*, which will be described in detail afterwards, and combined modes, the *Relaminarisation in Curved Flows*, the *Relaminarisation by Rotation*, the *Relaminarisation by Thermal Effects*, the *Relaminarisation by Surface Mass Transfer* and the *Magnetohydrodynamic Duct Flows*.

The most important modes of relaminarisation will be described briefly in the following sections.

Reversion by Dissipation

The decreasing Reynolds number in a turbulent flow results in a rising dissipation, that can exceed the production of turbulent energy and the flow may become laminar. The relaminarisation by dissipation, which e.g. can occur in a diffuser, is triggered the other

way round compared to transition to turbulent, where the transition process is triggered by a rising Reynolds number. Fig. 6.1 shows, that the skin friction coefficient c_f (open circles) faster reaches the laminar value than the velocity gradient of the center-line velocity and the section averaged flow velocity (black squares) within this form of relaminarisation.

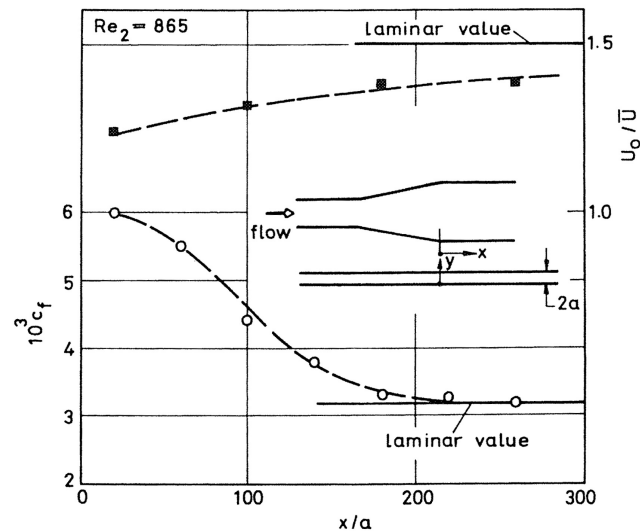


Figure 6.1.: Velocity and skin friction distribution in the case of relaminarisation in a diffuser caused by dissipation (black squares=velocity, open circles= skin friction coefficient), from Narasimha and Sreenivasan (1979)

Relaminarisation due to dissipation may also be found in the human body, where air flows during its way from the trachea to the segmental bronchi in human lungs (Gad-el Hak (2000)).

Reversion in Stable Stratified Flows

This form of relaminarisation can occur in horizontal boundary layers with varying density (or density fluctuations). If the density of a fluid decreases with height, a stable stratification can be assumed, if the density of a fluid increases with height the stratification is instable. The decrease of turbulent energy in a stable stratified flow leads to a transition from turbulent to laminar. The turbulence is suppressed by the outer forces (e.g. buoyancy force), which stabilizes the density gradient. Besides the Reynolds number Re also the Richardson number Ri is very important for such stable stratified flows. The Richardson number expresses the ratio of potential to kinetic energy and can be calculated as follows:

$$Ri = -\frac{g}{\rho} \cdot \frac{d\rho}{dy} \left(\frac{dU}{dy} \right)^{-2} \quad (6.1)$$

A stratified flow is supposed to be stable if the Ri number is greater than $1/4$ (see Durbin and Pettersson Reif (2001)) for negative buoyancy, although turbulence can exist for $Ri \simeq 0.15$, but it is completely absent when $Ri > 0.5$ (see Narasimha and Sreenivasan (1979)). For a horizontal plate flow a Ri number greater than $1/24$ indicates a stable boundary layer (see Schlichting and Gersten (1997)) .

Reversion in Highly Accelerated Flows

This mode is the most important mode occurring in turbomachinery. It is mostly driven by the pressure gradient over a surface. The effect of a low Reynolds number or outer forces is not as big as for the other two modes mentioned before. Relaminarisation due to highly accelerated flows occurs much faster than the reversion by dissipation. Mayle (1991) stated that the acceleration near the leading edge of the suction side of a turbine blade as well as the acceleration near the trailing edge of the pressure side is large enough to force the flow to become laminar or quasi-laminar, as for a flat plate with an adverse pressure gradient as shown in Fig. 6.2.

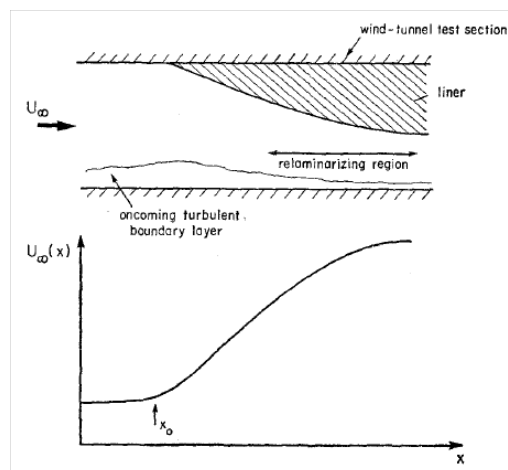


Figure 6.2.: Schematic diagram of relaminarisation in highly accelerated flows, from Sreenivasan (1982)

At the beginning only few experiments were done to investigate relaminarisation in highly accelerated flows. In most cases they were performed for compressible subsonic flows (see e.g. Kreskovsky et al. (1974)), whereas experiments nowadays are carried out more often at incompressible flow conditions (see e.g. Mukund et al. (2006), Bourassa et al. (2000), Ichimiya et al. (1998), Brandt (1993)) .

In this work and the referenced experiments (e.g. Brandt (1993), Nichtawitz (2009), Dorfer (2011)) relaminarisation by acceleration showed the highest importance.

Other modes

All other modes of relaminarisation are combinations of the first three modes. The author refers to the paper by Narasimha and Sreenivasan (1979) for more details.

6.2. Valuation Methods for Relaminarisation

The process of relaminarisation was described by Sreenivasan (1982). Fig. 6.3 shows the classification of the flow field in a nozzle, where flow relaminarises from turbulent to laminar and then again retransits to turbulent. The processes in Fig. 6.3 are summarized here briefly: The first step in the relaminarisation process (a) occurs at constant pressure. If the pressure starts decreasing smoothly, the flow becomes laminarescent at pressure changes between -0.005 and -0.015 . This region (b) can be interpreted as local equilibrium followed by the so called non-equilibrium region. Then the pressure decrease becomes almost linear (c) and it is known as the "onset of relaminarisation". In the following region the relaminarisation occurs until a value of $\lambda = 0(10^2)$, where the relaminarisation is complete. Finally the pressure drop decreases in the retransitional step until the pressure is again constant.

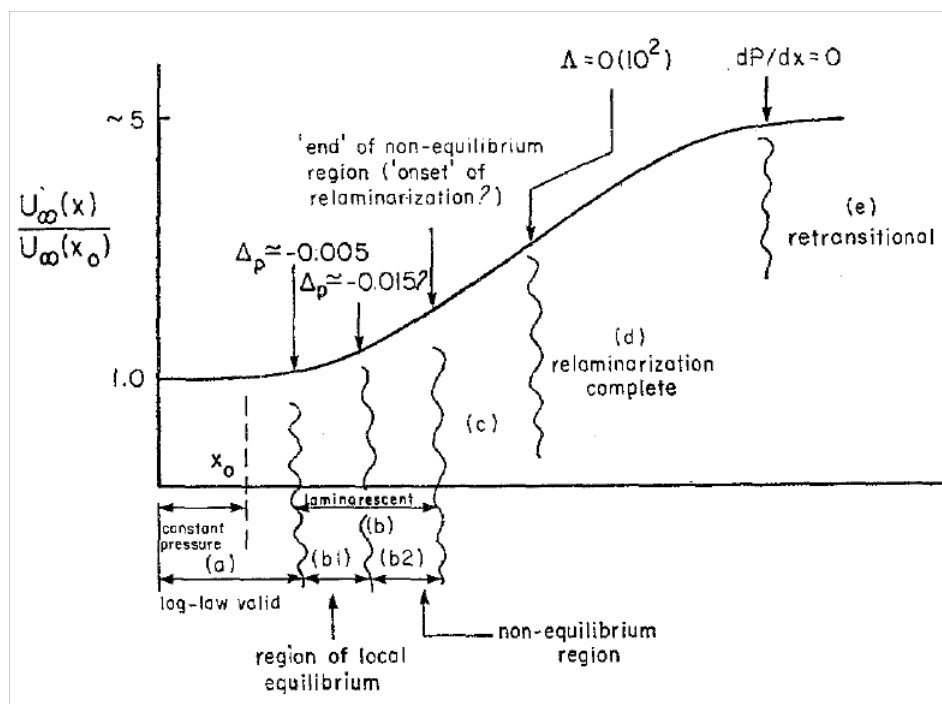


Figure 6.3.: Broad classification of the flow field into various regions, from Sreenivasan (1982)

Furthermore, Sreenivasan (1982) described the process of a turbulent boundary layer becoming again laminar due to acceleration by the following characteristics:

- boundary layer thickness decreases
- velocity profile changes to a Blasius profile (see Fig. 6.4)

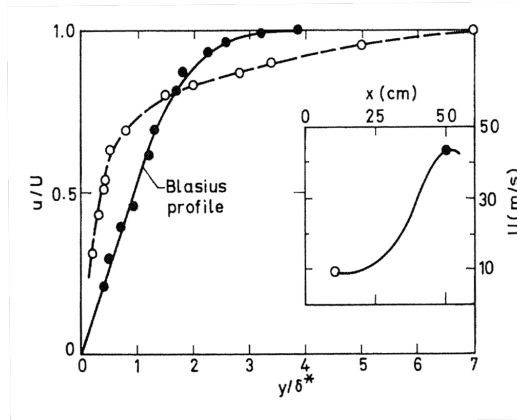


Figure 6.4.: Relaminarisation in an accelerated boundary layer just before and after acceleration, from Narasimha and Sreenivasan (1979)

- shape factor H_{12} (defined in eq. 6.2) rises after a slight decrease

$$H_{12} = \frac{\delta^*}{\theta} \quad (6.2)$$

where δ^* is the displacement thickness and θ is the momentum thickness

- skin friction coefficient c_f decreases strongly after rising for a short period
- heat transfer coefficient decreases
- turbulent intensity decreases
- Reynolds stresses near the wall decrease, whereas staying constant away from the wall

Mayle (1991) also concluded that the acceleration parameter is one of the most common indicators for relaminarisation. When the acceleration parameter K as given in eq. 6.3 is greater than a critical value of about $3 \cdot 10^{-6}$ relaminarisation can occur. But he stated that K is not a fixed critical value, because in some test cases relaminarisation occurred at smaller K -values.

$$K = \frac{v}{U^2} \frac{dU}{dx} \quad (6.3)$$

with U as the free-stream velocity, v as the kinematic viscosity and dU/dx as the velocity gradient in streamwise direction.

If the further acceleration after the relaminarisation is too small, the boundary layer can become turbulent again, so that transition back to turbulent can occur.

In the experiment at the Institute for Thermal Turbomachinery and Machine Dynamics at Graz University of Technology (see e.g. Fig. 6.5) the relaminarisation was described according to the *Valuation Methods for Relaminarisation* by describing the shape factor H_{12} , the acceleration parameter K and the boundary layer thickness δ .

6.3. Why is relaminarisation of interest?

The main reason for investigating relaminarisation were the results of the AIDA CFD calculations done with the SA turbulence model (described in Chapter 2.5.1). The SA turbulence model considers the tip gap effect (as described later in Paper 5), but it has some deficiencies predicting transition. These deficiencies are discussed in Paper 5 in detail, and as a consequence three new test cases were investigated to describe relaminarisation properly. The test cases TTMRelam, T100 and AIDA stator are discussed in detail in Chapters 6.5.1, 6.6 and 6.7 with respect to experimental and simulation results using the $\gamma - Re_\theta$ transition model.

First, pressure measurements at the inlet of the duct performed in the framework of AIDA project are presented here and compared with the corresponding unpublished simulations. Fig. 6.5 shows the comparison of CFD calculations using the SA turbulence model with experimental data from measurements of the total pressure distribution after the HP rotor (plane C) for two different tip gap heights.

In the experiment, the following characteristics was found: the experimental pressure reduced from a hub value of $p = 1.1$ bar with increasing passage height reaching a minimum at 0.3 relative passage height. Then the total pressure again increases to a value of $p = 1.1$ bar at 0.4 of relative passage height and further increases to higher values of maximal 1.15 bar at 0.5-0.7 relative passage height. Then the pressure again decreases at passage height of 0.8-0.9 to a value of 1.05 bar to further increase again at the maximum of passage height. Large differences are detected for the two gap heights.

The CFD simulation results show significant discrepancies to the experimental data, especially near the mid section but also at the hub. The calculations show a smaller pressure of approximately 0.05 bar in the relative passage height 0.4 - 0.7 as well as in the hub region with relative passage height 0-0.2.

A possible explanation for these pressure differences might be relaminarisation in the HP stator because of the large acceleration on the pressure side of the HP stator. The SA turbulence model simulates the flow along the whole blade as turbulent, and therefore the predicted total pressure might be lower than that of the experiments.

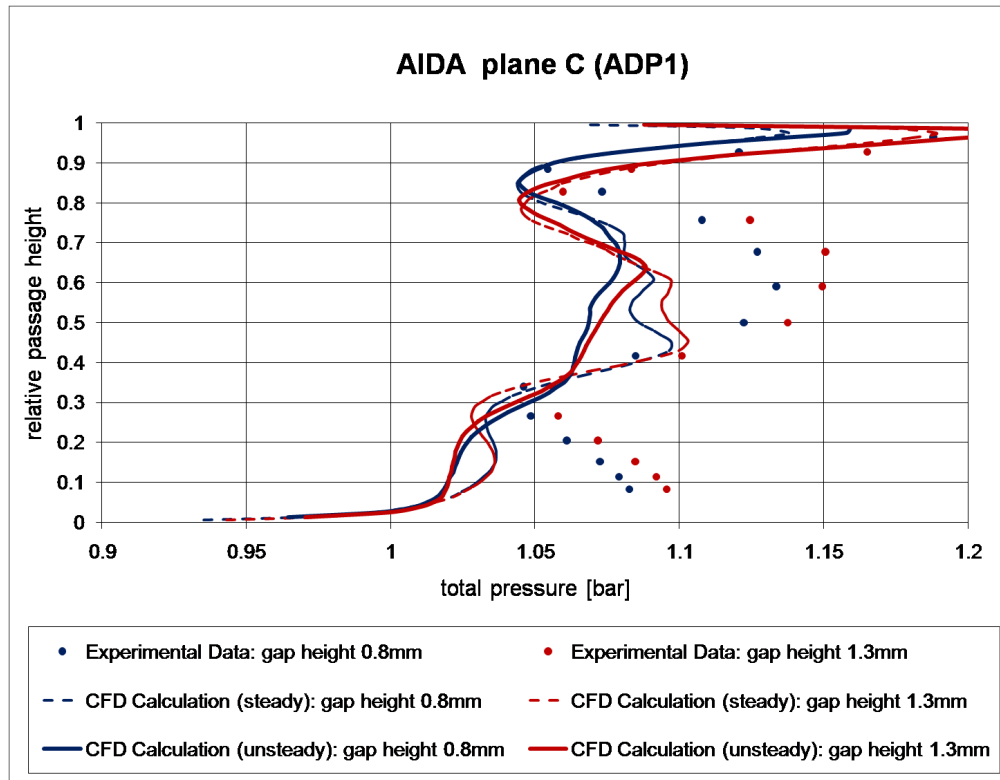


Figure 6.5.: AIDA: total pressure in plane C, comparison of CFD with experiments

To correct the shortcomings of the SA turbulence model regarding transition as also described in Paper 5 a more enhanced study on the topic relaminarisation, and especially on the application of the $\gamma - Re_\theta$ transition model to relaminarisation was necessary. For that purpose an in-house test case (TTMRelam) was designed where the pressure distribution of the AIDA HP stator, which is supposed to be the origin of the relaminarisation, should be imposed (see Chapter 6.5). The boundary layer was experimentally investigated with laser vibrometry and the experimental data are compared to the calculations using the $\gamma - Re_\theta$ transition model including the author's last correlation. Additionally a second 2D test case (T100) on relaminarisation will be presented in the ongoing chapter, where the CFD results are compared to the results of hot film measurements (see Chapter 6.6). Finally, the flow around the AIDA HP stator is investigated in more detail by applying the $\gamma - Re_\theta$ transition model (see Chapter 6.7).

6.4. Notes on Paper 5

Titel:	Numerical Investigation of the Effect of Tip Leakage Flow on an Aggressive S-Shaped Intermediate Turbine Duct.
Authors:	W.SANZ, M.E. KELTERER, R. PECNIK, A. MARN, E. GÖTTLICH
Published:	ASME paper GT2009-59535, Conference proceedings at the ASME Turbo Expo, Orlando, Florida, USA, 2009

Abstract

In Paper 5 a numerical investigation of the effect of the tip leakage flow on an aggressive S-shaped intermediate turbine duct (see *Fig. 1*) was carried out using the basic SA turbulence model. The flow was calculated for two different tip gap heights as also used in the experiments, as well as for zero tip gap. This investigation was done to get an idea of the influence of the tip gap on the downstream flow.

Results

The two different tip gap heights used in the experiments show quite similar results, therefore just the smaller tip gap is compared with the zero gap case. Comparing the radial distribution of the stage loading, it could be seen, that the loading in the shroud region of the zero gap case is higher than that of the small gap case (see *Fig. 3*). The reason can be found in the streamwise vorticity distribution in the plane right after the HP stage as explained by *Fig. 4*. There the tip gap vortex clearly influences the flow in the shroud region for the case with gap, whereas for the zero gap case this vortex does not exist. The radial Mach number distribution in planes after the HP stage is shown in *Figs. 9* and *10*; the tip gap flow energizes the boundary layer so that the flow can follow the outer duct wall much better (*Fig. 11*).

Except for the flow prediction on the outer duct casing in terms of the pressure rise coefficient (*Fig. 12*), the SA turbulence model shows good results.

Paper 5

W.Sanz, M.E. Kelterer, R. Pecnik, A. Marn, E. Göttlich

Numerical Investigation of the Effect of Tip Leakage Flow
on an Aggressive S-Shaped Intermediate Turbine Duct.

ASME paper GT2009-59535
presented at the ASME Turbo Expo
Orlando, USA, 2009

GT2009-59535

NUMERICAL INVESTIGATION OF THE EFFECT OF TIP LEAKAGE FLOW ON AN AGGRESSIVE S-SHAPED INTERMEDIATE TURBINE DUCT

W. Sanz, M. Kelterer, R. Pecnik¹, A. Marn, E. Göttlich

Institute for Thermal Turbomachinery and Machine Dynamics
 Graz University of Technology, Graz, Austria
 wolfgang.sanz@tugraz.at

ABSTRACT

The demand of a further increased bypass ratio of aero engines will lead to low pressure turbines with larger diameters which rotate at lower speed. Therefore, it is necessary to guide the flow leaving the high pressure turbine to the low pressure turbine at a larger diameter without any loss generating separation or flow disturbances. Due to costs and weight this intermediate turbine duct has to be as short as possible. This leads to an aggressive (high diffusion) S-shaped duct geometry. In order to investigate the influence of the blade tip gap height of a preceding rotor on such a high-diffusion duct flow a detailed measurement campaign in the Transonic Test Turbine Facility at Graz University of Technology has been performed.

A high diffusion intermediate duct is arranged downstream a high-pressure turbine stage providing an exit Mach number of about 0.6 and a swirl angle of -15 degrees (counter swirl). A low-pressure vane row is located at the end of the duct and represents the counter rotating low pressure turbine at larger diameter. At the ASME 2007, results of these investigations were presented for two different tip gap heights of 1.5 % span (0.8 mm) and 2.4 % span (1.3 mm).

In order to better understand the flow phenomena observed in the intermediate duct a detailed numerical study is conducted. The unsteady flow through the whole configuration is simulated for both gap heights as well as for a rotor with zero gap height. The unsteady data are compared at the stage exit and inside the duct to study the flow physics. The calculation of the zero gap height configuration allows to determine the influence of the tip leakage flow of the preceding rotor on the intermediate turbine duct. It turns out that for this aggressive duct the tip leakage flow has a very positive effect on the pressure recovery.

NOMENCLATURE

AR	[-]	area ratio
c_{ax}/u	[-]	flow coefficient
C	[mm]	chord length
h	[mm.]	average blade height
H	[kJ/kg]	total enthalpy
L	[m]	axial duct length
Ma	[-]	Mach number
p	[Pa]	pressure
t	[s]	Time, spacing
T	[s]	vane passing period
u	[m/s]	rotational speed
α	[deg]	yaw angle

Subscripts

ax	axial
t	total
C	measurement plane C
D	measurement plane D

Abbreviations

ITD	Intermediate Turbine Duct
LDV	Laser-Doppler-Velocimeter

INTRODUCTION

In dual-spool jet engines the low-pressure system has a much lower rotational speed and larger radius than the high-pressure core system. Therefore, S-shaped transition ducts are necessary to connect the large-diameter LP system to the small-diameter high-pressure (HP) system. Demands on improved efficiency and reduced noise levels lead to engines with very high by-pass ratios. This trend towards engines with large fans and small high-pressure-ratio cores gives larger radial differ-

¹ Current address: Center of Turbulence Research, Stanford University, Stanford, CA, USA.

ences and a need for more aggressive intermediate turbine ducts (ITD) to connect the different modules. It is obvious that high diffusing and shorter ducts can help to reduce length and weight of the engine significantly. It becomes clear that new duct designs are an enabling factor for future generations of efficient low-noise ultra-high-by-pass-ratio commercial jet engines.

One aim of the European project AIDA with many engine manufactures, research institutions and universities is to investigate the flow physics in aggressive intermediate turbine ducts and the interaction between the neighboring components in a detailed test arrangement under engine representative inlet conditions and to generate a unique database for CFD code verification. The flow field and interaction mechanisms that occur in low-aspect-ratio high-pressure turbine stages are highly three-dimensional due to rotating wakes as well as secondary and tip leakage flows. These flow structures have a significant downstream effect on the flow evolution within an intermediate turbine duct.

Some fundamental work has been performed to investigate the influence of non-rotating wakes (Dominy and Kirkham, [1]) and swirl (Dominy and Kirkham, [2]) on the performance of inter-turbine diffusers within an annular cascade test rig. Norris and Dominy [3] compared the diffusion of two duct geometries with different lengths. The research work has been continued by Dominy et al. [4] where the authors discuss data from experiments with and without an upstream turbine and compare them to computational predictions. First research work on the development of the exit flow from a transonic turbine stage within an interstage diffuser were published by Davis et al. [5], Miller et al. [6] and Miller et al. [7].

Within the AIDA project the influence of the tip leakage flow of a transonic high pressure turbine on the flow through a high diffusion S-shaped duct was investigated and results were published by Marn et al. [8] and Göttlich et al. [9] in 2007. They performed experimental investigations under engine representative conditions within the continuously operating Transonic Test Turbine Facility (TTTF) at Graz University of Technology for two different tip gap heights of 0.8 mm (1.5 % span) and 1.3 mm (2.4 % span). A strong influence of the tip clearance on the flow field within the entire duct was observed and a positive effect on the outer duct wall could be found. Based on these results the authors recommended to consider the whole configuration in a design process.

In order to better understand the observed flow phenomena a detailed numerical study is conducted in this work. The unsteady flow through transonic stage, intermediate duct and second stator is simulated for both gap heights as well as for a rotor with zero gap height. The unsteady and time-averaged data are compared between the different computations and with the measurement data in the duct and the flow physics leading to the observed differences in the duct are discussed. The calculation for zero gap height allows to clearly separate the influence of the tip leakage flow. Finally the efficiency of the whole system is evaluated and discussed.

EXPERIMENTAL SETUP

To investigate the flow physics in intermediate turbine ducts and the interaction between the neighboring components a detailed test arrangement under engine representative inlet conditions is necessary. Therefore the continuously operating Transonic Test Turbine Facility (TTTF) at Graz University of Technology has been adapted. Details of the test facility can be seen in Göttlich et al. [10]. The measurements are described in detail in [8, 9], so that only a short overview is given here.

AIDA Test Rig

Fig. 1 shows a meridional section of the TTTF together with the AIDA test rig. The aerodynamic blades and duct design was done by MTU Aero Engines. The flow direction is from left to right. The blade counts and the profiles are also given at the bottom. The incoming air is accelerated by the HP vanes in circumferential direction and impinges on the HP rotor with a cylindrical outer contour. The outer liner rings in the casing can be changed to investigate different rotor tip gaps. Then the flow is guided by the intermediate turbine duct to the vanes of a counter rotating LP turbine assembled at a larger radius. There it is accelerated again and turned in the opposite circumferential direction. A downstream deswirl turns the flow back and recovers some pressure. The air leaves the facility through a diffuser and the exhaust casing.

The HP and LP vanes are fitted into fully rotatable casings to change the relative position between vanes and the applied measurement system, which can be kept fixed in space during measurement. The deswirl is not rotatable and is always in the same position relative to the 5-hole probes (5HP). For probe measurements only one linear and one rotational axis is necessary to adjust the radial position and to turn the probe into the flow. The test rig allows probe measurements in seven different planes downstream the HP turbine, within the duct as well as upstream and downstream the LP vane (see Fig. 1a). Optical measurements by a 2D LDV were also performed in two different planes [9].

The main component of the test set-up is a high-diffusion duct mounted downstream of the transonic turbine stage. The inlet flow of the ITD can be described as strongly transient with periodically impinging wake structures from the passing rotor blades, three-dimensional and highly turbulent together with shocks extending from the blade trailing edges.

Table 1 explains the blading main parameters; there are 24 HP vanes and 36 rotor blades. The vanes of the downstream counter rotating low pressure turbine are mounted at the end of the ITD to provide an engine like radial mass flow distribution, which would be unrealistic without their blockage effect. The blade count of 48 was chosen to realise a blade count ratio of 2-3-4, which eases CFD modelling of this test arrangement.

The duct area ratio is approximately 1.5 and a non-dimensional duct length $L/h_{\text{exit,blade}}$ of 2 (see Fig. 1c) is used. This means that the designed duct geometry is well above the classical limit of length to change in area for a diffusing duct as defined in the classic limit by Sovran and Klomp [11]. In this paper this basic design of the ITD is numerically investigated.

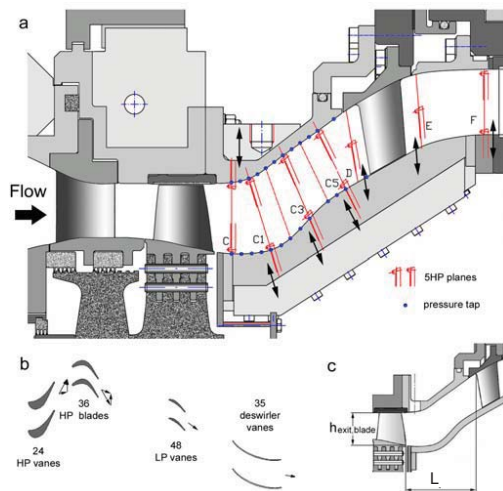


Fig. 1: (a) Meridional section with probe measurement planes, (b) Blade counts and profiles, (c) Definition of non dimensional duct length $L/h_{\text{exit,blade}} = 2$

Operating Conditions

At the design point of the applied HP turbine the stage pressure ratio is about 3.1 and the stage reaction based on the enthalpy is 0.46 (see Table 1). The stage pressure ratio, the total temperature at stage inlet and the speed, thus the corrected speed, were kept the same for both tip gap heights. This leads to a slightly different mass flow for both clearances. The blading has transonic conditions on the suction surface of the airfoils and at the exit of the blade rows. The turbine is choked for the whole operating area to be investigated. The mass averaged ITD inlet Mach number is adjusted to 0.6 and represents realistic duct inlet conditions of modern jet engines with a single stage HP turbine. The mass averaged inlet swirl angle is about -15 degrees measured from the engine axis. The Reynolds number level based on the chord length is here typically high and correlates with the HP turbine inlet pressure level and is in a similar range as for aero engines at take-off condition.

Instrumentation and Measurement Locations

Fig. 1a shows the probe measurement locations in the AIDA test rig. Full area traversing was performed in seven different planes: downstream the HP turbine (plane C), within the duct (planes C1, C3 and C5) as well as upstream (plane D) and downstream (planes E and F) the LP vane.

Furthermore, the rig is equipped with static pressure taps around the circumference of the inner and outer casing at the indicated measurement positions (see Fig. 1a) to get the pressure distribution along the flow path.

Table 1: Operating condition and blading parameters

Operating Point HP turbine				
mass flow	[kg/s]	15.9		
total temp. inlet	[K]	432		
total temp. exit	[K]	332		
total pressure inlet	[bar]	3.4		
$Ma_{\text{exit,absolute}}$	[-]	0.6		
α_{exit}	[deg]	-15		
stage pressure ratio	[-]	3.1		
power	[kW]	1590		
speed	[rpm]	11,000		
$\Delta H/u^2$	[-]	1.6		
c_{av}/u	[-]	0.64		
tip clearance	% span (mm)	1.5/2.4 (0.8/1.3)		
tip geometry	plenum type seals			
Parameter	HP vane	HP blade	ITD	LP vane
blade no.	24	36		48
t/C	0.89	0.76		0.88
C_{ax} (mm)	67.9	51		44.3
h_{exit} (mm)	47	58		63
h/C_{ax}	1.1	1.2		2.0
Re_c	$2 \cdot 10^6$	$1 \cdot 10^6$		$0.5 \cdot 10^6$
Ma_{inlet}	0.1	0.48	0.6	
Ma_{exit}	1.05	1.07		
α_{inlet}	0	34.4	-15	
α_{exit}	67.6	-57.2		-44.7
flow turning	67.6	91.6		

NUMERICAL METHOD

The computations were performed using the in-house Navier-Stokes code LINARS, developed at Graz University of Technology (Pecnik et al. [12], Pecnik and Sanz [13] and Pieringer et al. [14]).

The compressible Reynolds/Favre-averaged Navier-Stokes (RANS) equations are solved in conservative form by means of a fully-implicit time-marching finite-volume method on structured curvilinear grids in multiblock alignment. The inviscid (Euler) fluxes are discretized with the upwind flux-difference splitting method of Roe. In order to achieve a high order of spatial accuracy a total variation diminishing (TVD) scheme with third-order interpolation is applied to get the state vector at each cell interface. The viscous flux vector at the cell interfaces is constructed with a second-order accurate central-differencing scheme using Green's theorem. To obtain a linear set of the time dependent Navier-Stokes equations a Newton-Raphson procedure is applied for the discretization in time. The inviscid fluxes are treated with first order accuracy and the viscous fluxes with a thin-layer approximation to obtain a block-tridiagonal matrix for each grid index line. The resulting set of linear equations is solved by an alternating direction implicit (ADI) scheme coupled with the full-approximation-storage multigrid technique.

To save computational time and memory a pressure-gradient-sensitive wall-function based on the law-of-the-wall formulation by Spalding is used (Pieringer and Sanz [15]). The turbulence is calculated using the one equation turbulence

model of Spalart and Allmaras [16] which showed good results in previous numerical studies, e.g. [12-14].

For the unsteady calculations one stator passage, one rotor passage and two LP stator passages are modeled and phase-lagged boundary conditions based on the direct-store method [17] are imposed to cope with the unequal pitch ratios. 480 time steps with three Newton subiterations are used to model one blade passing period for the rotor and 320 time steps for the stator. About 40 000 time iterations are necessary to achieve a periodic convergent solution. This relatively large number of time steps is needed because of the complex interaction between the stage flow and the ITD.

The structured computational grid composed of 26 blocks is shown in Fig. 2. The geometrical details of the turbine stage containing all fillets, the rotor tip clearance and the clearance at the hub of the second vanes are modeled as well, with approximately 2.3 million cells. The number of grid cells is based on a grid independence study performed by Malzacher [18].

RESULTS AND DISCUSSION

For the numerical study the unsteady three-dimensional flow through the whole configuration consisting of first stator and rotor passage, ITD and second stator passage is simulated for a rotor blade tip gap height of 0 mm, 0.8 mm (1.5 % span) and 1.3 mm (2.4 % span). For the last two cases detailed measurements were performed, which were thoroughly discussed by Marn et al. [8] and Göttlich et al. [9]. For all cases the same radial pressure distribution from the measurements is imposed at the inlet. The overall pressure ratio is set to the same value of 4, which leads to a stage pressure ratio of about 3.1 for all three cases with slight differences depending on the pressure recovery in the ITD as discussed later.

Fig. 3 shows the radial distribution of the stage loading for the three cases investigated, which strongly varies along the blade height. For non-zero gap height the loading is the same in the lower part of the stage and differs slightly above 75 % span.

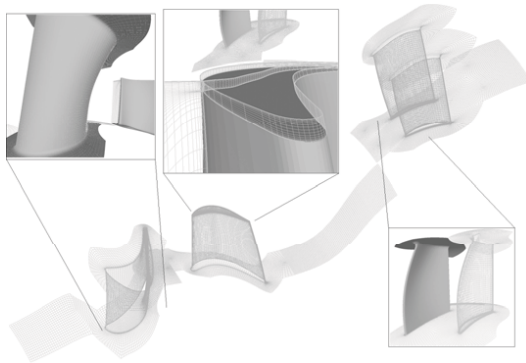


Fig. 2: Multiblock computational grid with details

There the loading is higher for the smaller gap height of 0.8 mm.

For zero gap height the loading is slightly smaller in the lower part of the stage due to a reduced stage pressure ratio there, but remarkably higher in the upper part of the stage because of the non-existing tip leakage flow.

The duct inlet is dominated by shocks emanating from the rotor blades, wakes and secondary flows all moving together in circumferential direction. In order to demonstrate the complex flow structure the simulated time-averaged streamwise vorticity distribution in plane C is shown in Fig. 4 for zero gap and 0.8 mm gap height. Additionally the streamlines through the vortical structures are depicted. Results for 1.3 mm gap height are very similar to 0.8 mm gap height and are not shown here.

Looking at the streamlines coming from pressure and suction side of the blade and running through the vortices "B" and "C", different radial flow angles can be observed at the rotor blade trailing edge. These opposite directed velocity components together with the shape of the bowed trailing edge cause a roll up of the flow after leaving the blade. Thus a pair of counter-rotating trailing edge streamwise shed vortices is evoked. This is consistent with the work of Pullan et al. [19] where this roll up of streamwise vorticity shed from a blade into one or more vortices was investigated.

Comparing both computational results one can see that the lower shed vortex "B" is approximately at the same radial location whereas the upper vortex "C" is slightly stronger and moved upwards in the zero-gap case because of the non-existing tip leakage flow.

In the lower half of the blade a pronounced passage vortex marked with "A" reaches upwards to nearly 50 % span for both cases. For zero gap height also a strong upper passage vortex "D" already merged with a scraping vortex generated by the moving endwall is observed. It reaches downwards to 75 % span. For 0.8 mm gap height the strong tip leakage vortex "E" dominates the flow in the outer endwall. It displaces the opposite rotating upper passage vortex downwards and reduces its strength (see [9]).

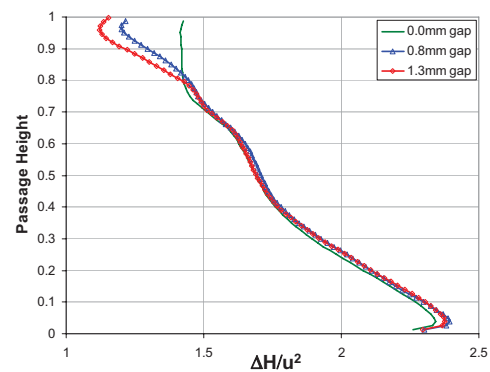


Fig. 3: Radial distribution of the stage loading

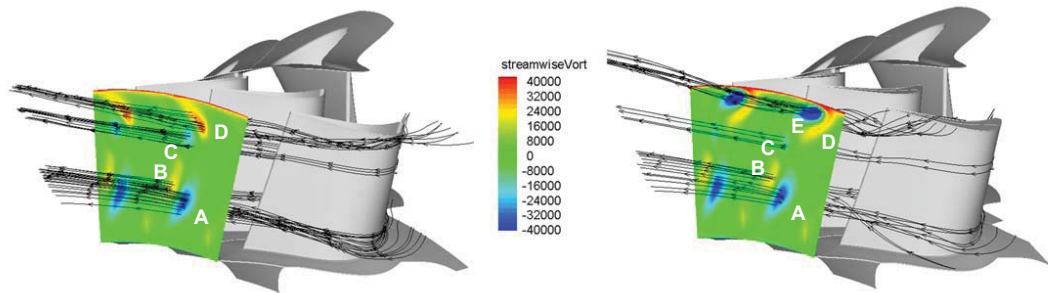


Fig. 4: Simulated streamwise vorticity distribution in plane C for zero gap and 0.8 mm gap height

The time-resolved streamwise vorticity is depicted in Figs. 5 – 8 for the planes C and C3 to show the influence of the nozzle guide vanes. The view is downstream in all figures (opposite to Fig. 4!), and moving with the rotor. From one to the next picture the rotor blades move 1.875 deg which corresponds to 1/8 of the stator blade passing period. After one cycle the rotor blade has passed one stator pitch.

Figs. 5 and 6 give a comparison of the unsteady vorticity distribution in plane C for zero gap and 0.8 mm gap height. The figures show the modulation of the vorticity distribution by the stator vanes. The vortices move up- and downwards and vary in their strength. The time evolution of the lower passage vortex “A” is very similar for both cases, although the vorticity is stronger for 0.8 mm gap height at all time instances. There is a slight interaction with the shed vortex “B”, as shown at $t/T=0.25$ by the change of the shape of vortex “A”. The shed vortex “B” behaves similar at all instances, its strength is again lower in the zero-gap case.

In the upper section of the channel the flow is dominated by the upper passage vortex for zero gap and by the tip leakage flow for 0.8 mm gap height. For zero gap height one can see that the core of the passage vortex “D” moves up- and downwards and changes its shape ($t/T=0.25$ vs. $t/T=0.75$ in Fig. 5). There is also an interaction between passage vortex and upper shed vortex “C” observable (see e.g. $t/T=0.75$).

During a period the formation and vanishing of a further vortex of the same direction of rotation can be seen (“F” in Fig. 5). This can be a scraping vortex originated from the moving endwall or a vortical structure emanating from the HP vane. During part of the period it merges with the upper passage vortex, whereas during the other part it forms as independent vortex of relatively large radial extent. It seems that the slight radial moving of the upper shed vortex “C” causes this phenomenon.

For 0.8 mm gap height there is a strong interaction between upper passage vortex “D” and tip leakage vortex “E”. Whereas the strength of the tip leakage vortex remains nearly unchanged, the passage vortex varies in strength and extent ($t/T=0$ vs. $t/T=0.75$ in Fig. 6). The upper shed vortex “C” moves slightly upwards and downwards and seems to merge with the tip leakage vortex at some instances (e.g. $t/T=0$). The

entropy contours in plane C (not shown here) indicate that the tip leakage flow is the dominant loss source.

These vortex structures are transported downstream through the ITD and loose their strength. Figs. 7 and 8 show the unsteady vorticity distribution for zero gap and 0.8 mm gap height in plane C3 where the inner duct contour changes its curvature (see Fig. 1). In the lower duct section the vortex structure remains nearly unchanged during a period for both cases. The inclined contours (marked by “G”) indicate that the trailing edge flow is turned in circumferential direction as a consequence of the radial variation of the yaw angle at the stage exit, which varies between -35 deg at the hub and 0 deg at the tip.

For zero gap there is only positive vorticity in the upper section, slight variations during a period indicate that there is still an influence from the stator blades. The vorticity in the endwall boundary layer is relatively low, indicating a small velocity gradient there and thus a boundary layer, which is close to separation. For 0.8 mm gap height the vorticity in the endwall boundary layer is much higher. In the endwall region there is a large zone of negative vorticity coming from the tip leakage flow. During a period this zone is stretched and nearly merges with the neighboring zone ($t/T=0.5$). Comparing the Figs. 5 to 8 one can see that the region influenced by the existence of the tip leakage vortex increases remarkably from plane C to C3 and comprises nearly a third of the flow channel.

The significant influence of the tip leakage vortex can also be seen in the relative Mach number distribution shown in Fig. 9. The shock position is marked by the dashed lines. For zero gap the shock emanating from the rotor extends from the hub to the tip in plane C with the strongest shock in the tip region. For 0.8 mm gap height the shock structure is very similar up to 75 % span, although it is differently inclined. But from there on the tip leakage flow dominates the Mach number distribution and no shock occurs in the tip region. The pressure gradients caused by the relative shock system propagates through the ITD. In plane C1 where the flow is turned in radial direction the shock systems can still be seen in the whole flow channel for zero gap. In plane C3 the shocks are still present in the tip region for zero gap, whereas the tip leakage flow is identifiable by the zones of low Mach number for 0.8 mm gap height.

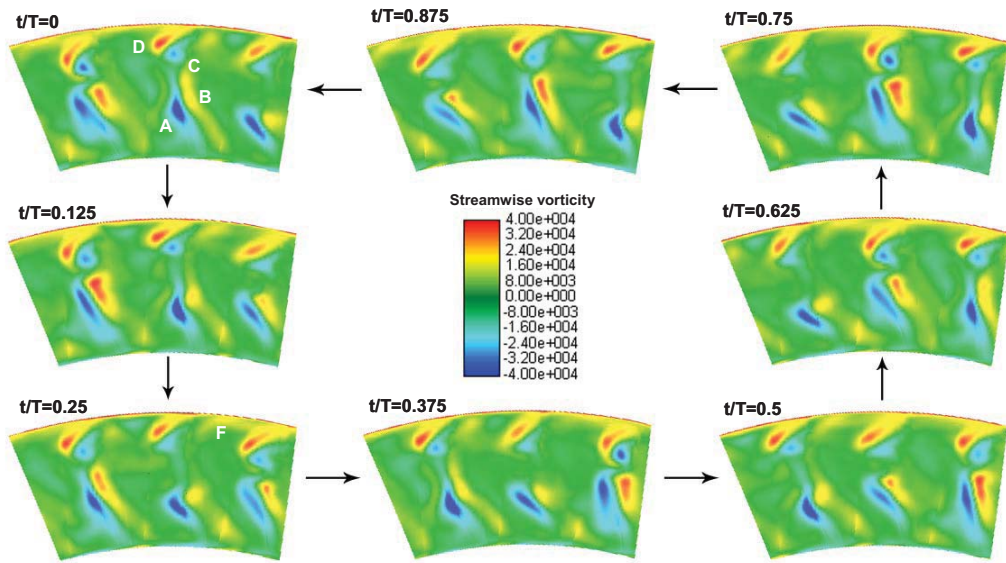


Fig. 5: Time-resolved streamwise vorticity distribution in plane C for zero gap (looking downstream)

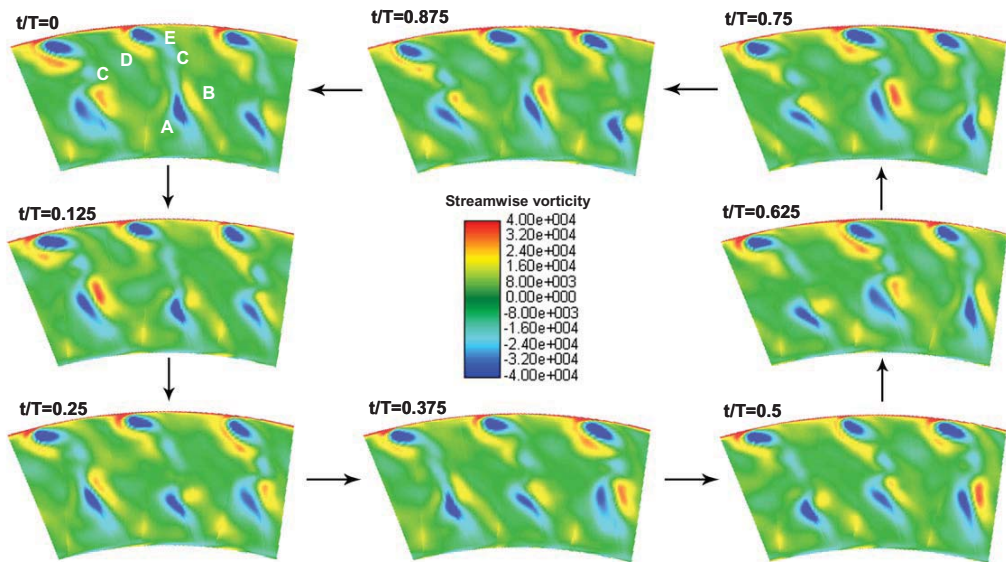


Fig. 6: Time-resolved streamwise vorticity distribution in plane C for 0.8 mm gap height (looking downstream)

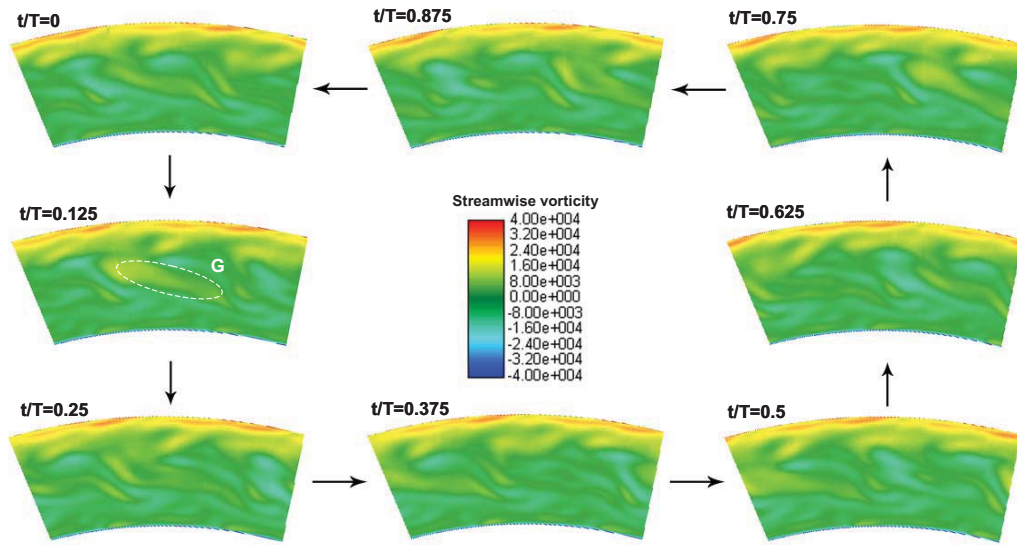


Fig. 7: Time-resolved streamwise vorticity distribution in plane C3 for zero gap (looking downstream)

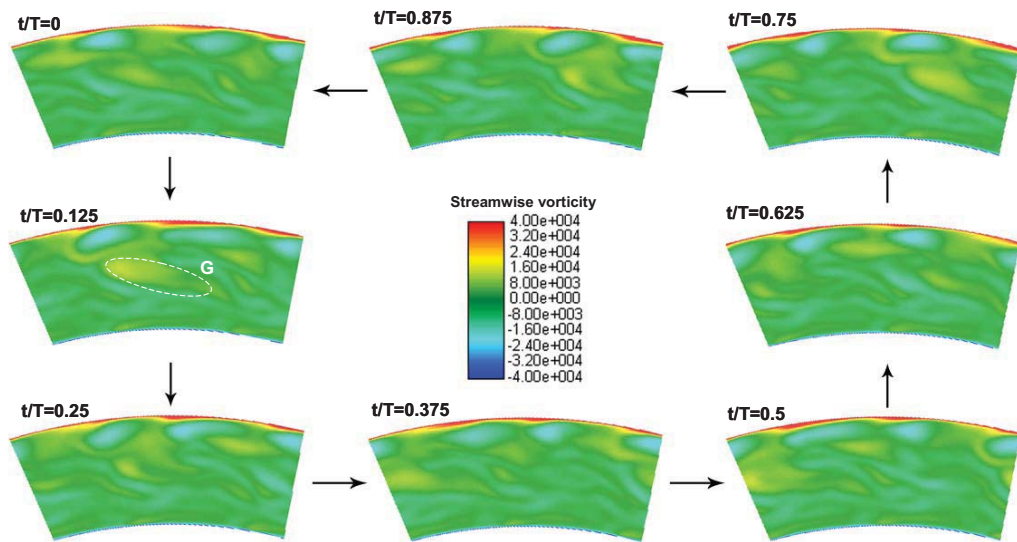


Fig. 8: Time-resolved streamwise vorticity distribution in plane C3 for 0.8 mm gap height (looking downstream)

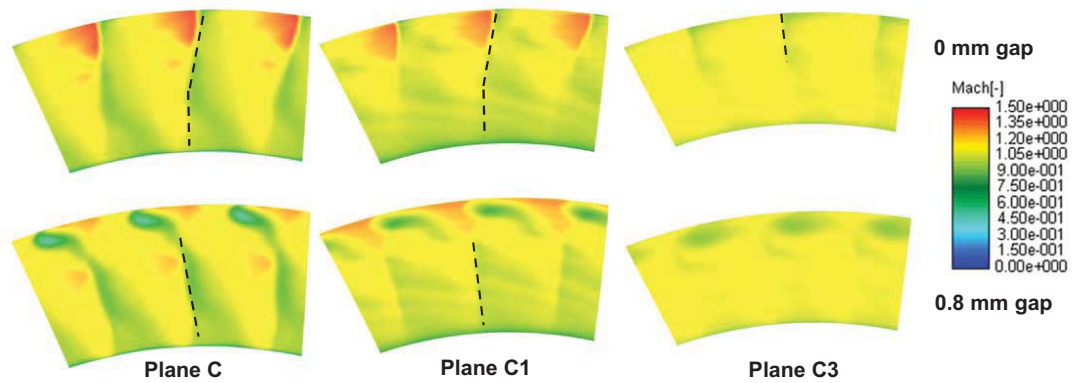


Fig. 9: Relative Mach number distribution in planes C, C1 and C3 (looking in streamwise direction)

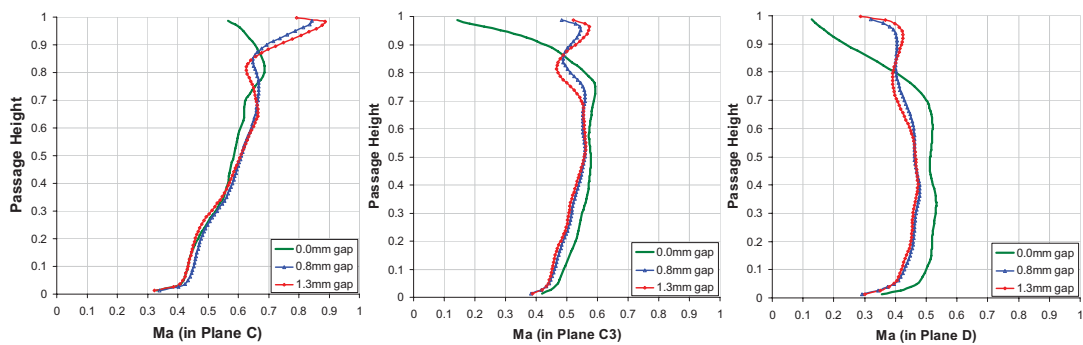


Fig. 10: Radial Mach number distribution in planes C, C3 and D

Fig. 10 shows the radial distribution of the time-averaged circumferentially-averaged Mach number at duct entry, in the midspan of duct and at duct exit (planes C, C3 and D). In plane C the tip leakage flow generates a jet of high velocity close to the endwall. It is followed by a region of lower velocity caused by the tip leakage vortex at a span height of about 80 %. It accelerates again up to $M=0.65$, before it gradually decreases to $M=0.3$. The peak Mach number is slightly higher and the local minimum is slightly smaller for the larger gap height. It is interesting to note that the Mach number contours start to deviate at about 40 % span indicating the wide influence of the tip leakage flow by redistributing the flow in the whole blade row. For zero gap the Mach number increases up to 80 % span where it reaches its maximum $M=0.65$. From there on it decreases to $M=0.55$ at the tip. This is caused by the blade profile there, which is designed to counteract the negative influence of tip leakage flow and leads to a higher loading in the endwall region as shown in Fig. 3.

In plane C3 a change in curvature takes place at the inner casing and the transition from a strong curved to a linear wall at the outer casing. For the two cases with gap the flow velocity remains nearly constant in the hub region from plane C to C3. In the outer region the flow is decelerated due to the increase in flow area there. Again the minimum and maximum in Mach number are more strongly pronounced for the larger gap height. For the zero gap the Mach number decreases remarkably in the outer region with a minimum of 0.15 close to the outer wall. The flow is not able to fill out the increased flow area there because of the low energetic tip flow at the inlet plane C. On the other hand, the Mach number at midspan and hub section is higher than for the cases with gap due to conservation of mass flow. From plane C3 to the duct exit at plane D the flow is decelerated and the trend for the zero-gap flow continues. The region of low velocity further increases, the minimum Mach is about 0.12. The Mach number at midspan and hub is nearly constant at 0.52 compared to about 0.46 for the cases with gap.

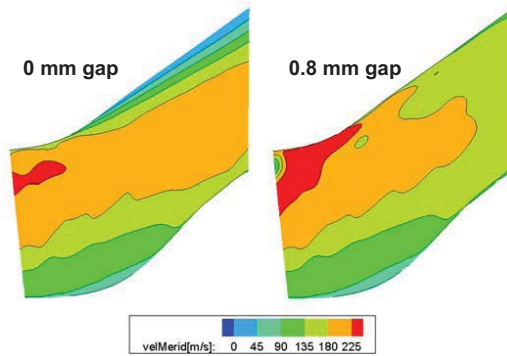


Fig. 11: Meridional velocity distribution in ITD for zero and 0.8 mm gap

For both gap heights the trend is very similar up to about 60 % span. From there on the difference in gap height leads to smaller minimum and larger maximum in Mach number for the larger gap height showing again the wide influence of the tip leakage flow.

The velocity in a meridional duct section also shows these observed differences in duct flow between zero gap and 0.8 mm gap height (see Fig. 11). For zero gap the flow is not able to follow completely the convex contour at the outer wall (at about plane C). The outer duct region is taken by stagnant fluid, so that the effective increase in flow area is smaller than designed and the main flow is less decelerated. On the other hand the tip leakage flow energizes the outer flow so that it can follow the strong curvature in plane C1.

This energizing is probably based on two effects: Firstly, the high energetic wall jet acts similar to the (unsteady) injection of high energetic fluid. This wall jet energises the outer duct boundary layer and minimises the risk of separation there. Secondly, the tip leakage vortex works as the vortex shed from a vortex generator. Due to the rotation higher energetic fluid from the mean flow is transported into or towards the casing boundary layer and low energy fluid is transported away from it. The mixing process is enhanced but the stronger the tip leakage vortex the higher the mixing losses [20].

The whole flow area is filled out up to the duct exit leading to higher deceleration and thus a better pressure recovery.

Fig. 12 shows the pressure distribution along the duct by means of the pressure rise coefficient, which is defined as

$$C_{pn} = (p_n - p_C) / (p_{t,C} - p_C) \quad (1)$$

where p_n is the local static pressure, p_C the area averaged static pressure in plane C and $p_{t,C}$ the mass averaged total pressure in plane C.

For both gaps the principal trend is very similar. The minimum static pressure at the outer wall is detected in plane C1 after the first bend where the flow is accelerated. From there on the pressure continuously increases. At the inner wall the maximum static pressure is found at a duct length x/L of about 0.46

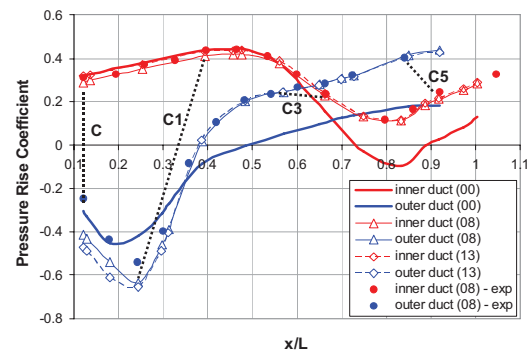


Fig. 12: Pressure rise coefficient at the inner and outer wall of the ITD (numerical and experimental values)

downstream of plane C1. Between C3 and C5 a distinct minimum occurs right after the change in curvature at the inner wall. There for 0.8 mm gap height the static pressure is slightly smaller up to plane C3. The comparison with measurement data shows a good agreement and confirms the reliability of the numerical investigation, although there are differences between the experiments and the computation for the outer duct wall for $x/L < 0.25$. These differences are partly caused by a larger measurement error at the beginning of the duct due to the high flow unsteadiness there.

For zero gap the pressure recovery behaviour is quite different. At the outer wall it starts with a higher static pressure and a smaller velocity (see Fig. 11) at plane C and accelerates around the first bend. Because of the lower dynamic pressure and since the flow is not able to follow the inner contour completely, the pressure minimum is less pronounced and occurs slightly earlier. From there on the pressure increases and ends significantly lower than for the duct flow with gap. The higher velocities outside the stagnant endwall flow and local zones of separated flow (not shown here) cause the lower pressure recovery. At the inner contour the trend is similar to the cases with gap up to nearly plane C3. From there on the pressure recovery is smaller due to the higher velocities at hub and midspan section as described above.

Estimation of efficiencies and losses

In order to evaluate the efficiency of the whole configuration consisting of the first stage and the ITD and to estimate the quality of the ITD following quantities are calculated and listed in Table 2:

- Stage total pressure ratio Π
- Stage loading coefficient H_{st}

$$H_{st} = \Delta H / u^2 \quad (2)$$

- Total isentropic stage efficiency η_{st} between plane A and C, calculated with the total values

- Total configuration efficiency η_{conf} between plane A and D, calculated with the total values
- ITD diffuser efficiency η_{ITD} as the ratio between the static pressure recovery and the ideal one for incompressible flow [11]

$$\eta_{\text{ITD}} = \frac{P_D - P_C}{(P_{t,C} - P_C)(1 - 1/AR^2)} \quad (3)$$

- ITD total pressure loss coefficient ω_{ITD}

$$\omega_{\text{ITD}} = \frac{P_{t,C} - P_{t,D}}{P_{t,C}} \quad (4)$$

Looking at the stage efficiency, the configuration with zero rotor gap has – as expected – the highest efficiency of 93.2 % due to the additional work generated in the tip region (see also Fig. 3). With increasing rotor tip gap height the efficiency decreases considerably (90.5 % and 89.3 %, respectively). It is only 33.5 % and thus much lower than for the cases with gap (67.4 % and 67 %, respectively), again showing the positive effect of the tip leakage flow on the flow in an aggressive ITD. The smaller recovery coefficient also leads to a slightly smaller stage pressure ratio for the zero gap case for the same overall pressure ratio. But despite this lower pressure ratio the total stage loading is still higher for the zero gap case because of a remarkably higher stage efficiency by 1.7 and 2.9 %-points, respectively. As a consequence the efficiency of the whole configuration (HP stage and ITD) is remarkably higher for the zero-gap case, and decreases with increasing gap height. The total pressure loss coefficient shows similar losses for the zero-gap and the 0.8 mm gap case. The losses generated by the stagnant flow at the outer wall for zero gap are balanced by losses generated by the tip leakage flow for 0.8 mm gap height. The increased gap height of 1.3 mm leads to a significant loss increase in the duct compared to 0.8 mm gap height.

It is important to remark that this loss evaluation does not consider that for the zero-gap case the inlet profile to the succeeding LP stage has a significant deficiency in the hub region (see Fig. 10, plane D) which will negatively influence the flow there.

Table 2: Efficiency and losses for stage and duct flow

	Zero gap	0.8 mm gap	1.3 mm gap
Π	3.08	3.15	3.12
H_{st}	1.72	1.70	1.66
η_{st}	93.2%	90.5%	89.3%
η_{conf}	91.6%	88.9%	87.2%
η_{ITD}	33.5%	67.4%	67.0%
ω_{ITD}	1.97%	2.01%	2.66%

CONCLUSIONS

At Graz University of Technology detailed measurements of the flow behavior of an S-shaped ITD after a HP turbine have been performed. Based on these measurements in an unsteady numerical study the flow in the ITD is investigated for zero, 0.8 mm and 1.3 mm rotor blade gap height.

The unsteady vorticity distribution at stage exit and in the midspan of the ITD shows the secondary flow systems evolving. In the upper region the tip leakage flow dominates the flow field and provides a high-energetic jet, which guides the flow around the first bend in the outer wall. As a consequence, the flow follows the increase in the flow area and achieves a good pressure recovery. On the other hand, the non-existence of a tip leakage flow leads to stagnant flow in the outer region and thus a worse pressure recovery. Although the tip leakage flow affects only 20 % span at duct inlet it causes a different flow behavior over an increased part of the channel height in the more downstream sections of the transition duct.

Looking at the efficiency of the whole configuration (HP stage and ITD), the zero-gap case still exhibits the best values, since the worse flow behavior in the duct is counteracted by the reduced losses due to the non-existence of the rotor blade gap. An increase in gap height quickly results in higher losses.

It can be concluded from this study that the tip leakage flow of a preceding stage has a positive influence on the ITD flow despite its eventual losses and that it has to be considered in the design of aggressive S-shaped ducts.

ACKNOWLEDGMENTS

This work was partly made possible by the European Union (EU) within the project AST3-CT-2003-502836, AIDA “Aggressive Intermediate Duct Aerodynamics” and the Austrian Federal Ministry for Education, Science and Culture (BMBWK). Also the support by the Austrian Federal Ministry of Transport, Innovation and Technology (BMVIT) within the Austrian Aviation Program “TAKE OFF” for the project “CFD-Trans” is gratefully acknowledged.

REFERENCES

- [1] Dominy, R. G., and Kirkham, D. A., 1996, “The Influence of Blade Wakes on the Performance of Inter-Turbine Diffusers,” *ASME J. Turbomach.*, **118**, pp. 347-352.
- [2] Dominy, R. G., and Kirkham, D. A., 1995, “The Influence of Swirl on the Performance of Inter-Turbine Diffusers,” *VDI Berichte* **1186**, pp. 107-122.
- [3] Norris, G., and Dominy, R. G., 1997, “Diffusion Rate Influences in Inter-Turbine Diffusers,” *IMEchE J. of Power and Energy*, **211** Part A, pp. 235-242.
- [4] Dominy, R. G., Kirkham, D. A., and Smith, A. D., 1998, “Flow Development Through Inter-Turbine Diffusers,” *ASME J. Turbomach.*, **120**, pp. 298-304.
- [5] Davis, R. L., Yao, J., Clark, J. P., Stetson, G., Alonso, J. J., Jameson, A., Haldeman, C. W., and Dunn, M. G., 2002, “Unsteady Interaction between a Transonic Turbine Stage and Downstream Components,” *ASME Paper No. GT-*

- 2002-30364, ASME Turbo Expo 2002, Amsterdam, The Netherlands
- [6] Miller, R. J., Moss, R. W., Ainsworth, R. W., and Harvey, N. W., 2003, "The Development of Turbine Exit Flow in a Swan-Necked Inter-Stage Diffuser," ASME Paper No. GT2003-38174, ASME Turbo Expo 2003, Atlanta, USA
- [7] Miller, R. J., Moss, R. W., Ainsworth, R. W., and Harvey, N. W., 2004, "The Effect of an Upstream Turbine on a Low-Aspect Ratio Vane," ASME Paper No. GT2004-54017, ASME Turbo Expo 2004, Vienna, Austria
- [8] Marn, A., Göttlich, E., Pecnik, R., Malzacher, F. J., Schennach, O., and Pirker, H. P., 2007, "The Influence of Blade Tip Gap Variation on the Flow Through an Aggressive S-Shaped Intermediate Turbine Duct Downstream a Transonic Turbine Stage - Part I: Time-Averaged Results," ASME Paper No. GT2007-27405, ASME Turbo Expo 2007, Montreal, Canada.
- [9] Göttlich, E., Marn, A., Pecnik, R., Malzacher, F. J., Schennach, O., and Pirker, H. P., 2007, "The Influence of Blade Tip Gap Variation on the Flow Through an Aggressive S-Shaped Intermediate Turbine Duct Downstream a Transonic Turbine Stage - Part II: Time-Resolved Results and Surface Flow," ASME Paper No. GT2007-28069, ASME Turbo Expo 2007, Montreal, Canada
- [10] Göttlich, E., Malzacher, F. J., Heitmeir F. J., Marn A., 2005, "Adaptation of a Transonic Test Turbine Facility for Experimental Investigation of Aggressive Intermediate Turbine Duct Flows", AIAA Paper No. ISABE-2005-1132.
- [11] Sovran, and G., Klomp, E. D., 1967, "Experimentally Determined Optimum Geometries for Rectilinear Diffusers with Rectangular Conical or Annular Cross Section," in Fluid Mechanics of Internal Flow (G. Sovran, ed.), Elsevier.
- [12] Pecnik, R., Pieringer, P., and Sanz, W., 2004, "Numerical Investigation of the Secondary flow of a Transonic Turbine Stage Using Various Turbulence Closures," ASME Paper No. GT2005-68754, ASME Turbo Expo 2004, Vienna, Austria
- [13] Pecnik, R., and Sanz, W., 2006, "Application of the Turbulent Potential Model to Heat Transfer Predictions on a Turbine Guide Vane", ASME Paper No. GT2006-90365, ASME Turbo Expo 2006, Barcelona, Spain
- [14] Pieringer P., Göttlich E., Woisetschläger J., Sanz, W., and Heitmeir F., 2005, "Numerical Investigation of the Unsteady Flow through a Transonic Turbine Stage Using an Innovative Flow Solver," Proceedings 6th European Conference on Turbomachinery, Lille, France, pp. 339-352.
- [15] Pieringer, P., and Sanz, W., 2005, "A Pressure Gradient Sensitive Wall Function for the Prediction of Turbulent Flow in Thermal Turbomachinery," ASME Paper No. GT2005-68471, ASME Turbo Expo 2005, Reno-Lake Tahoe, USA
- [16] Spalart, P.R., Allmaras, S.R., 1994, "A One-Equation Turbulence Model for Aerodynamic Flows", La Recherche Aerospaciale, No. 1, 5-21
- [17] Pieringer, P., 2008, "Methods for Unsteady Flow Calculations in Thermal Turbomachinery" (in German), Doctoral Thesis, Graz University of Technology
- [18] Malzacher, F., 2006, Sixth Framework Programm Priority 4 Aeronautics and Space, Aggressive Intermediate Duct Aerodynamics for Competitive & Environmentally Friendly Jet Engines, Project Acronym AIDA, Deliverable 2.3 Parameter Study Report MTU Part, Munich, Germany.
- [19] Pullan, G., Denton, J., and Dunkley, M., 2003, "An Experimental and Computational Study of the Formation of a Streamwise Shed Vortex in a Turbine Stage," ASME J. Turbomach., **125**, pp. 291-297.
- [20] Marn, A., 2008, "On the Aerodynamics of Aggressive Intermediate Turbine Ducts for Competitive and Environmentally Friendly Jet Engines", Doctoral Thesis, Graz University of Technology

6.5. Validation of the Relaminarisation Test Case TTMRelam

In the literature only few well documented relaminarisation test cases can be found. Therefore an in-house test case, called "TTMRelam", was designed and investigated in the wind tunnel of the Institute for Thermal Turbomachinery and Machine Dynamics within the Diploma Thesis by Dorfer (2011). The in-house test case TTMRelam was chosen as the first test case for the application of the $\gamma - Re_\theta$ transition model on relaminarisation using the latest in-house correlation as described in Chapter 5.

6.5.1. Testcase Description: TTMRelam

In the test case TTMRelam a pressure gradient similar to the pressure gradient of the HP turbine stator of the AIDA test rig (see Fig. 6.6) is applied to a flat plate. The circle in the figure shows the location of the high pressure stator in the test rig. The geometry of the TTMRelam test section was originally designed to exactly reproduce the pressure gradient occurring in the mid section of the AIDA HP turbine stator, but due to strength reasons a lower pressure level was necessary for the rig tests. The design of the geometry was done with CFD by calculating different counter contours. Fig. 6.7 shows the measurement section of the test case in the transonic wind tunnel. The experimental setup as well as the coordinates used in the calculation results are schematically depicted in Fig. 6.8. The plate in front of the actual test rig insert was built to ensure the flow being turbulent before the counter contour starts to contract. The origin of the x-coordinate is set to the starting point of the counter-contour contraction.

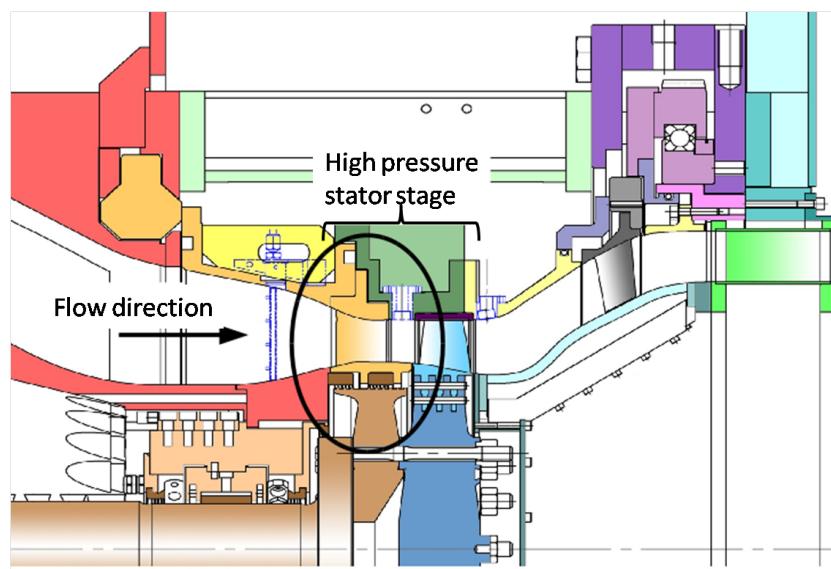


Figure 6.6.: AIDA test turbine with HP turbine stage

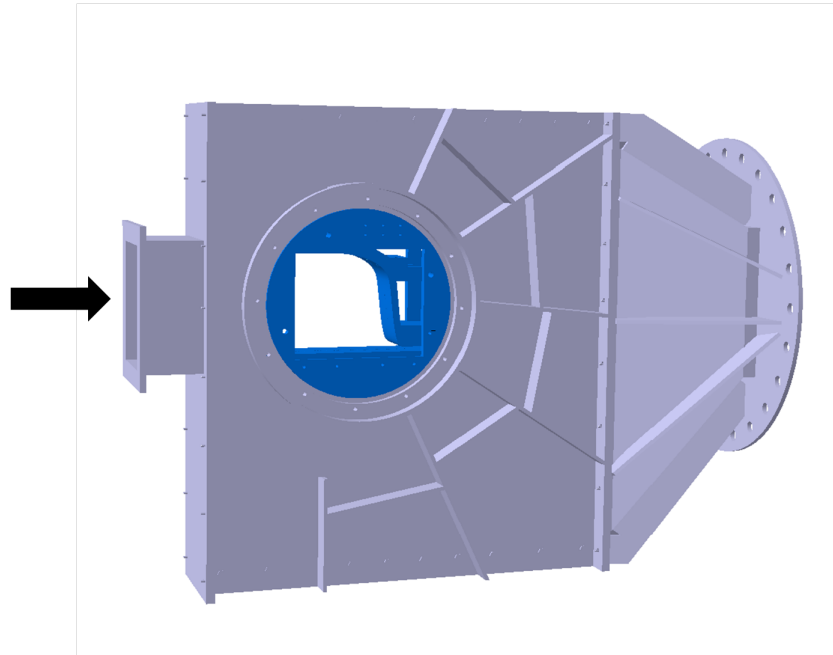


Figure 6.7.: TTMRelam measurement section in the transonic wind tunnel, from Dorfer (2011)

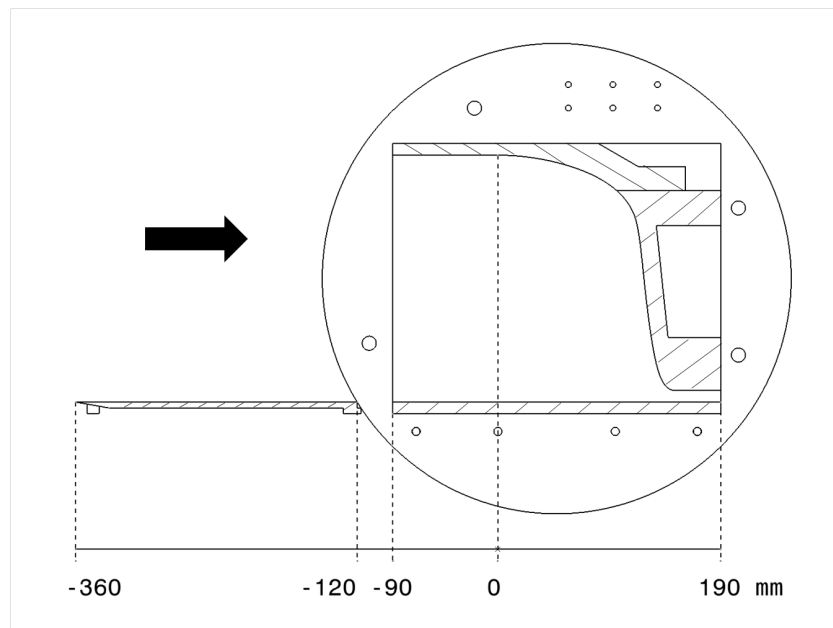


Figure 6.8.: TTMRelam measurement setup, from Dorfer (2011)

Fig. 6.9 shows the main principle of measuring density fluctuations with a laser vibrometer. Originally the laser vibrometer (LV) was developed to measure surface vibrations. The main principle of the laser vibrometer is the interferometry, that describes the superposition of waves. A laser light has the ability to superpose or to annihilate, depending on the relative phase of two laser beams. The laser produces a laser beam, that is divided into two parts. The first beam (object beam) goes through the measurement area and gets reflected back to the laser vibrometer. The second beam is the reference beam in the laser vibrometer. Due to density fluctuations in the measurement area the refraction index changes and that leads to different optical path lengths. A changing optical path length results in a changing runtime of the object beam, and furthermore a phase shift to the reference beam. The laser can detect a changing optical path length up to the laser wave length. To detect the inversion of the direction a bragg cell is used. The intensity change is detected by a photo detector that converts this intensity change into a voltage signal. This voltage signal is conform with a time signal, that can be transformed in a frequency spectrum using a Fast Fourier Transformation method. The laser vibrometer provides an integral signal throughout the whole measurement area (laser beam track).

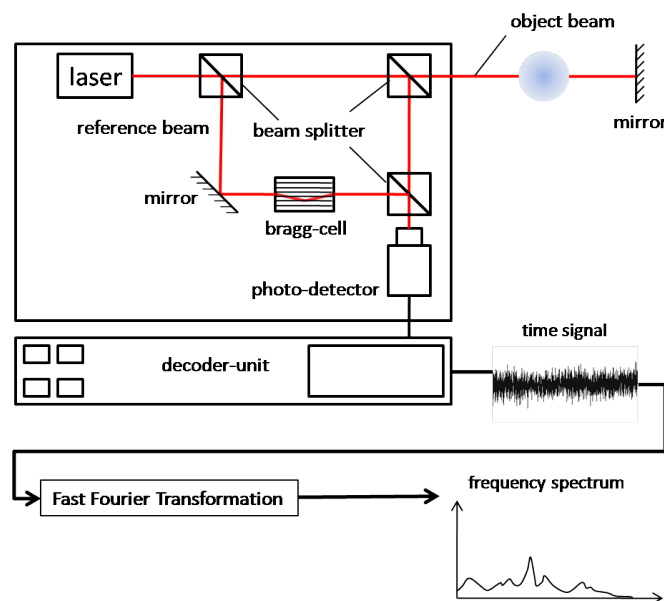


Figure 6.9.: Laser vibrometer design, from Köberl (2011)

In Fig. 6.10 the different possible positions of the laser vibrometer measurements are shown. The point of origin is located (as already described in Fig. 6.8) where the counter wall starts to contract. The laser beams was adjusted to be as close as possible to the wall. Only the data of the scanning laser vibrometer are shown in the experimental results.

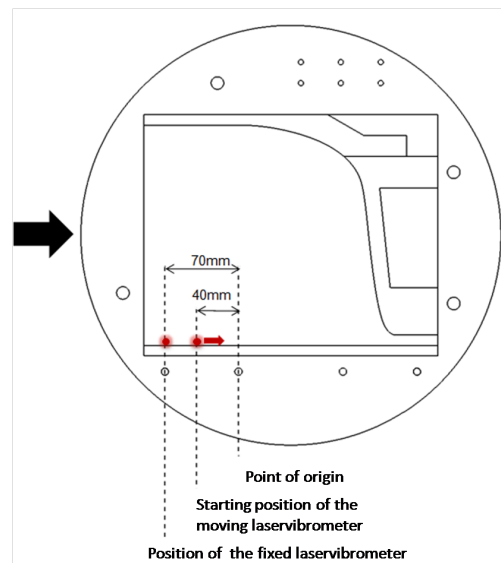


Figure 6.10.: TTMRelam: LV measurement positions, from Dorfer (2011)

6.5.2. Experimental Results: TTMRelam

Fig. 6.11 shows an experimental result displaying the power spectrum of the scanning laser vibrometer for all measured positions along the plate with the point of origin at the position 40 mm. The spectrum shows that the amplitude level is much higher at the point of origin than downstream. This leads to the assumption, that the flow at

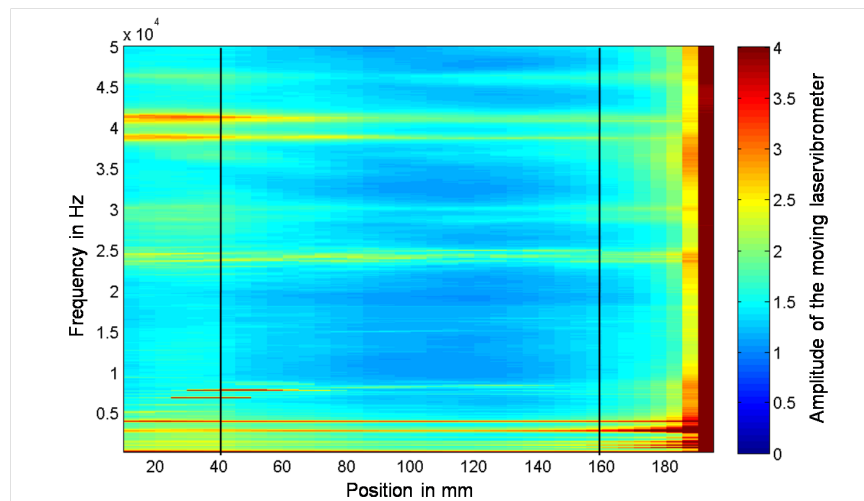


Figure 6.11.: TTMRelam power spectrum of scanning LV, from Dorfer (2011)

$x = 40$ mm is turbulent, then it relaminarises, before getting turbulent again after $x = 160$ mm, where the amplitudes again rise over the whole frequency range. More measurement details and results can be found in Dorfer (2011).

6.5.3. Calculation Results: TTMRelam

The following chapter presents the calculation results applying the $\gamma - Re_\theta$ transition model with the latest in-house correlation (see Chapter 5) to the TTMRelam test case. The boundary conditions for the calculations are displayed in Table 6.1 . The calculation grid used for this test case is shown in Fig. 6.12.

inlet total pressure $p_{totInlet}$	1.295 bar
inlet total temperature $T_{totInlet}$	323.0 K
inlet free-stream turbulent intensity FSTI	1.0 %
outlet static pressure $p_{statOutlet}$	0.972 bar

Table 6.1.: TTMRelam: Boundary conditions for the calculation

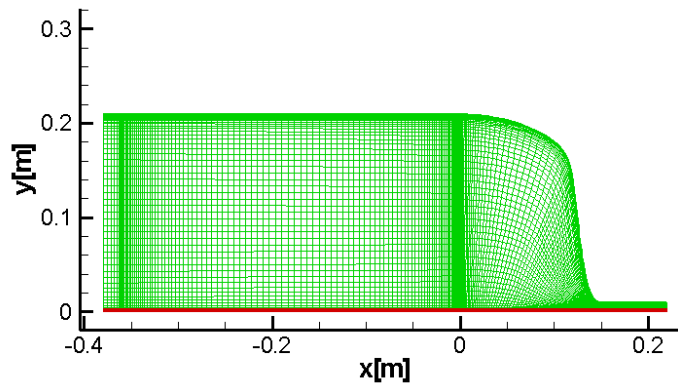


Figure 6.12.: TTMRelam: calculation grid

Fig. 6.13 shows the calculated boundary layer thickness and the geometry of the counter contour. The boundary layer thickness rises from the grid inlet with a maximum at $x = -0.14$ m before the contraction starts. Then it decreases to a level lower than the starting level at the end of the contract section at $x = 0.14$ m. There the boundary layer thickness increases again. This behaviour can be discussed in terms of the skin friction coefficient c_f and the shape factor H_{12} along the plate as shown in Fig. 6.14. The skin friction coefficient grows from the point of origin ($x = 0$ m) to the position where the boundary layer thickness has its minimum ($x = 0.14$ m), followed by a steep decrease before rising again towards the end of the plate. The shape factor shows the usual behaviour to the position of the minimum of the boundary layer thickness

where it rises to a small peak before decreasing again. All these calculated parameters and their characteristics support the assumption from experimental results, that the boundary layer starts from turbulent, relaminarises just for a short period at the end of the contracting section before getting turbulent again at the end of the test section. This agrees well with the known behaviour of accelerated flows as described schematically by Sreenivasan (1982) (see Chapter 6.2).

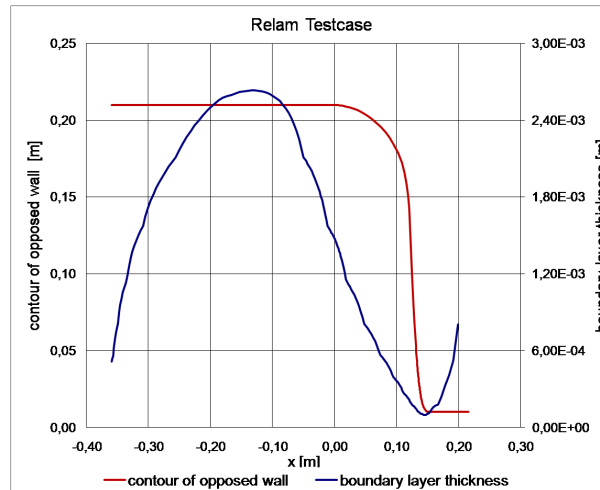


Figure 6.13.: TTMRelam: BL thickness and geometry of the counter contour

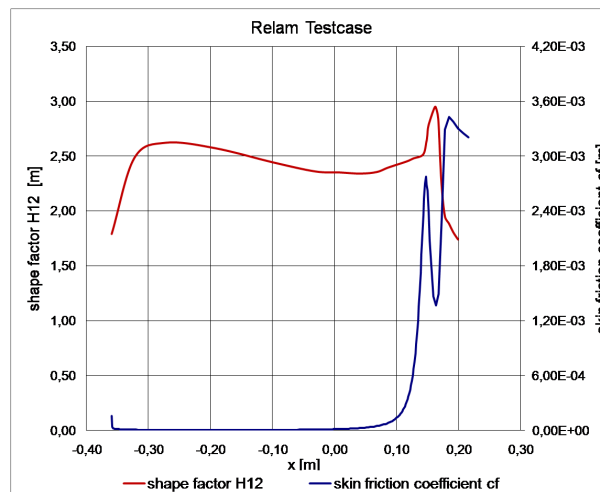


Figure 6.14.: TTMRelam:: skin friction coefficient c_f and shape factor H_{12}

So the result of the TTMRelam calculation is considered to be in good agreement with the experiments. It shows that the $\gamma - Re_\theta$ transition model is able to predict relaminarisation.

6.6. Validation of the Relaminarisation Test Case T100

The T100 turbine cascade test case was measured at the Institute for Energy Systems and Thermodynamics at Vienna University of Technology. The blade was designed for an industrial steam turbine in the high and intermediate pressure section. Hot film measurements were performed by Österreicher (2004) for the suction side and by Nichtawitz (2009) for the pressure side. In this work calculation results of the $\gamma - Re_{\theta}$ model are shown in detail only for the pressure side. The calculation results for the suction side can be found in Yagdi (2012).

6.6.1. Testcase Description: T100

The blade geometry and the positions of the hot film measurement points are shown in Fig. 6.15. The characteristic geometry data of the T100 test case are collected in Table 6.2. Table 6.3 shows the boundary conditions of that test case used in the calculations.

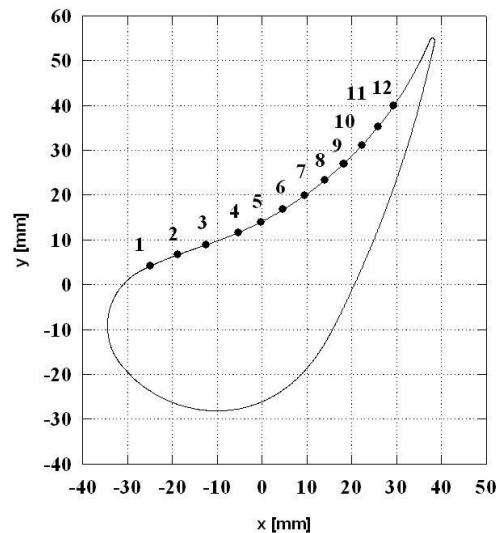


Figure 6.15.: Geometry of the T100 blade and positions of the hot film measurements, from Nichtawitz (2009)

Table 6.2.: Geometry data of the T100 cascade

chord length c	100 mm
blade thickness h	150 mm
blade pitch t	80 mm
stagger angle γ	51.5°
aspect ratio c/t	1.25

Table 6.3.: T100: Boundary conditions for the calculation

inlet total pressure $p_{totInlet}$	1.02660 bar
inlet total temperature $T_{totInlet}$	291.35 K
inlet free-stream turbulent intensity FSTI	5.0 %
outlet static pressure $p_{statOutlet}$	1.00178 bar

Hot film measurements are performed to get insight into the flow behaviour of a boundary layer. The experimental method is based on measuring the convective heat transfer of a small metal element, which is heated with the help of an electric bridge circuit. Empiric correlations allow to get a relation between convection heat and the wall shear stress (see Fig. 6.16).

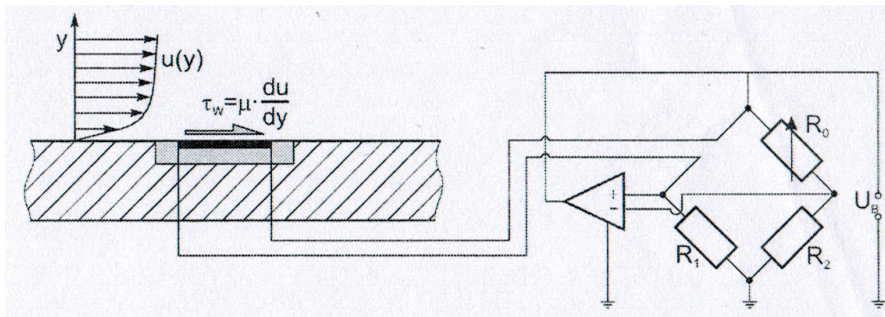


Figure 6.16.: Schematical description of the hotfilm measurement method, from Nitsche and Brunn (2005)

In Fig. 6.17 examples of the typical time signal for the different flow stages (laminar, transitional and turbulent) are shown. For laminar flow the signal is constant, if the flow is transitional there are peaks in the signal, and if the flow is turbulent the signal has a big amplitude.

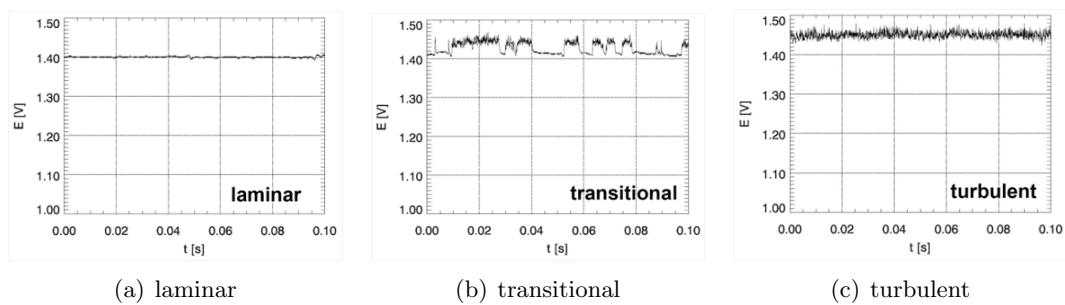


Figure 6.17.: Typical time signals of laminar, transitional and turbulent flow measured with hot film probes, from Nichtawitz (2009)

6.6.2. Experimental Results: T100

Nichtawitz (2009) performed hot film measurements on the pressure side of the T100 blade. Fig. 6.18 gives the time signals for all measurement points. From point 1 to 5 the amplitude of the fluctuations rises slightly; point 6 shows a much smaller signal amplitude than the points before. But then the rear points (7-12) show very high signal fluctuation amplitudes. This behaviour indicates that the boundary layer starts from laminar flow and gets more and more turbulent (points 1-5), before partly relaminarising near point 6 and finally transitions again to turbulent flow (points 7-12).

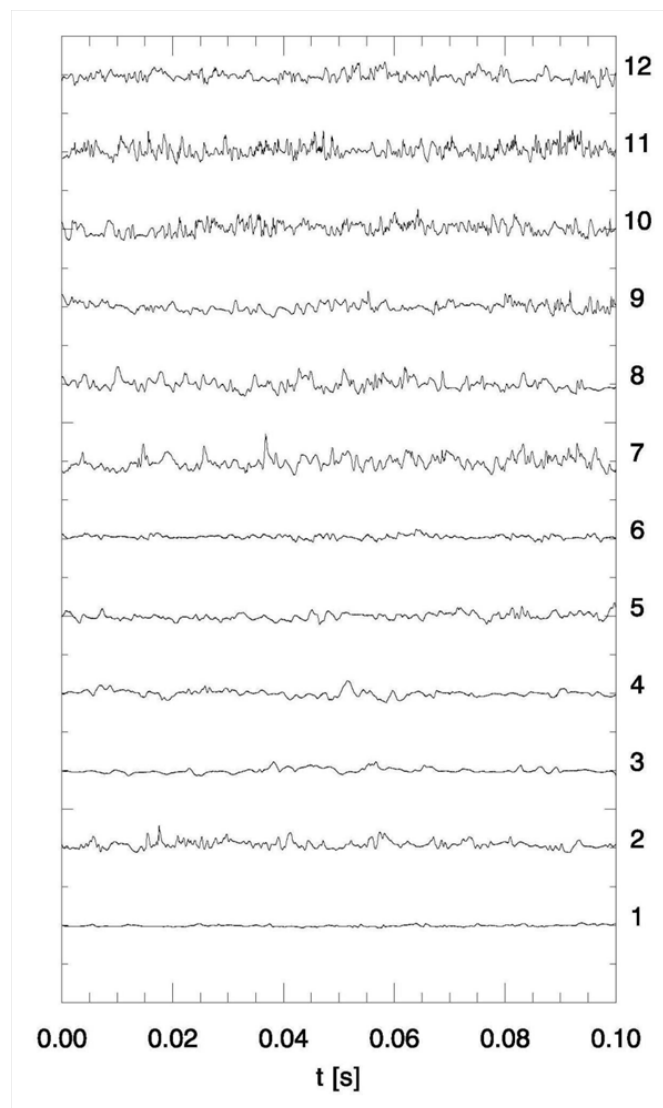


Figure 6.18.: T100 data from the hot film measurements, from Nichtawitz (2009)

6.6.3. Calculation Results: T100

This chapter presents the calculation results applying the $\gamma - Re_\theta$ transition model with the latest in-house correlation to the T100 cascade test case. Fig. 6.19 shows the calculated pressure coefficient distribution compared with the measurements and the blade geometry with the hot film measurement positions from Fig. 6.15. The pressure coefficient is defined as given in eq. 6.4. The simulated pressure side (PS) results fit well to the experimental data, whereas the pressure on the suction side (SS) is calculated slightly too low. The reason for the slight underestimation might be the fact, that this test case is an incompressible flow of very low Mach number ($Ma = 0.19$), which is calculated with a time-marching code without any preconditioning so that the outlet Mach number is set to 0.3 for convergence reasons. This procedure was also been chosen for the T106A test case presented in Paper 1 (see Chapter 4).

$$c_p = \frac{p - p_{stat,in}}{\rho U_\infty^2 / 2} \quad (6.4)$$

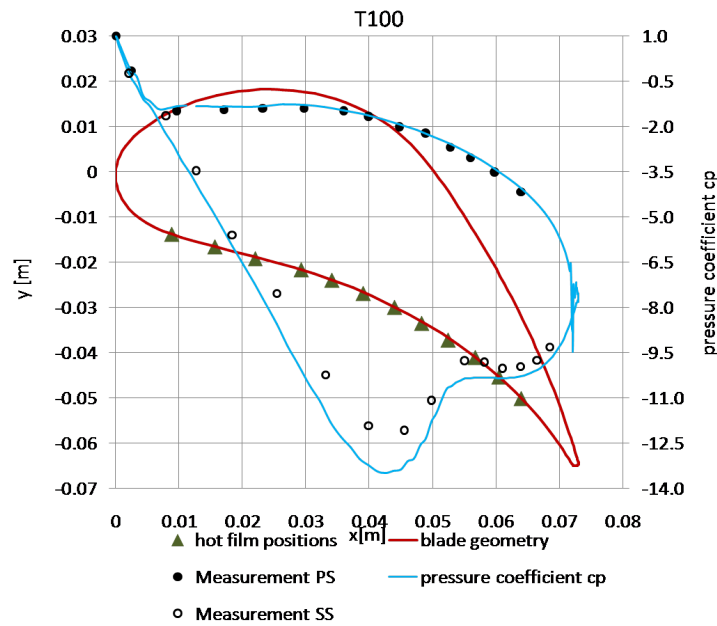


Figure 6.19.: T100 blade with pressure coefficient and hot film measurement positions

Fig. 6.20 shows the calculated shape factor H_{12} and acceleration parameter K for the T100 profile. The critical value for the acceleration parameter of $3 \cdot 10^{-6}$ is exceeded from $x = 0.032$ m to the end of the blade indicating the occurrence of relaminarisation. At the beginning the shape factor H_{12} shows a behaviour similar to the laminar boundary layer of a flat plate, where the shape factor decreases. At the position $x = 0.045$ m a peak of

the shape factor can be detected followed by an almost constant value, that is slightly higher than the value before the peak. This behaviour was also observed by Mukund et al. (2006), who explained the peak with retransition of the flow near the wall while the outer part of the boundary layer responds to the adverse pressure gradient without being affected by the onset of retransition. Although the measurements (compare measurement point 6 in Fig. 6.18) show the relaminarisation slightly earlier at position $x = 0.039$ m as shown in Fig. 6.19.

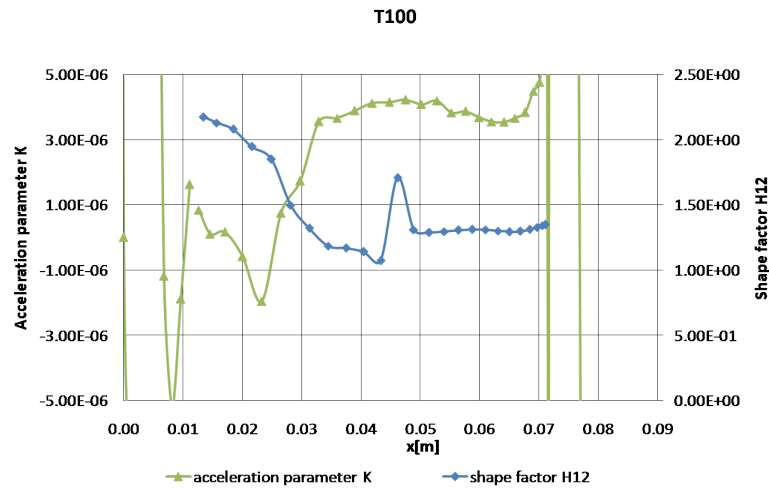


Figure 6.20.: T100 acceleration parameter K and shape factor H_{12}

Altogether the calculation results on the test case T100 agree well with the experimental measurements. Slight deviations are found in the pressure distribution on the suction side of the blade, but they can be explained by compressible effects similar to the results of the T106A turbine cascade shown in Paper 1 (Chapter 4). The acceleration factor as well as the shape factor of the calculations agree qualitatively with the work of other research groups working on relaminarisation (e.g. Mukund et al. (2006)) as well as with the hot film measurement results. Generally the $\gamma - Re_\theta$ transition model describes the relaminarisation for the T100 test case properly.

6.7. Investigation of AIDA HP Stator

The AIDA HP stator was the basis for the design of the TTM Relam test case. Because of the lack of the SA turbulence model and after the successful application of the $\gamma - Re_\theta$ transition model to the 2D test cases in the prediction of transition, the 3D test case AIDA HP stator serves as benchmark for the applicability of the $\gamma - Re_\theta$ transition model.

6.7.1. Testcase Description: AIDA HP Stator

The design of the 1.5 turbine stage AIDA was performed by MTU Aero Engines within the EU project AIDA (Aggressive Intermediate Duct Aerodynamics), which was part of the Sixth Framework Program. The whole configuration including the HP stage, the intermediate turbine duct and the LP stator was investigated at the Institute for Thermal Turbomachinery and Machine Dynamics at TU Graz. CFD studies of the tip gap influence on the flow behaviour in the intermediate turbine duct were carried out with the SA turbulence model (see Paper 5). Effects as the influence of the tip gap on the duct flow could be well predicted by the SA turbulence model. Because of the strong acceleration in the HP stator the differences between experiments and calculations can be possibly explained by relaminarisation on the HP stator. Since the SA turbulence model can not consider relaminarisation, a separate simulation of the AIDA HP stator was performed with the promising $\gamma - Re_\theta$ transition model in order to verify this assumption.

6.7.2. Calculation Results: AIDA HP Stator

This chapter presents the calculation results applying the $\gamma - Re_\theta$ transition model with the latest in-house correlation to the AIDA HP stator. In Table 6.4 the boundary conditions for the calculation, taken from the experimental data, are displayed. Fig. 6.21 shows the computed mesh for the AIDA stator calculations.

Table 6.4.: AIDA HP stator: Boundary conditions for the calculation

inlet total pressure $p_{totInlet}$	3.36 bar
inlet total temperature T_{tot}	435.0 K
inlet free-stream turbulence intensity FSTI	13.0 %
outlet static pressure $p_{statOutlet}$	1.915 bar

Fig. 6.22 shows the mid section blade geometry as well as the boundary layer thickness on the pressure side at mid section. The boundary layer thickness rises sharply close after the leading edge at $x = 0.004$ m and further increases to the location where the acceleration parameter reaches a value of $K = 2.5 \cdot 10^{-6}$ ($x = 0.016$ m) (see Fig. 6.23).

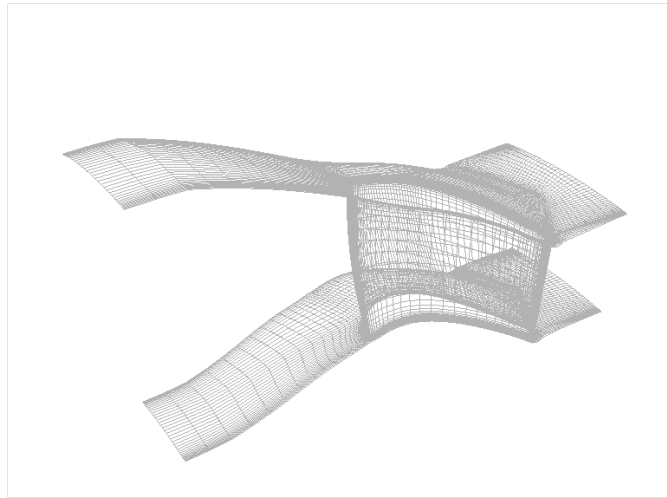


Figure 6.21.: AIDA HP stator: multiblock mesh

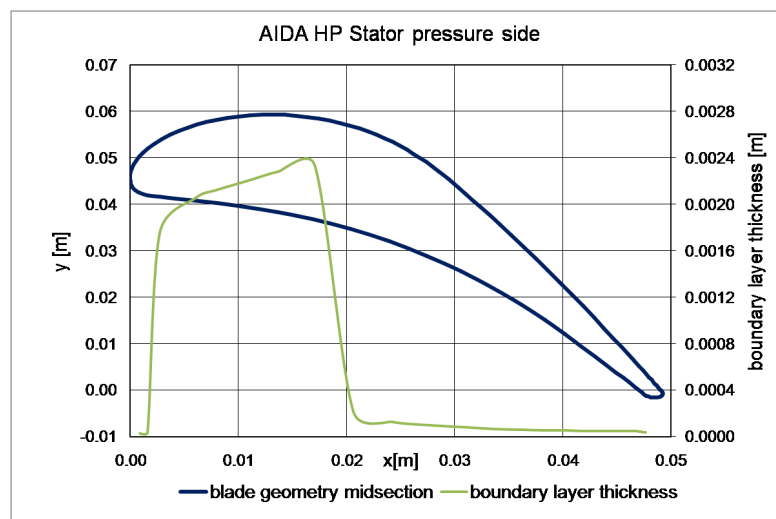


Figure 6.22.: AIDA HP stator: blade geometry at mid section and boundary layer thickness on the pressure side

Then it drops sharply to a very low level, which can be considered as a consequence of relaminarisation.

Fig. 6.23 shows the calculated acceleration parameter K and the shape factor H_{12} of the pressure side at mid section. The acceleration parameter reaches the critical value of $3 \cdot 10^{-6}$ only in a small zone near $x = 0.025$ m, but does not exceed this threshold, which means that relaminarisation might occur but not necessarily.

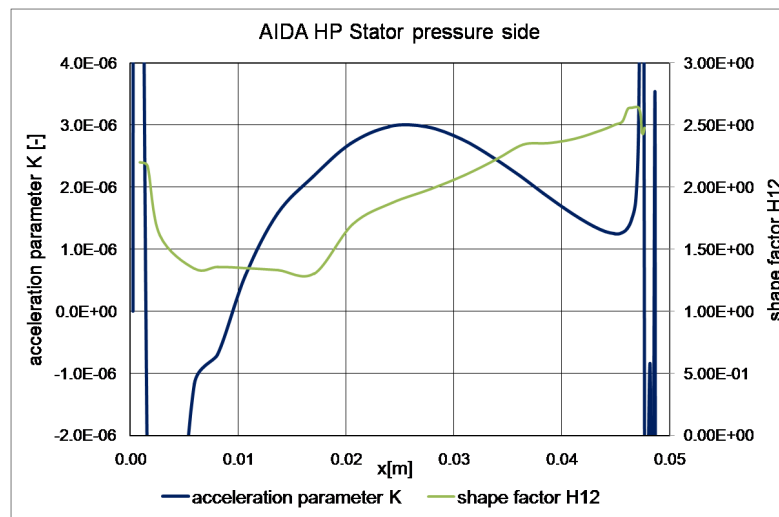


Figure 6.23.: AIDA HP stator: acceleration parameter K and shape factor H_{12} on the pressure side at mid section

The shape factor H_{12} does not give such a clear indication of relaminarisation as for the two test cases before discussed in Chapters 6.5 and 6.6. It shows a flat minimum at $x = 0.016$ m, followed by a rise of H_{12} in the same region, where the boundary layer thickness strongly decreases. Following the characterization for the accelerated relaminarisation mode by Sreenivasan (1982) the behaviour of the boundary layer thickness and of H_{12} can be interpreted more or less clearly as relaminarisation.

Keeping in mind the statement of Mayle (1991) that the acceleration parameter is not a fixed value, the author thinks that relaminarisation is also confirmed by the acceleration parameter K for the AIDA HP stator, but starting at a lower threshold $K = 2.5$. Concluding the $\gamma - Re_\theta$ calculation for this 3D test case the author interprets the results as relaminarisation in accelerated flows with the described restrictions.

7. Conclusion and Recommendations

Conclusion

The present work deals with the modeling of the transition process in turbomachinery with two different approaches and the validation for bypass transition, for separation-induced transition as well as for relaminarisation.

In Chapter 2 the basic principles of flow modeling are described, as well as the concept of the RANS equations for turbulent flow. An introduction to turbulence modeling in turbomachinery flow is given, followed by two approaches describing the Reynolds stresses, one is the so-called Reynolds Stress Transport Model (RSTM) which uses transport equations for the Reynolds stresses. The other is the Boussinesq-assumption by introducing an eddy viscosity, which is used as a basis for the description of three different turbulence models (Spalart Allmaras model, $k - \varepsilon$ model and $k - \omega$ model). In Chapter 3 an introduction to transition modelling in turbomachinery is given.

In Chapter 4 the $\zeta - f$ -model, a modern turbulence model is described in more detail. It is an enhancement of the $v^2 - f$ model which has been derived from the Reynolds stress transport model, which is a more general model considering also the turbulent anisotropy. Paper 1 and Paper 2 describe the validation of the $\zeta - f$ model for bypass-transition and for separation-induced transition using flat plate test cases as well as two 2D cascade test cases with different free-stream turbulence intensity and Re-number. Results are also compared with the $v^2 - f$ model. Both models show similar results when applying them on flat plate test cases as the T3A test case without pressure gradient, and the T3C2 test case with a pressure gradient. Applying both models on the steady transitional flow around the low pressure turbine cascade T106A the $\zeta - f$ -model performs better than the $v^2 - f$ model because the prediction of the suction side separation zone agrees much better with the measurements. The $v^2 - f$ model lacks in predicting the separation zone, and it has a too early transition to turbulence. In Paper 2 the comparison of the shape factor for two different freestream turbulent intensities (FSTI) is shown for the T106A test case using the $\zeta - f$ -model. For the lower FSTI of 0.5% the model shows a good agreement with the experiments, for the higher FSTI of 4.0% the shape factor shows a much too early transition onset.

In Chapter 5 the new $\gamma - Re_\theta$ transition model is presented in detail, as well as different correlations for closing the model originally presented by Menter et al. (2006). Correlations by Sorensen (2009), Elsner et al. (2008), Malan et al. (2009) and the authors of the original model Langtry and Menter (2009) as well as an own correlation which

was designed for the in-house code LINARS are presented and validated. Paper 3 and Paper 4 show the validation of the different correlations and the procedure of finding the author's own correlation. All model variations are validated for bypass transition and for separation-induced transition.

All correlations have a similar behaviour for the flat plate test cases. For the flat plate test cases without pressure gradient all correlations show a too early onset of the transition. For the T3C2 and the T3C4 test case a too late separation zone followed by a slightly too downstream transition to turbulent are shown, although the shown correlations show quite well fitting calculation results (compared to the experiments) in the code of the developers. For the cascade test case T106 the results are also quite similar for all compared correlations. For the lower FSTI of 0.5% all correlations show a good agreement according to the position of the separation zone and the following transition to turbulent, just with a slightly too early separation onset. For the higher FSTI of 4.0% only the Malan et al. (2009) correlation lacks in predicting the transition zone. The authors own correlation is comparable to the already published correlations.

In Chapter 6 a short introduction to the not-well-known transition mode relaminarisation is given. The shortcomings of the Spalart and Allmaras (1994) (SA) turbulence model when applied to complex flows like the flow in the AIDA configuration, where relaminarisation might occur, are discussed, although other effects can be predicted well by this model. Paper 5 shows the investigation of the influence of different tip gap heights on the following duct applying the SA turbulence model. A validation of the $\gamma - Re_\theta$ transition model introduced in Chapter 5 is presented by applying it to three different test cases where relaminarisation occurs. For the 2D test cases (TTMRelam, T100), the $\gamma - Re_\theta$ transition model with the author's latest correlations could give good results in describing relaminarisation, whereas the simulation of the 3D AIDA HP stator flow shows partly satisfying results, although the assumption of a relaminarisation in the HP stator could be confirmed.

Recommendations

As White (1974) already stated in his book *"... the final report on transition may never be handed in ..."* the author interprets this work as part of getting closer to the *final report*. And also Bradshaw (1998) stated in his speech at the ASME ME'98 Meeting in Anaheim, CA/USA *"The user of a turbulence model is more like a test pilot than a sunny Sunday Cessna flier"*. Indeed, to find a suitable prediction method for transition, much work has already been and still has to be done. Modeling transition with RANS and empiric correlations will maybe never lead to a generally valid procedure, but it can become a very useful engineering tool.

A. Appendix

How to determine the BL thickness?

Method of Arnone and Pacciani

The calculation of the boundary layer thickness suggested by Arnone and Pacciani (1996) (see also Fig. A.1) is described by a distribution function $G_{(y)}$ as follows:

$$G_{(y)} = \frac{1}{y} \int_0^y \Omega D_{\nu,D} dy \quad (\text{A.1})$$

with the damping function $D_{\nu,D}$ by Van Driest (1956):

$$D_{\nu,D} = 1 - \exp\left(-\frac{y^+}{A^+}\right) \quad (\text{A.2})$$

with the parameters

$$A^+ = 26 \quad y^+ = y \frac{u_\tau \rho_w}{\mu_w} \quad u_\tau = \sqrt{\frac{\tau_w}{\rho_w}} \quad (\text{A.3})$$

$$\Omega_{ij} = 0.5 \left(\frac{\partial u_i}{\partial x_j} - \frac{\partial u_j}{\partial x_i} \right)$$

With this equations the distribution of $G_{(y)}$ can be calculated along each mesh line normal to the wall. The position of the maximum of this function indicates the boundary layer edge. Using the quadratic interpolation computing the y_{max} value, the boundary layer thickness δ can be calculated as follows:

$$\delta = 1.145 \cdot y_{max} \quad (\text{A.4})$$

The displacement thickness δ^* is defined as follows:

$$\delta^* = \int_0^y \left(1 - \frac{\rho}{\rho_\infty} \frac{u}{U_\infty} \right) dy \quad (\text{A.5})$$

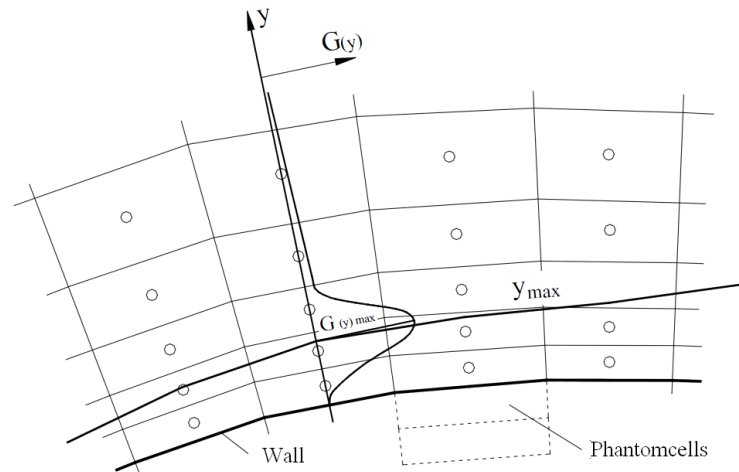


Figure A.1.: Boundary layer thickness calculation, from Pecnik (2001)

The momentum thickness θ is defined as follows:

$$\theta = \int_0^y \frac{\rho}{\rho_\infty} \frac{u}{U_\infty} \left(1 - \frac{u}{U_\infty}\right) dy \quad (\text{A.6})$$

This method was used to calculate the boundary layer thickness in Chapter 6.

Method of Schobeiri and Ozturk (2009)

Another method of calculating the boundary layer thickness was suggested by Schobeiri and Ozturk (2009). This method is an iterative method. Fig. A.2 shows the velocity distribution on the pressure side (PS) and the suction side (SS).

Using a least square fit to find the intersection between the velocity profile outside the boundary layer and the u -axis by applying the following formula for the area F^1 , is starting from a guessed value for δ^1 :

$$F^1 = \int_0^{\delta^1} (U_{pot} - u) dy \quad (\text{A.7})$$

Iteratively very small increments are used for the next δ^i and the area F^i is calculated

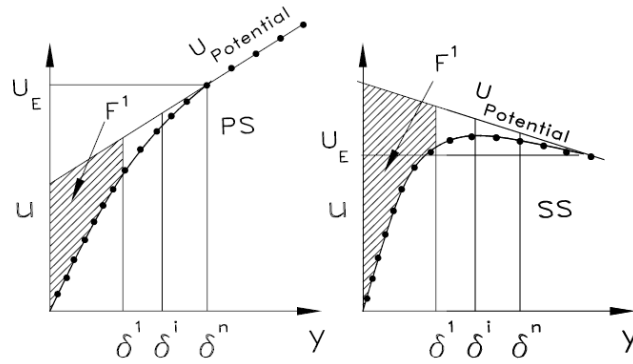


Figure A.2.: Boundary layer edge velocity on pressure and suction side, from Schobeiri and Ozturk (2009)

as follows:

$$F^i = \int_0^{\delta^i} (U_{pot} - u) dy \quad (\text{A.8})$$

With the help of the following ratio and the accuracy ϵ the boundary layer thickness can be calculated.

$$R = \frac{F^i - F^{i+1}}{F^i} \leq \epsilon = 10^{-6} \quad (\text{A.9})$$

With this boundary layer thickness additional validation parameters (e.g. shape factor H_{12} , etc.) can be calculated.

This method was used to calculate the boundary layer thickness for Paper 2.

Bibliography

- B. J. Abu-Ghannam and R. Shaw. Natural transition of boundary layers – the effects of turbulence, pressure gradient and flow history. *Journal of Mechanical Engineering Science*, 22:213–228, 1980.
- V. Adumitroaie, J. R. Ristorcelli, and D. B. Taulbee. Progress in Favré-Reynolds Stress Closures for Compressible Flows. Technical Report TR-98-21, ICASE, NASA Langley Research Center, Hampton, VA, 1998.
- A. Arnone and R. Pacciani. Igv-rotor interaction analysis in a transonic compressor using the navier-stokes equations. In *ASME Turbo Expo 1996, paper 96 – GT -141*, 1996.
- C. Bourassa, F.O. Thomas, and Nelson R.C. Experimental Investigation of Turbulent Boundary Layer Relaminarization with Application to High-Lift Systems: Preliminary Results. *AIAA Paper 2000-4017*, 2000.
- J. Boussinesq. Theorie de l'Écoulement tourbillant. *présentés par Diverse Savants à l'Académie des Sciences de l'Institut de France*, 23:46–50, 1877.
- R.J. Boyle and F.F. Simon. Mach number effects on turbine blade transition length prediction. In *ASME Turbo Expo 1998, paper 98-GT-367*, 1998.
- P. Bradshaw. Highlights of Turbulence Modelling...-... Or, You Don't Get What You Don't Pay For. In *ASME "ME'98" Meeting Anaheim CA*, November 1998.
- R. Brandt. *Relaminarisation of Turbulent Boundary Layers*. PhD thesis, University of Cambridge, 1993.
- P.Y. Chou. On velocity correlations and the solutions of the equations of turbulent fluctuations. *Quarterly Applied Mathematics*, 3(1):38–54, 1945.
- S. Dhawan and R. Narasimha. Some Properties of Boundary Layer Flow During Transition from Laminar to Turbulent Motion. *Journal of Fluids Engineering*, 3:418–436, 1958.
- S. Dorfer. Auslegung und experimentelle Untersuchung eines Relaminisierungs - Testfalls. Master's thesis, Institute for Thermal Turbomachinery and Machine Dynamics - Graz University of Technology, 2011.

- P. A. Durbin. Near-wall turbulence modeling without damping functions. *Theoretical and Computational Fluid Dynamics*, 3:1–13, 1991.
- P. A. Durbin. A Reynolds stress model for near-wall turbulence. *Journal of Fluid Mechanics*, 249:465–498, 1993.
- P.A. Durbin and B.A. Pettersson Reif. *Statistical Theory and Modeling for Turbulent Flows*. John Wiley & Sons Ltd, 2001.
- W. Elsner, W. Piotrowski, and S. Drobniak. Transition prediction on turbine blade profile with intermittency transport equation. In *ASME Turbo Expo 2008, Berlin, Germany, paper GT 2008-50796*, 2008.
- R. Emmons. The laminar-turbulent transition in boundary layer – Part I. *Journal of the Aeronautical Sciences*, 18:490–498, 1951.
- A. Favré. Equations des gaz turbulents compressibles. *Journal de Mécanique*, 4:361–390, 1965.
- M. Gad-el Hak. *Flow control : passive, active, and reactive flow management*. Cambridge University Press, 2000.
- E. Göttlich, F. J. Malzacher, F. J. Heitmeir, and A. Marn. Adaptation of a Transonic Test Turbine Facility for Experimental Investigation of Aggressive Intermediate Turbine Duct Flows. In *AIAA Paper No. ISABE-2005-1132*, 2005.
- E. Göttlich, A. Marn, R. Pecnik, F. J. Malzacher, O. Schennach, and H. P. Pirker. The Influence of Blade Tip Gap Variation on the Flow Through an Aggressive S-Shaped Intermediate Turbine Duct Downstream a Transonic Turbine Stage - Part II: Time-Resolved Results and Surface Flow. In *ASME Turbo Expo 2007, Montreal, Canada, Paper No. GT2007-28069*, 2007.
- K. Hanjalić. *Turbulence And Transport Phenomena - Modelling and Simulation*. Technical report, Darmstadt, 2005.
- K. Hanjalić, M. Popovac, and M. Hadžiabdić. A robust near-wall elliptic-relaxation eddy-viscosity turbulence model for CFD. *International Journal of Heat and Fluid Flow*, 25:1047–1051, 2004.
- H. Hoheisel. Entwicklung neuer Entwurfskonzepte zweier Turbinengitter - Teil III: Ergebnisse T106. Technical Report Measurement Report 129-81/26, Institute of Design Aerodynamics, University Braunschweig, 1982.
- H. Hoheisel. Test Case E/CA-6 Subsonic Turbine Cascade T106. *Test Cases for Computation of Internal Flows in Aero Engine Components, AGARD AR-275*, pages 112–123, July 1990.
- P. G. Huang and Y. B. Suzen. An Intermittency Transport Equation for Modelling Flow Transition. *AIAA Paper*, 287, 2000.

- M. Ichimiya, I. Nakamura, and S. Yamashita. Properties of a relaminarizing turbulent boundary layer under a favorable pressure gradient. *Experimental Thermal and Fluid Science*, 17:37–48, 1998.
- M. Kato and B. E. Launder. The Modeling of Turbulent Flow Around Stationary and Vibrating Square Cylinders. In *Proc. 9th Symposium on Turbulent Shear Flows, Kyoto*, pages 1041–1046, 1993.
- S. Köberl. *Development and Application of Interferometric Measurement Techniques for Multi-Flame Gas Turbine Combustion*. PhD thesis, Institute of Thermal Turbomachinery and Machine Dynamics, Graz University of Technology, 2011.
- M.E. Kelterer, R. Pecnik, and W. Sanz. Computation of Laminar-Turbulent Transition in Turbomachinery Using The Correlation Based $\gamma - Re_\theta$ Transition Model. In *ASME Turbo Expo 2010, Glasgow, Scotland, paper GT2010-22207*, 2010.
- S. Kikuchi, M. Shimoji, H. Watanabe, and Y. Kohama. Control of Bypass Transition for Textile Surface. *JSME International Journal - Series B*, 417:777–785, 2004.
- J.P. Kreskovsky, S.J. Shamroth, and H. McDonald. Parametric Study of Relaminarization of Turbulent Boundary Layers On Nozzle Walls. Technical Report NASA CR-2370, United Aircraft Research Laboratories, East Hartford, CO, 1974.
- S. Kubacki, K. Lodefier, R. Zarzycki, W. Elsner, and E. Dick. Further Development of a Dynamic Intermittency Model For Wake-Induced Transition . *Flow, Turbulence and Combustion*, 83:539–568, 2009.
- R.B. Langtry. *A Correlation-Based Transition Model using Local Variables for Unstructured Parallelized CFD codes*. PhD thesis, Institute of Thermal Turbomachinery and Machinery Laboratory, University Stuttgart, 2006.
- R.B. Langtry and F.R. Menter. Correlation-Based Transition Modelling for Unstructured Parallelized Computational Fluid Dynamics Code. *AIAA Journal*, 47(12):2894–2906, December 2009.
- R.B. Langtry, F.R. Menter, S.R. Likki, Y.B. Suzen, P.G. Huang, and S. Völker. A Correlation Based Transition Model Using Local Variables Part 2: Test Cases and Industrial Applications. *Journal of Turbomachinery*, 128(3):423–434, 2006.
- B.E. Launder and B.I. Sharma. Application of the energy-dissipation model of turbulence to the calculation of flow near a spinning disc. *Lett.Heat Mass Transf.*, 1:131–138, 1974.
- J.R. Lücke. *Turbulenzmodellierung zur Berechnung abgelöster Strömungen in Turbomaschinen*. PhD thesis, RWTH Aachen, 1997.
- F.S. Lien and P.A. Durbin. Non-linear $k - \varepsilon - v^2$ modeling with application to high-lift. In *Proceedings of the Summer Program 1996, Center for Turbulence Research, NASA-Ames/Stanford University*, pages 5–26, 1996.

- F.S. Lien, G. Kalitzin, and P.A. Durbin. RANS modeling for compressible and transitional flows. In *Proceedings of the Summer Program 1998, Center for Turbulence Research, NASA-Ames/Stanford University*, pages 267–286, 1998.
- K. Lodefier and E. Dick. Modelling of unsteady transition in low-pressure turbine blade flows with two dynamic intermittency equations. *Flow, Turbulence and Combustion*, 76:103–132, 2005a.
- K. Lodefier and E. Dick. An unsteady rans transition model with dynamic description of intermittency. In *ASME Turbo Expo 2005, Reno-Tahoe, NV, paper GT 2005-68714*, 2005b.
- P. Malan. Private Communication, 2010.
- P. Malan, K. Suluksna, and E. Juntasaro. Calibrating the gamma-ReTheta Transition Model for Commercial CFD. In *AIAA Paper 2009-1142*, 2009.
- A. Marn. *On the Aerodynamics of Aggressive Intermediate Turbine Ducts for Competitive and Environmentally Friendly Jet Engines*. PhD thesis, Institute of Thermal Turbomachinery and Machine Dynamics, Graz University of Technology, 2008.
- A. Marn, E. Göttlich, R. Pecnik, F. J. Malzacher, O. Schennach, and H. P. Pirker. The Influence of Blade Tip Gap Variation on the Flow Through an Aggressive S-Shaped Intermediate Turbine Duct Downstream a Transonic Turbine Stage - Part I: Time-Averaged Results. In *ASME Turbo Expo 2007, Montreal, Canada, Paper No. GT2007-27405*, 2007.
- R. E. Mayle. The role of laminar-turbulent transition in gas turbine engines. *Journal of Turbomachinery*, 113:509–537, 1991.
- F.R. Menter. Two-Equation Eddy-Viscosity Turbulence Models for Engineering Applications. *AIAA Journal*, 32(8):1598–1605, August 1994.
- F.R. Menter. A Comparison of Some Recent Eddy-Viscosity Turbulence Models. *Journal of Fluid Engineering*, 118:514–519, September 1996.
- F.R. Menter, T. Esch, and S. Kubacki. Transition Modelling Based on Local Variables. In *Proceedings of the 5th International Symposium on Engineering Turbulence Modelling and Measurements, Elsevier, Amsterdam*, pages 555–564, 2002.
- F.R. Menter, R.B. Langrty, S.R. Likki, Y.B. Suzen, P.G. Huang, and S. Völker. A Correlation Based Transition Model Using Local Variables Part 1: Model Formulation. *Journal of Turbomachinery*, 128(3):413–422, 2006.
- R. Mukund, P.R. Visvanath, R. Narasimha, A. Prabhu, and J.D. Crouch. Relaminarization in highly favourable pressure gradients on a convex surface. *Journal of Fluid Mechanics*, 566:97–115, 2006.

- R. Narasimha and K.R. Sreenivasan. Relaminarization of Fluid Flows. *Advances in Applied Mechanics*, 19:221–309, 1979.
- M. Nichtawitz. Messung der Relaminarisierung der druckseitigen Grenzschicht einer Turbinenschaufel mittels Heißfilmanemometrie. Master's thesis, Institute for Energy Systems and Thermodynamics - Vienna University of Technology, 2009.
- W. Nitsche and A. Brunn. *Strömungsmesstechnik*. Springer, 2005.
- M. M. Opoka and H. H. Hodson. An experimental investigation of the unsteady transition process on the high lift t106a turbine blade. In *ISABE 2005, Munich, Germany, paper ISABE-2005-1277*, 2005.
- R. Pecnik. Modellierung der Transition mit Hilfe eines Eingleichungs-Transportansatzes. Master's thesis, Institute for Thermal Turbomachinery and Machine Dynamics - Graz University of Technology, 2001.
- R. Pecnik. *Transitionsmodellierung in thermischen Turbomaschinen*. PhD thesis, Institute for Thermal Turbomachinery and Machine Dynamics - Graz University of Technology, 2007.
- R. Pecnik, W. Sanz, A. Gehrler, and J. Woisetschläger. Modeling of Laminar-Turbulent Transition Using Two Different Intermittency Transport Equations. *Flow, Turbulence and Combustion*, 70:299–323, 2003.
- B.S. Pope. *Turbulent Flows*. Cambridge University Press, 2000.
- L. Prandtl. Über die ausgebildete Turbulenz. *Zeitschrift für Angewandte Mathematik und Mechanik*, 5:136–139, 1925.
- K. Ramadani. Transitionsmodellierung in thermischen Turbomaschinen. Master's thesis, Institute for Energy Systems and Thermodynamics - Vienna University of Technology, 2007.
- O. Reynolds. On the dynamical theory of incompressible viscous fluids and the determination of the criterion. *Philosophical Transactions of the Royal Society of London, Series A*, 186:123–164, 1895.
- D.-H. Rhee and H.H. Cho. Local heat/mass transfer characteristics on a rotating blade with flap tip in a low speed annular cascade: Part1 Near-Tip Surface. In *ASME Turbo Expo 2005, Reno-Tahoe, Nevada, USA, paper GT 2005-68723*, 2005.
- J. Rotta. Statistische Theorie nichthomogener Turbulenz I. *Zeitschrift für Physik*, 129: 547–572, 1951.
- J.C. Rotta. *Turbulente Strömungen*. B.G. Teubner Stuttgart, 1972.
- A.M. Savill. A synthesis of T3 Test Case Predictions. In *Numerical Simulation of Unsteady Flows and Transition to Turbulence*, pages 404–442. Cambridge University Press, editors: Pironneau O. et al., 1992.

- H. Schlichting and K. Gersten. *Genzschicht-Theorie*. Springer, 1997.
- M.T. Schobeiri and B. Ozturk. Experimental Study of the Effects of Periodic Unsteady Wakes on Flow Separation in Low Pressure Turbines. Technical Report NASA/CR-2009-214831, NASA Glenn Research Center, 2009.
- G.B. Schubauer and P.S. Klebanoff. Contribution to the Mechanism of Boundary-Layer Transition. Technical Report NACA TN 3489, NACA, 1955.
- S. Shin. *Reynolds-Averaged Navier-Stokes Computation of Tip Clearance Flow in a Compressor Cascade Using an Unstructured Grid*. PhD thesis, Virginia Polytechnic Institute and State University, Blacksburg, Virginia, USA, 2001.
- N.N. Sorensen. CFD Modelling of Laminar-turbulent Transition for Airfoils and Rotors - Using the $\gamma\text{-}\tilde{\text{Re}}_\theta$ Model. *Wind Energy*, 2009.
- P.R. Spalart and S.R. Allmaras. A One Equation Turbulence Model for Aerodynamic Flows. *La Recherche Aerospaciale*, 1:5–21, 1994.
- C. G. Speziale, S. Sarkar, and T.B. Gatski. Modelling the pressure-strain correlation of turbulence: An invariant dynamical systems approach. *J. Fluid Mech.*, 227:245–272, 1991.
- K. R. Sreenivasan. Laminarescent, relaminarizing and retransitional flows. *Acta Mech.*, 44:1–48, 1982.
- J. Steelant and E. Dick. Modeling of Bypass Transition with Conditioned Navier-Stokes Equations coupled to an Intermittency Equation. *International Journal for Numerical Methods in Fluids*, 23:193–220, 1996.
- J. Steelant and E. Dick. Modeling of Laminar-Turbulent Transition for High Freestream Turbulence. *Journal of Fluids Engineering*, 123(1):22–30, 2001.
- W. Österreicher. Messung des laminar/turbulent-Übergangs an Turbinenschaufeln mittels Heißfilmanemomentrie. Master's thesis, Institute for Energy Systems and Thermodynamics - Vienna University of Technology, 2004.
- R.D. Stieger. *The Effects of Wakes on Separating Boundary Layers in Low Pressure Turbines*. PhD thesis, Cambridge University Engineering Department, February 2002.
- E.R. Van Driest. On Turbulent Flow Near a Wall. *Journal of Aeronautical Sciences*, 123, 1956.
- C. Wang and B. Perot. Prediction of turbulent transition in boundary layers using the turbulent potential model. *Journal of Turbulence*, 3, 2002.
- F.M. White. *Viscous Fluid Flow*. McGraw-Hill, 1974.
- D.C. Wilcox. Reassessment of the scale determining equation for advanced turbulence models. *AIAA Journal*, 27(11):1299–1310, 1988.

D.C. Wilcox. *Turbulence Modeling for CFD*. DCW Industries, Inc, 2002.

B. Yagdi. Numerische Untersuchung von Transition in Turbinenkaskaden. Master's thesis, Institute for Thermal Turbomachinery and Machine Dynamics - Graz University of Technology, 2012.

Curriculum Vitae

Maria Elisabeth Collins

Personal:

Date of birth: March 24, 1984
Place of birth: 8020 Graz, Austria
Citizenship: Austria
Maiden name: Kelterer
Family status: married with Herbert Collins

Education:

09/02 - 09/06 University for Applied Sciences in Graz/Austria
Study Course: Aviation
Certificate: Diplom-Ingenieur
09/06 - 07/12 Graz University of Technology
Department for Thermal
Turbomachinery and Machine Dynamics
Doctoral Student

Research Experience:

03/08 - 08/11 Research Assistant at the Department for Thermal
Turbomachinery and Machine Dynamics
Graz University of Technology

Profession:

09/11 - 05/12 CFD engineer at VACE in Linz/Austria
06/12 - current research engineer at Andritz Hydro GmbH in Linz/Austria

Programming Skills:

C/C++, FORTRAN, Visual Basic